Analysis of the wave-plasma interaction in electrodeless plasma thrusters

---

by

Pedro Jiménez

A dissertation submitted by in partial fulfillment of the requirements for the degree of Doctor of Philosophy in

Aerospace Engineering

uc3m | Universidad Carlos III de Madrid

Advisors:
Mario Merino
Eduardo Ahedo

Tutor:
Mario Merino

March 2024

To my family.

Acknowledgements

Being so lucky and grateful as I am to so many people, this was one of the most challenging parts of my thesis to write. Words cannot fully express my gratitude, but I will try:

My colleagues at Universidad Carlos III, especially my friends from the brilliant, yet natural, and easy-going class of 2018, they gave me unforgettable times. A special mention goes to Javier, David, Pau, Alex, Dani, and Guille, who remain very good friends. I hope our ski trips resume soon. To Alberto, who has been with me since our Bachelor's days and continues as my coworker, I wish for more opportunities to work together in the future. Brainstorming and learning with you have been among the most inspiring moments of my PhD years. I must also mention Álvaro Sánchez, whose excellent work laid the groundwork for this thesis, and whose counsel was always invaluable; I hope we meet again soon. Jiewei and Adrian, your help meant a lot, and working with Jaume and Pablo was a genuine pleasure; together, you made HIPATIA possible. Also, thanks to many others like Scherezade, Marco, Borja, Matteo, and Jesus, who, although not working directly with me, are great friends and colleagues, contributing to the amazing atmosphere at the Plasma and Space Propulsion team.

Luis Chacon hosted me at Los Alamos National Laboratory with incredible generosity. He spent many hours with me in the lab, making what could have been years of work possible in a few months. My time in New Mexico was the most satisfying of these four years, not only due to my growth as a researcher, but also because of the amazing people I met. My friend Giovanni, Luis' family, his collaborators, and so many others... You have made beautiful New Mexico forever memorable, and I will definitely go back.

My mentor and brilliant professor, Mario Merino, has been key in my professional development. He has always bet on my skills and potential, even in tough times when results came slow. Eduardo Ahedo has always been a role model, and I have learned so much from him. Both have been kind and supportive of my ambitions, teaching me almost everything I know about research.

Last but not least, thanks to my incredibly supportive family. My parents, who have always encouraged my curiosity and education. And my brother, who is both my companion in adventures and my best friend. To my childhood and still best friends, Javier, Fernando, Ernesto, Isma, and Carlos; our years together have been key to my being here today. As the saying goes, "You are the average of the five people you spend the most time with". And Mónica, who appeared later in my life but has since shaped it profoundly. She is the person with whom I can share projects and dreams, my perfect companion, propelling me to new heights. Together, we are the dream team.

Pedro Jiménez
Madrid, January 2024

The research activities leading to the results presented in this thesis have been primarily funded within the HIPATIA (grant agreement 87054) and ZARATHUSTRA (grant agreement 950466) projects, both of which are part of European Union's Horizon 2020 Research and Innovation Program. Initial research funding also came from PROMETEO project, funded by the Comunidad de Madrid, under grant reference Y2018/NMT-4750 PROMETEO-CM. The work of Pedro Jiménez was partially funded by the Spanish Ministry of Science, Innovation and Universities under the FPU Scholarship Program with grant FPU19/05658. Furthermore, the same program funded the research stay carried out by the candidate at Los Alamos National Laboratory in the summer of 2022.

Published and submitted content

Scientific Journals

[1] Jiménez, P., Merino, M., & Ahedo, E. (2022). Wave propagation and absorption in a helicon plasma thruster and its plume. *Plasma Sources Science and Technology*, 31(4), 045009. DOI: 10.1088/1361-6595/ac5ecd

This work constitutes Chapter 4 of this document.

Jiménez, P.: Investigation, Writing-Original draft preparation, Methodology, Software. **Merino, M.**: Conceptualization, Methodology, Writing-Reviewing, and Editing. **Ahedo, E.**: Conceptualization, Methodology, Writing-Reviewing, and Editing.

The authors want to thank the developers of the HYPHEN code, especially J. Zhou and A. Domínguez-Vázquez. The work of Pedro Jiménez has been supported by the HIPATIA project, funded by the European Union's Horizon 2020 Research and Innovation Program, under Grant Agreement number 870542. The work of Mario Merino and Eduardo Ahedo has been supported by the PROMETEO project, funded by the Comunidad de Madrid, under Grant reference Y2018/NMT-4750 PROMETEO-CM.

[2] Jiménez, P., Zhou, J., Navarro, J., Fajardo, P., Merino, M., & Ahedo, E. (2023). Analysis of a cusped helicon plasma thruster discharge. *Plasma Sources Science and Technology*, 32(10), 105013. DOI: 10.1088/1361-6595/ad01da

This work constitutes Chapter 5 of this document.

Jiménez, P.: Investigation, Writing- Original draft preparation, Methodology, Software. **Zhou, J.**: Software, Methodology. **Navarro, J.**: Investigation, Data Curation. **Fajardo, P.**: Supervision, Project administration. **Merino, M.**: Conceptualization, Methodology, Writing-Reviewing, and Editing. **Ahedo, E.**: Conceptualization, Methodology, Writing-Reviewing, and Editing.

The authors would like to thank Adrian Dominguez-Vazquez for his useful comments, especially on the use of the HYPHEN simulation code. Initial support for the activities leading to work came from the HIPATIA project, funded by the European Union's Horizon 2020 Research and Innovation Program, under Grant Agreement number 870542. The completion of this work was carried out with funding from the European Research Council (ERC) under the European Union's Horizon 2020 research and innovation programme (grant agreement No 950466, project ZARATHUSTRA)

[3] Jimenez, P., Chacon, L., & Merino, M. (2023). An implicit, conservative electrostatic particle-in-cell algorithm for paraxial magnetic nozzles. *Journal of Computational Physics*, 112826. DOI: 10.1016/j.jcp.2024.112826

This work constitutes Chapter 6 of this document.

Pedro Jimenez: Conceptualization, Methodology, Software, Validation, Writing-Original

draft preparation. **Luis Chacon**: Methodology, Software, Validation, Writing- Reviewing and Editing. **Mario Merino**: Methodology, Validation, Writing- Reviewing and Editing.

The authors would like to thank Jiewei Zhou and Eduardo Ahedo at Universidad Carlos III de Madrid and Guangye Chen and Oleksandr Koshkarov at Los Alamos National Laboratory for the insightful discussions and inputs. PJ and MM were funded by the European Research Council (ERC) under the European Union's Horizon 2020 research and innovation programme (grant agreement No 950466). LC was funded by the Applied Mathematics Research program of the Department of Energy Office of Applied Scientific Computing Research, and the research was performed under the auspices of the National Nuclear Security Administration of the U.S. Department of Energy at Los Alamos National Laboratory, managed by Triad National Security, LLC under contract 89233218CNA000001. Funding for APC: Universidad Carlos III de Madrid (Agreement CRUE-Madroño 2024).

Other Research Merits

Publications in International Conference Proceedings

[1] *36th International Electric Propulsion Conference, Vienna, Austria, 2019*. J. Zhou, P. Jiménez, M. Merino, P. Fajardo & E. Ahedo. Numerical simulations of the plasma discharge in a helicon plasma thruster.

[2] *7th Edition of the Space Propulsion Conference (SPC 2020+1). March 2021, France.* Jiménez, P., Merino, M., & Ahedo, E.. Preliminary investigation of the electromagnetic fields in the far plume of a Helicon Plasma Thruster.

[3] *The 56th Annual Microwave Power Symposium. Savannah, GA, June 2022: International Microwave Power Institute (IMPI), 2022*. Mario Merino, Pedro Jiménez, Célian Boyé, Marco Riccardo Inchingolo, Jaume Navarro-Cavallé, Jiewei Zhou, and Eduardo Ahedo. Radiofrequency Plasma Heating For Electrodeless Space Thruster Applications.

[4] *37th International Electric Propulsion Conference. IEPC-2022-498. Boston, MA, June 19-23: Electric Rocket Propulsion Society, 2022.* Pedro Jiménez, Jiewei Zhou, Pablo Fajardo, Mario Merino, and Eduardo Ahedo. Numerical Simulations of the Discharge and the Plasma-wave Interaction in a Helicon Plasma Thruster.

[5] *IEEE International Conference on Plasma Science (ICOPS). Santa Fe, New Mexico (USA), May 21–25, 2023*. Pedro Jiménez, Luis Chacón, and Mario Merino. Implicit conservative particle-in-cell kinetic simulations of magnetic nozzles.

Research Stays

- Los Alamos National Laboratory, Applied Mathematics and Plasma Physics Group. Supervised by Luis Chacon, Ph.D., May - September 2022, Los Alamos (NM), USA.

Abstract

The presented thesis contributes to the understanding and numerical modeling of electrodeless plasma thrusters (EPTs). With an approach that combines mid-fidelity fast simulation software and fundamental research models capturing a wider range of phenomena, the study tackles the current modeling needs of the electric propulsion community and presents new insights into the physics of these devices.

The understanding of the physics and the modeling of electromagnetic wave-plasma interaction phenomena is at the forefront of the research. The study starts with an in-depth analysis of the cold-plasma dielectric tensor model, tailored to understand wave propagation in Helicon Plasma Thrusters (HPT). A central development is the introduction of PWHISTLER, a full-wave simulation tool employing the finite element (FE) method. This model stands out for its improved speed, accuracy, and ability to handle complex geometries, significantly improving the modeling of electromagnetic phenomena in magnetized plasmas. Notable new features compared to previous models include the introduction of azimuthal Fourier modes and waveport boundary conditions.

Detailed analyses using both a finite-difference (FD) and the above-mention model underscore their effectiveness in characterizing wave propagation and absorption in HPTs, with a key finding being the concentrated power absorption at the electron-cyclotron resonance (ECR) surface that appears in downstream plume.

The integration of PWHISTLER with the HYPHEN plasma transport solver facilitates a comprehensive study of a novel cusp magnetic HPT field topology. The simulations, verified against experimental data, offer insights into performance losses and thrust efficiency, highlighting the role of plasma currents to walls, the electron temperature, and the magnetic ring cusp's influence.

Finally, the study presents the formulation of an advanced implicit particle-in-cell (PIC) algorithm, specifically designed for magnetic nozzles. This innovative approach in the Electric Propulsion (EP) field significantly enhances computational efficiency, marking a step in the simulation and optimization of magnetic nozzles for EPTs and paving the way for future studies of other EP systems.

Resumen

La tesis presentada contribuye a la comprensión y el modelado numérico de propulsores de plasma sin electrodos (EPTs). Con un enfoque dual que combina herramientas prácticas de diseño y modelos de investigación fundamental, este trabajo ofrece un conjunto de herramientas versátil y completo para avanzar el estado del arte en física de plasmas de baja temperatura aplicada a propulsión eléctrica.

El núcleo de la investigación lo constituyen los avances en el estudio de EPTs y tecnologías para su modelado y simulación. Estos se enfocwan principalmente en la interacción de ondas electromagnéticas y su relación con fenómenos de transporte en el plasma. El estudio comienza con un análisis detallado del modelo de plasma frío, aplicado a problemas de propagación de ondas en propulsores de plasma de clase Helicón (HPT). Cabe destacar la introducción de PWHISTLER, una herramienta de simulación de ondas que emplea el método de elementos finitos (FE). Este modelo destaca por su mayor velocidad, precisión y capacidad para simular geometrías complejas, mejorando significativamente el estudio de fenómenos electromagnéticos en plasmas magnetizados.

Una serie de análisis utilizando tanto un modelo de diferencias finitas (FD) como PWHISTLER demuestran su efectividad en la caracterización de la propagación y absorción de ondas en HPTs, siendo una observación clave la absorción de potencia concentrada en la superficie de resonancia electrónica-ciclotrónica (ECR).

La integración de PWHISTLER con el código de simulación para el transporte de plasma HYPHEN facilita un estudio exhaustivo de una nueva topología de campo magnético con cúspide en HPT. Las simulaciones, verificadas con datos experimentales, ofrecen conclusiones sobre las pérdidas de rendimiento y la eficiencia de empuje, destacando el papel de las corrientes de plasma a pared, la temperatura de electrones y la influencia de la topología magnética.

Finalmente se presenta una nueva formulación de un algoritmo implícito de partículas en celda (PIC), diseñado específicamente para toberas magnéticas. El método PIC implícito mejora la eficiencia computacional frente a métodos bien establecidos, y constituye un avance sustancial en la simulación y optimización de toberas magnéticas para EPTs.

Contents

List of Figures

List of Tables

1. *Introduction*

1.1. Background

Electric Propulsion (EP) is a form of in-space propulsion that utilizes electric power from an external source, such as solar panels or batteries, to ionize a neutral gas and accelerate charged particles that collectively form a plasma. This approach has a major advantage in terms of propellant efficiency compared to chemical rocket propulsion (CP). The potential of this moderate power, low thrust, high efficiency, and long-duration propulsion method for in-space applications was first noticed in the early 20th century by space pioneers Goddard and Tsiolkovsky [1], and can be explained using the latter's renowned *rocket equation*.[2]:

$$\frac{m_p}{m_0} = \exp \frac{\Delta V}{v_e} - 1 \tag{1.1}$$

For a given space mission, characterized by a certain ΔV budget, the ratio of propellant to dry mass m_p/m_0 decreases exponentially with the effective exhaust velocity v_e provided by the rocket or thrusters. In a context where the cost of getting 1 kg of payload to low-earth orbit averages tens of thousands of dollars, reducing on-board satellite propellant mass is of paramount importance to the space industry. This explains the need for a high effective exhaust velocity v_e, which has led to the widespread adoption of efficient electric propulsion technologies.

EP systems can break the achievable v_e limitation intrinsic to CP due to the finite availability of potential energy in the chemical bonds of the propellant/s. EP systems typically have a specific impulse of $I_{sp} \approx v_e = 10000 - 50000$ m/s, compared to only $1000 - 5000$ m/s . Today, almost half of all commercial spacecraft deployed carry some kind of EP onboard. Applications range from low-thrust station keeping and attitude control operations to transferring from LEO to higher orbits for navigation and telecommunication satellites [3]. Deep-space scientific missions, with the most demanding ΔV budgets, also rely heavily on EP, some examples are the BepiColombo Venus orbiter (ESA), Hayabusa 1 and 2 asteroid sample return spacecraft (JAXA) or the NASA Evolutionary Xenon Thruster (NEXT) platform powering future missions.

Since the first EP systems were launched in the late 1960s [4], many devices have been designed and flown successfully; a typical classification of existing technologies is the following[5]:

1. **Electrothermal:** Electric power is used to heat the plasma which expands as a result of the rising pressure and accelerates in a nozzle. These devices share similarities with CP, but the additional I_{sp} is modest compared to the former.
2. **Electrostatic:** The primary means of generating thrust is the acceleration of ions in an electric field created between two electrodes with a very high voltage difference. Gridded-ion thrusters (GITs) are a well-established technology in this group. These devices use biased grids placed after an ionization chamber to accelerate ions. The plasma beam is then neutralized by electrons from an external cathode. GITs offer a specific impulse of more than 30000 m/s and an energy efficiency of around 70%. However, thrust density

and throatability are restricted by grid current saturation. Despite modern improvements in the systems lifetime, grid erosion caused by high-energy ions continues to be a major concern. High voltages in the device and the need for several circuits require complex power processing units (PPUs) and careful design to avoid uncontrolled discharges.

3. **Electromagnetic:** The thrust generation mechanism is the reaction forces between the thruster magnetic circuit (composed of coils and/or permanent magnets) and the plasma currents. The Hall Effect Thruster (HET) is the most mature device in this class. It has an internal anode and an external hollow cathode emitting an electron current which serves a dual purpose: a fraction of the electron current is directed to the chamber where it ionizes the neutral gas, while the other part neutralizes the downstream ion jet. Inside the source, the magnetic circuit creates a quasi-radial magnetic field that produces an $\boldsymbol{E}\times\boldsymbol{B}$ azimuthal drift, which is essential for increasing the electron residence time and boosting the ionization rate. The reaction of the azimuthal electron current against this magnetic field is the main contributor to the total thrust. Compared to GITs, HETs usually have a lower specific impulse and efficiency ($\sim$ 20000 m/s and $\sim$ 50%), however, their high thrust density, reduced system complexity, and potential to use alternative propellants instead of expensive Xenon (Xe), are driving the industry toward adoption of this technology for many applications.

Research into GIT and HET continues to be conducted to overcome some of their limitations; yet another option that has become increasingly popular in the past two decades is to move away from the traditional architectures and develop new concepts that do not require electrodes. Electrodeless Plasma Thrusters (EPTs) are electromagnetic devices that do not require a complementary hollow cathode to act as an ion beam neutralizer and do not suffer from erosion problems associated with electrodes and grids. In addition, they simplify the complex power unit control system of more mature technologies. EPTs offer the potential to use alternative propellants with a lifetime longer than that of GIT or HET ($\sim$ 60000 hours and $\sim$ 20000 hours, respectively, expected for the newest generation devices) and are more cost-effective due to the simplification of the PPU and the lack of electrodes. These thrusters can be used for a variety of applications, from low-power propulsion for cube and nanosatellites to high-power interplanetary and deep-space exploration propulsion plants, such as the Variable Specific Impulse Magnetoplasma Rocket (VASIMR) [6].

Two types of EPTs, Helicon Plasma Thrusters (HPTs) [7]–[11] (also known as radiofrequency or RF thrusters, see Figure 1.1) and Electron Cyclotron Thrusters (ECRs) [12]–[15] (also known as microwave thrusters), currently dominate the research in the low and mid-power EPT segment. They have a similar operating principle and consist of (1) a cylindrical discharge chamber made of dielectric walls, (2) a gas inlet, usually at the back of the chamber, (3) an inductor/antenna, emitting the EM power to be absorbed by the plasma, and (4) an external magnetic circuit, generating a magnetic field, which aims to make the plasma partially transparent to the EM waves, to confine the plasma, and to guide and accelerate it externally through a magnetic nozzle (MN) configuration. The main differences between the two technologies are the plasma heating mechanism and the operating frequency. HPTs work in the MHz range and use the geometric coupling of RF power provided by a helical antenna via Helicon and Trivelpiece Gould (TG) waves [16]. Conversely, ECRs employ a resonant mechanism, the Electron Cyclotron Resonance (ECR), to deposit most of the electromagnetic power in a localized region where the applied magnetic field intensity meets the resonant condition dictated by the excitation frequency, usually in the low-GHz

range. Due to the short characteristic vacuum wavelengths at these high frequencies, comparable to the dimensions of the device, some ECRT have replaced the antenna with a waveguide that feeds EM power into the source [17].

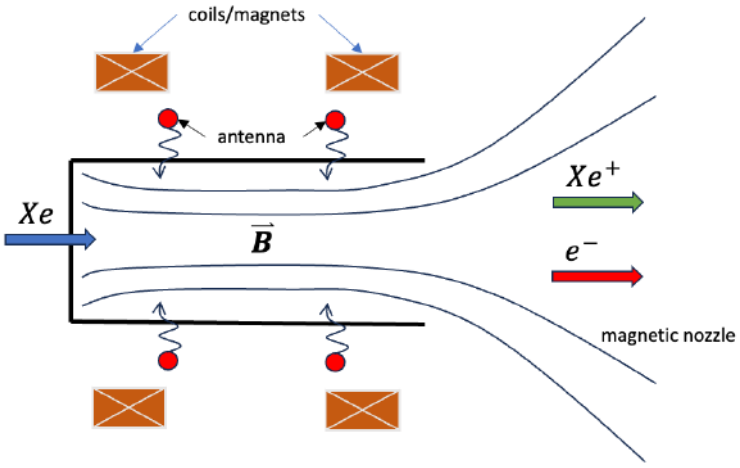

Figure 1.1: Schematic of a Helicon Plasma Thruster

Despite their potential, the current specific impulse and thrust efficiency of these thrusters are not as competitive as those of their more mature GIT and HET counterparts. Gaining a better understanding of the physical mechanisms and plasma dynamics is essential for revealing loss mechanisms and optimizing performance. EPTs share with other types of plasma thrusters a wide range of complex plasma physics phenomena that are actively being studied by the EP community, such as turbulence and instabilities, anomalous cross-field transport, kinetic effects, wall-plasma interaction, and plasma chemistry. Furthermore, the electromagnetic wave propagation and absorption problem, which is a key phenomenon in the operation of EPTs, is also a factor that adds complexity to the study of these new-generation thrusters. Needless to say, wave phenomena are coupled to some extent to each of the mechanisms mentioned above. This results in a very intricate non-linear behavior of the plasma, which explains the difficulty of thruster designers in understanding and optimizing these devices.

1.2. State-of-the-art in EPT modeling

Modeling EPTs is a challenging undertaking, as it requires taking into account a variety of interrelated processes. To begin with, the magnetized plasma transport must be addressed, including ionization, the interaction with the walls, and the external expansion and acceleration to infinity in the MN. Additionally, the plasma-wave interaction must be considered, which involves the RF fields and the RF power deposition in the plasma. Since the timescales of the fast RF fields and the slow plasma transport are significantly different, it is possible to address each subproblem independently to some degree.

Regarding the fast electromagnetic (EM) fields, early work on helicon sources characterized the EM wave normal modes in simplified geometries [16] identifying two main propagation modes, namely Helicon (H) and Trivelpiece-Gould (TG) waves [18], their damping rates and the power deposition inside the plasma. In a cold-plasma description that includes electron inertia,

these two modes are instances of the right-hand polarized whistler wave [19] at different propagation angles with respect to the stationary magnetic field. Full-wave frequency-domain models for EM wave propagation [20] are needed for an accurate simulation of realistic configurations. These models study a stationary plasma through which waves can travel from an excitation region (a volumetric current density) that corresponds to the antenna or coupler. Additionally, boundary conditions can be introduced for an incoming wave (waveport) that is fed into the thruster through a waveguide in some ECRT prototypes. Under the cold-plasma assumption, the magnetized plasma response is linear and can be captured by a full dielectric tensor [19]. The solution for the electric-field components can then be used to compute the induced currents and calculate the cycle-averaged power deposition into the plasma. Early one-dimensional radial models already detected H and TG waves in the cylindrical plasma source, as evidenced in several studies [21]–[23]. However, these models do not account for the effects of axial variations in density and axial magnetic field. To address these limitations, more advanced two-dimensional asymmetric full-wave codes were developed [20], [24], albeit with the assumption of a magnetic field aligned along the axis. More recently, Tian et al. [25] expanded upon these models by incorporating a segment of the diverging MN plume, thus enabling the exploration of the magnetic field topology and its impact on wave propagation. Following Tian's finite difference (FD) approach, Jiménez et al. [26] improved the capabilities of the model by introducing azimuthal Fourier modes to simulate helical antennas. In a different approach, Melazzi et al. [22] applied the method of moments (MoM) to calculate both the surface electric current density in the antenna and the volumetric polarization current within the plasma. The introduction of more versatile, accurate, and efficient finite element (FE) models [26], [27] has been a significant recent development in EM modeling for EPTs.

On the slow plasma transport side, investigations of plasma dynamics [28] and acceleration mechanisms [29] preceded the development of two-dimensional (2D) simulation tools for plasma transport. Fruchtman et al. were the first to apply such a model to HPTs [30], although it was limited to axial magnetic field topologies. Ahedo and Navarro [31] then advanced the state-of-the-art by extending the simulation to the plume region, applying the convergent-divergent MN model of Merino and Ahedo [32] and performing extensive parametric studies on device performance. Similar multifluid simulation codes have been extensively used in the study of EP systems [33]–[35]. Instead, hybrid models treat heavy species kinetically while considering a fluid formulation for much faster electrons [36]. The hybrid particle in cell (PIC) / fluid code HYPHEN [37], based on previous models originally devised for HET studies [38], [39], was generalized to the study of several EPTs including RF [40] and microwave thrusters [41]. This simulation platform overcame important shortcomings of previous tools, such as the arbitrary imposition of current ambipolarity at the boundaries, assuming isothermal or polytropic laws for the electron temperature at the plume or assuming full magnetization of the electron fluid.

Although it is a valid initial approach to consider the wave and transport subproblems separately, the self-consistent simulation of EPTs must take into account the interaction between them. In particular, the propagation and absorption of EM power depend on plasma density and electron collisionality, whereas the slow plasma dynamics is affected by the power deposition term that drives the plasma energy balance [28]. At present, the self-consistent simulation of the coupled slow-transport and fast-EM fields is still an open area of research. Magarotto et al. followed this approach to study an HPT, connecting a fluid code for the HPT plasma source, a three-dimensional

PIC model for the MN region, and a cold-plasma Maxwell solver to solve for fast fields [42]. However, this work does not consider any power deposition in the plume region or kinetic effects at the source. Sánchez-Villar et al. [41] used the HYPHEN code in combination with a full wave vector finite element (FE) frequency domain code to simulate an ECRT thruster, taking advantage of the difference in time scales of the two subproblems to solve them sequentially. This work evaluated power deposition, particle and energy fluxes to the walls, and thruster performance figures. Furthermore, the simulations were recently compared with experimental data [43] to validate the models. Two-dimensional coupled simulations of this kind, some of which are presented in this work for the study of an HPT prototype, constitute the most advanced reasonably affordable numerical models to date in EPT research.

In certain areas and conditions, kinetic effects may be essential, rendering the fluid approximation for electrons inaccurate. Examples include low collisionality expansions in magnetic nozzles [44]–[46], plasma sheaths at source walls [47], and kinetic instabilities that can lead to macroscopic turbulence and phenomena such as anomalous transport [48]. The addition of phenomenological parameters to the electron-fluid equations of the hybrid transport solver can effectively capture phenomena such as anomalous transport. Zhou et al. [40] studied the role of phenomenological parameters (which can be fitted using experimental data) in the characterization of missing physics and the correct simulation of device performances. These include anomalous cross-field transport of momentum and energy, tackled by a modification to the effective local Hall parameter, and electron cooling at the plume, for which an empirical collisionality parameter is added, which reduces the electron fluid parallel (to magnetic field lines) conductivity. Realistic device simulations using this approach require a significant amount of experimental data. The purpose of these data is two-fold: (1) to fit the parameters and (2) to verify the model after fitting. This methodology was employed in [49] and is replicated in this thesis, resulting in reasonable agreement between the experimental and numerical results. It is important to note that two-dimensional numerical profiles offer insights that cannot be obtained through experiments, particularly in the plasma source. The downside to this approach is that those phenomenological parameters tend to be device-dependent and, consequently, it cannot replace experiments for rapid prototyping and optimization.

Modeling from first principles, not requiring the introduction of additional phenomenological terms, might be addressed by introducing two-dimensional (or even three-dimensional) fully kinetic simulations. However, these simulations are very expensive. The particle-in-cell (PIC) method, despite having a higher numerical noise than other alternatives, is the preferred option for the integration of the Vlasov-Poisson system in the time domain due to its cost savings and better phase-space dimensionality scaling than direct Vlasov algorithms [50]. PIC codes have been used in the past to study electric propulsion systems, mainly Hall effect thrusters. Numerous one-dimensional [51]–[53], and two-dimensional models [54]–[56] have appeared. Despite the potential of the method, the high cost of executing these codes has led, in some cases, to the use of numerical tricks such as an enlarged vacuum permittivity and the reduction of the ion mass to alleviate the numerical load [57]. Few examples of realistic three-dimensional PIC simulations applied to EP sources exist, and they require a large amount of computing power (large computing clusters) and months of running time [58]. The current literature on EPTs includes only a few examples of high-dimensional full PIC electrostatic simulations of the plume [42], [59] but not many of the source (where the Debye length constraint in the resolution is more stringent) of the devices.

Because of the importance of EM wave propagation, kinetic electromagnetic algorithms that can solve the Vlasov-Maxwell system in a self-consistent manner are better suited to study the heating mechanisms and several wave-related phenomena in EPTs. However, these algorithms are even more demanding than electrostatic PIC models because of the fast wave dynamics. Porto et al. [60] conducted a one-dimensional study on an ECRT magnetic nozzle using a semi-Langrangian scheme for the propagation of EM waves, which allows for a relaxation of the otherwise restrictive time step constraint. The work revealed anisotropic plasma heating along a Doppler-widened zone in the vicinity of the electron cyclotron resonance (ECR) surface and showed that a trapped population of electrons with a larger perpendicular energy can form in the plume. Two-dimensional studies have also been conducted, which rely on approximations, including the reduction of ion mass and a modified effective speed of light [61].

Classical PIC algorithms have a major limitation in that they require a more demanding time and space resolution than is necessary for the evolution of the macroscopic fields in a quasi-neutral plasma. This is due to stability, Courant-Friedrichs-Lewy (CFL)-like conditions for the integration timestep, and aliasing effects on a finite grid, which can lead to undesired numerical heating [62]. This means that the time step must be on the order of the inverse plasma frequency ω_{pe}, and the cell size must be comparable to the local Debye length λ_D. Additionally, a statistically significant number of particles per cell is needed to prevent excessive numerical noise, which increases with a finer mesh. This is especially problematic in two or three dimensions, since the total number of particles needed to resolve the Debye length increases as $\sim (L/\lambda_D)^d$, where L is the characteristic length of the plasma macroscopic gradients and d is the number of spatial dimensions. If, as a first approach, we take the number of floating point operations proportional to the number of particles, with typical $L/\lambda_D \approx O(10)$ in most quasineutral propulsion plasmas, the computational load increases by about $\sim$ 100 (for 2D) or $\sim$ 1000 (for 3D) due to the need to prevent finite grid instability, rather than for accuracy in the resolution of the macroscopic plasma profiles or probability distribution functions. In the case of electromagnetic PIC algorithms, this problem is exacerbated because the time step and cell size are conditioned by the speed of light constant, which, for most cases of interest in EP, is greater than the plasma thermal speed $\lambda_D \omega_{pe}$.

In the last decade, the energy- and charge-conserving implicit PIC algorithm (IPIC) has been developed as a solution to the above-mentioned problems. This algorithm has enabled a significant reduction in computational resources when simulating a wide range of plasmas, as it eliminates the need to consider the Debye length and plasma frequency resolution constraints. Furthermore, when combined with the Darwin method for propagating fast EM fields [63], [64], it provides a fast and accurate method to solve the Vlasov-Maxwell system without the need to consider the very short time steps related to the light speed constant. The first model of this kind was a 1D uniform grid electrostatic version [65], and since then, generalizations have been made to mapped meshes [66], higher dimensions, electromagnetic cases [67], and even collisional plasmas [68]. Examples of the use of IPIC in radiofrequency magnetized plasmas have been presented with many similarities to the plasmas found in EPTs [69], [70]. However, its application to EP studies has only recently been explored [49], and there are still many practical problems that need to be addressed to fully mature the existing simulation technology.

1.3. Thesis scope and objectives

The fundamental goal of this thesis is to gain insight into the fundamental physics of EPT discharges, enabling the optimization of performance that could promote their widespread adoption. This is achieved by improving the modeling and simulation tools used in the design and development of these propulsion systems. The thesis focuses on the electromagnetic wave side of the problem, as well as on its connection to plasma transport phenomena. It builds on the gradual introduction of models and simulation codes of increasing complexity and works toward the current research community's goal of cost-effective, high-precision, and self-consistent 2D/3D kinetic electromagnetic models. The main objectives of this work are:

1. **Develop and implement cold-plasma simulation models:** Create and verify a versatile, fast, accurate and user-friendly simulation platform for the study of the wave propagation through cold-plasmas for EPTs, accomplished with the introduction of the full-wave two-dimensional finite element (FE) PWHISTLER solver. Additionally, a previously developed finite difference (FD) model will be used to characterize wave propagation and absorption in an HPT. Both approaches will be compared, showing the improved accuracy and efficiency of the FE model.
2. **Couple the wave model with a hybrid plasma transport solver:** Perform two-dimensional coupled simulations using the full-wave PWHISTLER code and the HYPHEN plasma transport solver, using experimental data for validation and parameter adjustment.
3. **Apply these models to realistic HPT prototypes:** Investigate, using the previously validated models, a novel cusp magnetic HPT field topology, assess performance, identify loss mechanisms, and explore optimization avenues. This also aims to demonstrate the applicability of our in-house developed models for routine aid in the design and optimization of new prototypes.
4. **Introduce a new implicit PIC Algorithm:** Develop a novel electrostatic energy- and charge- conserving IPIC algorithm for magnetized plasmas to achieve fast and accurate simulations of magnetic nozzles in a one-dimensional geometry. This work is among the first studies to apply the fully implicit PIC method in EP. It also brings about significant improvements to previous particle movers and introduces new boundary conditions, thus laying the groundwork for more complex and higher-dimensional models. In addition, model verification is carried out with several numerical experiments and a comparison with the results of a magnetic nozzle study in the literature.

1.4. Thesis structure

This thesis begins by examining the cold-plasma model to address the issue of wave propagation in EPTs. Under certain assumptions, this simplified model offers an insightful description of the propagation of electromagnetic waves and the power deposition in the plasma. **Chapter 2** reviews the cold-plasma model which is the basic theoretical framework for wave propagation phenomena in plasmas, such as wave topology (normal surfaces), cutoffs and resonances, absorption and reflection, and the different propagation parametric regimes in a uniform plasma as a function of the governing parameters, i.e. the applied magnetic field strength and direction, the plasma density,

and the effective electron collision frequency. Additionally, we include the particularization of the basic theory and dispersion relation to HPTs, which leads to the identification of Helicon and Tivelpiece-Gould (TG) modes.

Chapter 3 presents the PWHISTLER simulation platform, a parallel two-dimensional finite element full-wave solver in the frequency domain. This software offers several pre- and post-processing utilities that allow for the rapid simulation of plasma wave problems, particularly those related to the simulation of electromagnetic phenomena in EPTs. Compared to previous solvers, PWHISTLER introduces several noteworthy advances, such as Fourier azimuthal modes for the spectral decomposition and solution of 3D problems in a 2D spatial discretization, and waveport boundary conditions. The code is validated through a comprehensive set of tests.

In **Chapter 4**, two-dimensional full-wave simulations of a realistic HPT setup are presented, corresponding to the journal publication [26]. These simulations, carried out with an existing finite difference (FD) solver previously developed by the candidate, reveal the mechanisms of wave propagation and the regions of plasma heating. Although this approximation does not take into account the macroscopic long-term plasma response to the wave fields and, thus, does not solve for the steady-state discharge self-consistently; it still provides useful insights into the physics of the discharge. For instance, it is found that there is an important per-electron power deposition on the downstream ECR surface.

To solve for the complete discharge, a self-consistent loop is established in which the deposited power is updated by the wave solver and the plasma transport is evolved accordingly via the existing hybrid HYPHEN solver. This coupled strategy is used in **Chapter 5** to study an HPT prototype developed at the UC3M premises. In addition, experiments are used (1) to adjust some phenomenological parameters in the transport model and (2) to validate the approach and the numerical results. This is the most precise description of the HPT discharge our group has developed to date. The validated simulations serve to analyze the novel cusp magnetic field topology, which lacks extensive previous investigation, assessing performances and loss mechanisms and suggesting avenues for optimization. The contents of this chapter have recently been published [49].

Finally, **Chapter 6** presents a new electrostatic implicit PIC algorithm designed for the analysis of paraxial magnetic nozzles of HPTs and other electrodeless plasma thrusters. This chapter contains proofs of exact global energy and local charge conservation properties, as well as numerical experiments that show the accuracy and computational speed advantages over other algorithms. The contents of this chapter have been submitted for publication in the Journal of Computational Physics (JCP) [71].

2. *Cold-Plasma wave interaction physics*

This chapter derives the cold-plasma model [19] from first principles, specifically the fundamental electromagnetic theory based on Maxwell's equations. It examines plasma dynamics, which under the small perturbation assumption, leads to a linear response. This response is represented by a dielectric tensor in the wave equation, which depends on plasma conditions (density and effective collisionality) as well as the orientation and strength of the magnetic field.

This framework is then applied to derive analytical solutions for electromagnetic wave propagation through a uniform, magnetized, and anisotropic cold plasma. The analysis yields a rich parametric classification of various propagating and evanescent waves, as illustrated in the Clemmow-Mullaly-Allis (CMA) diagram.

Lastly, the chapter focuses on particularizing the general dispersion relation to the specific operational regime of Helicon Plasma Thrusters (HPT). This approximation results in a simpler expression that helps in identifying characteristic modes of operation.

2.1. Basic Electromagnetic Theory

The dynamics of electromagnetic fields are fully described by the four Maxwell's equations:

$$\nabla \times \boldsymbol{E} = -\frac{\partial \boldsymbol{B}}{\partial t} \tag{2.1}$$

$$\nabla \times \boldsymbol{H} = \frac{\partial \boldsymbol{D}}{\partial t} + \boldsymbol{j} \tag{2.2}$$

$$\nabla \cdot \boldsymbol{D} = \rho \tag{2.3}$$

$$\nabla \cdot \boldsymbol{B} = 0 \tag{2.4}$$

Here, $\boldsymbol{E}(t, \mathbf{x})$, $\boldsymbol{B}(t, \mathbf{x})$ are the *electric field* and *magnetic flux* vectors; $\boldsymbol{D}(t, \mathbf{x}) = \epsilon_0 \boldsymbol{E}$, $\boldsymbol{H}(t, \mathbf{x}) = \boldsymbol{B}/\mu_0$ are the *electric displacement* and *magnetic field* vectors; where the *vacuum permittivity* constant is $\epsilon_0 = 8.854187817 \cdot 10^{-12}$ F/m and the *permeability of vacuum* is $\mu_0 = 4\pi \cdot 10^{-7}$ H/m. Taking the divergence of Ampere's equation (2.2) and substituting Gauss's Law for the electric dispacement field (2.3), we find the *charge continuity equation*:

$$\frac{\partial \rho}{\partial t} + \nabla \cdot \boldsymbol{j} = 0, \tag{2.5}$$

likewise taking the divergence of Faraday's equation (2.1) we obtain:

$$\frac{\partial}{\partial t} \nabla \cdot \boldsymbol{B} = 0. \tag{2.6}$$

The last two equations demonstrate that, if (2.3) and (2.4) are fulfilled at a certain instant, they will still hold for any other time after the system evolves according to (2.2)-(2.1). Taking the curl

of either Ampere's or Faraday's equation and substituting, we obtain, respectively:

$$\left(\frac{1}{c^2}\frac{\partial^2}{\partial t^2} - \nabla^2\right)\boldsymbol{E} = -\mu_0\frac{\partial \boldsymbol{j}}{\partial t} - \frac{1}{\varepsilon_0}\nabla\rho, \tag{2.7}$$

$$\left(\frac{1}{c^2}\frac{\partial^2}{\partial t^2} - \nabla^2\right)\boldsymbol{B} = \mu_0\nabla\times\boldsymbol{j}, \tag{2.8}$$

where we have used the vector identity $\nabla\times(\nabla\times\boldsymbol{V}) = \nabla(\nabla\cdot\boldsymbol{V}) - \nabla^2\boldsymbol{V}$, and introduced the *speed of light in free space* $c = 1/\sqrt{\mu_0\epsilon_0} = 2.99792\cdot 10^8$ m/s. These are the so-called *Wave Equations*, hyperbolic equations that describe the propagation of electromagnetic waves. In the absence of source terms, this is, with zero right-hand side in (2.7), the solution of this equations are waves traveling at speed c in the $\boldsymbol{E}\times\boldsymbol{B}$ direction. An alternative form of (2.7) comes from undoing the previous vector transformation. It is known as the curl-curl equation:

$$\frac{1}{c^2}\frac{\partial^2\boldsymbol{E}}{\partial t^2} + \nabla\times(\nabla\times\boldsymbol{E}) = -\mu_0\frac{\partial\boldsymbol{j}}{\partial t} \tag{2.9}$$

2.1.1. Energy density and Power Flow

We dot multiply Faraday's equation (2.1) by $\boldsymbol{H}$ and Ampere's equation (2.2) by $\boldsymbol{E}$

$$\boldsymbol{H}\cdot\nabla\times\boldsymbol{E} = -\boldsymbol{H}\cdot\frac{\partial\boldsymbol{B}}{\partial t}, \tag{2.10}$$

$$\boldsymbol{E}\cdot\nabla\times\boldsymbol{H} = \boldsymbol{E}\cdot\frac{\partial\boldsymbol{D}}{\partial t} + \boldsymbol{E}\cdot\boldsymbol{j}, \tag{2.11}$$

then, using the vector identity $\nabla\cdot(\boldsymbol{E}\times\boldsymbol{H}) = \boldsymbol{H}\cdot(\nabla\times\boldsymbol{E}) - \boldsymbol{E}\cdot(\nabla\times\boldsymbol{H})$ and subtracting the previous equations,

$$\boldsymbol{E}\cdot\frac{\partial\boldsymbol{D}}{\partial t} + \boldsymbol{H}\cdot\frac{\partial\boldsymbol{B}}{\partial t} + \nabla\cdot(\boldsymbol{E}\times\boldsymbol{H}) = -\boldsymbol{E}\cdot\boldsymbol{j}, \tag{2.12}$$

which can be expressed in the following conservative form:

$$\frac{\partial u}{\partial t} + \nabla\cdot\boldsymbol{S} = -\boldsymbol{j}\cdot\boldsymbol{E}. \tag{2.13}$$

Above the *electromagnetic energy* stored in the fields is:

$$u = \frac{1}{2}(\boldsymbol{E}\cdot\boldsymbol{D} + \boldsymbol{B}\cdot\boldsymbol{H}) = \frac{1}{2}\left(\varepsilon_0 E^2 + \frac{1}{\mu_0}B^2\right) \tag{2.14}$$

and the *Poynting vector* i.e. the flux of electromagnetic energy is:

$$\boldsymbol{S} = \boldsymbol{E}\times\boldsymbol{H} = \frac{1}{\mu_0}\boldsymbol{E}\times\boldsymbol{B} \tag{2.15}$$

2.1.2. Time harmonic fields

We may now express any time varying field as:

$$F(t,\boldsymbol{x}) = \Re[\hat{F}(\boldsymbol{x})\exp(-i\omega t)] = \frac{1}{2}\left[\hat{F}(\boldsymbol{x})\exp(-i\omega t) + \hat{F}^*(\boldsymbol{x})\exp(+i\omega t)\right] \tag{2.16}$$

where $\omega \in \mathbb{R}$ is the *angular frequency* such that $f = \omega/(2\pi)$ is the standard frequency of the oscillating fields. The hat in $\hat{F}$ denotes the *complex amplitude* of the field; the argument for the complex amplitude is the phase angle. Note that any function of time can be decomposed into a generally infinite superposition of $\hat{F}(\boldsymbol{x})\exp(-i\omega t)$ time harmonic components using a Fourier transform. Thereafter, any time derivative in the equations transforms to $\partial/\partial t \rightarrow -i\omega$, and the curl-curl equation 2.9 takes the form:

$$\nabla \times (\nabla \times \hat{\boldsymbol{E}}) - \frac{\omega^2}{c^2}\hat{\boldsymbol{E}} = i\omega\mu_0\hat{\boldsymbol{j}} \tag{2.17}$$

which is an elliptic equation that can be solved for the spatial distribution of the complex amplitude $\hat{\boldsymbol{E}}(\boldsymbol{x})$ for a given excitation frequency ω. The curl-curl operator in a Cartesian coordinate system with vector basis $\{\mathbf{1}_x, \mathbf{1}_y, \mathbf{1}_z\}$ is:

$$\nabla \times (\nabla \times) = \begin{bmatrix} -\partial_y^2 - \partial_z^2 & \partial_x\partial_y & \partial_x\partial_z \\ \partial_x\partial_y & -\partial_x^2 - \partial_z^2 & \partial_y\partial_z \\ \partial_x\partial_z & \partial_y\partial_z & -\partial_x^2 - \partial_y^2 \end{bmatrix}, \tag{2.18}$$

similarly in right-handed cylindrical coordinates with vector basis $\{\mathbf{1}_z, \mathbf{1}_\rho, \mathbf{1}_\theta\}$, reads:

$$\nabla \times (\nabla \times) = \begin{bmatrix} -\partial_r^2 - \frac{1}{r^2}\partial_\theta^2 & \partial_z\partial_r & \frac{1}{r}\partial_z\partial_\theta \\ \partial_z\partial_r & -\partial_z^2 - \frac{1}{r^2}\partial_\theta^2 & \frac{1}{r}\partial_r\partial_\theta \\ \frac{1}{r}\partial_z\partial_\theta & \frac{1}{r}\partial_r\partial_\theta & -\partial_z^2 - \partial_r^2 \end{bmatrix} + \begin{bmatrix} -\frac{1}{r}\partial_r & \frac{1}{r}\partial_z & 0 \\ 0 & 0 & \frac{1}{r^2}\partial_\theta \\ 0 & -\frac{1}{r^2}\partial_\theta & \frac{1}{r^2} - \frac{1}{r}\partial_r \end{bmatrix} \tag{2.19}$$

Finally, the power deposition of a source $\boldsymbol{j}$, i.e. the right-hand side of (2.13), when we consider time harmonic fields is:

$$\begin{aligned} \boldsymbol{j}\cdot\boldsymbol{E} &= \frac{1}{4}\left[\hat{\boldsymbol{j}}\exp(-i\omega t) + \hat{\boldsymbol{j}}^*\exp(+i\omega t)\right]\cdot\left[\hat{\boldsymbol{E}}\exp(-i\omega t) + \hat{\boldsymbol{E}}^*\exp(+i\omega t)\right] \\ &= \frac{1}{4}\left[\hat{\boldsymbol{j}}\cdot\hat{\boldsymbol{E}}^* + \hat{\boldsymbol{j}}^*\cdot\hat{\boldsymbol{E}}\right] + \frac{1}{4}\left[\hat{\boldsymbol{j}}\cdot\hat{\boldsymbol{E}}\exp(-2i\omega t) + \hat{\boldsymbol{j}}^*\cdot\hat{\boldsymbol{E}}^*\exp(+2i\omega t)\right] \\ &= \frac{1}{2}\Re\left(\hat{\boldsymbol{j}}^*\cdot\hat{\boldsymbol{E}}\right) + \frac{1}{2}\Re[\hat{\boldsymbol{j}}\cdot\hat{\boldsymbol{E}}\exp(-2i\omega t)]. \end{aligned} \tag{2.20}$$

Above, $\Re\left(\hat{\boldsymbol{j}}^*\cdot\hat{\boldsymbol{E}}\right)/2$ is a stationary DC term that represents the cycle-averaged power deposition by the EM fields. The double frequency term is an oscillatory power exchange between fields and charges with zero mean that vanishes upon time integration over a wave cycle. The real part of $\boldsymbol{J}\cdot\boldsymbol{E}$ is also known as *resistive power* while the imaginary part is commonly known as *inductive power*.

2.1.3. Linear media

The presence of electric charges in a medium other than vacuum can generate non zero macroscopic current density $\boldsymbol{j_m}$ and charge density ρ_m source terms in response to the wave electromagnetic fields. In some special cases, $\hat{\boldsymbol{j}}_{\boldsymbol{m}}$ is linear to the local value of $\hat{\boldsymbol{E}}$ for a given frequency, then,

$$\hat{\boldsymbol{j}}_{\boldsymbol{m}} = \overline{\overline{\sigma}}\hat{\boldsymbol{E}} = -i\omega\varepsilon_0\overline{\overline{\chi}}\hat{\boldsymbol{E}} \tag{2.21}$$

where $\overline{\overline{\chi}}$ is the *susceptibility tensor* and $\overline{\overline{\sigma}}$ the *conductivity tensor* of the medium. We then redefine the source term in (2.17) to refer only to external current density sources $\hat{\boldsymbol{j}} \rightarrow \hat{\boldsymbol{j}} + \hat{\boldsymbol{j}}_{\boldsymbol{m}}$ and, introducing the *relative permittivity tensor* $\overline{\overline{\kappa}} = 1 + \overline{\overline{\chi}}$, we may rewrite (2.17) as:

$$\nabla \times (\nabla \times \hat{\boldsymbol{E}}) - \frac{\omega^2}{c^2} \overline{\overline{\kappa}} \cdot \hat{\boldsymbol{E}} = i\omega\mu_0 \hat{\boldsymbol{j}} \tag{2.22}$$

where the $\hat{\boldsymbol{j}}_m$ was moved to the left-hand side of the equation. This is equivalent to a modification of the electric displacement field $\hat{\boldsymbol{D}} = \varepsilon_0 \hat{\boldsymbol{E}} + i/\omega \hat{\boldsymbol{j}}_{\boldsymbol{m}} = \varepsilon_0 \overline{\overline{\kappa}} \cdot \hat{\boldsymbol{E}} = \overline{\overline{\varepsilon}} \cdot \hat{\boldsymbol{E}}$. In addition to the introduction of a *permittivity tensor* $\overline{\overline{\varepsilon}}$, a more general local and linear medium may require a *permeability tensor* $\overline{\overline{\mu}}$ such that $\hat{\boldsymbol{H}} = \overline{\overline{\mu}}^{-1} \cdot \hat{\boldsymbol{B}}$. This is sometimes refer to as the *macroscopic formulation* of Maxwell's equations.

2.1.4. Planar waves

In many problems of interest, such as the propagation of waves through a uniform, infinite linear medium or through a sourceless vacuum, the solution to (2.22) is a planar wave, or clollection of planar waves, of the form:

$$\boldsymbol{E}(t, \boldsymbol{x}) = \tilde{\boldsymbol{E}} \exp(-i\omega t + i\boldsymbol{k} \cdot \boldsymbol{x}), \tag{2.23}$$

where $\tilde{\boldsymbol{E}}$ is a new complex amplitude that captures both the harmonic time and space variations of the field. Equation(2.23) represents an infinite collection of *wavefronts*, i.e. surfaces at constant phase angle $\theta(t, \boldsymbol{x}) = arg(\tilde{\boldsymbol{E}}) + \boldsymbol{k} \cdot \boldsymbol{x} - \omega t$ traveling at a speed $v_{ph} = \omega/k$. The *wavevector* $\boldsymbol{k}$ indicates the direction of propagation $\mathbf{1}_{\boldsymbol{k}}$ and the distance between wavefronts or *wavelength* is $\lambda = 2\pi/k$. While $\omega \in \mathbb{R}$, $\boldsymbol{k} \in \mathbb{C}^3$, the imaginary part indicating wave attenuation/amplification.

Introducing fields of the (2.23) form into the curl-curl equation (2.17) with right-hand side 0, the curl operator transforms $\nabla\times \rightarrow i\boldsymbol{k}\times$, and we arrive to the following algebraic equation:

$$\boldsymbol{k} \times (\boldsymbol{k} \times \tilde{\boldsymbol{E}}) + \frac{\omega^2}{c^2} \overline{\overline{\kappa}} \cdot \tilde{\boldsymbol{E}} = -i\omega\mu_0 \tilde{\boldsymbol{j}} \tag{2.24}$$

Equation (2.24), constitutes the *dispersion relation* for wave-propagation through a medium characterized by $\overline{\overline{\kappa}}$. Non trivial solutions require:

$$\det\left(\frac{\omega^2}{c^2} \overline{\overline{\kappa}} + \boldsymbol{k}\boldsymbol{k} - k^2 \overline{\overline{1}}\right) = 0 \tag{2.25}$$

which gives a resulting $\omega(\boldsymbol{k})$. The solution to the system in vacuum is simply $\omega(\boldsymbol{k}) = \pm ck$.

For a given $\boldsymbol{k}$ there are two independent planar wave solutions for the vector $\tilde{E}$, these are the *wave polarizations*. We can represent any polarization using a polarization basis. Common choices are the linear polarization basis and circular polarization basis. For $\mathbf{1}_{\boldsymbol{k}} = \mathbf{1}_z$ these take respectively the form $\{\mathbf{1}_{\boldsymbol{x}}, \mathbf{1}_{\boldsymbol{y}}\}$ or $\left\{(\mathbf{1}_{\boldsymbol{x}} + i\mathbf{1}_{\boldsymbol{y}})/\sqrt{2}, (\mathbf{1}_{\boldsymbol{x}} - i\mathbf{1}_{\boldsymbol{y}})/\sqrt{2}\right\}$, the later corresponding to a rotating field $\perp \boldsymbol{k}$ representing either *right-hand side* or *left-hand side* waves.

It is customary to introduce the *refractive index vector* $\boldsymbol{n} = (c/\omega)\boldsymbol{k}$. This vector is directed along the wave propagation direction and is has a magnitude inverse to the phase velocity over the

speed of light. The dispersion relation then reads:

$$\det\left(\bar{\bar{\kappa}} + \boldsymbol{nn} - n^2\bar{\bar{1}}\right) = 0 \tag{2.26}$$

In vacuum $n = 1$ while for a general medium the dispersion relation admits solutions with $n < 1$ implying $v_{ph} > c$, i.e. a wavefront traveling faster than the speed of light. However, it can be shown that the group velocity, which is the velocity at which information travels $\boldsymbol{v_g} = \partial\omega/\partial\boldsymbol{k}$, always has a magnitude $v_g < c$.

2.1.5. Boundary conditions

In most problems, the solution as the superposition of planar waves presented in 2.1.4 is not valid due to the presence of a finite domain. In that case, boundary conditions must be included in the formulation. These will affect the eigenmodes of the wave operator. Beyond some simple cases, such as rectangular or cylindrical cavities, general studies require the numerical integration of (2.17). As presented in the next chapter, the implementation of the boundary conditions is then particular to the simulation method used. In practice, some idealized boundary conditions are usually employed, constraining some of the electric and magnetic field vector components at the boundaries:

- A *perfect electric conductor* (PEC) is a material in which the tangential components of the electric field $\boldsymbol{E}$, as well as the normal component of the wave magnetic field $\boldsymbol{B}$, are both zero. Metals, which are good conductors, can be accurately represented as PECs.
- As a dual condition to PEC, a *perfect magnetic conductor* (PMC) is a material in which the tangential components of $\boldsymbol{B}$ and the normal component of the wave electric field $\boldsymbol{E}$ are 0.

In the presence of a sudden transition or discrete jump between two different media, certain conditions must be met. The normal components of $\boldsymbol{D}$ and $\boldsymbol{B}$ must be equal on each side, as indicated by the divergence equations 2.3 and 2.4, unless a thin layer of charge is allowed at the interface, in which case the normal component of $\boldsymbol{D}$ would jump accordingly. Similarly, the tangential components of $\boldsymbol{E}$ and $\boldsymbol{H}$ must be equal on each side, as indicated by the curl equations 2.1 and 2.2, unless a thin layer of charge current is allowed at the interface, in which case the tangential components of $\boldsymbol{H}$ change accordingly [72].

2.2. Plasma response

The strong relationship between plasmas and electromagnetic fields is a consequence of the fact that plasmas are composed of free charged particles i.e. sources in the free-space formulation of Maxwell's equations. The motion of the plasma is significantly affected by the electric and magnetic fields, and the electric and magnetic fields are also affected by the plasma currents. To accurately capture these phenomena, complex models are often necessary, particularly when kinetic effects are taken into account. This subsection will focus on an approximate formulation, the cold plasma model, which is capable of revealing the most dominant effects of the plasma response on the electromagnetic field under certain assumptions.

2.2.1. Cold plasma dielectric tensor

We start by considering the momentum equation of a species s in the cold fluid limit; that is, we neglect forces related to the divergence of the pressure tensor $-\nabla \cdot \mathcal{P}$ compared to the EM or *Lorentz's force* on charged particles $q_p/m_p(\boldsymbol{E} + \boldsymbol{v_p} \times \boldsymbol{B})$. The macroscopic momentum equation equation for a species s with particle density n_s and average velocity $\boldsymbol{u_s}$ reads:

$$m_s n_s \left(\frac{\partial \boldsymbol{u}_s}{\partial t} + \boldsymbol{u}_s \cdot \nabla \boldsymbol{u}_s \right) = n_s q_s \left(\boldsymbol{E} + \boldsymbol{u}_s \times \boldsymbol{B} \right) - m_s n_s \nu_s \boldsymbol{u}_s \tag{2.27}$$

We rewrite all variables as the sum of a zeroth-order plus a time-harmonic, first-order perturbation. The species are assumed to be at rest, with a negligible velocity compared to the wave phase velocity. This assumption may not be valid in the presence of large flows or drifts, or near resonances.

$$\begin{aligned} \boldsymbol{B} &\mapsto \boldsymbol{B}_0 + \hat{\boldsymbol{B}}_1 \exp(-i\omega t), \\ n_s &\mapsto n_{s0} + \hat{n}_{s1} \exp(-i\omega t), \\ \boldsymbol{E} &\mapsto \hat{\boldsymbol{E}}_1 \exp(-i\omega t), \\ \boldsymbol{u}_s &\mapsto \hat{\boldsymbol{u}}_{s1} \exp(-i\omega t). \end{aligned} \tag{2.28}$$

We introduce these approximations into (2.27), then keeping only first order terms and canceling out the time harmonic exponential everywhere, we get:

$$-i\omega m_s \hat{\boldsymbol{u}}_{s1} = q_s \left(\hat{\boldsymbol{E}}_1 + \hat{\boldsymbol{u}}_{s1} \times \boldsymbol{B}_0 \right) - m_s \nu_s \hat{\boldsymbol{u}}_{s1}, \tag{2.29}$$

and, without loss of generality, we may assume that the DC magnetic field $\boldsymbol{B_0}$ is directed along $\mathbf{1}_z$ to arrive to the following expression for the Cartesian components of the perturbed velocity:

$$\begin{bmatrix} \hat{u}_{sx1} \\ \hat{u}_{sy1} \\ \hat{u}_{sz1} \end{bmatrix} = \frac{q_s}{m_s} \begin{bmatrix} -is & -d & 0 \\ d & -is & 0 \\ 0 & 0 & -ip \end{bmatrix} \cdot \begin{bmatrix} \hat{E}_{x1} \\ \hat{E}_{y1} \\ \hat{E}_{z1} \end{bmatrix} \tag{2.30}$$

where,

$$\begin{aligned} s &= \frac{r+l}{2}, \quad d = \frac{r-l}{2}, \\ r &= -\frac{1}{(\omega + i\nu_s) + \omega_{cs}}, \quad l = -\frac{1}{(\omega + i\nu_s) - \omega_{cs}}, \quad p = -\frac{1}{(\omega + i\nu_s)}, \end{aligned} \tag{2.31}$$

where we introduced the angular *cyclotron frequency* of species s, $\omega_{cs} = q_s B_0/m_s$. The species current density is simply $\tilde{\boldsymbol{j}}_{\boldsymbol{s1}} = q_s n_s \hat{\boldsymbol{u}}_s$, after which the conductivity and susceptibility tensors (2.21) read:

$$\overline{\overline{\sigma}}_s = \frac{q_s^2 n_{s0}}{m_s} \begin{bmatrix} -is & -d & 0 \\ d & -is & 0 \\ 0 & 0 & -ip \end{bmatrix}; \quad \overline{\overline{\chi}}_s = \frac{\omega_{ps}^2}{\omega} \begin{bmatrix} s & -id & 0 \\ id & s & 0 \\ 0 & 0 & p \end{bmatrix}. \tag{2.32}$$

By virtue the problem linearity, we may sum over all charged species to find [19]:

$$\overline{\overline{\varepsilon}} = \varepsilon_0 \left(\overline{\overline{1}} + \sum_s \overline{\overline{\chi}}_s \right) = \varepsilon_0 \overline{\overline{\kappa}} = \varepsilon_0 \begin{bmatrix} S & -iD & 0 \\ iD & S & 0 \\ 0 & 0 & P \end{bmatrix} \tag{2.33}$$

where,

$$S = \frac{R+L}{2}, \quad D = \frac{R-L}{2},$$

$$R = 1 - \sum_s \frac{\omega_{ps}^2}{\omega\left[(\omega + i\nu_s) + \omega_{cs}\right]}, \quad L = 1 - \sum_s \frac{\omega_{ps}^2}{\omega\left[(\omega + i\nu_s) - \omega_{cs}\right]}, \tag{2.34}$$

$$P = 1 - \sum_s \frac{\omega_{ps}^2}{\omega\left(\omega + i\nu_s\right)},$$

with the *plasma frequency* of species s defined as $\omega_{ps} = \sqrt{q_s^2 n_{s,0}/(m_s \varepsilon_0)}$. The nondimensional parameters that governed the plasma response are thus ω_{ps}/ω (proportional to the square root of the density), ω_{cs}/ω (proportional to the magnetic field strength), and ν_s/ω. According to (2.33) the magnetic field introduces anisotropy in the medium and the dielectric tensor should be rotated so that $\mathbf{1}_z = \boldsymbol{B_0}/B_0$. In many problems of interest $\omega >> \omega_{pi}, \omega_{ci}$ and the ion response can be ignored. The dielectric tesor $\overline{\overline{\kappa}}$ can also be expressed in terms of its Hermitian and anti-Hermitian parts, $\overline{\overline{\kappa}} = \overline{\overline{\kappa}}^{\mathrm{H}} + \overline{\overline{\kappa}}^{\mathrm{A}}$, with:

$$\overline{\overline{\kappa}}^{\mathrm{H}} = \frac{1}{2}\left(\overline{\overline{\kappa}} + \overline{\overline{\kappa}}^{\dagger}\right) = \begin{pmatrix} \Re\{S\} & -i\Re\{D\} & 0 \\ i\Re\{D\} & \Re\{S\} & 0 \\ 0 & 0 & \Re\{P\} \end{pmatrix}, \tag{2.35}$$

$$\overline{\overline{\kappa}}^{\mathrm{A}} = \frac{1}{2}\left(\overline{\overline{\kappa}} - \overline{\overline{\kappa}}^{\dagger}\right) = i\begin{pmatrix} i\Im\{S\} & \Im\{D\} & 0 \\ -\Im\{D\} & i\Im\{S\} & 0 \\ 0 & 0 & i\Im\{P\} \end{pmatrix}. \tag{2.36}$$

where $\overline{\overline{\kappa}}^{\dagger}$ denotes the conjugate transpose of $\overline{\overline{\kappa}}$, also known as Hermitian transpose. The dielectric tensor elements S, D, P only have an imaginary part when the collisional term in the denominator of (2.34) is nonzero, therefore $\overline{\overline{\kappa}}^{\mathrm{A}} = 0$ if $\nu_s = 0$ for all species [27].

2.2.2. Infinite uniform plasma dispersion relation

The solutions to the Maxwell system in a uniform infinite cold magnetoplasma without external sources are plane waves of the form 2.23. Such a solution is valid everywhere except at singularities where thermal and/or kinetic effects might be important. The dispersion relation for plane waves in an anisotropic medium is:

$$\left(\overline{\overline{\kappa}} + \boldsymbol{nn} - n^2\overline{\overline{1}}\right) \cdot \tilde{\boldsymbol{E}}_1 = \mathbf{0} \tag{2.37}$$

which in a Cartesian basis $\{\mathbf{1}_z, \mathbf{1}_x, \mathbf{1}_y\}$ reads:

$$\begin{bmatrix} S - n_y^2 - n_z^2 & -iD + n_x n_y & n_x n_z \\ iD + n_x n_y & S - n_x^2 - n_z^2 & n_y n_z \\ n_x n_z & n_y n_z & P - n_x^2 - n_y^2 \end{bmatrix} \cdot \begin{bmatrix} \tilde{E}_{x1} \\ \tilde{E}_{y1} \\ \tilde{E}_{z1} \end{bmatrix} = \mathbf{0} \tag{2.38}$$

which, with no loss of generality, can be expressed as:

$$\begin{bmatrix} S - n^2\cos^2\theta & -iD & n^2\cos\theta\sin\theta \\ iD & S - n^2 & 0 \\ n^2\cos\theta\sin\theta & 0 & P - n^2\sin^2\theta \end{bmatrix} \cdot \begin{bmatrix} \tilde{E}_{x1} \\ \tilde{E}_{y1} \\ \tilde{E}_{z1} \end{bmatrix} = \mathbf{0}, \tag{2.39}$$

where we expressed $\boldsymbol{n} = n\cos(\theta)\mathbf{1_z} + n\sin(\theta)\mathbf{1_x}$ and $\boldsymbol{n}\cdot\mathbf{1_y} = 0$. This is an eigenvalue problem that, after some algebra, results in the following equation for non-trivial solutions:

$$\tan^2\theta = -\frac{P\left(n^2 - R\right)\left(n^2 - L\right)}{\left(Sn^2 - RL\right)\left(n^2 - P\right)}. \tag{2.40}$$

For each value of θ, that is, for each propagation angle of $\boldsymbol{k}$ with respect to $\boldsymbol{B_0}$, we obtain a different set of solutions to this equation. For example:

- For propagation parallel to $\boldsymbol{B_0}$, $\theta = 0$:

$$n^2 = R, \qquad n^2 = L, \qquad P = 0. \tag{2.41}$$

- For propagation perpendicular to $\boldsymbol{B_0}$, $\theta = \pi/2$:

$$n^2 = RL/S, \qquad n^2 = P. \tag{2.42}$$

For each solution, it is possible to find the eigenmodes in (2.39) giving the relative phases and the relation between the $\tilde{\boldsymbol{E}}_\mathbf{1}$ components. The polarization of the transverse fields can be found straightforwardly from the middle line of Equation 2.39,

$$\frac{i\tilde{E}_{x1}}{\tilde{E}_{y1}} = \frac{n^2 - S}{D} \tag{2.43}$$

Using the definitions in (2.41) for the case of $\theta = 0$ with $n^2 = R$, Equation (2.43) becomes $iE_x/E_y = 1$, while for the case of $\theta = 0$ with $n^2 = L$, we get $iE_x/E_y = -1$. Thus, the polarization is circular with a right-hand or left-hand sense according to $n^2 = R$ or $n^2 = L$, respectively.

Likewise after some algebra for the 1st order fluid velocities,

$$\frac{i\tilde{u}_{sx1}}{\tilde{u}_{sy1}} = -\frac{(\omega + \omega_{cs})\left(n^2 - R\right) + (\omega - \omega_{cs})\left(n^2 - L\right)}{(\omega + \omega_{cs})\left(n^2 - R\right) - (\omega - \omega_{cs})\left(n^2 - L\right)} \tag{2.44}$$

The denominator of (2.44) is in agreement with the resonance condition for electrons and ions. Electrons, which are negatively charged, rotate in a *right-handed* direction in the presence of the static zeroth-order magnetic field $\boldsymbol{B_0}$ and resonate with the R-wave when $\omega = -\omega_{ce}$. On the other hand, ions, which are positively charged, gyrate in a left-handed sense and resonate with an L-wave when $\omega = \omega_{ci}$.

2.2.3. Cutoffs and resonances

The solution to the cold-plasma dispersion relation is, in general, a complex vector $\boldsymbol{n}$ (or $\boldsymbol{k}$), characterized by its magnitude n and a given propagation angle with respect to $\boldsymbol{B_0}$, θ. In the absence of damping, n is either real, corresponding to propagating waves, or imaginary, corresponding to an evanescent mode.

In the parametric space of plasma properties, we speak of a *cutoff* whenever n goes to 0. When propagating modes cross a cutoff, they become evanescent and vice versa. Following (2.40) a cutoff takes place when:

$$P = 0; \quad R = 0; \quad L = 0 \tag{2.45}$$

The other kind of critical transitions are called resonances, taking place when $n \to \infty$ (only in the absence of collisional damping). This is a singularity in the cold-plasma model, and a proper treatment requires adding kinetic effects to recover physical solutions, at least in the collisionless limit. Taking the limit of (2.40) we find the resonant condition:

$$\tan^2(\theta) = -P/S \tag{2.46}$$

Contrary to cutoffs, which are independent of the angle of propagation, resonances can occur at some definite value of θ, for some propagating modes, this leads to the formation of a *resonance cone*. Approaching the critical value of θ, shorter wavelength modes propagate. Beyond the critical values, all waves become evanescent.

For parallel propagation $\theta = 0$, some cases of interest are $S \to \infty$ that can take place for $R \to \infty$ (electron cyclotron resonance) and $L \to \infty$ (ion cyclotron resonance); and $P \to 0$ that corresponds to both a cutoff and resonance and is an ill-defined double limit (also known as the underdense-overdense transition) that has been shown to be difficult to solve in numerical simulations [26]. For perpendicular propagation $\theta = \pi/2$, we find the so-called hybrid resonances when $S \to 0$. These particular solutions for parallel and perpendicular propagation are called principal resonaces.

The addition of collisions eliminates the above-mentioned singularities, i.e. the refractive index does not diverge to infinite values. The only damping mechanism in the cold-plasma model comes from a collisional term in the fluid momentum equation (2.27). It is well known that kinetic effects can be the main damping mechanism, especially near resonances. These effects are not captured by the cold-plasma model, although some works have shown that an effective collisional term can act as a very good phenomenological parameter to model all damping phenomena recovering an acceptable solution even when the cold-plasma model is used in the vicinity of resonances [73].

It is possible to plot the refractive index vector solution for a uniform plasma as a *wave normal surface*. This kind of figure indicates the magnitude of the vector at different propagating angles with respect to $\boldsymbol{B_0}$, an example is shown in Figure 2.1. There are two solutions to the dispersion relation in Figure 2.1, these are an interior ellipse and a exterior hyperbola-like wave normal surface. The latter presents a resonance cone at a certain angle with the vertical; the waves become evanescent (with fully imaginary n) for higher propagation angles. Normal surfaces are actually 3D figures of revolution, the axis of revolution corresponds to the 0th order magnetic field direc-

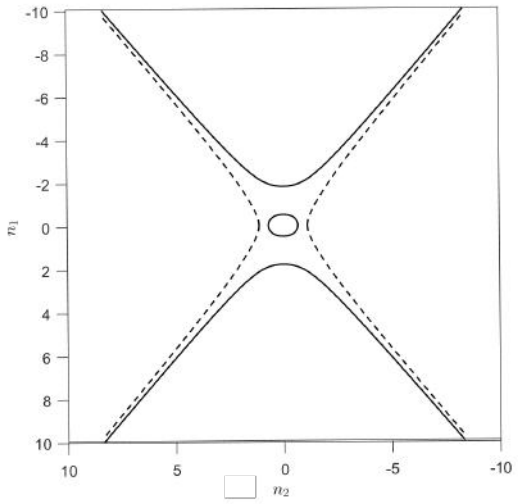

Figure 2.1: Wave normal surfaces of a fast wave (interior ellipse) and an ion cyclotron wave. Solid lines correspond to real solutions, and dashed lines correspond to imaginary n. The magnetic field is oriented along the vertical.

tion, in the case of Figure 2.1 this is the vertical. In the literature (see [19]) it is common to plot the normalized phase velocity vector $\boldsymbol{u} = (1/n^2)\boldsymbol{n}$. In this representation, the branches that diverge to infinity go to 0 instead, and a close figure is obtained for all cases (the topology of the ellipse-like normal surfaces is unchanged). We can plot the zoo of all possible possible waves that might propagate through a cold magnetized plasma as a function of the plasma parameters ω_{cs} and ω_{ps} normalized by the excitation angular frequency ω. For a single-ion species plasma this results in a 2D diagram as displayed in Figure 2.2. Notice that for visualization purposes, an non-realistic mass ratio $m_i/m_e = 2.5$ was chosen.

The different propagation regions, in which the topology of propagation modes remains constant are delimited by cutoffs and principal resonances. Upon crossing from one region to another, a wave may suffer partial or total reflection, mode conversion, or, if collisions are added, absorption leading to power deposition into the plasma. The labels next to each normal surface correspond to the polarization. There is a label for parallel propagation, with R being the right-hand and L the left-hand circularly polarized waves; while in the perpendicular direction we define the counterparts O (ordinary) and X (extraordinary) waves. At intermediate angles, the polarization is not that well defined, and we can find any general orientation of the wave vectors $\boldsymbol{E}$ and $\boldsymbol{B}$ vectors with respect to the propagation direction.

2.2.4. Power deposition

The oscillatory wave-induced plasma current can be found from (2.21); in terms of the plasma dielectric tensor, it reads:

$$\hat{\boldsymbol{j}}_1 = -i\omega\varepsilon_0\left(\overline{\overline{\kappa}} - \overline{\overline{1}}\right)\cdot\hat{\boldsymbol{E}}_1. \tag{2.47}$$

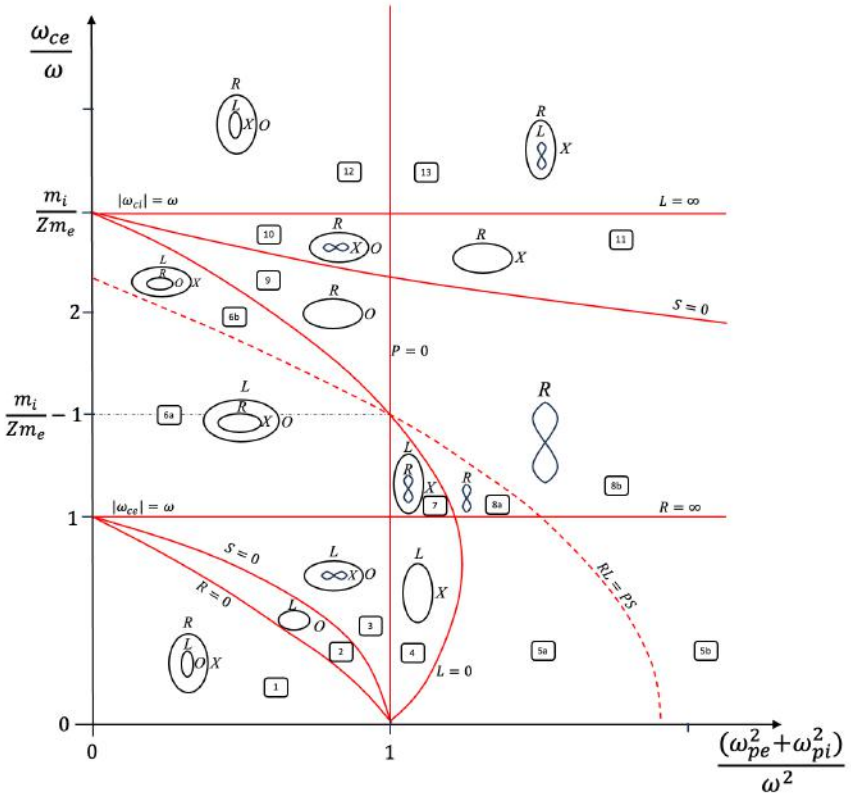

Figure 2.2: Clemmow–Mullaly–Allis (CMA) diagram of the wave propagation through a infinite cold magnetized plasma. Plasma with a single ion species and $Z = 1$, $m_i/m_e = 2.5$, $\boldsymbol{B_0}$ oriented in the vertical direction. Region numbering following [19].

We can introduce this definition to look for the DC power term in (2.20); the wave-cycle-averaged volumetric power delivered by the electromagnetic fields into the plasma is:

$$Q_a = \frac{\Re\left(\hat{\boldsymbol{j}}^* \cdot \hat{\boldsymbol{E}}_{\boldsymbol{1}}\right)}{2} = -\frac{\omega\varepsilon_0}{2}\Im\left\{\hat{\boldsymbol{E}}_{\boldsymbol{1}}^* \cdot \bar{\bar{\kappa}}^{\dagger} \cdot \hat{\boldsymbol{E}}_{\boldsymbol{1}}\right\} = -\frac{\omega\varepsilon_0}{2}\Im\left\{\hat{\boldsymbol{E}}_{\boldsymbol{1}}^* \cdot \left(\bar{\bar{\kappa}}^{\mathrm{H}} - \bar{\bar{1}} - \bar{\bar{\kappa}}^{\mathrm{A}}\right) \cdot \hat{\boldsymbol{E}}_{\boldsymbol{1}}\right\}. \tag{2.48}$$

The term $\bar{\bar{\kappa}}^{\mathrm{H}} - \bar{\bar{1}}$ is Hermitian and, according to the properties of any Hermitian matrix $\bar{\bar{H}}$, the double product with a generic complex vector $\boldsymbol{v}^* \bar{\bar{H}} \boldsymbol{v}$ is always a real number (this is related to the fact that all the eigenvalues of $\bar{\bar{H}}$ are real). The opposite occurs for an anti-Hermitean matrix, in which case the double product is always purely imaginary. We can finally write

$$Q_a = \frac{\omega\varepsilon_0}{2i}\hat{\boldsymbol{E}}_{\boldsymbol{1}}^* \cdot \bar{\bar{\kappa}}^{\mathrm{A}} \cdot \hat{\boldsymbol{E}}_{\boldsymbol{1}}, \tag{2.49}$$

which, recalling that $\bar{\bar{\kappa}}^{\mathrm{A}} = 0$ if $\nu_s = 0$ for all species, demonstrates that the only energy transfer mechanism from an electromagnetic wave to the plasma is (in the cold plasma formalism) the collisional damping modelled through ν_s in the plasma momentum equation (2.27).

2.3. Approximations in the HPT regime

We next attempt to derive a simplified dispersion relation for the typical plasma conditions in HPT sources. This approximation is useful for recognizing the electromagnetic waves and operational modes of the devices. One might verify that the assumptions that follow are reasonable by looking at the characteristic plasma conditions for an HPT prototype in Table 4.1 of Chapter 5.

Due to its much larger mass over unit charge, ions are considerably less mobile than electrons and it is a usual approximation to consider them static at high enough frequencies i.e. they do not contribute significantly to the plasma current induced by the wave. In particular, ions might be neglected far away from the lower hybrid resonant frequency $\omega >> \omega_{lh}$, where $\omega_{lh} = eB_0/\sqrt{m_e m_i}$ [19]. If we ignore the displacement current — a good approximation in dense plasmas far from cutoffs and, in particular, when $\omega_{pe} >> \omega$ — the dielectric tensor becomes $\overline{\overline{\kappa}} = \overline{\overline{1}} + \overline{\overline{\chi}}_e \simeq \overline{\overline{\chi}}_e$ and the components in (2.34) are:

$$R = -\frac{\tilde{\omega}_{pe}^2}{1+\tilde{\omega}_{ce}}, \quad L = -\frac{\tilde{\omega}_{pe}^2}{1-\tilde{\omega}_{ce}}, \quad P = -\tilde{\omega}_{pe}^2, \tag{2.50}$$

where the tildes denote normalization with the excitation frequency $\tilde{\omega}_x = \omega_x/\omega$. We also find

$$RL = \frac{\tilde{\omega}_{pe}^4}{1-\tilde{\omega}_{ce}^2}, \quad S = \frac{R+L}{2} = -\frac{\tilde{\omega}_{pe}^2}{1-\tilde{\omega}_{ce}^2}, \quad \frac{RL}{S} = -\tilde{\omega}_{pe}^2 = P \quad \text{and} \quad \frac{P}{S} = 1-\tilde{\omega}_{ce}^2. \tag{2.51}$$

Equation (2.39) can be written as:

$$\tan^2\theta = \frac{1}{\cos^2\theta} - 1 = -\frac{P}{S}\frac{n^4 - 2Sn^2 + RL}{(n^2-P)^2} = -\frac{(P/S)n^4 - 2Pn^2 + P^2}{(n^2-P)^2}. \tag{2.52}$$

Introducing $x = n^2/P$,dividing the numerator and denominator by P^2 and substituting the above expressions:

$$\frac{1}{\cos^2\theta} = -\frac{(1-\tilde{\omega}_{ce}^2)x^2 - 2x + 1}{(x-1)^2} + 1 = \frac{\tilde{\omega}_{ce}^2 x^2}{(x-1)^2} \tag{2.53}$$

$$x(-1 \pm \tilde{\omega}_{ce}|\cos\theta|) = 1 \tag{2.54}$$

and the simplified dispersion relation is:

$$n^2 = \frac{\omega_{pe}^2}{\omega(\pm\omega_{ce}|\cos\theta| - \omega)}, \tag{2.55}$$

or, following the same procedure and keeping track of the collisonal term,

$$n^2 = \frac{\omega_{pe}^2}{\omega(\pm\omega_{ce}|\cos\theta| - (\omega + i\nu_e))}, \tag{2.56}$$

It is common to express this dispersion relation as:

$$k^2 d_e^2 = \frac{\omega}{\pm\omega_{ce}|\cos\theta| - (\omega + i\nu_e)} \tag{2.57}$$

where we have introduced the plasma skin depth $d_e = c/\omega_{pe} = \sqrt{m_e/(e^2\mu_0 n_e)}$. This eliminates the

dependence on the plasma density on the right-hand side of (2.57). It is evident that, in the absence of collisions, the only polarization that potentially propagates is the one with $-\omega_{ce}$ (because $\omega_{ce} < 0$ for electrons); this corresponds to the whistler wave in region 8b of the CMA diagram in Figure 2.2. Next, we use (2.57) with $-\omega_{ce}$ to plot the nondimensional parallel $k_{\parallel}d_e$ and perpendicular $k_{\perp}d_e$ wave numbers in Figure 2.3.

Analyzing (2.57) and Figure 2.3 several propagation regimes can be identified. For simplicity, we focus on the collisionless case (a), finding [74]:

- **Inductive Regime (IR):** There is no real k which implies that there cannot be propagating modes. This regime takes place for applied magnetic fields lower than the ECR condition, i.e. $\omega_{ce}/\omega < 1$. We find such conditions in the downstream plume of EPTs as the magnetic field necessarily decays far from the magnets and solenoids that are used to generate it. At high excitation frequencies, e.g. in ECRT thrusters, this region can appear inside the plasma source.
- **Single Wave Regime (SWR):** There is only one $k_{\perp}$ for each $k_{\parallel}$ i.e, if we plot a vertical line from this value in Figure 2.3a, we only find one crossing with the dispersion relation curve. This single wave has been identified in the literature as the Trievelpiece-Gould (TG) mode and propagates at relatively high angles with respect to $\mathbf{B_0}$. Usually, $k_{\perp} >> k_{\parallel}$ so $\theta >> 45\,\text{deg}$, implying that TG waves propagate near perpendicular to the applied field. This regime appears when $2 > \omega_{ce}/\omega > 1$.
- **Double wave regime (DWR)**. Both TG waves and Helicon waves propagate. For a given $k_{\parallel}$ there are two possible $k_{\perp}$s; the smallest solution, propagating at small angles from the $\mathbf{B_0}$ direction, corresponds to the Helicon wave, whilst the one with largest $k_{\perp}$ is the TG wave. The transition condition from SWR to DWR can be found in Figure 2.3a. In order to have a double crossing for vertical lines traced from a given $k_{\parallel}$ value, there should be at least one point where $\mathrm{d}k_{\perp}/\mathrm{d}k_{\parallel} = \infty$, which is equivalent to $\mathrm{d}k_{\parallel}/\mathrm{d}\theta = 0$. Differentiating $(2.55)\cdot\cos\theta$, it is easy to find that the DWR regime exists for $\omega_{ce}/\omega > 2$.

This traditional terminology can be somewhat misleading. It is important to remark that both the TG and Helicon waves are instances of the whistler wave (the eight-shaped wave normal surface in region 8b of Figure 2.2). For a given propagation angle θ, there is a single solution given by one $k_{\parallel}$ and one $k_{\perp}$. In early works, the dispersion relation was derived using different approaches, which often included some less precise approximations. The Helicon mode was first identified and only after taking into account the electron inertia ($m_e \neq 0$) was the TG wave discovered [16].

Analyzing Figure 2.3, it can be seen that the wavenumber decreases with increasing B_0 for both Helicon and TG waves. This is especially relevant in Helicon thrusters, as it is usual to find resonant conditions when some mode wavelength matches the geometric dimensions of the thruster source, yielding higher wave fields and stronger absorption. Some works have found that there can therefore be an optimal B_0 particular to the thruster [75] and operating frequency.

Another important consideration is that HPTs generally operate best in the DWR regime. To explain this, we might analyze Figure 2.3b where some collisionality, typical of the dense plasma of an HPT source, is added. Tracing a line from the origin at some angle, we find the real and imaginary parts of $k_{\parallel}$ and $k_{\perp}$ at the point where that line intersects the solid (real) and dashed (imaginary) lines, respectively. The imaginary part of the wavenumber for TG modes is large

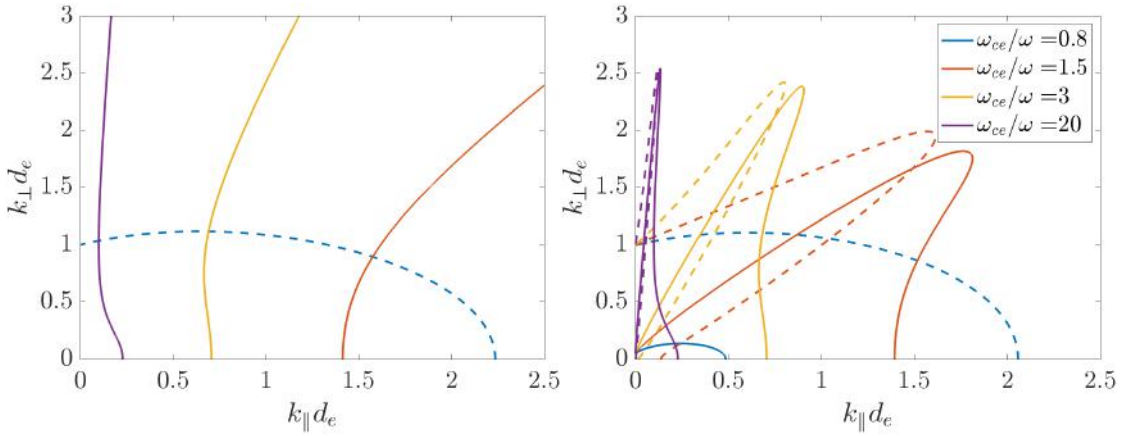

(a) $\nu_e/\omega = 0$ (b) ν_e/ω =0.1

Figure 2.3: Simplified whistler wave dispersion relation (2.57) for a collisionless and collisional plasma with different magnetic field strength. Solid lines correspond to the real part of k, dashed lines correspond to the imaginary part. Two DWR cases (purple and yellow), one SWR (red) and one IR case (blue).

compared to the Helicon one. This means that these waves are quickly damped and absorbed in the surface of the dense plasma column and are generally not capable of penetrating toward the thruster's axis. Being exited by an external antenna, TG waves heat the plasma near the lateral thruster walls; on the other hand, in order to avoid wall losses, it is generally desired to concentrate heating near the axis and this is better achieved with the weakly damped Helicon wave. However, there is considerable debate in the literature about which is the main power carrier in many HPT devices [76].

There are some other interesting findings from the collisional case dispersion relation. The real branches are little affected by the addition of damping for angles smaller than the resonant one. Infinite wavenumbers are eliminated and, instead, we find highly damped solutions outside of the resonant cone. The evanescent mode for $\omega_{ce} < 1$ now has a small real component, but the damping rate continues to be high, similar to the collisionless one.

3. *Finite Element (FE) simulation code for the cold-plasma full-wave model*

This chapter introduces a Finite Element simulation platform designed for the discretization and solution of the cold plasma Maxwell system discussed in the previous chapter. The platform operates within a 2D domain and allows for the utilization of azimuthal Fourier modes. This enables the simulation of not only axisymmetric systems but also inherently 3D problems, such as those encountered when dealing with helical antennas in Helicon plasma thrusters.

The development of the code prioritizes usability and rapid configuration. This chapter explains the structure of the code, including its modules and functionalities. In addition, it presents boundary conditions, notably perfect electric conductor (PEC) and axial continuity boundary conditions that apply to arbitrary azimuthal modes. The chapter also addresses the modeling of helical antennas and the implementation of waveports. These advances extend the capabilities beyond previous axisymmetric solvers [27].

To verify the code, it is tested against analytical solutions for the normal modes of rectangular/cylindrical cavities. Furthermore, a convergence analysis is conducted using the Method of Manufactured Solutions (MMS), considering scenarios both with and without plasma and utilizing finite elements of different orders.

3.1. Formulation

The Finite Element method is a powerful technique for discretizing partial differential equations (PDEs), particularly well-suited for solving elliptic PDEs. It operates as a variational method with the aim of minimizing the residual of a chosen quantity across the entire integration domain. In this method, a trial function denoted $\boldsymbol{E}$ is used to represent the unknown field throughout the domain, which, in our case, represents the electric field vector. Additionally, a test function labeled $\boldsymbol{T}$ is introduced and multiplied by the PDE under study, serving as a weighting term. The objective is to minimize the residual of the weighted equation.

Both the test and trial functions are discretized within a mesh using finite elements. These elements can assume various shapes and orders, but possess a limited spatial support or application area within the simulation domain. For instance, in the simplest scenario, one could utilize a mesh with — typically triangular or quadrilateral — elements with a constant test function across each mesh entity (discontinuous Galerkin elements of order 0).

By employing this procedure, integral forms are derived, which can subsequently be transformed into a linear system whose unknowns are the degrees of freedom of the problem. These degrees of freedom are the coefficients associated with the unknown field $\boldsymbol{E}$. When both the trial function $\boldsymbol{E}$ and the test function $\boldsymbol{T}$ share the same finite element basis and only differ in the coefficients that multiply $\boldsymbol{E}$, this approach is known as the Galerkin method.

3.1.1. Variational form

We start by considering the time harmonic wave equation (2.17) and taking the inner product with a generic time harmonic testing function $\hat{\boldsymbol{T}}$, then integrating over a volume Ω,

$$\iiint_\Omega \nabla \times (\nabla \times \hat{\boldsymbol{E}}) \cdot \hat{\boldsymbol{T}}\, \mathrm{d}V - k_0^2 \iiint_\Omega \bar{\bar{\kappa}} \hat{\boldsymbol{E}} \cdot \hat{\boldsymbol{T}} \mathrm{d}V = i\omega\mu_0 \iiint_\Omega \hat{\boldsymbol{j}}_a \cdot \hat{\boldsymbol{T}}\, \mathrm{d}V, \tag{3.1}$$

where $k_0 = \omega/c_0$ and the inner (Hermitian) product of two complex vectors is defined taking the complex argument of one of its factors,

$$\boldsymbol{u} \cdot \boldsymbol{v} = \sum_{i=1}^{n} u_i^* v_i. \tag{3.2}$$

After integration by parts, the first term in (3.1) can be expressed as,

$$\iiint_\Omega \nabla \times \left(\nabla \times \hat{\boldsymbol{E}}\right) \cdot \hat{\boldsymbol{T}}\, \mathrm{d}V = \iiint_\Omega \left(\nabla \times \hat{\boldsymbol{T}}\right) \cdot \left(\nabla \times \hat{\boldsymbol{E}}\right) \mathrm{d}V + \iint_{\delta\Omega} \hat{\boldsymbol{T}} \cdot \left(\boldsymbol{n} \times \nabla \times \hat{\boldsymbol{E}}\right) \mathrm{d}S \tag{3.3}$$

where $\delta\Omega$ denotes the boundary surface enclosing the domain and $\boldsymbol{n}$ is a normal vector to the boundary pointing in the outwards direction. To solve non-axissymmetric cylindrical 3D problems in a 2D domain characterized by axial z and radial r coordinates with associated unit vectors $\mathbf{1}_z$ and $\mathbf{1}_r$, a Fourier expansion of the time harmonic complex amplitudes $\hat{\boldsymbol{E}}$ and $\hat{\boldsymbol{j}}_a$, is taken in the periodic $\mathbf{1}_\theta$ direction,

$$\begin{aligned} \hat{\boldsymbol{E}}(z, r, \theta) &= \sum_{m=-\infty}^{\infty} \boldsymbol{E}^{(m)}(z, r) e^{im\theta}, \\ \hat{\boldsymbol{j}}_{\boldsymbol{a}}(z, r, \theta) &= \sum_{m=-\infty}^{\infty} \boldsymbol{j}_{\boldsymbol{a}}^{(m)}(z, r) e^{im\theta}. \end{aligned} \tag{3.4}$$

where m is the azimuthal Fourier mode number. Then we select the testing function to be

$$\hat{\boldsymbol{T}}(z, r, \theta) = \sum_{m=-\infty}^{\infty} \boldsymbol{T}^{(m)}(z, r) e^{im\theta}, \qquad \hat{\boldsymbol{T}}^*(z, r, \theta) = \sum_{m=-\infty}^{\infty} \boldsymbol{T}^{(m),*}(z, r) e^{-im\theta}. \tag{3.5}$$

Upon integration in θ and canceling out 2π terms, the volumetric integrals naturally convert to surface integrals over Σ — the 2D simulation domain corresponding to a meridian plane of the cylindrical geometry — and we finally obtain the weak formulation of the time harmonic wave equation for each azimuthal mode m,

$$\begin{aligned} &\iint_\Sigma \left\{ \left[\left(\nabla_t + \mathbf{1}_{\boldsymbol{\theta}} \frac{im}{r} \right) \times \boldsymbol{T}^{(m)} \right] \cdot \left[\left(\nabla_t - \mathbf{1}_{\boldsymbol{\theta}} \frac{im}{r} \right) \times \boldsymbol{E}^{(m)} \right] - k_0^2 \boldsymbol{T}^{(m)} \cdot \bar{\bar{\kappa}} \cdot \boldsymbol{E}^{(m)} \right\} \mathrm{d}S + \\ &+ ik_0 \int_{\delta\Sigma} \boldsymbol{T}^{(m)} \cdot \left[\boldsymbol{n} \times \left(\nabla_t - \mathbf{1}_{\boldsymbol{\theta}} \frac{im}{r} \right) \times \boldsymbol{E}^{(m)} \right] \mathrm{d}l = i\mu_0\omega \iint_\Sigma \boldsymbol{T}^{(m)} \cdot \boldsymbol{j}_{\boldsymbol{a}}^{(m)} \mathrm{d}S \end{aligned} \tag{3.6}$$

where ∇_t is the in-plane differential operator:

$$\nabla_t \times \boldsymbol{F} = \frac{1}{r} \frac{\partial F_\theta}{\partial r} \mathbf{1}_z - \frac{\partial F_r}{\partial z} \mathbf{1}_r + \left(\frac{\partial F_r}{\partial z} - \frac{\partial F_z}{\partial r} \right) \mathbf{1}_{\boldsymbol{\theta}} \tag{3.7}$$

If sources can be broken down into or approximated by a finite number of Fourier components, the 3D solution can be determined by solving for each mode separately and adding up all the modes

considered, taking advantage of the linearity of the system. In general, this spectral procedure is computationally much faster than solving its 3D counterpart.

3.2. Boundary conditions

To close the problem, a suitable set of boundary conditions must be imposed at the external borders of the domain, in particular the path integral term over $\delta\Sigma$ in (3.6) must be determined. If Perfect Electric Conductor (PEC) conditions are imposed at some walls of the problem, the electric field must locally satisfy the following:

$$\boldsymbol{n} \times \boldsymbol{E}^{(m)} = 0, \quad \partial\Sigma \in \partial\Sigma_{PEC} \tag{3.8}$$

rearringing the boundary term, and considering a Galerkin's formulation i.e. with $\boldsymbol{T}^{(m)}$ and $\boldsymbol{E}^{(m)}$ sharing the same functional space,

$$\int_{\delta\Sigma_{PEC}} \boldsymbol{T}^{(m)} \cdot \left[\boldsymbol{n} \times (\nabla \times \boldsymbol{E}^{(m)})\right] \mathrm{d}l = -\int_{\delta\Sigma_{PEC}} \left(\boldsymbol{n} \times \boldsymbol{T}^{(m)}\right) \cdot \left(\nabla \times \boldsymbol{E}^{(m)}\right) \mathrm{d}l = 0. \tag{3.9}$$

Consequently, the integral term vanishes and the Dirichlet conditions for the tangential component of the electric field (essential BCs, $\boldsymbol{E}_t = 0$) can be imposed without the need to compute the $\nabla \times \boldsymbol{E}^{(m)}$ at the PEC boundary. Likewise, Perfect Magnetic Conductor (PMC) conditions require:

$$\boldsymbol{n} \times \boldsymbol{B}^{(m)} = (i/\omega)\boldsymbol{n} \times \left(\nabla \times \boldsymbol{E}^{(m)}\right) = 0, \quad \partial\Sigma \in \partial\Sigma_{PMC} \tag{3.10}$$

where we have used Faraday's equation (2.1) to find the magnetic field vector as a function of the electric field. Substitying in the boundary integral, we find,

$$\int_{\delta\Sigma_{PMC}} \boldsymbol{T}^{(m)} \cdot \left[\boldsymbol{n} \times (\nabla \times \boldsymbol{E}^{(m)})\right] \mathrm{d}l = 0. \tag{3.11}$$

The latter is a Neumman condition for the electric field, also known as a natural condition, which is automatically satisfied —i.e. with no need to impose Dirichlet conditions as before— if the boundary integral is not included in the weak formulation and the tangential components of the electric field remain unknown.

Finally, in an isotropic medium or vacuum, when a plane wave impacts a surface perpendicularly, the surface can absorb all the incoming energy without any reflection if its surface impedance matches the intrinsic impedance of the propagation medium. It can be easily verified that, under such circumstances, the electric field $\hat{\boldsymbol{E}}$ satisfies the relation,

$$\boldsymbol{n} \times (\nabla \times \hat{\boldsymbol{E}}) + ik_0 \boldsymbol{n} \times (\boldsymbol{n} \times \hat{\boldsymbol{E}}) = 0, \tag{3.12}$$

this is equivalent to Sommerfeld radiation condition [77]. Then the boundary integral in (3.6) becomes,

$$\int_{\delta\Sigma_{ABC}} \boldsymbol{T}^{(m)} \cdot \left(\boldsymbol{n} \times \nabla \times \boldsymbol{E}^{(m)}\right) \mathrm{d}l = ik_0 \int_{\delta\Sigma_{ABC}} \left(\boldsymbol{T}^{(m)} \times \boldsymbol{n}\right) \cdot \left(\boldsymbol{E}^{(m)} \times \boldsymbol{n}\right) \mathrm{d}l. \tag{3.13}$$

This represents a first-order absorbing boundary condition (ABC), utilized to truncate simulation domains. It functions effectively when the boundaries are set at a considerable distance from the

source, where most waves impact the truncation boundary at minimal angles from the normal, resulting in their effective absorption. For plasma thruster simulations, the density should also be sufficiently low to approximate free space conditions, e.g. in the downstream plume or thruster periphery.

3.2.1. Axial boundary conditions

Previously, the Fourier expansion into azimuthal modes was introduced as a means of eliminating the functional dependence of the fields on the azimuthal coordinate θ, allowing 2D simulations to solve inherently 3D problems. However, concerning the treatment of the fields at the domain's axis, we note that the truncation of this domain is not straightforward, and a set of boundary conditions must be identified. Here, a suitable, though not necessarily unique, procedure for finding those BCs is described.

It should be noted that, if a cylindrical reference system is used, the coordinate θ is not precisely defined on the axis. Therefore, the dependence on the angle θ should vanish at the axis for any physical field. This dependence is revealed by expressing the fields in Cartesian coordinates:

$$E_x^{(m)} = \left[E_r^{(m)}\cos(\theta) - E_\theta^{(m)}\sin(\theta)\right]e^{im\theta} = \left[E_r^{(m)}\frac{e^{i\theta}+e^{-i\theta}}{2} - iE_\theta^{(m)}\frac{e^{-i\theta}-e^{i\theta}}{2}\right]e^{im\theta} \tag{3.14}$$

$$E_y^{(m)} = \left[E_r^{(m)}\sin(\theta) + E_\theta^{(m)}\cos(\theta)\right]e^{im\theta} = \left[iE_r^{(m)}\frac{e^{-i\theta}-e^{i\theta}}{2} + E_\theta^{(m)}\frac{e^{i\theta}+e^{-i\theta}}{2}\right]e^{im\theta} \tag{3.15}$$

$$E_z^{(m)} = E_z^{(m)}e^{im\theta} \tag{3.16}$$

Considering, for example, $m = 0$, it is easy to observe that, the axial field E_z is well posed since the only explicit function of θ, the complex exponential is exactly one and no longer depends on θ. To eliminate sinusoidal terms for the other fields, E_r and E_θ must be set to zero. The following conditions eliminate the θ dependence and must be met on the axis $r = 0$ for the complex amplitudes of the time and azimuthally expanded fields and for any mode number:

$$\begin{aligned} E_r^{(0)} &= E_\theta^{(0)} = 0 && m = 0, \\ E_r^{(\pm1)} &= \mp iE_\theta^{(\pm1)}, \quad E_z^{(\pm1)} = 0 && m = \pm1, \\ E_r^{(m)} &= E_\theta^{(m)} = E_z^{(m)} = 0 && |m| > 1. \end{aligned} \tag{3.17}$$

As shown next, these conditions are naturally implemented through the selection of an appropriate finite element basis for the the trial and testing functions $\boldsymbol{E}^{(m)}$ and $\boldsymbol{T}^{(m)}$.

3.2.2. Waveport modeling

Analytical solutions for the waves propagating in rectangular, cylindrical waveguides or coaxial transmission lines can be found. The reflected field in a homogeneous and isotropic waveguide can be expressed as the combination of orthogonal TEM (if it exists), TE, and TM waveguide modes. Separating the contribution of the incoming wave (prescribed), the total electric field reads:

$$\hat{\boldsymbol{E}} = \hat{\boldsymbol{E}}^{\text{inc}} + \hat{\boldsymbol{E}}^{\text{ref}} = \hat{\boldsymbol{E}}^{\text{inc}} + a_0\hat{\boldsymbol{e}}_0^{\text{TEM}}e^{\gamma_0^{\text{TEM}}z} + \sum_{m=0}^{\infty}\sum_{n=1}^{\infty} a_{mn}\hat{\boldsymbol{e}}_{mn}^{\text{TE}}e^{\gamma_m^{\text{TE}}z} + \sum_{m=0}^{\infty}\sum_{n=1}^{\infty} b_{mn}\hat{\boldsymbol{e}}_{mn}^{\text{TM}}e^{\gamma_m^{\text{TM}}z} \tag{3.18}$$

where $\gamma_m = \sqrt{k_{cm}^2 - k_0^2}$ is a propagation constant in the axial direction that depends on the waveguide geometry and material and k_{cm} is the characteristic cutoff wavenumber. Since there is no internal conductor, TEM waves cannot propagate through a rectangular or circular waveguide and $\hat{\boldsymbol{e}}_0^{\mathrm{TEM}} = 0$, though it is generally finite in coaxial lines. Equipped with this description, it is possible to find an expression for the boundary integral term in (3.6), in particular, after some algebra [77]:

$$\begin{aligned}\boldsymbol{n} \times (\nabla \times \hat{\boldsymbol{E}}) =& n \times \left(\nabla \times \hat{\boldsymbol{E}}^{\mathrm{inc}}\right) + \gamma_0^{\mathrm{TEM}} a_0 \boldsymbol{e}_0^{\mathrm{TEM}} e^{\gamma_0^{\mathrm{TEM}} z} + \\ &+ \sum_{m=0}^{\infty} \sum_{n=1}^{\infty} \gamma_m^{\mathrm{TE}} a_{mn} \boldsymbol{e}_{mn}^{\mathrm{TE}} e^{\gamma_m^{\mathrm{TE}} z} + \sum_{m=0}^{\infty} \sum_{n=1}^{\infty} \frac{-k^2}{\gamma_m^{\mathrm{TM}}} b_{mn} \boldsymbol{e}_{mn}^{\mathrm{TM}} e^{\gamma_m^{\mathrm{TM}} z}.\end{aligned} \tag{3.19}$$

A possible normalized basis for circular waveguide modes is [78]:

$$\begin{aligned}\hat{\boldsymbol{e}}_{mn}^{\mathrm{TE}} &= e^{im\theta} \boldsymbol{e}_{mn}^{\mathrm{TE}} = \\ &= \frac{e^{im\theta} \sqrt{\nu/2}}{\pi \sqrt{p_{mn}'^2 - m^2} J_m(p'_{mn})} \left[\mathbf{1}_{\boldsymbol{r}} \frac{m(1+i)}{r} J_m(p'_{mn} r/a) - \mathbf{1}_{\boldsymbol{\theta}} \frac{p'_{mn}(1-i)}{a} J'_m(p'_{mn} r/a) \right],\end{aligned} \tag{3.20}$$

$$\begin{aligned}\hat{\boldsymbol{e}}_{mn}^{\mathrm{TM}} &= e^{im\theta} \boldsymbol{e}_{mn}^{\mathrm{TM}} = \\ &= \frac{e^{im\theta} \sqrt{\nu/2}}{\pi p_{mn} J'_m(p_{mn})} \left[\mathbf{1}_{\boldsymbol{r}} \frac{p_{mn}(1-i)}{a} J'_m(p_{mn} r/a) + \mathbf{1}_{\boldsymbol{\theta}} \frac{m(1+i)}{r} J_m(p_{mn} r/a) \right].\end{aligned} \tag{3.21}$$

where $\nu = 1$ for $m = 0$ and $\nu = 2$ for $m \neq 0$; $J_m(r)$ is a Bessel function of the first kind, whose nth root is p_{nm}, and $J'_m(r)$ is its first derivative with roots p'_{mn}. Particularizing at the port surface, and by virtue of orthogonality of the azimuthal modes, the coefficients in (3.18) are

$$a_{mn} = \iint_{\delta\Omega_p} \hat{\boldsymbol{e}}_{mn}^{\mathrm{TE}} \cdot \left[\hat{\boldsymbol{E}} - \hat{\boldsymbol{E}}^{\mathrm{inc}}\right] \mathrm{d}S = 2\pi \int_{\delta\Sigma_p} \boldsymbol{e}_{mn}^{\mathrm{TE}} \cdot \left[\boldsymbol{E}^{(m)} - \boldsymbol{E}^{(m),\mathrm{inc}}\right] \mathrm{d}l, \quad m = 1, 2, \ldots \tag{3.22}$$

$$b_{mn} = \iint_{\delta\Omega_p} \hat{\boldsymbol{e}}_{mn}^{\mathrm{TM}} \cdot \left[\hat{\boldsymbol{E}} - \hat{\boldsymbol{E}}^{\mathrm{inc}}\right] \mathrm{d}S = 2\pi \int_{\delta\Sigma_p} \boldsymbol{e}_{mn}^{\mathrm{TM}} \cdot \left[\boldsymbol{E}^{(m)} - \boldsymbol{E}^{(m),\mathrm{inc}}\right] \mathrm{d}l, \quad m = 1, 2, \ldots \tag{3.23}$$

where $\delta\Omega_p$ denotes the 2D port surface in 3D and $\delta\Sigma_p$ is the port 1D surface in the quasi-axissymmetric problem. The new weak formulation for the wave problem reads:

$$\begin{aligned}&\iint_{\Sigma} \left\{ \left[\left(\nabla_t + \mathbf{1}_{\boldsymbol{\theta}} \frac{im}{r} \right) \times \boldsymbol{T}^{(m)} \right] \cdot \left[\left(\nabla_t - \mathbf{1}_{\boldsymbol{\theta}} \frac{im}{r} \right) \times \mathbf{E}^{(m)} \right] - k_0^2 \boldsymbol{T}^{(m)} \cdot \bar{\bar{\kappa}} \cdot \mathbf{E}^{(m)} \right\} \mathrm{d}S - \\ &- \int_{\delta\Sigma_p} \frac{2\pi}{\mu_r} \boldsymbol{T}^{(m)} \cdot P(\boldsymbol{E}^{(m)}) \mathrm{d}l = i\mu_0\omega \iint_{\Sigma} \boldsymbol{T}^{(m)} \cdot \boldsymbol{j}_{\boldsymbol{a}}^{(m)} \mathrm{d}S - \int_{\delta\Sigma_p} \frac{2\pi}{\mu_r} \boldsymbol{T}^{(m)} \cdot \boldsymbol{U}^{(\mathrm{m}),\mathrm{inc}} \mathrm{d}l,\end{aligned} \tag{3.24}$$

where we have introduced:

$$\begin{aligned}P(\boldsymbol{E}^{(m)}) = &- \gamma_0^{\mathrm{TEM}} \mathbf{e}_0^{\mathrm{TEM}} \int_{\delta\Sigma_p} \mathbf{e}_0^{\mathrm{TEM}} \cdot \boldsymbol{E}^{(m)} \mathrm{d}l - \sum_{n=1}^{\infty} \gamma_m^{\mathrm{TE}} \mathbf{e}_{mn}^{\mathrm{TE}} \int_{\delta\Sigma_p} \mathbf{e}_{mn}^{\mathrm{TE}} \cdot \boldsymbol{E}^{(m)} \mathrm{d}l - \\ &- \sum_{n=1}^{\infty} \frac{-k^2}{\gamma_m^{\mathrm{TM}}} \mathbf{e}_{mn}^{\mathrm{TM}} \int_{\delta\Sigma_p} \boldsymbol{e}_{mn}^{\mathrm{TM}} \cdot \boldsymbol{E}^{(m)} \mathrm{d}l,\end{aligned} \tag{3.25}$$

and

$$\begin{aligned}\boldsymbol{U}^{(m),\mathrm{inc}} =& \boldsymbol{n}\times\left(\nabla\times\boldsymbol{E}^{(m),\mathrm{inc}}\right)-\gamma_0^{\mathrm{TEM}}\mathbf{e}_0^{\mathrm{TEM}}\int_{\delta\Sigma_p}\mathbf{e}_0^{\mathrm{TEM}}\cdot\boldsymbol{E}^{(m),\mathrm{inc}}\mathrm{d}l- \\ &-\sum_{n=1}^{\infty}\gamma_m^{\mathrm{TE}}\mathbf{e}_{mn}^{\mathrm{TE}}\int_{\delta\Sigma_p}\mathbf{e}_{mn}^{\mathrm{TE}}\cdot\boldsymbol{E}^{(m),\mathrm{inc}}\mathrm{d}l-\sum_{n=1}^{\infty}\frac{-k^2}{\gamma_m^{\mathrm{TM}}}\mathbf{e}_{mn}^{\mathrm{TM}}\int_{\delta\Sigma_p}\mathbf{e}_{mn}^{\mathrm{TM}}\cdot\boldsymbol{E}^{(m),\mathrm{inc}}\mathrm{d}l.\end{aligned} \tag{3.26}$$

If a waveguide is designed in such a way that only one or a few modes can propagate through it at a given frequency (higher order m,n modes have higher cutoff frequencies and are usually evanescent) instead of the infinite combination of modes in (3.25) and (3.26), only some of them may be taken into account in the simulations, since for a sufficiently long waveguide, any other reflected wave will decay before reaching the port.

3.3. Mixed finite element discretization

Nédélec elements are a class of finite elements specifically designed to solve electromagnetic problems within the framework of the finite element method (FEM). They emerged from the need to address a critical challenge in electromagnetic simulations: the accurate representation of vector fields that obey Maxwell's equations, requiring the tangential components of electric and magnetic fields to be continuous across material interfaces [79]. Nédélec elements are uniquely tailored to enforce this tangential continuity, making them particularly suitable for electromagnetic simulations where field behavior at interfaces is a key concern. This attribute is essential for modeling phenomena like wave propagation, scattering, and resonance in complex geometries and diverse materials.

In practical simulations, these elements exhibit a remarkable ability to reduce the occurrence of spurious modes, non-physical solutions that can compromise the accuracy of results [80]. In many plasma thruster applications, it is important to consider the behavior of EM waves passing through the (dielectric) source walls. Nédélec elements are well suited for representing the discontinuity in the dielectric tensor of certain devices, like HPTs, where the walls are transparent to EM waves but near-vacuum conditions are found on one side and an overdense plasma on the other.

For an edge that joins the nodes l and k the associated first-order Nédélec basis function reads:

$$\mathbf{N}_{lk}^{e}(\mathbf{r}) = \ell_{lk}\left(\lambda_l\nabla\lambda_k-\lambda_k\nabla\lambda_l\right) \tag{3.27}$$

where l_{lk} denotes the edge length and λ_i is the simplex coordinate associated to node i. Figure 3.1 shows the three basis functions in a triangular element, which are used to represent the electric vector field in the plane $\{E_z, E_r\}$. In our quasiaxisymmetric formulation, the azimuthal out-of-plane direction is periodic, and the dielectric tensor is considered to be uniform along this coordinate. Therefore, simple nodal element basis functions L_i, that is, Lagrange polynomials with degrees of freedom corresponding to the field at the mesh nodes, are chosen to represent the azimuthal field E_θ, and the tangential continuity is automatically satisfied. This mixed element formulation has proven to be quite effective and accurate in overcoming issues related to spurious noise in traditional all-nodal implementations [81]. The final expression for the electric field vector used

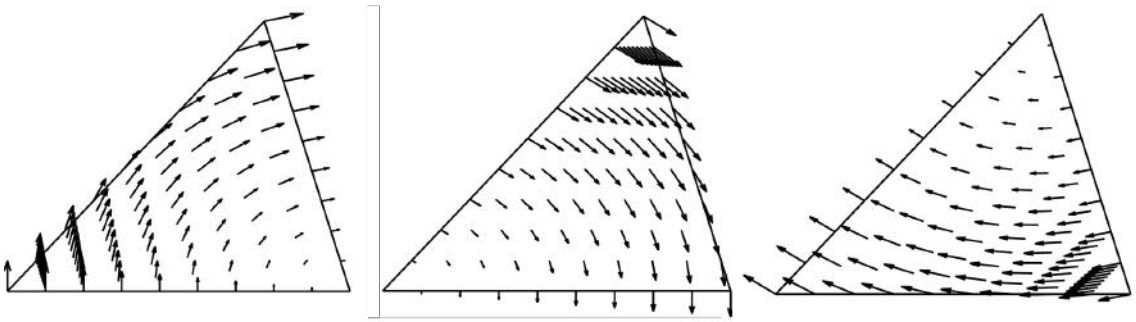

Figure 3.1: First order Nédélec vector basis functions for a triangular element.

in the weak formulation of the frequency harmonic wave equation (3.6) is:

$$\boldsymbol{E}^{(m)} = \begin{cases} \sum_{i=1}^{N_{\text{edge}}} \boldsymbol{N}_i(z,r)e_{t,i}^{(m)} + \mathbf{1}_\theta \sum_{i=1}^{N_{\text{node}}} L_i(z,r)e_{\theta,i}^{(m)} & m = 0 \\ \sum_{i=1}^{N_{\text{edge}}} r\boldsymbol{N}_i(z,r)e_{t,i}^{(m)} + (\mathbf{1}_\theta \mp i\mathbf{1}_r) \sum_{i=1}^{N_{\text{node}}} L_i(z,r)e_{\theta,i}^{(m)} & m = \pm 1 \\ \sum_{i=1}^{N_{\text{edge}}} r\boldsymbol{N}_i(z,r)e_{t,i}^{(m)} + \mathbf{1}_\theta \sum_{i=1}^{N_{\text{node}}} L_i(z,e)e_{\theta,i}^{(m)} & |m| > 1 \end{cases} \tag{3.28}$$

Above, the electric field is projected such that some field components automatically vanish and the boundary conditions in (3.17) are naturally imposed. As usual, the Galerkin method is used, where the testing function $\boldsymbol{T}^{(m)}$ is selected to match the trial function $\boldsymbol{E}^{(m)}$ except for the solution coefficients $e^{(m)}$ (which, rather than unknown, are exactly 1 for $\boldsymbol{T}^{(m)}$).

3.4. Antenna modeling

Helical antennas are known to be effective in the radiofrequency operating range in terms of power delivery to the plasma [16], as they have been found to be capable of exciting whistler wave normal modes, driving up the effective plasma resistance. At typical operation frequencies, the characteristic vacuum wavelength is much longer than the antenna $\lambda >> l_a$ and the plasma currents are in phase with the antenna current. The effectiveness of the Helicon wave as a power carrier in HPTs and plasma sources is often attributed to the geometric resonance of wave modes in the source cavity under certain plasma conditions [76]. This drives up the field magnitude and power absorption. Recent works have also highlighted additional mechanisms such as ECR heating [26], [82] and kinetic effects [83]. This section focuses on the modeling of helical antennas, which are essential in Helicon Plasma Thruster (HPT) simulations.

Figure 3.2: Nagoya III and half turn helical antenna [20], [84]

The helix angle of an antenna, located at a radius r_a, with length l_a, thickness d_t and h turns per loop, is $\alpha = \arctan(2\pi h r_a / l_a)$. The axial and azimuthal currents in the central helix are found by projecting along the helix direction $j_{za} \propto I_a \cos(\alpha)$ and $j_{\theta a} \propto I_a \sin(\alpha)$. The radial current density component is exactly zero. The water-bag function is used to limit the antenna in the axial

direction,

$$G\left(z;z_1,z_2\right)=H\left(z-z_1\right)-H\left(z-z_2\right)=\begin{cases}1, & z_1<z<z_2\\ 0, & \text{otherwise}\end{cases}, \tag{3.29}$$

where $H(z-z_0)$ is Heaviside unit step function. Then, for the upper branch, we obtain

$$j_{za,up}\propto\frac{I_a}{\sqrt{(2\pi h r_a/l_a)^2+1}}G(z;z_1,z_2)\delta\left(\theta-\frac{2\pi h[z-z_1]}{l_a}\right), \tag{3.30}$$

where the Dirac Delta $\delta(\theta-\theta_0)$ represents the twisting of the branch in the azimuthal direction. The current density must be normalized to ensure that the prescribed current intensity flows through the cross section of each of the branches $i=[up,down]$, $\iint j_{za,i}r\mathrm{d}\theta\mathrm{d}r=I_a$. Once the lower branch is included:

$$j_{za}(z,r,\theta)=\frac{I_aF(r)}{r_a\sqrt{(2\pi h r_a/l_a)^2+1}}G(z;z_1,z_2)\left[\delta\left(\theta-\frac{2\pi h[z-z_1]}{l_a}\right)-\delta\left(\theta-\pi-\frac{2\pi h[z-z_1]}{l_a}\right)\right]. \tag{3.31}$$

Above, we assumed $d_t<<r_a$ and introduced an arbitrary function, $F(r)$ that gives some thickness to the antenna in the radial direction. This function is such that its integral from 0 to the radius of the rectangular domain, r_w, is equal to 1. For an infinitely thin antenna, $F(r)$ is equal to $\delta(r-r_a)$. A normalized Gaussian profile of characteristic thickness d_t is a good choice for numerical simulations, as it provides a smooth current that does not lead to numerical artifacts upon discretization,

$$\begin{gathered}F(r)=w^{-1}\exp\left(-\frac{(r-r_a)^2}{d_t^2}\right)\\ \text{with } w=\int_0^{r_w}\exp\left(-\frac{(r-r_a)^2}{d_t^2}\right)dr=\frac{1}{2}\sqrt{\pi}d_t\left[\operatorname{erf}\left(\frac{r_a}{d_t}\right)-\operatorname{erf}\left(\frac{r_a-r_w}{d_t}\right)\right]\approx\sqrt{\pi}d_t.\end{gathered} \tag{3.32}$$

In the azimuthal direction, in addition to the central helix, two lateral loops, through which half the total current flows, must be included,

$$\begin{aligned}j_{\theta a}(z,r,\theta)=&I_a\left[\frac{2\pi hF(r)}{l_a\sqrt{(2\pi hr/l_a)^2+1}}G(z;z_1,z_2)\left\{\delta\left(\theta-\frac{2\pi h[z-z_1]}{l_a}\right)-\delta\left(\theta-\pi-\frac{2\pi h[z-z_1]}{l_a}\right)\right\}-\right.\\ &-\frac{1}{2}\delta\left(z-z_1\right)\left\{G(\theta;0,\pi)-G(\theta;\pi,2\pi)\right\}+\\ &\left.+\frac{1}{2}\delta(z-z_2)\left\{G(\theta;2\pi h,2\pi h+\pi)-G(\theta;2\pi h+\pi,2\pi h+2\pi)\right\}\right],\end{aligned} \tag{3.33}$$

An expansion in Fourier series along the θ direction is used to model the 3D antenna in the 2D axisymmetric code,

$$f(\theta)=\sum_{m=-\infty}^{\infty}f^{(m)}e^{im\theta},\qquad f^{(m)}=\frac{1}{2\pi}\int_0^{2\pi}f(\theta)e^{-im\theta}d\theta. \tag{3.34}$$

The Fourier series terms, as a function of the selected mode number m, are:

$$j_{za}^{(m)}(z,r)=\frac{I_aF(r)(1-e^{-im\pi})}{r\sqrt{(2\pi hr_a/l_a)^2+1}}\left[G(z;z_1,z_2)\frac{e^{-2im\pi h[z-z_1]/l_a}}{2\pi}\right], \tag{3.35}$$

The $(1 - e^{-im\pi})$ term makes the current vanish for even modes and double for odd m, a well-known characteristic of Helical antennas. To find the azimuthal component, we might enforce current continuity per mode, $\nabla \cdot \boldsymbol{j}_a^{(m)} = 0$,

$$\nabla \cdot \boldsymbol{j}_a^{(m)} = \frac{\partial j_{za}}{\partial z} + \frac{1}{r}\frac{\partial j_{\theta a}}{\partial \theta} = 0 \tag{3.36}$$

$$j_{\theta a} = -\frac{ir}{m}\frac{\partial j_{za}}{\partial z}, \tag{3.37}$$

or alternatively, take the Fourier transform of (3.33).

3.5. Code structure and description

The **P**lasma-**W**ave **HI**gh-fidelity **S**imulation fini**t**e-e**LE**ment solve**R** (PWHISTLER) code developed for this thesis covers the entire simulation process, from the initial setup to the generation of outputs in formats amenable to result visualization. The code is written in Python and is structured in a modular fashion, emphasizing extensibility and the reuse of routines. This design approach not only facilitates the customization of the simulation process but also promotes the efficient integration of different computational tasks. Central to the code's capabilities is its use of the FEniCSx library, which enables the efficient and parallelized solution of large-scale problems.

FEniCSx is the latest version of the FEniCS Project [85], a collection of free software with a wide range of features for solving differential equations. It is commonly used for the solution of mathematical formulations (weak forms), allowing for the direct translation of models from mathematical notation into parallelized code. FEniCSx has been developed to provide improved performance and flexibility, particularly for large-scale and complex simulations. Its design is geared towards high-level problem solving while still providing the necessary low-level control for sophisticated algorithm development. The library is especially robust in handling finite element method (FEM) computations, which is the basis of the simulation code discussed in this thesis. PWHISLTLER leverages the powerful FEniCSx routines through access to its user facing interface DOLFINx that provides a convenient Python API. However, compute-intensive operations, abstracted from the high-level Python code, are conducted in the background, harnessing the speed and efficiency of lower-level programming languages, in particular C++.

The next subsections describe the main modules of the simulation platform, these and the corresponding data flow are displayed in Figure 3.3. The usual workflows of a standard and a PWHISTLER - HYPHEN (hybrid transport solver) coupled simulation are presented in Section 3.5.5.

3.5.1. User Configuration and Input

The configuration of the simulation code is managed through a *.yaml* file, which serves as the interface for user input. This file allows for the specification of various simulation parameters, including the simulation frequency, azimuthal modes, and the degree of finite elements. In addition, it includes the definition of sources, antennas, and post-processing options in a readable format.

The properties of the different materials are defined per domain and can be specified in the

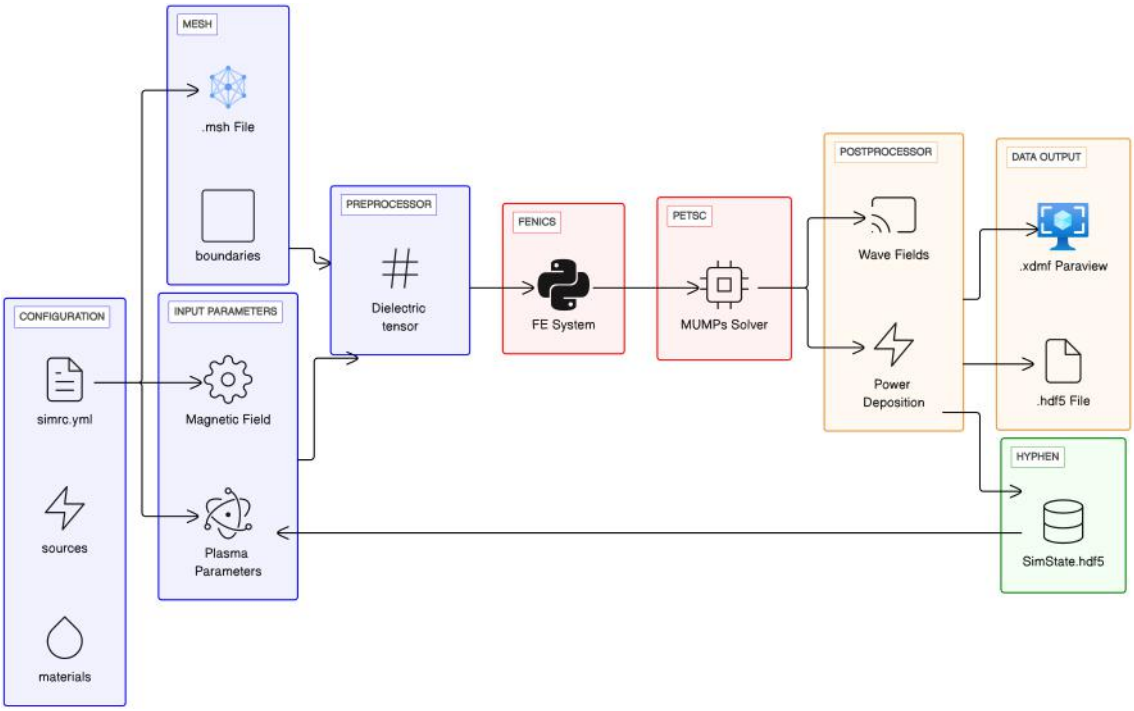

Figure 3.3: PWHISTLER simulation platform FlowChart. Preprocessor module (blue), solver (red), postprocessor modules (yellow) and HYPHEN wrapper (green).

.yaml file. This includes the assignment of different materials by either defining the full dielectric tensor, specifying cold plasma properties, using isotropic materials, or interpolating plasma profiles from the output files of the HYPHEN transport solver (plasma density, collisionality, and magnetic field). The boundary conditions are also configured in the *.yaml* file. These include the specification of waveport mode, phase, and power.

The geometric layout and mesh discretization are imported from a *.msh* file whose path is indicated in the configuration file. This file is typically generated using the Gmsh software [86]. Within the *.msh* file, geometric entities are tagged to identify different domains and boundaries. These tags are then referenced in the *.yaml* configuration file for the assignment of materials to the respective domains and for the accurate definition of boundary conditions. The use of tags in the *.msh* file and their reference in the *.yaml* file facilitates a coherent integration between the geometric setup and the simulation parameters.

3.5.2. Preprocessor Module

The preprocessor module is tasked with parsing the user-provided configuration from the *.yaml* file and initializing the simulation. Modifications to the file setup can be performed via a Python dictionary passed to the PWHISTLER PRE function, which takes as input the path to the configuration file and the user options dictionary. This can be used to overwrite specific options, an essential feature for parametric studies.

The module also creates the required FEM function spaces and interpolates the necessary information and profiles into these spaces. The preprocessor is parallelized, employing MPI (Message Passing Interface) routines to enhance computational efficiency.

The output of the PRE function is a dictionary of discretized FEM functions (DOLFINx objects), in particular the dielectric tensor and source current functions, miscellaneous objects such as the Dirichlet boundary condition object, and configuration options (azimuthal modes, antenna frequency, solver options, etc.).

3.5.3. Solver Module

This module is accessed through the SOLVE function that reads the dictionary previously output by PRE containing the interpolated FEM functions and several other configuration parameters.

The module proceeds to assemble the linear system from the weak formulation written in UFL (Unified Form Language) that resembles the original mathematical form. This assembly process is a pivotal step where the weak formulation is converted into an algebraic system of equations. Both the assembly of the linear system and the handling of the FEM functions are parallelized and managed using DOLFINx routines.

The solver module uses the PETSc toolkit to solve the assembled equations. PETSc is a suite of data structures and routines intended for the scalable solution of systems of equations. It is particularly adept at managing large, sparse linear systems, which are typical in FEM analyses.

Within this framework, the MUMPS (MUltifrontal Massively Parallel Sparse direct Solver) solver has been integrated. MUMPS is a distributed memory parallel direct solver, optimized for large sparse systems. Additional iterative and direct solvers are planned to be implemented in PWHISTLER in future versions.

Finally, the solver module includes an eigensolver functionality, leveraging the SLEPc [87] platform. SLEPc extends PETSc's capabilities to handle large-scale sparse eigenvalue problems.

3.5.4. Post-Processor Module

The post-processor module, accessed through the high level POST function, primarily focuses on the computation of derived fields from the electric field components. Key among these are the volumetric power absorption term and the induced plasma currents.

Furthermore, the module is responsible for the parallel output of *.xdmf* files. These files contain the interpolated results mapped onto the mesh. The *.xdmf* format is particularly suited and straightforwardly readable by the Paraview visualization toolkit, allowing a detailed and intuitive exploration of the simulation results.

Another significant capability of the post-processor is the interpolation and writing of the electromagnetic (EM) power deposition term into the HYPHEN *SimState.hdf5* file [88]. This is required for coupled plasma transport and EM wave simulations [71].

3.5.5. Integration and Dataflow

The internal data flow leverages Python dictionaries for managing and transferring data. This approach is chosen for its simplicity and readability, making it convenient for handling the simulation's internal data structures. Python dictionaries efficiently store pointers to DOLFINx objects.

This method does not compromise performance, as the actual computational operations on the DOLFINx objects are executed by optimized and parallelized routines.

Externally, for mesh reading and handling files that by default use the *.hdf5* format, the code utilizes parallel libraries. The nature of these dependencies aligns with the overall computational strategy of the code, which is designed to handle extensive numerical calculations and data-intensive tasks in a parallel computing environment. The output process also follows this parallel approach, particularly in the generation of *.xdmf* files.

A standard PWHISTLER simulation is performed by calling the three highest-level functions:

- **PRE Function:**
  - *Input:* Path to the *.yaml* configuration file and an optional Python dictionary for user-specific configuration overrides (‘user_config_dict‘).
  - *Output:* ‘simdata‘ object, containing the prepared simulation environment and data structures.
- **SOLVE Function:**
  - *Input:* ‘simdata‘ object from the PRE function.
  - *Output:* Updated ‘simdata‘ with the resulting electric field components, FEM functions, holding the numerical results of the simulation.
- **POST Function:**
  - *Input:* ‘simdata‘ from SOLVE function.
  - *Output:* Output *.xdmf* file per azimuthal mode *m* for visualization and/or interpolated fields into the HYPHEN *SimState.hdf5* file.

PWHISTLER has been fully integrated with HYPHEN. The simulation procedure is similar, but the user must provide a path to a HYPHEN *SimState.hdf5* in the material definition section of the *.yaml* file for every domain whose plasma properties (density, collisionality, magnetic field) will be interpolated from the transport solver output. Additionally, a configuration option can be set to interpolate the output power deposition back into the HYPHEN mesh in its corresponding *SimState.hdf5*.

Standard coupled simulations will execute this loop (HYPHEN → PWHISTLER → HYPHEN) until convergence to steady in the transport solution as described in Section 5.3 and Figure 5.4. Coupled simulations are called from within HYPHEN.

3.5.6. Customization and Extensibility and Scalability

While the high-level functions have been highlighted, the simulation code also encompasses a set of internal (private) functions that offer further customization and tailoring capabilities. These functions, embedded within the three main modules, are accessible to experienced users who wish to adapt or extend the code for specific applications. They cover a wide range of tasks, including but not limited to:

- Interpolation into FEM spaces.
- Post-processing of results and computation of derived fields such as power deposition.

Scalability is a critical aspect of the code, addressed through the adoption of the parallel MPI (Message Passing Interface) paradigm across all processes. This approach ensures that the code is well suited for multi-core architectures and can be efficiently scaled up for use in computer clusters.

A notable point in terms of scalability is the current use of direct solvers like MUMPS, which can be a bottleneck in certain scenarios. However, this limitation is mitigated by the flexibility of the PETSc toolkit, which includes various iterative Krylov methods, although this approach has not yet been tested and may require the use of preconditioners.

3.6. Verification

Three verification cases are implemented. The first two test core PWHISTLER functionality and the last one is meant to verify the new waveport boundary conditions.

3.6.1. Rectangular and cylindrical cavity resonant frequencies

If we set the right-hand side of (3.6) to 0, with PEC walls, we find the following weak formulation of the wave equation:

$$\iint_{\Sigma} \left(\nabla \times \boldsymbol{T}^{(m)}\right) \cdot \left(\nabla \times \boldsymbol{E}^{(m)}\right) \mathrm{d}S = k_0^2 \iint_{\Sigma} \boldsymbol{T}^{(m)} \cdot \bar{\bar{\kappa}} \cdot \mathbf{E}^{(m)} \mathrm{d}S \tag{3.38}$$

After discretization of the two integrals into finite element forms, the system can be expressed as a generalized eigenvalue problem:

$$\boldsymbol{A}\phi_i = \lambda_i \boldsymbol{B}\phi_i, \quad \forall i \in \{1, \ldots, d\}, \tag{3.39}$$

where $\boldsymbol{A}$ and $\boldsymbol{B}$ correspond to the discretization of the right and left-hand-side respectively in matrix form. Note that $\phi_i \in \mathbb{C}^d$ and $\lambda_i \in \mathbb{C}$ for a system with d degrees-of-freedom. The eigenvalues λ_i correspond to many, but discrete, k_0^2 that make the system have a nontrivial solution $\boldsymbol{E}^{(m)} \neq 0$.

SLEPc is a software library for computing eigenvalues and their corresponding eigenvectors in large sparse matrices. It is built on top of PETSc and follows the same programming paradigm. The library is designed for problems in which the associated matrices are sparse, such as those arising from the discretization of partial differential equations. It offers a variety of methods, including projection methods like Arnoldi and Lanczos, as well as more advanced algorithms like the Krylov-Schur method [89]. It also provides built-in support for spectral transformations, such as the shift-and-invert technique. SLEPc can handle standard and generalized eigenvalue problems, both Hermitian and non-Hermitian, with real or complex arithmetic [87].

Support for SLEPc eigensolvers was added to PWHISTLER leveraging the built-in DOLFINx PETSc interface. All preprocessing operations are equivalent to the standard problem solution, but sources are ignored if an eigensolver is set in the configuration file. In a general scenario,

with $\boldsymbol{A}$ and $\boldsymbol{B}$ not symmetric and non-Hermitean, the Krylov-Schur method appears as the fastest solution and is set as default for the following analyses. Furthermore, to speed up the computation of solutions, a spectral transformation technique is used, which relocates the original eigenvalues within the spectrum while preserving the eigenvectors [87]. The tolerance of the iterative solver is set to a value of $\sim 10^{-10}$, which is considerably lower than the expected discretization error.

The numerical values of the resonant k_0 should correlate well with the analytical solution for the resonant frequencies of the system if the latter can be found in close form. For a rectangular cavity of length a and b, setting the propagation wavenumber to zero in the out-of-plane direction $k_y = 0$, and with PEC boundary conditions, the analytical resonant frequencies can be found as [78]:

$$f_{mn} = \frac{ck_0}{2\pi} = \frac{c}{2\pi\sqrt{\mu_r\epsilon_r}}\sqrt{\left(\frac{\pi m}{a}\right)^2 + \left(\frac{\pi n}{b}\right)^2} \quad \forall (m,n) \in \mathbb{N} \tag{3.40}$$

In this particular case, using the usual nomenclature for waveguide normal modes, the resonant frequencies coincide for both the Transverse Electric mode TE_{mn} and the Transverse Magnetic mode TM_{mn}. As a consequence, multiple eigenvalues are found with different corresponding eigenmodes.

As a verification test for planar simulations, WFEM was used to find resonant frequencies for a square cavity with $a = b = 1$ m in vacuum, that is, $\varepsilon_r = \mu_r = 1$. An initial guess for the eigenvalue is set through the usual configuration file and a search of 10 eigenvalues around the target one is performed. Using a mesh with 41984 elements, the relative error in the eigenvalues of the discretized system compared to the analytical solution was found to be $< 10^{-7}$ for $(m,n) \in [0,4]$ (in addition to the trivial $k_0 = 0$ for $m = n = 0$), these are 24 modes with frequencies $f_{mn} \in [149.89, 847.94]$ MHz.

A more interesting study case, also serving as verification of the axial boundary conditions, is to consider a cylindrical cavity or truncated circular waveguide. For a cylinder of radius R and length d, with the axis oriented in the z-direction and PEC walls, the transverse electric field eigenmode can be found to be [78]:

$$\begin{aligned} E_z &= 0, \\ E_r &= \frac{-i\omega\mu_0 n}{k_c^2 r}(A\cos m\theta - B\sin m\phi)J_m(k_c r)\sin(\pi\ell z/d), \\ E_\theta &= \frac{i\omega\mu_0}{k_c}(A\sin m\theta + B\cos m\theta)J'_m(k_c r)\sin(\pi\ell z/d), \end{aligned} \tag{3.41}$$

which is very similar to (3.20) with an added sinusoidal term in z to satisfy the PEC boundary conditions. Finally, $\ell = 1, 2, ...$ is the axial mode number. The resonant frequency of the $\mathrm{TE}_{mn\ell}$ mode is

$$f_{mn\ell} = \frac{c}{2\pi\sqrt{\mu_r\epsilon_r}}\sqrt{\left(\frac{p'_{mn}}{R}\right)^2 + \left(\frac{\ell\pi}{d}\right)^2}, \tag{3.42}$$

Performing the analysis for $R = d = 1$ m and using a discretization with just 2720 elements, WFEM is capable of finding the 27 resonant frequencies (in the range $f_{mn\ell} \in [173.74, 661.72]$ MHz) and their corresponding normal modes for $m \in [0,2]$, $n \in [1,3]$ and $\ell \in [1,3]$ with a relative error $< 10^{-4}$ for all cases and in less than a minute of single core total (for all modes) compute time on an Intel Xeon 6230 machine. An example of one of these normal modes is shown in

Figure 3.4, which is in excellent agreement with the analytical solution in (3.41).

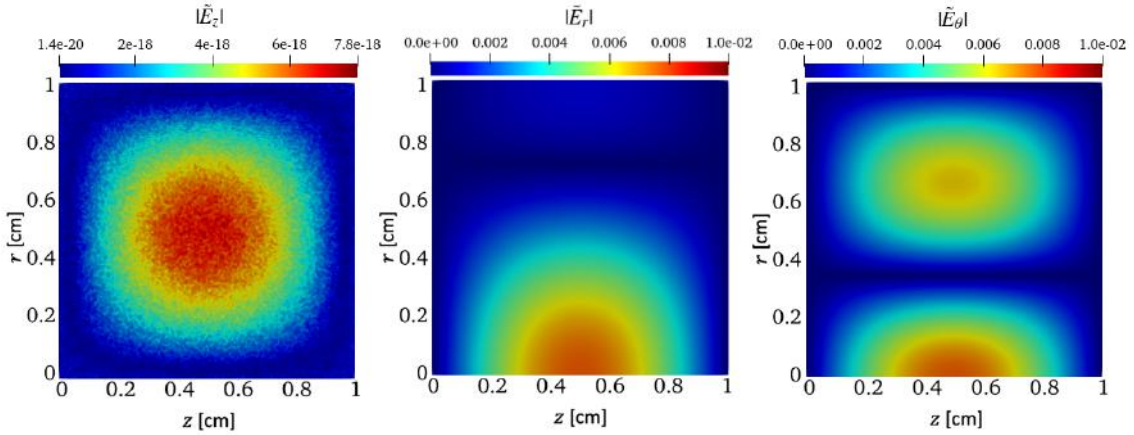

Figure 3.4: Electric field components of the numerical normal mode TE_{121} of a circular waveguide at 295.24 MHz. The magnitude of the axial field $||E_z||$ is of the order of the machine round-off error.

It is also possible to find the transverse magnetic modes $\mathrm{TM}_{nm\ell}$ whose resonant frequency is

$$f_{mn\ell} = \frac{c}{2\pi\sqrt{\mu_r \epsilon_r}} \sqrt{\left(\frac{p_{nm}}{R}\right)^2 + \left(\frac{\ell\pi}{d}\right)^2} \tag{3.43}$$

where p_{mn} is the nth root of $J_m(r)$.

3.6.2. Method of manufactured solutions

The Method of Manufactured Solutions (MMS) is a common technique to validate and verify the accuracy of numerical simulations and, in particular, of the solution of Partial Differential Equations (PDEs) with Finite Element analysis or other techniques.

Considering the frequency domain wave equation 2.17 we can create a known solution to the problem that complies with the boundary conditions $\hat{\boldsymbol{E}}_{\boldsymbol{a}}$. Afterwards, we can compute the resulting forcing term $\hat{\boldsymbol{j}}_{\boldsymbol{a}}$ by the straightforward application of the Helmholtz operator $\left(\nabla \times \nabla \times -k_0^2 \overline{\overline{\kappa}}\right) \hat{\boldsymbol{E}}_a$. Notice that the method is valid for any generic non-uniform anisotropic linear material characterized by the dielectric tensor $\overline{\overline{\kappa}}$. The forcing term is then fed into the FE solver and the solution $\hat{\boldsymbol{E}}_{\boldsymbol{n}}$ is compared to the original $\hat{\boldsymbol{E}}_{\boldsymbol{a}}$. In particular, we will use:

$$\begin{aligned}
\boldsymbol{E}_a^{(m=0)} &= (1-r^2)\mathbf{1}_z + r\sin(2\pi z)\mathbf{1}_{\boldsymbol{r}} \\
\boldsymbol{E}_a^{(m=\pm 1)} &= r\sin(2\pi r)\mathbf{1}_z + (1-r^2)\sin(2\pi z)\mathbf{1}_{\boldsymbol{r}} + im(1-r^2)\sin(2\pi z)\mathbf{1}_{\boldsymbol{\theta}} \\
\boldsymbol{E}_a^{(||m||>1)} &= r\sin(2\pi r)\mathbf{1}_z + r^2\sin(2\pi z)\mathbf{1}_{\boldsymbol{r}} + imr^2\sin(2\pi z)\mathbf{1}_{\boldsymbol{\theta}}
\end{aligned} \tag{3.44}$$

The vectors in (3.44) satisfy the axial boundary conditions outlined in 3.2.1 and do not diverge to infinity on the axis when the curl-curl operator in (2.17) is applied; this imposes certain conditions on the radial derivatives of the vector components. The following study is carried out on a metallic cylinder of radius 1 m and length 1 m. The manufactured electric field vector components are shown in Figure 3.5 for mode $m = -1$. The nominal frequency is set at $f = 500$ MHz. These parameters push the simulation model, resulting in wavelengths considerably shorter than

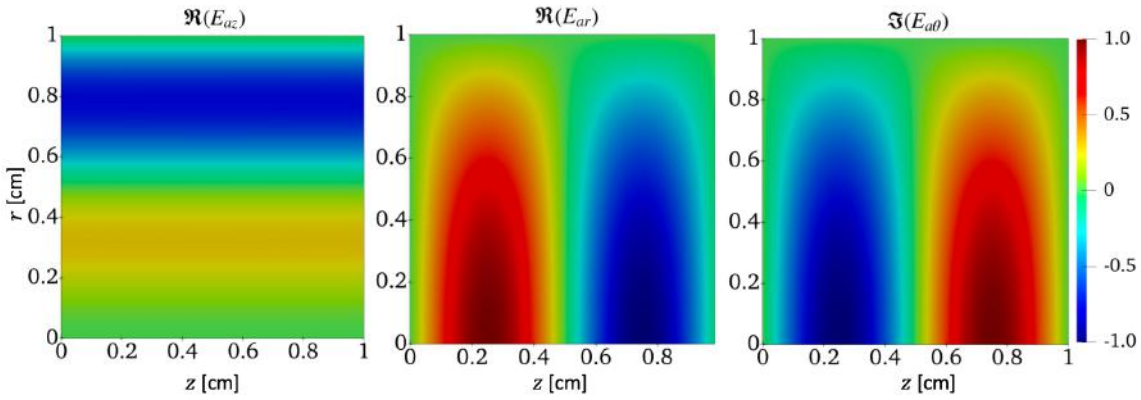

Figure 3.5: Test solution used in the manufacture of solutions verification for mode $m = -1$.

the typical ones for HPTs (length of *cm* and frequencies of tens of MHz).

We want to carry out a convergence analysis using the MMS method, for which we define the following global residual using the L_1-norm of the difference between the numerical and the manufactured electric field vectors:

$$\text{residual} = \iint_{\Sigma} \left\| \boldsymbol{E}^{(m)} - \boldsymbol{E}_{\boldsymbol{a}}^{(m)} \right\| \mathrm{d}S \tag{3.45}$$

With this definition, a parametric analysis is performed, refining the mesh and varying the order of the finite elements employed. The order, p, of the vector (for E_z and E_r) and node elements (for E_θ) are kept the same for simplicity. The results are shown in Figure 3.6 with two different materials, these are vacuum and an overdense and magnetized plasma in region 8 of the CMA diagram 2.2.

The error decreases as expected with the average node spacing h, which, in 2D, is proportional to the square root of the number of elements N_e. For both vacuum and uniform plasma conditions, a very strong residual correlation $\propto h^{-p}$ is observed. The additional dissipation provided by the collisional plasma seems to enhance the convergence rates even further, although the difference from the expected scaling law is small. The simulation times show a near linear relationship with the number of elements when the system size is greater than approximately 100,000 elements.

When an Electron Cyclotron Resonance (ECR) was added to the domain (at $z = 0.85$ m), a significant deviation was observed in the convergence rate of the high-order element cases. The behavior is observed even when the plasma frequency and collisionality are increased. This suggests the excitation of spurious high k modes in the vicinity of the resonant surface [73] that, according to the breakdown in the convergence rates of Figure 3.7-(left), might only be present when using high-order elements. As shown in Figure 3.7-(right), numerical noise seems to propagate to other regions and is particularly prominent near the symmetry axis. A dedicated study to find the cause of this numerical behavior is needed. The need for mesh refinement near the resonance has already been highlighted by Sanchez et al. [41]. For the rest of the simulations presented in this thesis, first-order elements will be used, and mesh refinement will be performed whenever needed. This methodology is allegedly the most robust, although probably not optimal in terms of computational resources.

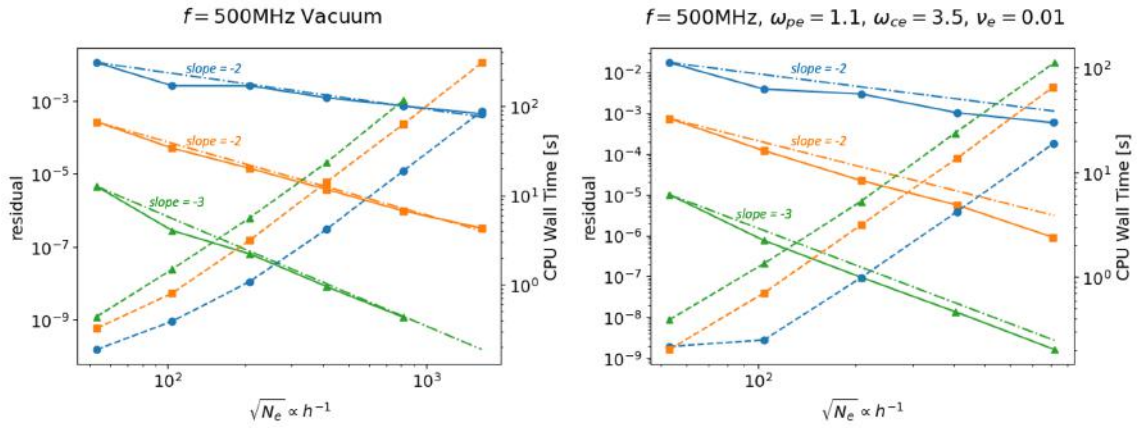

Figure 3.6: Residual (left-axis, continuous lines) as defined in (3.45) and CPU wall times (right-axis, dashed lines) as a function of the average node spacing h . Convergence study for vacuum (left) and uniform magnetized plasma (right). Different lines correspond to different finite element orders: 1st order (blue circles), 2nd order (orange squares) and 3rd order (green triangles). All solutions are for $m = -1$.

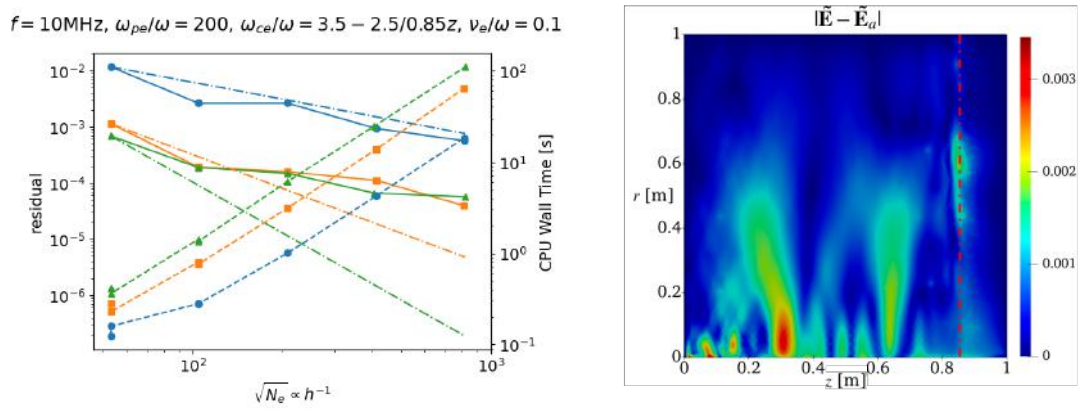

Figure 3.7: Left: Convergence of the solution in the method of manufactured solutions for a plasma with an ECR resonance surface at $z = 0.85$ m. Right: local error (L_1-norm) in the manufactured solution for $m = -1$, the red dashed line corresponds to the ECR surface location. Simulation with 43130 2nd order elements.

3.6.3. Port BCs Verification

We verify next the wave port boundary conditions presented in section 3.2.2. We set up a waveguide with a radius of $R = 0.018$ m and a length of 0.2 m. At a frequency of $f = 5.8$ GHz, the only propagating mode is TE_{11} with a cutoff frequency of approximately 4.9 GHz. All other modes are evanescent at this excitation frequency. The upper wall is a perfect electric conductor, and the lower domain boundary corresponds to the axis of symmetry. We send a wave from the leftmost wall, an inbound port with equal power in $m = 1$ and $m = -1$ components. The right wall, an outbound port, is set to absorb all incoming waves, i.e. $\hat{\boldsymbol{E}}^{inc} = 0$. To verify the correct functioning of the ports and the absence of any reflection or numerical artifacts, we tracked the motion of a wavefront and observed an axial displacement of $L = 0.096$ m in one period $T = 1/f$, obtaining a corresponding phase velocity $v_{ph} = L/T = 5.57 \cdot 10^8 \mathrm{m/s} > c_0$. Similarly to in Section 3.2.2, the

analytical solution for propagation of a right-traveling TE mode through a waveguide is:

$$\boldsymbol{E} \propto \hat{\boldsymbol{e}}_{11}^{\mathrm{TE}} e^{i(\omega t - \beta z)}, \tag{3.46}$$

where $\beta = \sqrt{k_0^2 - k_{c11}^2} = 65.69$ rad/s and $k_{c11} = p'_{11}/R$. From this we can compute an analytical phase velocity $v_{ph} = 2\pi f/\beta$ that coincides with the measured value up to the third significant digit, the error mainly attributed to the lack of precision in computing L. Despite the superluminal phase velocity, it can be shown that the group velocity remains physical ($\leq c_0$).

3.7. Finite element vs finite differences discretization

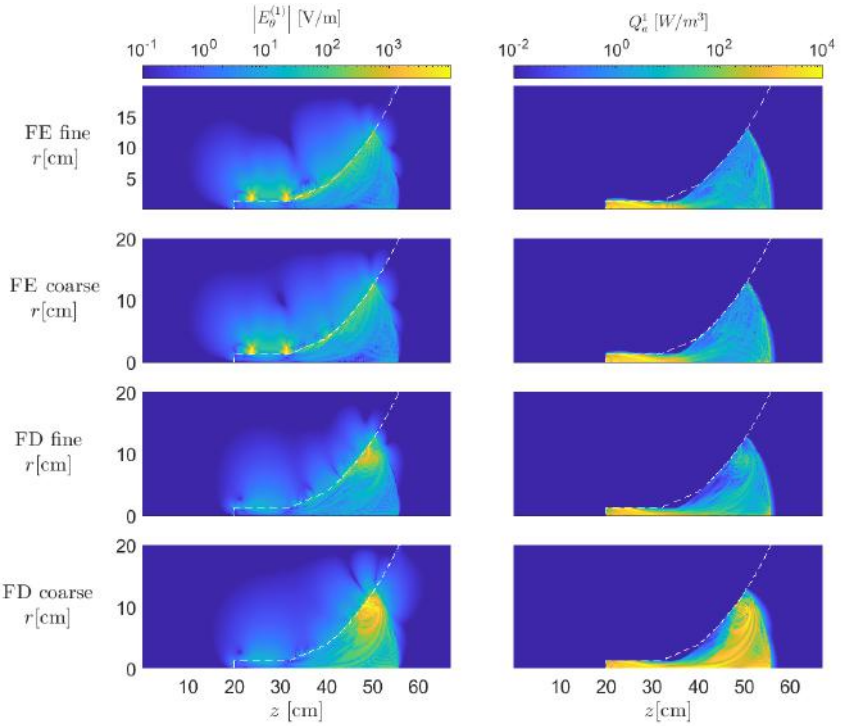

Figure 3.8: Finite Element (FE) and Finite Difference (FD) full thruster and plume wave solutions [26]. E_θ^1 electric field magnitude (1st column), and power deposition (2nd column). Putative spurious noise is localized near the $\omega = \omega_{pe} = \omega_{ce}$ crossing in the FD simulations and, in the coarse case, extends throughout most of the plume region. Coarse meshes have about $\sim 3 \cdot 10^5$ nodes and fine meshes $\sim 1.4 \cdot 10^6$ nodes.

Previous full-wave solvers [25], [90] applied to Helicon thrusters have relied on Finite Difference (FD) discretizations of Maxwell's equations, predominantly based on structured staggered grids and Yee's method [91].

The presence of a full dielectric tensor for waves traveling through a magnetized plasma medium introduces the need for interpolations in the electric field components placed at different nodes of the staggered grid. These interpolations can induce spurious noise in transition regions where the dielectric tensor does not vary smoothly [26]. Additionally, the quality of the solution seems to depend on the relative alignment of the mesh and the applied magnetic field, and, moreover, the spatial variation of the dielectric tensor with plasma properties calls for widely dif-

ferent mesh sizes at locations with long and short wavelengths. A conforming Finite Element (FE) discretization on an unstructured grid allows us to partially tackle these problems.

The performance of the new FE code is compared with the older FD code from [26] and presented in Chapter 4, for the same simulation setup of that work (see Section 4.2). Figure 3.8 shows the magnitude of the azimuthal field and the power deposition map for $m = 1$. Although the FE results are essentially invariant under two different mesh sizes and therefore we can claim mesh convergence, this is not true for the FD results with comparable or even finer grids. Furthermore, the FD results feature spurious large field values near the triple point where $\omega = \omega_{pe} = \omega_{ce}$, around $z = 50$ cm, $r = 10$ cm. This numerical error is prevalent in most of the plume region and clearly affects the power deposition maps.

In addition to the increase in accuracy and the elimination of spurious features, the efficiency of the FE solver is much higher than that of the FD one, achieving an average reduction factor of 5 in the CPU wall time with comparable meshes. These advances come mainly from the parallelization of the FE library and the solvers used.

4. *Wave propagation and absorption in a Helicon plasma thruster and its plume*

The contents of the following chapter have been peer-reviewed and published in [26] and are reproduced here without modifications. Please excuse any duplicity or repeated information, especially in the introduction, that might occur as a result of its inclusion in other chapters of this work.

A two-dimensional, full-wave, frequency domain, cold plasma model is used to study electromagnetic power propagation and absorption in a helicon plasma thruster, including its far plume region and surrounding space. Results show that a fraction of power is absorbed in the plume region, and that power deposition in the source is essentially unperturbed by the simulation domain size, the presence of metallic obstacles, or the plasma density in the environment. An electron-cyclotron resonance (ECR) surface always exists downstream that effectively prevents radiation to the space beyond along the plume. In the presence of an overdense environmental plasma, like the one expected in a vacuum chamber, fields are fully evanescent beyond this transition, and vacuum chamber boundary conditions affect but little the wavefields before this surface. In the absence of an environmental plasma, a double wave regime transition exists at the interface between the plasma and vacuum that hinders accurate numerical simulation in the plume region.

4.1. Introduction

Helicon Plasma Thrusters (HPTs) are electric propulsion devices currently under research and development [28], [31], [92]–[98]. Their operation relies on the heating of a magnetically-confined plasma in a cylindrical vessel via oscillating electromagnetic fields generated with an inductor/antenna [99], [100], and the expansion and acceleration of that plasma in an external magnetic nozzle (MN), where magnetic thrust is generated before detachment occurs [32], [101], [102]. Being electrodeless, HPTs promise certain advantages compared to traditional electric propulsion technologies such as gridded ion thrusters or Hall thrusters, such as a potentially enhanced lifetime and the simplification of the overall system and electrical architecture [5]. The ease of control of the magnetic nozzle topology suggests a high throttlability. Moreover, the absence of hollow cathodes with sensitive material inserts opens the possibility of using alternative propellants. However, reported thrust efficiencies are still bellow 20% [95], [103], and there are still open questions in the understanding of the physical mechanisms that drive the performance of the HPT, in particular the problem of plasma heating by the electromagnetic waves.

The propagation and absorption of the electromagnetic fields is central to the operation of the device, and constitutes the object of study of the present work. These processes depend on the antenna geometry and currents, the shape of the source, the magnetic topology and strength, the plasma density map and, to a lesser extend, on the plasma temperature affecting the effective collisionality. In turn, the electromagnetic power deposition determines the plasma properties in the device. While the two aspects are intimately coupled, the timescale of the electromagnetic

problem (10^{-7} s, or tens of MHz) is much faster than that of the plasma transport problem (ion transit times are in the order of 10^{-5} s). This enables the approximate study of these phenomena separately, an approach that has been successfully used to analyze the slow plasma dynamics in the source on the one hand [104]–[107], and the internal electromagnetic field problem on the other hand [22], [108].

At the MHz-level frequencies used, typically 13.56 MHz, the ion response to the fast fields is negligible, and the electron response determines the propagation and absorption characteristics. For plasma densities n greater than 10^{12}–10^{13} m^{-3} and applied magnetic field strengths B_a greater than 1–10 G, the excitation frequency ω is smaller than the electron plasma frequency ω_{pe} and the electron cyclotron frequency ω_{ce}, i.e. $\omega < \omega_{pe}, \omega_{ce}$. This means that the left-hand polarized (L) wave is evanescent and only the right-hand polarized (R) whistler wave propagates inside the HPT plasma, and only if its wavevector $\boldsymbol{k}$ falls within a cone of half angle α_c about the magnetic field vector $\boldsymbol{B}_a$ [19]. On the surface of this cone, $k \to \infty$ and therefore it is referred to as a resonance cone. Traditionally, this wave has been called helicon (H) wave [99], [109] (longer wavelengths) when $\boldsymbol{k}$ is essentially parallel to $\boldsymbol{B}_a$, and Trivelpiece-Gould (TG) [110] waves (shorter wavelengths) when $\boldsymbol{k}$ is essentially parallel to the resonance cone (and therefore has an important $k_\perp$ component). For high B_a, both types of R waves are present, meaning that there are some values of $k_\parallel$ for which there are two solutions of $k_\perp$, one associated to the H wave and another to the TG wave. This is known as the double wave regime (DWR) [16]. In contrast, at lower B_a, only a single value of $k_\perp$ exists for each propagating $k_\parallel$, this is known as the single wave regime (SWR). In general, both H and TG waves contribute to plasma heating, but a larger share of the power deposition is sometimes attributed to TG waves, especially near the surface of the plasma [67].

As the plasma expands into the MN, the magnetic field strength and plasma density gradually decrease. At some surface downstream in the plume, the electron-cyclotron resonance (ECR) eventually takes place where $\omega = \omega_{ce}$. With the typical operating frequency the resonant magnetic field strength is 4.84 G. Beyond the ECR surface, and as long as the plasma continues to be overdense ($\omega < \omega_{pe}$), the fields become evanescent. Eventually, the critical density transition ($\omega = \omega_{pe}$) is also reached, albeit typically this happens much farther out from the device.

Also, part of the electromagnetic excitation may leak out into the surrounding peripheral space. The situation here depends on the environmental conditions: in a perfect vacuum, both L and R waves propagate equally and unaffected by $\boldsymbol{B}_a$, with speed c and wavelength of tens of meters, obviously much larger than the device dimensions. At the interface between the dense HPT plasma and the vacuum, the L wave cutoff and the critical density transition are quickly traversed in succession.

However, in an the environment with a tenuous plasma, propagation continues to be determined by n and $\boldsymbol{B}_a$. The ECR transition also exists in the peripheral space, and may affect the wavefields substantially. In particular, for plasma densities higher than the critical one, the propagation regime for R waves is qualitatively the same as inside the device—whistler waves propagating up to an angle with $\boldsymbol{B}_a$, and evanescence beyond the ECR surface And, for densities roughly twice the critical value, the L wave does not propagate. These environmental conditions are relevant to experiments in laboratory vacuum chambers, which are intended to be representative of in-flight conditions, but where only a non-perfect vacuum may be achieved.

The simplest 1D radial models already show the presence of H and TG waves inside the cylindrical plasma source [21]–[23]; however, they miss the effect of axial nonuniformities in n and $\boldsymbol{B}_a$. Full-wave 2D asymmetric codes have been developed in the past to tackle this problem [20], [24], but under the assumption of an axially-aligned magnetic field $\boldsymbol{B}_a = B_{az}\mathbf{1}_z$. Recently, Tian et al. [25] relaxed this limitation and included a small portion of the diverging MN plume in the model, enabling the analysis of the influence of the magnetic field topology on the wave propagation. Melazzi et al. [22] used a different approach relaying on the Method of Moments to solve for the surface electric current density on the antenna and the volume polarization current within the plasma. Relatedly, Sánchez-Villar et al. [41] presented a full-wave Finite Element Method (FEM) tool that has been successfully used for the simulation of a different type of electrodeless thruster, the Electron Cyclotron Resonance Thruster (ECRT).

Existing studies of the electromagnetic fields in HPTs have been restricted to the plasma source and the very near plume. This leaves out several major questions on the propagation and absorption problem, such as whether this limited simulation domain is sufficient to understand power absorption by the plasma as a whole; or whether part of the radiofrequency (RF) radiation can escape downstream along the plume and be absorbed there. The role of the distant ECR surface has not been considered, to the best of our knowledge, in the operation of HPTs. Finally, it is relevant to ask what are the effects of the surrounding environment, i.e. whether a tenuous plasma or metallic obstacles can change the performance of the absorption by opening/closing propagation paths.

This work extends the 2D Finite Difference Frequency Domain (FDFD) model of [25] with an improved numerical implementation and interpolation routines for larger domains, and uses it to simulate the propagation and absorption of the RF fields in the source, surroundings, and far plume of an HPT, beyond the ECR surface, increasing the axisymmetric domain size from 15 cm to 67 cm axially and 2 cm to 20 cm radially, enabling the full simulation of the ECR transition. Furthermore, instead of a simple expansion for the plasma density and a constant collision frequency in the whole domain, a realistic map of plasma density is obtained from transport codes, one for the internal plasma dynamics [111], and another for the external expansion in the MN [32], and a collisionality map based on this density is used. Four different simulation cases are used to explore the questions above. Finally, we identify and comment on the modeling and numerical difficulties found when solving for the wavefields in the presence of critical density transition that takes place between the dense HPT plasma and a perfect vacuum.

The device of reference for the study is a medium size HPT (about 350–500 W) similar to the HPT05 prototype developed jointly by SENER Aeroespacial and UC3M [10].

The rest of this paper is structured as follows: Section 4.2 describes the plasma-wave model, the numerical implementation, and the the geometry and plasma profile inputs to the simulations. Section 4.3 provides a discussion of the electromagnetic fields and power deposition profiles obtained in four different simulation cases. Finally the difficulties of modeling and simulating the electromagnetic fields across critical density transitions, and the convergence of the numerical results, are surveyed in Section 4.4. Section 4.5 gathers the conclusions of this work.

4.2. Electromagnetic model

The 2D, frequency-domain, electromagnetic model considers the physical domain represented in figure 4.1. The HPT source and its near plume are labelled as region 1, the magnetically guided far plume as region 2, and the periphery of the device as region 3. An axisymmetric plasma of known properties fills regions 1 and 2. The regions are determined based on the plasma transport code used to obtain the input profiles to the wave code as described in section 4.2.2. Additionally, an environmental plasma may exist in region 3, depending on the study case. With the exception of the axis of symmetry, the domain is terminated at metallic walls representing a vacuum chamber, which can be considered perfect conductors. Additionally, the magnetic coils and the HPT support equipment box (power processing unit, gas feed system, etc) inside the domain are treated as perfect-conductor metallic boxes.

The domain of figure 4.1 is excited by a known applied electric current $\boldsymbol{\mathcal{J}}_a$ at frequency $\omega/(2\pi) = 13.56$ MHz in the half-helical antenna located around the source. The applied magnetic field $\boldsymbol{B}_a$ is also shown in the figure. The $\boldsymbol{B}_a$ topology is slowly converging inside the source and diverging in the plume, with the magnetic throat placed approximately at the exit of the thruster tube. As the magnetic field strength decreases away from the source, an electron-cyclotron resonance surface appears on which $\omega = \omega_{ce}$. Following the nomenclature of [16], the plasma source and part of the plume is in the DWR, and only as B_a decreases, the plasma enters the SWR (near the ERC surface).

The HPT dimensions and characteristics are displayed in table 4.1. Four simulation cases are defined as follows:

Case R This is the main simulation case and used as reference in the discussion. Region 3 is filled with a tenuous plasma of density $n = 10^{14}$ m^{-3}, a reasonably low value for a typical laboratory vacuum chamber operation. This results in an overdense plasma in the peripheral space of the thruster. The internal metallic elements (coils, electronics ...) are treated as perfect electric conductors.

Case T This case is identical to Case R, except that the internal metallic boxes are removed from the simulation and therefore are transparent to the fields. The comparison of this case with Case R illustrates the effect of obstacles on the propagation of the electromagnetic fields.

Case V The difference with respect to Case R is that the plasma density in region 3 is removed, $n = 0$, i.e. region 3 is a perfect vacuum. The comparison of this case with Case R shows the influence of the environmental plasma, and the complexities associated with the critical density transition that takes place at the plasma-vacuum edge.

Case S This smaller version of Case R restricts the integration domain to region 1 and just the minimal part of region 3 to make the domain rectangular, with size [20–40] cm ×[0–4] cm.

In the following, we employ a cylindrical right-handed vector basis $\{\mathbf{1}_z, \mathbf{1}_r, \mathbf{1}_\theta\}$. The unitary vectors parallel and perpendicular to the locally applied magnetic field also allow forming an auxiliary vector basis, $\{\mathbf{1}_\parallel, \mathbf{1}_\perp, \mathbf{1}_\theta\}$.

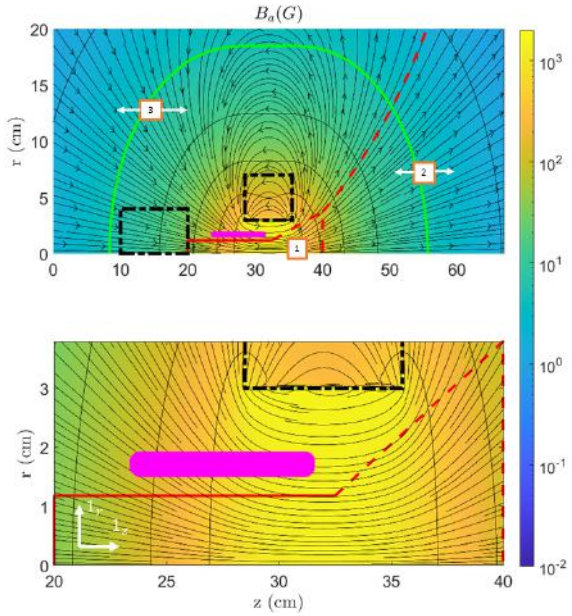

Figure 4.1: (top). Simulation regions, applied magnetic field strength and field lines. The red line is the limit between the 3 different domains considered, the solid section corresponding to the plasma source. The green line depicts the electron cyclotron resonance location. The antenna is highlighted in magenta. The black dashed lines are additional conductor boundaries that represent thruster subsystems like the magnetic coils, structure, power processing unit, etc. (bottom). Zoom of Region 1.

Parameter	
Full simulation domain size	67 cm × 20 cm
Chamber length l_c	12.5 cm
Chamber radius r_c	1.25 cm
Antenna type	Half-turn Helical
Coil current	$11 \cdot 10^3$ Ampere-turn
Antenna frequency $f = \omega/(2\pi)$	13.56 MHz
Antenna Power	350 W
Antenna loop radius r_a	1.75 cm
Antenna length l_a	7.5 cm
Antenna central position z_a	27.5 cm
Antenna thickness d_t	0.5 cm
Propellant species	Xe
Propellant mass flow rate	1.0 mg/s

Table 4.1: Design and operational parameters.

4.2.1. Model formulation

A cold plasma model is used to describe the linearized plasma response to the electromagnetic fields. While the plasma itself is axisymmetric, we allow for non-axisymmetric fields, which we decompose into azimuthal m modes. Any vector quantity $\mathcal{F}(z, r, \theta, t)$ is expressed as the real part

of a superposition of such modes,

$$\mathcal{F}(z, r, \theta, t) = \Re\left[\sum_{m=-\infty}^{\infty} \boldsymbol{F}^m(z, r) \exp(-\mathrm{i}\omega t + \mathrm{i}m\theta)\right], \tag{4.1}$$

where $\boldsymbol{F}^m(z, r)$ is the complex magnitude vector at $t = 0, \theta = 0$ for mode m. We do this, in particular, for the fast electric and magnetic fields $\boldsymbol{\mathcal{E}}$ and $\boldsymbol{\mathcal{B}}$. Under these premises, the m-th complex amplitude of the electric displacement field $\boldsymbol{\mathcal{D}}$ can be expressed as

$$\boldsymbol{D}^m(z, r) = \varepsilon_0 \bar{\bar{\kappa}}(z, r) \cdot \boldsymbol{E}^m(z, r), \tag{4.2}$$

where $\bar{\bar{\kappa}}(z, r)$ is the (axisymmetric) local cold plasma dielectric tensor [19], whose components in the vector basis $\{\mathbf{1}_\parallel, \mathbf{1}_\perp, \mathbf{1}_\theta\}$, after neglecting the contribution of ions, are:

$$\bar{\bar{\kappa}}(z, r) = \begin{pmatrix} P & 0 & 0 \\ 0 & (R+L)/2 & -i(R-L)/2 \\ 0 & i(R-L)/2 & (R+L)/2 \end{pmatrix}, \tag{4.3}$$

with

$$R = 1 - \frac{\omega_{pe}^2}{\omega(\omega + i\nu - \omega_{ce})},$$
$$L = 1 - \frac{\omega_{pe}^2}{\omega(\omega + i\nu + \omega_{ce})},$$
$$P = 1 - \frac{\omega_{pe}^2}{\omega(\omega + i\nu)};$$

where the electron cyclotron and plasma frequencies are defined as

$$\omega_{ce}(z, r) = \frac{eB_a}{m_e}, \qquad \omega_{pe}(z, r) = \sqrt{\frac{ne^2}{m_e \varepsilon_0}}; \tag{4.4}$$

and the rest of symbols are conventional. The electron cyclotron and plasma frequencies, $\omega_{ce} \propto B_a$ and $\omega_{pe} \propto n^{-1/2}$, are the main plasma parameters in the electromagnetic model, while the electron collisionality, ν, is secondary as long as $\nu/\omega \ll 1$. The ECR transition occurs when $\omega = \omega_{ce}$ and $R \to \infty$, while the critical density transition occurs when $\omega = \omega_{pe}$ and $P \to 0$. The L wave cutoff takes place when $L = 0$. The tensor $\bar{\bar{\kappa}}$ is rotated to the cylindrical vector basis used in the problem discretization.

To model the antenna current $\boldsymbol{\mathcal{J}}_a$, we define the helicity number h as the number of complete turns of the antenna wire around the cylindrical source; for a half-turn helical antenna, $h = 0.5$. Inside the antenna, for $z \in [z_a - l_a/2, z_a + l_a/2]$ and $r \in [r_a - d_t/2, r_a + d_t/2]$, the axial current density is proportional to

$$\mathcal{J}_{za} \propto \delta\left(\theta - \frac{2\pi h}{l_a}(z - z_1)\right) - \delta\left(\theta - \pi - \frac{2\pi h}{l_a}(z - z_1)\right), \tag{4.5}$$

where δ is the Dirac delta distribution and $z_1 = z_a - l_a/2$. This equation represents the two wires of the antenna as they wind about the cylindrical source a number of turns determined by the helix

number (one full turn for h=1). The antenna is 1D in the z, θ plane and has thickness d_t in the radial direction. For further reference in the modelling of helical antennas see [20], [84]. The radial current density $\mathcal{J}_{ar}$ is zero, and the azimuthal current density is determined by continuity, $\nabla \cdot \boldsymbol{\mathcal{J}}_a = 0$ [25]. As the electromagnetic problem is linear, the total current in the antenna is normalized to 1 A to compute the fields response.

Faraday's and Ampère's laws in (ω, m) space yield the following equations on the complex field amplitudes:

$$\frac{\mathrm{i}m}{r}E_z^m - \frac{\partial}{\partial z}E_\theta^m - \mathrm{i}\omega B_r^m = 0, \tag{4.6}$$

$$\frac{\partial}{\partial z}E_r^m - \frac{\partial}{\partial r}E_z^m - \mathrm{i}\omega B_\theta^m = 0, \tag{4.7}$$

$$\frac{1}{r}\frac{\partial}{\partial r}\left(rE_\theta^m\right) - \frac{\mathrm{i}m}{r}E_r^m - \mathrm{i}\omega B_z^m = 0, \tag{4.8}$$

$$\frac{\mathrm{i}m}{r}B_z^m - \frac{\partial}{\partial z}B_\theta^m + \mathrm{i}\omega\mu_0 D_r^m = \mu_0 J_{ar}^m, \tag{4.9}$$

$$\frac{\partial}{\partial z}B_r^m - \frac{\partial}{\partial r}B_z^m + \mathrm{i}\omega\mu_0 D_\theta^m = \mu_0 J_{a\theta}^m, \tag{4.10}$$

$$\frac{1}{r}\frac{\partial}{\partial r}\left(rB_\theta^m\right) - \frac{\mathrm{i}m}{r}B_r^m + \mathrm{i}\omega\mu_0 D_z^m = \mu_0 J_{az}^m, \tag{4.11}$$

As boundary conditions, the lateral and top walls in cases R, T, V and S are modelled as Perfect Electric Conductors (PEC), and so are the support equipment boxes in cases R and V. PEC boundaries are characterized by a null tangential electric field $\boldsymbol{E} \times \mathbf{1}_n = 0$ and a null normal magnetic field $\boldsymbol{B} \cdot \mathbf{1}_n = 0.$, where $\mathbf{1}_n$ is the unit normal vector to the domain boundaries. At the axis of symmetry, the following smoothness conditions apply for each mode m for any field $\boldsymbol{F}^m$ [77],

$$\begin{aligned}
&F_r^m = F_\theta^m = 0 && \text{for } m = 0,\\
&F_r^m = \mp i F_\theta^m, \quad F_z^m = 0 && \text{for } m = \pm 1,\\
&F_r^m = F_\theta^m = F_z^m = 0 && \text{for } |m| > 1
\end{aligned}$$

(where the components of $\boldsymbol{F}$ correspond to either $\boldsymbol{E}$ or $\boldsymbol{B}$).

The plasma current density induced by the wave electric field is

$$\boldsymbol{J}_p^m = \mathrm{i}\omega\epsilon_0(\overline{\overline{1}} - \overline{\overline{\kappa}}) \cdot \boldsymbol{E}^m, \tag{4.12}$$

where $\overline{\overline{1}}$ is the identity tensor and the time-averaged power density deposited into the plasma by mode m is $Q_a^m = \Re\left((\boldsymbol{J}_p^m)^* \cdot \boldsymbol{E}^{\boldsymbol{m}}/2\right)$. The total resistive power seen at the antenna can be computed as the sum of the volume integral over the simulation domain for all the azimuthal modes,

$$P_a = \sum_m \int_\Omega Q_a^m \mathrm{d}\Omega. \tag{4.13}$$

(alternativa)

$$P_a = \sum_m P_a^m, \qquad P_a^m = \int_\Omega Q_a^m \mathrm{d}\Omega. \tag{4.14}$$

While we used a total power of 350 W to obtain the realistic plasma profiles from the transport simulations, observe that the wave problem is linear, and therefore fixing the antenna current at 1 A makes P_a numerically equal to the total resistance of the plasma, as seen by the antenna, and makes Q_a^m numerically equal to the local plasma resistivity, in SI units.

In the light of previous studies [107], [112] showing that the vast majority of the plasma resistance corresponds to the interaction of the electromagnetic fields with the currents in the azimuthal mode $m = 1$, this work focuses on this mode; the importance of higher modes is evaluated in section 4.3.

4.2.2. Magnetic field and plasma profiles

The cold plasma dielectric tensor $\bar{\bar{\kappa}}$ at each point depends on the applied magnetic field $\boldsymbol{B}_a$, the plasma density n, and—to a lesser extent—the effective electron collisionality ν. The magnetic field $\boldsymbol{B}_a$, already shown in figure 4.1, is obtained analytically by modeling the magnetic coils of the device as a collection of current loops.

The plasma density n inside the source region 1, shown in figure 4.2, is obtained from the simulation of the plasma transport with the HYPHEN hybrid code [107]. The full details of HYPHEN can be found in [113]. This code solves the plasma properties in the source and near plume treating heavy species (ions and neutrals) kinetically and magnetized electrons as a fluid. Neutral gas injection, plasma sheaths, recombination at the walls and both elastic collisions and ionization are included in the model. Once HYPHEN reaches a stationary solution, the plasma density and ion flux at the right border of region 1 are used as the input to the open-source magnetic nozzle DIMAGNO code [32], which solves the plasma transport in region 2. DIMAGNO uses a fluid formulation for partially-magnetized ions and fully-magnetized electrons. The plasma collisions are neglected in the plume, and the supersonic plasma expansion is propagated using the method of characteristics. Notice that the HYPHEN domain (region 1) is polygonal while the DIMAGNO domain (region 2) follows the magnetic topology. A constant plasma density is imposed in region 3, which is outside of the domain of the transport codes, the value of this background density depends on the simulation case.

This approach combines the strengths of both transport codes, each specialized in one of the regions. As expected, the denser plasma is located in the source with values in the order of 10^{19} m^{-3} and decays rapidly in the plume to values near 10^{14} m^{-3} in the outer section. Finally, a low but nonzero constant value of $n = 10^{14}$ m^{-3} is prescribed in region 3 in simulation Cases R, T and S, representative of the operation inside a vacuum chamber with imperfect vacuum, while $n = 0$ is used in Case V.

While HYPHEN evaluates several collisional elastic and inelastic processes in region 1, DIMAGNO assumes negligible collisionality in region 2 to compute the plasma transport solution. Since an effective electron collision frequency map ν is needed in the full domain of the wave code, HYPHEN's collisionality map is used in region 1, whereas in region 2 (and region 3 in simulation cases R, T, S), the map for e-i elastic collisions are used, $\nu = \nu_{ei} \sim nR_{ei}$, with

$$R_{ei} = \left(\frac{1\mathrm{eV}}{T_e}\right)^{3/2} \times \ln\Lambda \times 2.9 \cdot 10^{-12}\ \mathrm{m}^3\ \mathrm{s}^{-1} \tag{4.15}$$

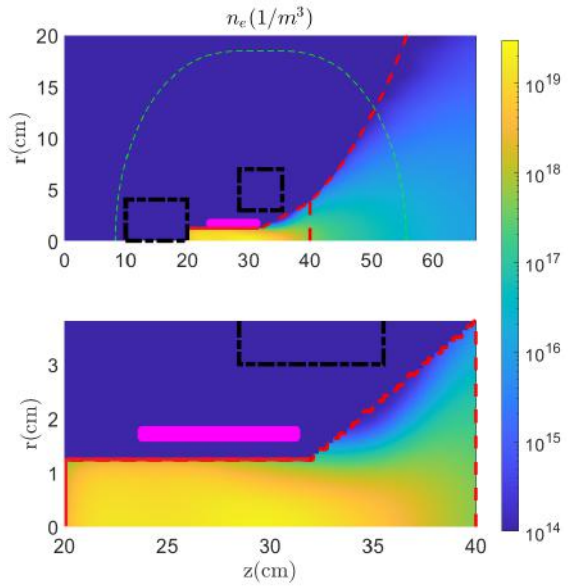

Figure 4.2: (top). Plasma density for the reference Case R in the simulation domain. (bottom). Zoom at Region 1.

where $\ln\Lambda \approx 10$ is Coulomb's logarithm. A reference value, based on the conditions in the outer far plume of region 2, $T_e = 1$ eV is used in region 3. The reason to consider ν_{ei} as the relevant map in these regions is that the transport codes reveals that e-i collisions already dominate clearly compared to the second most important process, namely, e-n elastic collisions, at the interface between regions 1 and 2 (where the average values are $\nu_{ei} = 7.3 \cdot 10^5$ Hz and $\nu_{en} = 3.8 \cdot 10^4$ Hz) and the difference is expected to grow along the plume. Finally, as explained at length in section 4.4 and after checking that this does not perturb the essential electromagnetic field solution nor the power deposition maps, collisionality is scaled up by a factor of 20 to improve numerical convergence. Figure 4.3 displays the used map of ν in the wave code.

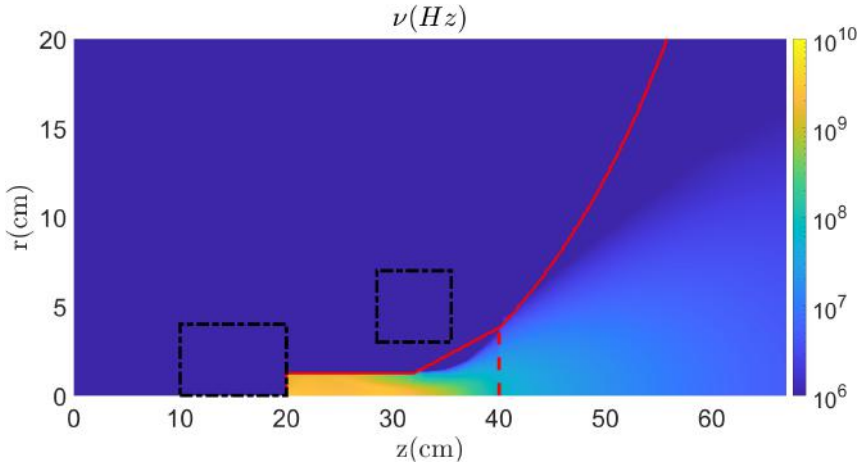

Figure 4.3: Effective collision frequency map. The numerical scaling factor has already been applied.

4.2.3. Numerical integration

The numerical implementation of the model follows the general outline of [20], [25]. A brief summary of the main aspects of the integration approach are summarized next for self-completeness.

The numerical solution of the electromagnetic fields in the frequency domain is obtained with a frequency domain Finite Difference method (FDFD), in particular, a modification of the well-known Yee's method [20], [91]. The use of staggered grids, on which only some components of the fields are stored, and depicted by different symbols in figure 4.4, allows for the direct discretization of equations (4.6) to (4.11) and for the easy implementation of boundary conditions. A major difference of a plasma with vacuum arises from the non-diagonal nature of tensor $\overline{\overline{\kappa}}$, which couples each component of $\boldsymbol{D}$ with all components of $\boldsymbol{E}$. This complicates the process of computing $\boldsymbol{D}$ as only some components of $\boldsymbol{E}$ are known on each node.

While in [112] this is accomplished by interpolating $(\kappa_{i,j}E_i)$ from the surrounding nodes to the desired position, in this work we interpolate E_i only, and then multiply by the value of $\kappa_{i,j}$ at the desired position. The approach of [112] leads to good results when $\overline{\overline{\kappa}}$ varies slowly, however, it was found to produce unacceptable high frequency noise at sharp transitions, and in particular at the critical density transition present in Case V, when the mesh is not aligned with the transition. This is attributed to the imbalance between some of the components $\kappa_{i,j}$ used for the interpolation. Although the issue does not completely disappear with the new scheme, as further discussed in section 4.4, a numerical investigation has shown a reduction in the noise across this transition with the new interpolation scheme.

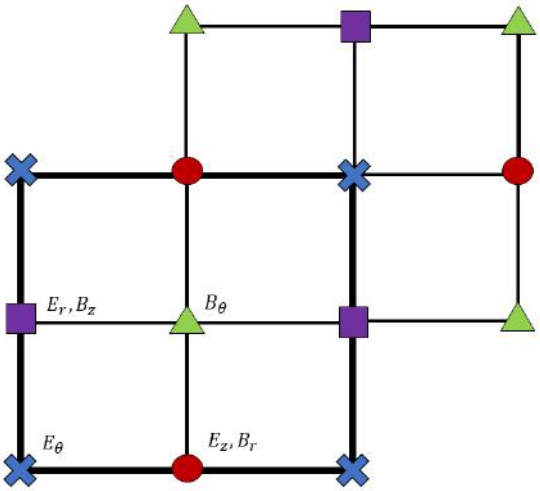

Figure 4.4: 2D staggered grid and electromagnetic fields. Each cell comprises a central node and four border nodes. E_θ is located in the blue X, E_z and B_r in the red circle, E_r and B_z in the purple square and finally B_θ in the green triangle.

For a domain discretization with N_z cells in the axial direction and N_r cells in the radial direction, the set of $6 \times N_z \times N_r$ equations (including boundary conditions) is assembled into the a linear system form $A\boldsymbol{x} = \boldsymbol{b}$, where A is the matrix of coefficients and $\boldsymbol{b}$ is the forcing vector (containing the prescribed currents in the antenna). A direct solver is applied to obtain the electric and magnetic field components contained in the solution vector $\boldsymbol{x}$.

The results presented in the following section correspond the azimuthal mode number $m = 1$,

with a grid a resolution of 1000×1000 cells. The total number of degrees of freedom is 6 million and the computation time using a direct parallel linear solver was on the order of 100 min in a 32 core, 200 GB RAM computing node.

4.3. Results and discussion

In the reference simulation **Case R** the plasma is overdense everywhere, i.e. $\omega_{ce} > \omega$. Additionally, as explained in section 4.6, the metallic obstacles in the surroundings of the source are present in the simulation. The first row of figure 4.5 displays the magnitude and phase of E_θ^1, i.e. the azimuthal electric field of mode $m = 1$. The RF field is clearly constrained by the ECR surface, as it must be evanescent beyond it. Overall, the field is strongest inside the cylindrical source (region 1), suggesting good coupling with the dense plasma. While the fields decay in the plume (region 2) and the periphery (region 3), it is evident that they are not zero: the electromagnetic fields propagate in these regions and are not confined to the source. Fields are small in the rear part of the cylindrical source. There is a partially-standing wave structure inside the plasma source, as evidenced by the localized drop in magnitude and the near 180 deg step. From the monotonic phase along the axis in region 2, a rightward-traveling wave exists up to the ECR surface, with an essentially-axial propagation direction. It is possible to estimate its wavelength to be around 20 cm by taking the distance for a full 360 deg phase cycle in the phase diagrams of figure 4.5. Notice that the wavelength is larger than the source tube due to the high magnetic field. This corresponds well with the analytical wavelength expression for H waves, $\lambda \approx 2\pi d_e \sqrt{\omega_{ce}/\omega}$, where $d_e = c/\omega_{pe}$ is the local electron skin depth, for a plasma density $n \approx 5 \cdot 10^{17}$ m^{-3} and a magnetic field intensity $B_a \approx 100$ G (resulting in $\omega_{pe} = 4.0 \cdot 10^{10}$rad/s and $\omega_{ce} = 1.8 \cdot 10^{9}$rad/s), which are characteristic values near the axis at $z \approx 40$ cm. Interestingly, the analytical wavelength varies very little as both the density and magnetic field decrease along the plume.

Away from the axis, this axial wave develops a non-negligible $k_\perp$ wavevector with increasing r, i.e., its propagation takes place at an angle with the magnetic field vector. The larger fields in the plume exist in a magnetic tube in this lateral region, indicating that $\boldsymbol{B}_a$ defines to some extent the propagation paths of the electromagnetic fields. Propagation stops at the ECR surface, and the field magnitude drops quickly beyond it.

The electric field in region 3 is not negligible, especially close to the antenna, and its propagation is also affected by the direction of $\boldsymbol{B}_a$. Small wavelength structures of low magnitude can be observed in the space above the magnetic coils, where radiation is diffuse and standing wave patterns form. This radiation seems to be confined between the ECR surface in region 3 and the denser plasma of regions 1 and 2.

The power deposition profile, Q_a^1 is shown in the first panel of figure 4.6. The largest absorption is not correlated with the largest fields, and takes place inside the dense plasma in the cylindrical source ($\sim$ 95 %). A non-negligible part of the power is absorbed downstream in the MN, before the ECR surface, indicating the relevance of including this region 2 in the model to understand the power absorption.

A thin absorption layer exists at the ECR surface; however, this layer curves away from the ECR in the top part of the domain, in region 3, partially guided by the magnetic field vector. Less than 0.6% of the power emitted by the antenna is absorbed in the space beyond the ECR

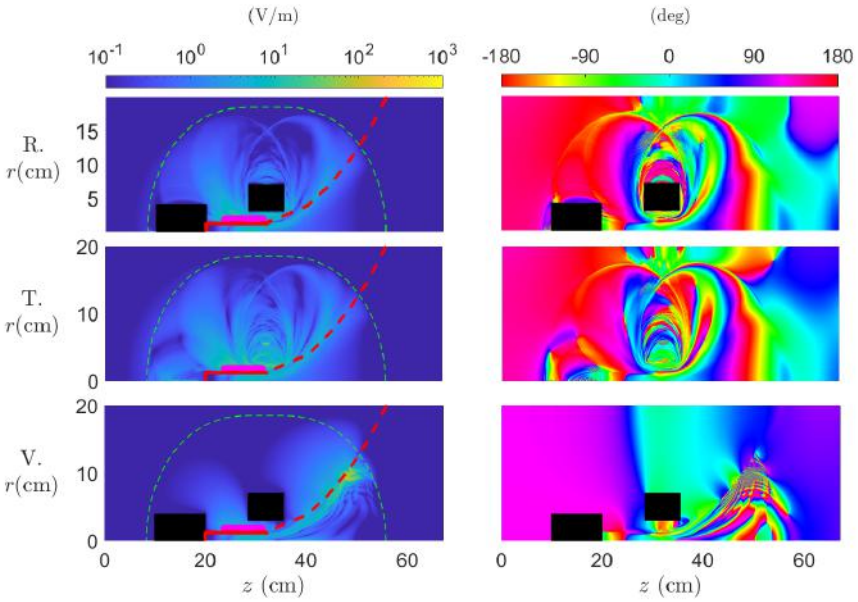

Figure 4.5: E_θ^1 field magnitude (left) and phase angle (right) for different simulation cases, for a total antenna current of 1 A. The electron cyclotron resonance line is depicted in green and the limit of the dense plasma in red.

surface, where the solution is evanescent. This result suggests that the ECR surface acts as an efficient shield to prevent radiation losses when operating in free space, i.e. to stop RF power from escaping the HPT plasma and its neighborhood, as long as the environment is overdense.

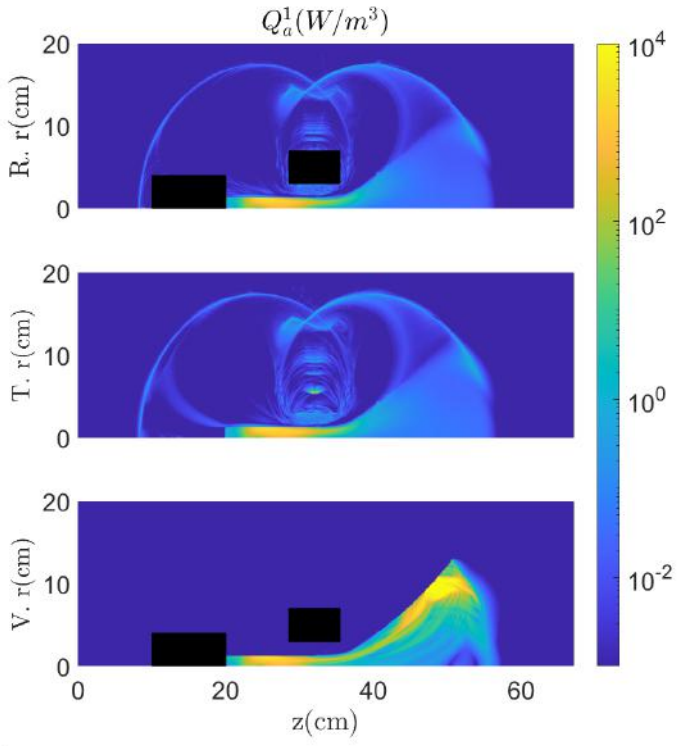

Figure 4.6: Power absorption maps Q_a^1 for the different simulation cases.

The removal of the metallic parts inside the domain in simulation **Case T** does not result

in any major changes in the wavefields nor the power deposition profile, as can be observed in the second row of figure 4.5 and 4.6. The only apparent difference is a slightly higher RF field traveling toward the rear part of the device, previously blocked by a metallic obstacle, and some additional absorption in the rear part of region 3. The small effect of these metallic boxes suggests that obstacles of this type essentially do not affect the solution.

Changing the environment into a perfect vacuum in **Case V** has a far more dramatic effect on the RF fields (and on the accuracy of the numerical solution). This case is represented in the last row of figures 4.5 and 4.6. Firstly, the absence of plasma in region 3 also removes the possibility of a resonance at the ECR surface in this region, which now becomes transparent to the fields. Indeed, in the absence of plasma density, the value and direction of $\boldsymbol{B}_a$ becomes irrelevant for the wave propagation problem. This means that the fields have access to the metallic boundary conditions that represent the vacuum chamber. Note that, in free space, any power traveling outward would give rise to radiation losses; however, in the present setup, representative of the operation in a laboratory vacuum chamber, this power is reflected back toward the domain by the boundary conditions, until all power is absorbed by the plasma in regions 1 and 2. The short-wavelength structures that existed in the presence of a tenuous plasma in region 3 in Case R disappear in Case V, and radiation is partially delimited by the conductive boxes immersed in the domain. The ECR surface continues to be active in region 2, however. Secondly, fields in regions 1 and 2 become essentially a standing wave as evidenced by the node lines where $E_\theta^1 = 0$ in the magnitude plot of figure 4.5, suggesting that wall reflection indeed plays a role in this case. The propagation direction develops a major perpendicular component $k_\perp$ to $\boldsymbol{B}_a$, and shorter wavelengths are observed, especially in the peripheral part of the MN plume. This suggests a more relevant role of the TG mode, which corresponds with shorter wavelengths and more perpendicular propagation than the H mode. As in previous cases, propagation within the plasma plume ends at the ECR. Thirdly, the importance of the fields in the plume is larger than in the previous cases, especially downstream, and so is the power absorption.

Notwithstanding these general observations, it is noted that simulation Case V does not show the same numerical convergence characteristics in the plume region with mesh refinement as in the other cases. This issue, and its putative causes are discussed in section 4.4.

Figure 4.7 displays a zoomed view of the power deposition profile inside this region, and includes the short-domain simulation of **Case S**. The four solutions show that the power absorption profile is essentially independent of the simulation case. This conclusion is valuable for two reasons. First, it supports the robustness of the modeling procedure, as changes in the details of the surrounding of the thruster have no major influence on the computation of power deposited inside the source, which accounts for the larger share of absorption. In fact, the power inside the source appears almost independent of the chamber conditions and the propagation in the plume. Second, these results show that when only the computation of the power absorbed in the source is needed, it can be reliably obtained with a smaller simulation domain containing only this region (simulation Case S).

Compared to the absorption map presented in [25] in which 2 to 3 stationary Helicon wave cycles are visible inside the source, the deposition in figure 4.7 shows just one high absorption region covering much of the source. This is consistent with the plasma conditions used in this work (in particular, $\simeq$ 1500 Gauss at the axis), which differ from those of [25] ($\simeq$ 150 Gauss at the

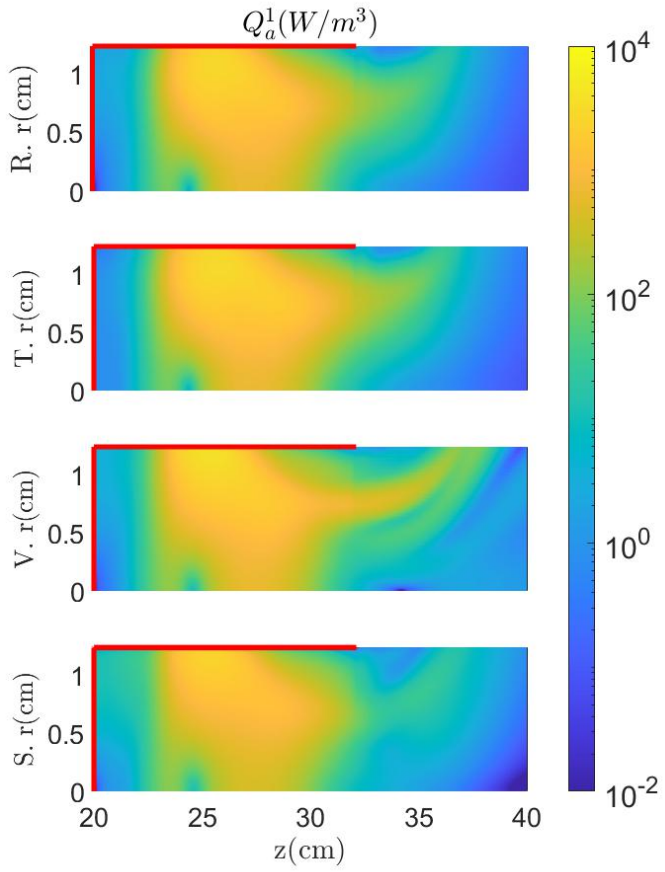

Figure 4.7: Power absorption maps Q_a^1 for the different simulation cases. Zoom at Region 1.

axis), which result in an increase of the Helicon mode wavelength.

To conclude this section, the relevance of the azimuthal mode $m = 1$ is briefly discussed. Previous studies [25], [99] have already established the dominance of the $m = \pm 1$ azimuthal modes in the power coupling for different antenna types of helicon sources. Indeed, this antenna is designed to excite predominantly the $+1$ mode. Accordingly, the results presented above have considered this dominant mode only. To assess the validity of this approach, figure 4.8 compares the power absorption associated to $m = \pm 1, \pm 3$ in the whole domain of the simulation Case R (the helical antenna only excites odd modes). As it can be inferred, after mode $m = +1$ the next mode in importance is $m = -1$. The power absorption of higher m modes drops quickly.

4.4. Critical density transition and numerical convergence

The critical density transition takes place when $\omega = \omega_{pe}$, or equivalently, when $P = 0$ in equation (4.3). For an excitation frequency of 13.56 MHz, this happens when the plasma density drops below roughly $2.3 \cdot 10^{12}$ m^{-3}. In our simulations, this occurs only at the plasma-vacuum interface in Case V.

The treatment of this transition presents a twofold difficulty. First, in the cold plasma dielectric tensor model and in the collisionless limit, the dispersion relation for an infinite uniform plasma with the critical density becomes singular, the $P = 0$ condition being a cutoff or a resonance

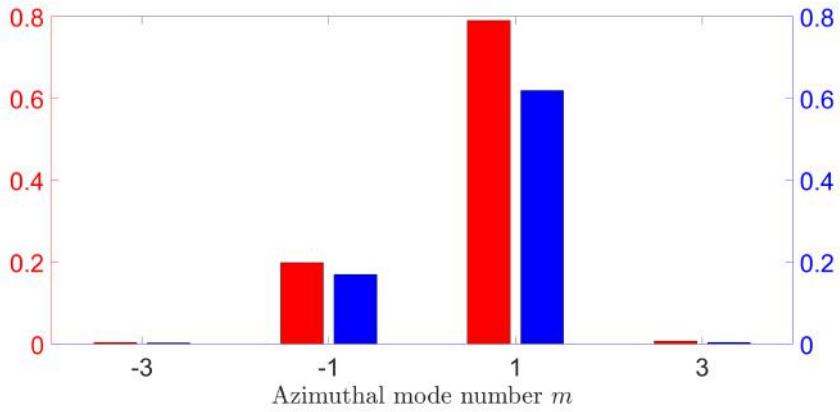

Figure 4.8: Fraction of total power (red) and fraction of power deposited inside the source (region 1, blue) for different azimuthal mode numbers, m.

depending on the direction of the propagation of the waves, given by the wavevector $\boldsymbol{k}$ [19]. This conditional/directional limit disappears strictly when collisions are present, but for small ν, the dielectric tensor $\overline{\overline{\kappa}}$ retains its wild, directional variation in the neighborhood of the transition. Indeed, near the critical density, electrostatic electron oscillation modes exist, whose description needs from thermal corrections. Therefore, the study of the electromagnetic fields in the vicinity of $\omega = \omega_{pe}$ cannot be properly approached from within the cold plasma model, and electron temperature effects need to be taken into account.

Second, but related to the first point above, the numerical discretization of the problem becomes ill-conditioned when the $P = 0$ transition is inside the domain, as in Case V. Numerical analysis shows that this situation can give rise to spurious, highly oscillating fields near the transition, with wavelengths comparable to the numerical mesh. This problem is aggravated in the Cartesian numerical discretization employed in Yee's method wherever the grid directions differ substantially from the applied magnetic field direction at the transition ("staircase conditions"). Indeed, small wavelength structures are observed in Case V in the plume-vacuum edge in region 2 (figure 4.5) that are linked to a high localized power deposition density (figure 4.6). These structures are insidious and could not be fully resolved with the available computational resources. They are seen to be smaller than the mesh size even in the finest simulation reported here. This phenomenon is not present near other regime transitions such as the ECR surface downstream ($R \to \infty$), where the fields are well-behaved in all simulations.

Figure 4.9 displays the error in the integrated power absorption of Case R and Case V for different grid sizes (mesh #), relative to the finest mesh simulations that was carried out (which are the ones reported in previous section),

$$\frac{|\int Q_a^1(\text{mesh \#})\mathrm{d}\Omega - \int Q_a^1(\text{best mesh})\mathrm{d}\Omega|}{\int Q_a^1(\text{best mesh})\mathrm{d}\Omega}.$$

(alternativa)

$$\frac{|P_a^1(\text{mesh \#}) - P_a^1(\text{best mesh})|}{P_a^1(\text{best mesh})}.$$

In the light of the relevance of the power deposition in the source region 1, the convergence of this quantity is plotted too.

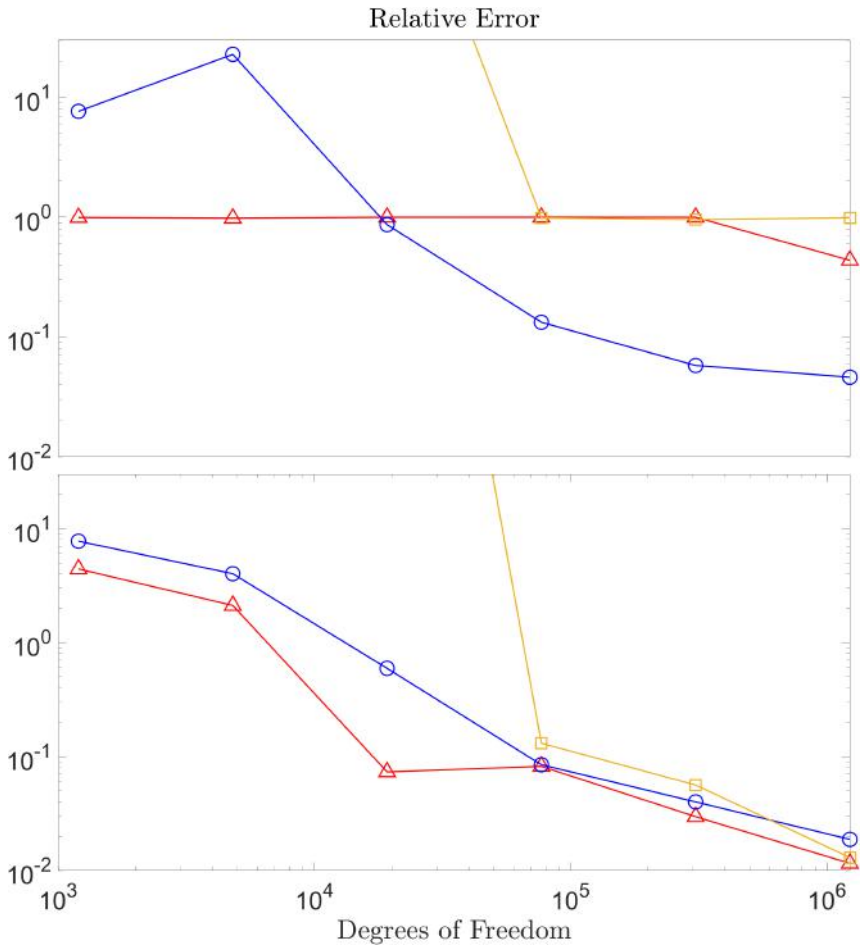

Figure 4.9: (top). Error to the most accurate simulation of the power deposited in the full domain as a function of the degrees of freedom of the system (i.e. 6 times the number of Yee cells). Cases R (blue, ∘) and V (red, △) The error with the previous interpolation scheme from [25] for Case V is also shown for comparison (yellow, □). (bottom). Error for the power integrated only in Region 1

.

As it can be observed, the reference Case R gradually converges, with errors below 2% inside the source for 1 million degrees of freedom, as shown in figure 4.9b. Cases T and S behave essentially identically to Case R, regarding convergence. This behavior gives confidence on the numerical convergence of the method, and the error trend agrees with the expected one for the used numerical scheme. On the other hand, the vacuum Case V behaves differently. While the error in the source decreases roughly as in Case R, indicating similar convergence characteristics there, the error in the whole domain does not diminish as the grid is refined. Far from it, the power deposited in the whole domain exhibits unsatisfactory values, driven by the spurious fields existing in the plume edge.

This convergence behavior was only observed in Case V, and demonstrates the modeling and numerical difficulties commented on above in the neighborhood of the critical plasma density transition. In all other simulation Cases this interface is not associated to a parametric regime transition, and the only existing transition is the ECR surface downstream.

It is noted that smoothing out the plasma density profile near the edge does not solve the issue, as the $P = 0$ transition remains sharp and the $\bar{\bar{\kappa}}$ coefficients continue to vary rapidly across it. Several strategies are proposed to mitigate problems associated with these abrupt transitions, without requiring abandoning the cold plasma tensor formalism. Firstly, it is noted that increasing the imaginary component of P through added damping moves the zero away in the complex plane, improving the mathematical conditioning of the problem. A larger damping also helps suppress the small-wavelength noisy fields in a shorter distance. However, while this may be desirable to mitigate these oscillations, an excessively larger damping might hide some physical short wavelength structures. For this reason, after some numerical experimentation, a factor of 20 was used to scale collisionality in the problem, which improved convergence without altering essentially the solution.

Secondly, the transition noise was seen to be highly dependent on the interpolation strategy used in the Yee method to fix the value of $\boldsymbol{D}$ at the nodes. It was observed that the interpolation scheme introduced in this work reduces the noise level and the error with respect to the former approach, proposed in [20] and used in [25]. The improvement is shown by the convergence lines of figure 4.9, specially by the faster convergence of the new scheme (red ∘) in the source with a limited number of degrees of freedom when compared to the former interpolation strategy (yellow □). The enhanced convergence is directly linked to a reduction of noise along the $P = 0$ surface. It is hypothesized that further exploration in this direction, as well as in the addition of auxiliary divergence equations near and at the transition, may help further improve the issue [114].

Thirdly, the fact that the mesh direction relative to $\boldsymbol{B}_a$ affects the appearance of noise suggests that a mesh-aligned numerical discretization may also be instrumental in tackling it. Unfortunately, in the general case this would require irregular and non-structured meshes, for which finite difference methods are hard to implement. Much progress has been carried out in the field of finite elements for electromagnetic problems in the last decades, notably since the introduction of vector elements very successful in full-wave simulations [115]. This formulation is more suitable for non-structured and adaptable meshes. Indeed, finite elements have already been used with success to simulate the electromagnetic fields of other electric thrusters [41].

To conclude, it is noted that, in spite of this unsolved problem, the error associated to it seems to be local to a small region in the plume of Case V. As shown in figure 4.9, this noisy region does not invalidate the convergence of the power deposited inside the source and near plume. While the solution in the plume region of Case V is not acceptable and must be revisited in future work, the conclusions pertaining the power deposition in the source exhibit good convergence with mesh size and seem robust.

4.5. Summary

A finite-difference, frequency-domain, full-wave model has been used to investigate the propagation and absorption of electromagnetic fields in an HPT, including the far plume region and the surrounding space, with the goal of understanding the amount of power deposited in the plume and the influence of the environment in the electromagnetic problem. Plasma density and applied magnetic field coming from plasma transport simulations of a thruster similar to the HPT05 prototype were used as inputs in the study. While most of the power absorption occurs inside the cylindrical

source, the fraction of power taken in by the plasma plume is not negligible. The fields propagate along the magnetic nozzle up to the electron-cyclotron resonance surface that always exists downstream. The wavelength and propagation direction corresponds to a helicon wave around the axis of the device. In the plume periphery, waves have a shorter wavelength and more important perpendicular wave vector component, approaching the Trivelpiece-Gould mode.

A tenuous plasma of density $n > 2.3 \cdot 10^{12}$ m^{-3} in the neighborhood of the device and its plume suffices to make that region overdense ($\omega_{pe} > \omega$) for the usual excitation frequencies (13.56 MHz). This is the usual situation in laboratory vacuum chamber experiments, where pumping is not perfect. Even in a space environment, a faint low density plasma may envelope the thruster, keeping the effect of the ECR surface in the surrounding space active. In these conditions, the ECR surface has been shown to concentrate some of the power absorption and to play a fundamental role in confining the radiation away from the device, as the fields become evanescent beyond it. This, in particular, has great relevance for the "free space" representativeness of vacuum chamber experiments which are normally made of conductive metal, and therefore constitute a closed, reflective cavity for the fields. If the ECR surface is located within the chamber, the effect of these reflective walls on the fields becomes negligible, as they are in contact only with the region of space where fields are evanescent.

In strict vacuum, the ECR surface plays no role in the surrounding space, as in this case there are no electrons to resonate with the fields, and a path for radiation losses opens up in the radial direction away from the thruster (but not along the plume, where the plasma continues to be overdense and fields continue to be evanescent beyond the ECR transition). Indeed, the propagation and absorption maps change and exhibit standing-wave structures as a consequence of the reflective bounding box used in the simulation.

The influence of reflective boxes inside the domain (representing support equipment of the thruster) was seen to be small. Moreover, the power absorption in the source region was seen to be stable and essentially the same across simulations, suggesting that all aspects that affect the plume and the environmental region are superfluous for the source power absorption. This adds confidence to the small-domain, source-only simulations carried out in previous works, albeit they miss the information of the power absorption in the plume.

Finally, numerical convergence studies showed good convergence characteristics for all cases except the vacuum environment one, where the strong and ill-conditioned critical density transition surface at the interface between the plasma plume and vacuum, plus the numerical staircase mesh conditions there, are identified as the sources of small-scale numerical noise. The implementation used in this work is based on a new interpolation scheme which partially mitigates this problem and restricts noise to a small region without affecting results much elsewhere. Notwithstanding this, future work must address the theoretical modeling and the numerical treatment of these transitions. Some additional avenues of research have been suggested in section 4.4, namely the use of enhanced damping in this region, and aligning the mesh geometry to the transition, perhaps by switching to other schemes such as finite elements to simplify the implementation of unstructured meshes.

The validation against experimental data of the present wave model requires direct measurement of the electromagnetic fields and their phase, notably inside the plasma source, without perturbing the operation of the thruster. Currently, no such data is known to exist to the authors.

However, coupled plasma transport and wave simulations (employing the same FDTD solver as this work) compare reasonably well to experimental studies with a similar HTP setup in terms of indirect measurements such as thrust and several efficiencies. In particular for the HPT05 prototype, numerical [107] and experimental [95] results show about 30% relative discrepancy in key performance figures like thrust efficiency in similar operation regimes (although the comparison is not perfect, as the configuration of [95] has a slightly higher antenna power). Further work in this direction and new, more precise experimental measurements, are still necessary to close the validation gap.

5. *Self-consistent plasma transport and wave propagation simulations*

The contents of the following chapter have been peer-reviewed and published in [49] and are reproduced here without modifications. Please excuse any duplicity or repeated information, especially in the introduction, that might occur as a result of its inclusion in other chapters of this work.

Experiments and simulations are used to analyze a compact helicon plasma thruster with a cusp in its internal magnetic field. The former rely on a compensated Langmuir probe and a Faraday cup, while the latter employ a hybrid PIC/fluid transport model combined with a frequency-domain electromagnetic field model. Measurements serve to tune the anomalous transport parameters of the model and overall show the same trends as the numerical results, including a secondary peak of electron temperature downstream in the magnetic nozzle, where electron cyclotron resonance conditions for the 13.56 MHz excitation frequency are met. The cusp plays a central role in determining the plasma losses to the walls and the profile of electron temperature, which in turn defines the excitation and ionization losses. While losses to the rear wall are reduced, losses to the lateral wall are increased, which, together with the low production efficiency, limit the performance of the device.

5.1. Introduction

The helicon plasma thruster (HPT) [7]–[11] belongs to the family of electrodeless plasma thrusters (EPTs). It consists of (1) a cylindrical discharge chamber made of dielectric walls, (2) a gas inlet, usually at the back of the chamber, (3) an external inductor/antenna, emitting the RF power to be absorbed by the plasma, and (4) an external magnetic circuit, generating a magnetic field, which aims to make the plasma transparent to the RF waves, to confine partially the plasma, and to guide an accelerate it externally through a magnetic nozzle (MN) configuration. The HPT concept avoids the need for a supplementary hollow cathode acting as ion beam neutralizer, the erosion problems linked to electrodes and grids, and simplifies the complex power processing and control unit with respect to mature technologies, such as Hall Effect and Gridded Ion Thrusters. In contrast to these advantages on lifetime and system simplicity, until now, testing on existing HPT prototypes still reports rather low thrust efficiencies[10], [116]–[118].

The conventional magnetic topology of an HPT is quasi-axial and near-uniform inside the chamber [98], thus confining the lateral walls but permitting large losses on the back wall [31]. The low thrust efficiency also suggests an anomalously small magnetic confinement of the lateral walls (for a given magnetic strength). This may be due to the existence of anomalous cross-field electron transport, similar to the one found in Hall thrusters and presumably caused by turbulence due to azimuthal instabilities [119]. For many low-power HPTs and sources, magnetic confinement issues are being addressed using permanent magnets (PMs) instead of electromagnets [74]. There are three main reasons for this choice. First, PMs can provide a higher magnetic strength,

and thus improve confinement in the presence of anomalous transport. Second, solenoid power consumption would drastically penalize the total efficiency of a low-power system. And third, PMs yield further flexibility in implementing non-uniform magnetic topologies, such as those with internal cusps, with potential benefits.

The enhancement of thrust force using a higher magnetic flux density in a PM-HPT was experimentally demonstrated by Takahashi et al. [7]. The impact of different cusped topologies on the plasma behavior and thruster performances has been addressed experimentally by several groups testing different prototypes. Virko et al. [120] found that cusp location relative to antenna position affects wave accessibility, plasma production, and ion acceleration. Trezzolani et al. [9] also opted for cusped technology to optimize a small HPT system. A more systematic study is due to Ito et al. [121], who measure the thrust performance of two pairs of magnetic field configurations, without and with cusps, finding that the latter could lead to higher plasma density, better propellant utilization, and, ultimately, better thrust efficiency. Consistent with these findings, Takahasi's recent experimental study [122] has provided evidence that cusped field topologies could reduce wall energy losses, with a resulting increase in device performance.

These results encourage experimental research on PM-HPTs to be complemented with a modeling/simulation counterpart to explain the physics of plasma transport and RF power coupling, shed light on the dominant loss mechanisms, and help design optimization. This paper reports, first, test results on a magnetically cusped PM-HPT prototype [123]. This is followed by a numerical investigation on the plasma response and thruster performances with an axisymmetric hybrid model. The focus of this study is to provide an understanding of the specific features of this magnetic topology, without aiming for a particular optimal design. Indeed, we anticipate that the current configuration does not lead to an optimal prototype. Still, the results are valuable for further development of this technology.

Section 5.2 of the paper presents a set of vacuum chamber measurements of the plasma density, temperature, and electric potential obtained in the plasma plume. The posterior sections apply an axisymmetric simulation code to fit those measurements and then investigate the plasma discharge properties inside the chamber and the plume, and the related performances. Special attention is given to the current and power balances, in order to quantify the different sources of mass and energy losses.

The simulation code used is HYPHEN-EPT, which includes different modules to model the plasma-wave energy deposition process [W(ave)-module], and the production and quasi-steady transport of the several plasma species [I(on)- and E(lectron)-modules]. The I-module operates on a PIC formulation of several heavy species (ions and neutrals), and the E-module deals with a diffusive, magnetized fluid model for electrons. These modules are common for simulations of EPTs and Hall-effect thrusters and have been described in detail in recent publications [40], [124], and briefly overviewed in Section 5.3.1. The W-module deals with the Maxwell equations for the RF electromagnetic fields, assuming a quasi-steady cold plasma dielectric tensor, determined from the I- and E-modules. Reciprocally, the W-module provides the energy-deposition map for the E-module. All modules run sequentially to achieve a self-consistent steady-state solution.

The W-module builds on and improves previous models. Tian et al. [25] solved the Maxwell equations in the frequency domain with a finite difference (FD) model in the source and near plume of an HPT with quasi-parallel magnetic topology. Jiménez et al. [26] extended the FD

model to include RF propagation in the far plume and found a significant power deposition per particle at the downstream electron-cyclotron resonance surface, a fact corroborated recently by the experimental measurements of Vinci et al. [125], and previously studied by Chung et al. and Lafleur et al. [82], [126], [127]. Sánchez-Villar [41] proposed an alternative finite element (FE) model for the W-module, although limited to the axisymmetric azimuthal mode number $m = 0$. This was applied to simulate a coaxial electron cyclotron resonance thruster (ECRT). A combined experimental-numerical analysis of the ECRT, similar to the one proposed here for the HPT, followed in [128]. Despite the increased complexity, FE formulations are more suited to general geometries and computationally more efficient than FD formulations. As part of the contributions of the present work, in Section 5.3.2, the FE model is extended to any azimuthal mode number m, as required for application to an HPT with a helical antenna (with $m = 1$ as the dominant azimuthal wave numbers).

The electron formulation within the E-module makes use of some empirical parameters to adjust the anomalous transport properties, known from experiments but still elusive to consistent fluid modeling. Section 5.4.1 compares the experimental and numerical results for the best fit of the above empirical parameters. Section 5.4.2 presents a sensitivity analysis of the numerical results to those parameters. Sections 5.5.1 to 5.5.3 discuss the EM wave fields, the power deposition, the maps of plasma magnitudes, and the thruster performances, identifying the main causes of low efficiency. Section 5.6 summarizes the conclusions.

5.2. Device and experimental results

The device under study is the thruster unit breadboard model developed jointly by Sener Aeroepacial and Universidad Carlos III de Madrid [123]. The device is a compact 400W-class HPT with a 12.5 mm source radius and a 60mm source length, made of boron nitride. Xenon is injected through a multi-hole injector plate, which is embedded at the back side of the discharge tube. RF power is fed to a half-helical antenna wrapped around the source. RF power is generated using an industrial power supply, an RF Seren 2001 amplifier, and is coupled to the antenna through a customized matching network in order to match the system impedance for all operating conditions, with less than 2% of reflected power. The device under vacuum chamber operation is shown in figure 5.1, and its design and operational parameters are shown in the first part of table 5.1.

The magnetic field is generated by a set of radially-polarized neodymium magnets, which are assembled in an annular aluminum support. The width of the magnet assembly is 40 mm and the inner radius is 50 mm. This magnet arrangement generates a cusp with a separatrix plane inside the source, 35 mm upstream of the outlet. The azimuthally-averaged magnetic field is shown in Figure 5.2. The forward peak of the on-axis magnetic field occurs at the magnetic nozzle (MN) throat, coinciding with the source outlet section, and is about 750 G. The rear peak of the on-axis magnetic field lies behind the backplate injector. The rationale for this setup was to avoid the use of bulky and power-consuming solenoids, which were used in previous developments [10].

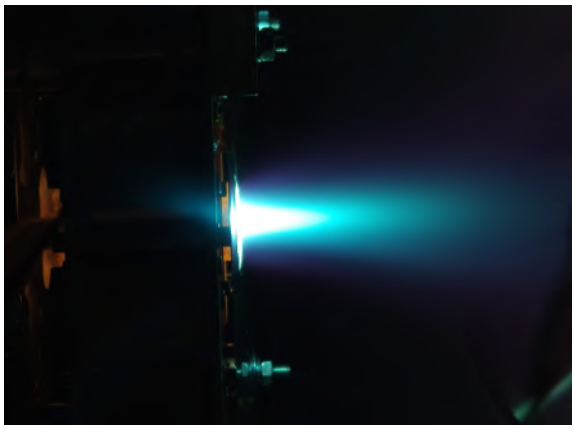

Figure 5.1: HPT prototype lateral view, operating with Xe in the UC3M lab vacuum chamber.

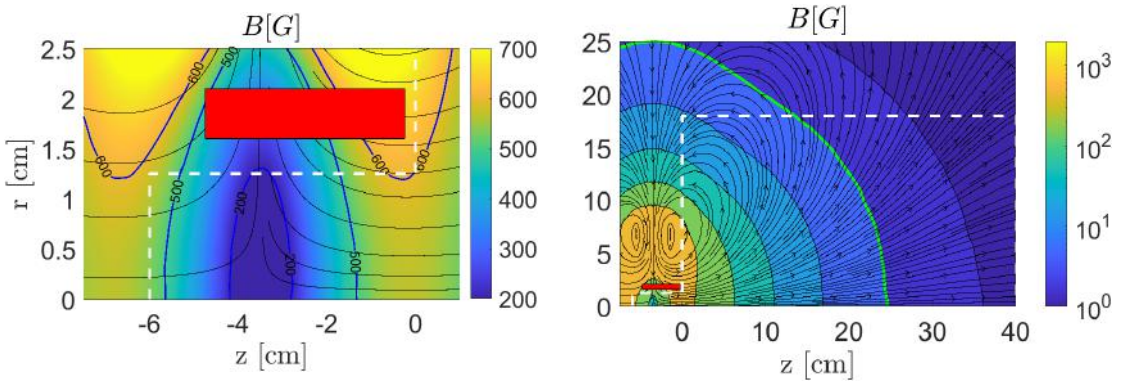

Figure 5.2: Applied Magnetic Field (azimuthally-averaged). Zoom in to the source region (left) and full wave domain (right). The antenna is depicted in red and the boundary of the transport domain is represented by a white dashed line. The green line is the Electron Cyclotron Resonance (ECR) surface.

5.2.1. Setup description

The experimental results presented next are part of the first coupling test campaign of the propulsion system assembly, which, in addition to the thruster unit, includes a dedicated power processing unit and a gas valve optimized for this thruster. The thruster prototype has been tested in a 1.5 m diameter, 3.5 m length stainless steel vacuum chamber. The ultimate dry vacuum is 10^{-7} mbar, while the background pressure stands at $5.9 \cdot 10^{-6}$ to $4.6 \cdot 10^{-5}$ mbar for a flow rate of Xe between 5 and 50 sccm. Additional results of interest for this work are the Laser induced fluorescence (LIF) measurements of the plasma plume, recently presented in [129].

Two operating points have been tested. RF power has been kept constant at 450 W, while the Xe flow rate has been set at 12.5 sccm (low flow rate case) and 20 sccm (high flow rate case). A set of electrostatic probes was mounted on a radial-polar robotic arm, which allows us to inspect intrusively the plasma properties within a semicircular horizontal plane, $\rho \in (0, 400)$ mm, $\theta \in (-\pi/2, \pi/2)$, centered at the thruster outlet. The set of probes includes a radio-frequency compensated Langmuir probe [130] to infer plasma density, electron temperature, and plasma potential along the axis line, 100-400 mm downstream from the thruster outlet. The second probe is a Faraday cup that has been used to characterize the ion current density along a semi-arch of radius $\rho = 350$ mm [10].

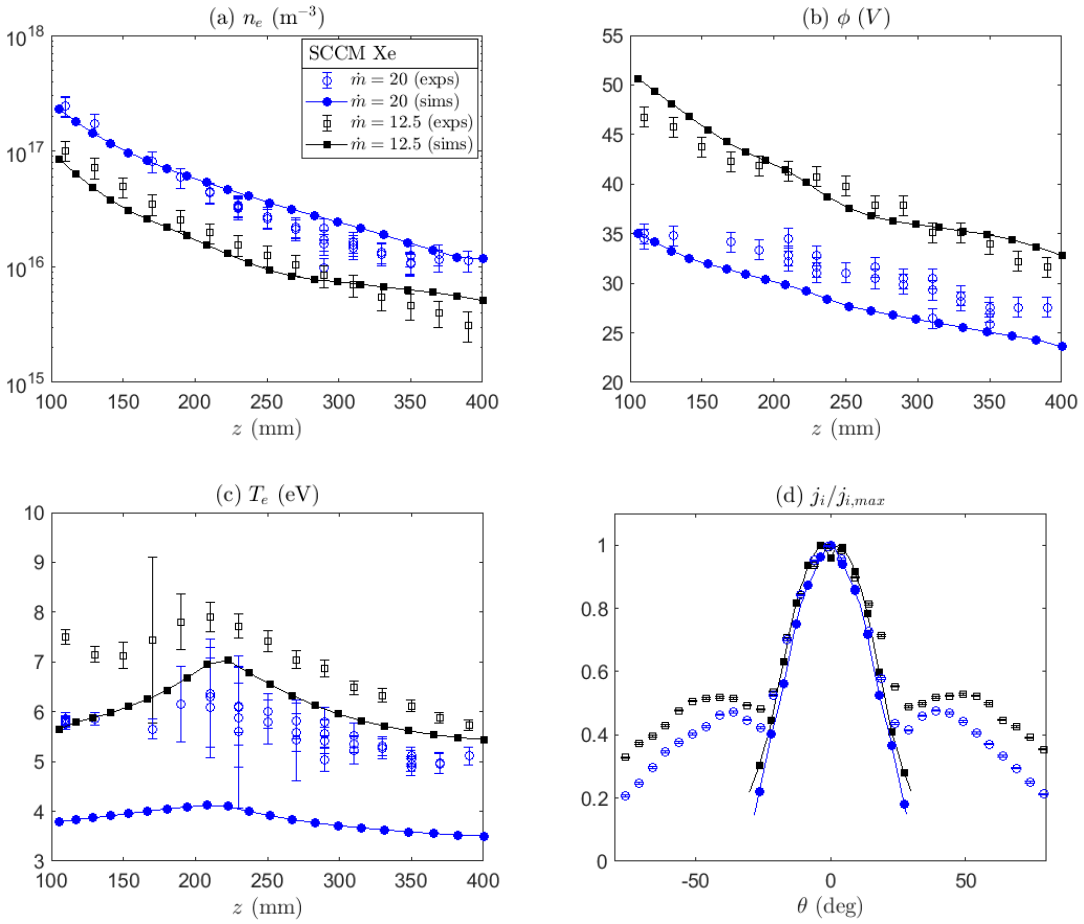

Figure 5.3: Experimental (hollow symbols) and numerical profiles (solid lines, filled symbols) for electron density n_e (a), electrostatic potential ϕ (b), electron temperature T_e (c), and ion current density j_i (d). Results are for two different mass flows $\dot{m}$ = 12.5 sccm (black squares) and $\dot{m}$ = 20 sccm (blue circles), at constant RF power 450 W. Error bars consider only the propagation of instrument uncertainty, except for the density where 20% minimum uncertainty is assumed.

5.2.2. Experimental results

The main results are shown in Figure 5.3, together with the anticipated numerical results. We discuss here the experimental profiles and leave for Section 5.4.1 the comparison with the simulation results. For all experimental profiles, error bars were estimated by propagating the error of the instrument uncertainties and the parameters involved in the measurement of each physical property. Importantly, for LP measurements, the error bars do not include the uncertainty of the theoretical model as in [131], which is potentially large (e.g., it could be about a factor of 2 in the electron temperature). For the specific case of the ion density, strongly affected by the uncertainty in the effective collection area, a minimum uncertainty of 20 % is assumed. For the rest of the properties, no additional uncertainty has been added.

The electron density profile on the axis is shown in Figure 5.3(a). The electron density drops almost 2 orders of magnitude in the explored range. It is seen to decrease at a slightly lower rate in the high mass flow case. Plasma potential and electron temperature are shown in panels (b) and (c) of Figure 5.3, respectively. The trend of potential is monotonically decreasing, as expected in

Parameter	Symbol	Value
Thruster length	L	6 cm
Thruster radius	R	1.25 cm
Injector radius	R_{inj}	0.625 cm
Mass flow rate	$\dot{m}$	12.5–20 sccm
Antenna frequency	$f = \omega/(2\pi)$	13.56 MHz
Antenna Power	P_a	450 W
Antenna loop radius	r_a	1.85 cm
Antenna length	l_a	4.5 cm
Antenna central position	z_a	-2.5 cm
Antenna thickness	d_t	0.5 cm
Plume length	L_p	40 cm
Maximum plume radius	R_p	18 cm
I-mesh size	-	4961 cells
E-mesh size	-	3671 cells
I-module time step	Δt_I	$2.5 \cdot 10^{-8} s$
E-module time step	Δt_E	$5 \cdot 10^{-9} s$
W-module update time-step	Δt_W	$1.25 \cdot 10^{-6} s$
Total simulation time	t_{sim}	3.75 ms
Rectangular wave mesh	-	$z \in [-13.5, 43]$cm, $r \in [0, 25]$ cm
W-mesh size	-	10^6 cells
Maximum Applied Magnetic Field	B_a	10^3 G
Gyro-frequency	ω_{ce}	10^7-10^{10} s^{-1}
Density	n_e	10^{15}-10^{20} $1/m^3$
Debye Length	λ_D	10^{-6}-10^{-3} m
Temperature	T_e	2-6 eV
Effective Collision Frequency	ν_e	10^4-10^8 s^{-1}

Table 5.1: Cusped HPT parameters (upper part of the table), numerical parameters used in the simulation (mid part of the table) and characteristic plasma conditions in the simulation domain (bottom part of the table).

a MN [132]. The electron temperature is larger in the low-mass flow rate case, and consistently, the potential drop is also larger in that case. The electron temperature profile shows a mild peak at 200–250 mm of the source, contrasting with the typically monotonically decreasing profiles reported in the literature [102], [133].

Finally, the normalized profiles of the ion current density are shown in panel (d). The current density is measured with the Faraday probe in a semi-arch of radius $\rho = 350$ mm. The ion beam features a single symmetric peak with lateral wings. The first indicates the formation of a well-collimated ion beam, while the second could be the consequence of the interaction of the plasma with the background pressure, or the presence of secondary beams linked to heating/ionization in the periphery of the main plasma column.

5.3. Simulation model

The HYPHEN-EPT simulation model is composed of different modules to solve the plasma profiles and electromagnetic fields in the meridian plane. First, there is the E-module that solves for the slow dynamics of electrons; a magnetized, drift-diffusive, quasineutral fluid model [40], [134], with finite difference and finite volume techniques. Second, there is the I-module that solves for the dynamics of ions and neutrals, using a PIC formulation and a Monte Carlo collision scheme [37]. The I-module determines the quasinuetral electron density used in the E-module. The E- and I-modules are completed by a S(heath)-module for the nonneutral Debye sheaths around all the walls of the integration domain. Together, the E-, I- and S-modules constitute the slow plasma transport part of HYPHEN-EPT. In the present study, we consider the quasineutral, low-β limit of the plasma transport problem. Quasineutrality is a key element of the transport model to keep the computational cost affordable in a workstation. The lowβ assumption allows neglecting the stationary plasma-induced magnetic field with respect to the applied one.

Third, the W-module solves Maxwell's equations, with finite element discretization in the frequency domain, for the high-frequency electron-wave interaction and the subsequent deposition of wave energy into the electrons. Figure 5.4 shows a sketch of main model blocks and the plasma magnitudes (defined later in this Section) acting as inputs/outputs between them.

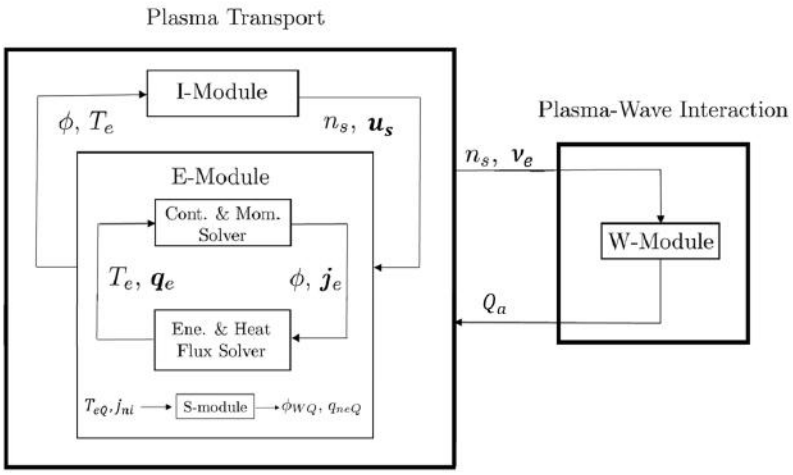

Figure 5.4: Simulation model structure, modules and interfaces.

The second part of table 5.1 summarizes the simulation parameters. Two simulations, corresponding to the cases with mass flow rates 12.5 and 20 sccm are run. An overview of the computational domain is shown in figure 5.5. The I-module uses a nonuniform Cartesian-type mesh, adapted to the expected plasma gradients and to keep a statistically acceptable number of macroparticles per cell. The E-module integrates the fluid equations in a magnetic field aligned mesh (MFAM) to minimize numerical diffusion in the anisotropic slow dynamics of the magnetized electrons [40]. Finally, the W-module uses a much finer unstructured mesh, tailored to resolve the small wavelengths present in the problem. Linear interpolation between the meshes is used to communicate the various modules.

As in [26], the simulation domain includes the electron-cyclotron resonance (ECR) surface present in the MN (the green line in Figure 5.2), located where the cyclotron frequency of the

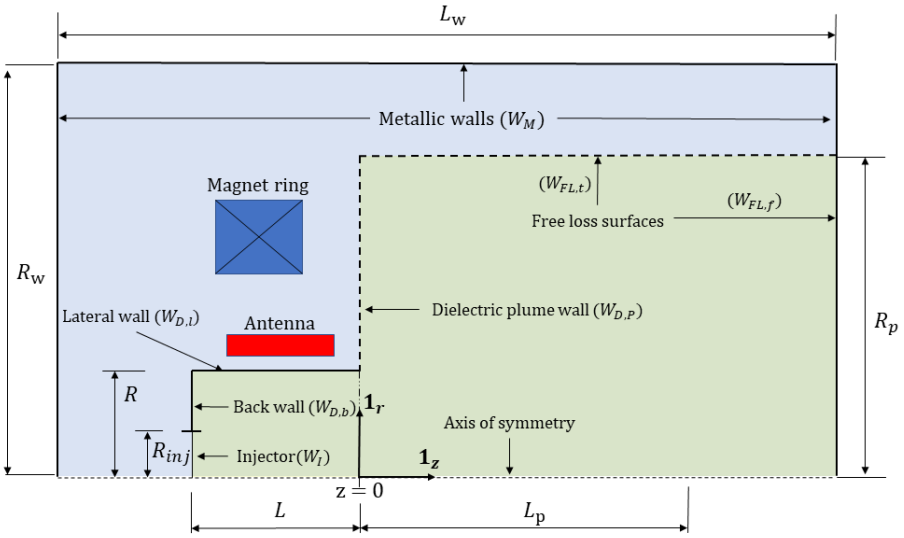

Figure 5.5: Simulation domain and boundary conditions (not to scale). The transport domain corresponds to the green area. The W-module domain is the union of the green and blue areas.

applied magnetic field is 13.56 MHz.

The numerical model is run sequentially until steady state is reached, both in thrust and other performance figures; this takes place after 3.75 ms of physical time. As in [40], the simulation is pre-initialized by calling the I-module alone, with a Boltzmann relation-like model for the electrostatic potential. This allows the simulation domain to be quickly filled with macroparticles that come from the injector before calling the E- and W-modules. The main timestep Δt_I is the one advancing the I-module. The E-module generally requires 5-10 subiterations, each with timestep Δt_E. In contrast, the W-module, which solves the fields in the frequency domain, is called after a fixed number of transport timesteps, about each 50-250 depending on the problem, in order to update the cycle-averaged power deposition. Customary to PIC simulations, the results presented here are time-averaged over 200 I-module steps to filter noise and short period oscillations.

In the following, additional details of the transport and wave parts of HYPHEN-EPT are provided. The cylindrical vector basis $\{\mathbf{1}_z, \mathbf{1}_r, \mathbf{1}_\theta\}$ and the magnetic vector basis $\{\mathbf{1}_\parallel, \mathbf{1}_\perp, \mathbf{1}_\theta\}$, with $\mathbf{1}_\parallel = \boldsymbol{B}/B$ and $\mathbf{1}_\perp = \mathbf{1}_\theta \times \mathbf{1}_\parallel$, are used.

5.3.1. Plasma transport model

The reader is referred to [40] for a full description of the hybrid transport model used in this work; in the following, only an overview of the key characteristics for this work is given.

The E-module integrates the following fluid equations for electrons:

$$n_e = \sum_{s \neq e} Z_s n_s, \tag{5.1}$$

$$\nabla \cdot \boldsymbol{j}_e = -\nabla \cdot \boldsymbol{j}_i, \tag{5.2}$$

$$0 = -\nabla (n_e T_e) + e n_e \nabla \phi + \boldsymbol{j}_e \times \boldsymbol{B} + \boldsymbol{F}_{res} + \boldsymbol{F}_{ano}, \tag{5.3}$$

$$\frac{\partial}{\partial t}\left(\frac{3}{2}n_e T_e\right) + \nabla\cdot\left(\frac{5}{2}T_e n_e \boldsymbol{u}_e + \boldsymbol{q}_e\right) = -\nabla\phi\cdot\boldsymbol{j}_e - Q_{inel} + Q_a, \tag{5.4}$$

$$0 = -\frac{5n_e T_e}{2e}\nabla T_e - \boldsymbol{q}_e\times\boldsymbol{B} + \boldsymbol{Y}_{\text{res}} + \boldsymbol{Y}_{\text{ano}}\,, \tag{5.5}$$

where the unknowns are n_e, ϕ, $\boldsymbol{j_e}$, T_e and $\boldsymbol{q_e}$. The I-module provides the right hand side of Eqs.(5.1,5.2). In the energy equation, Q_{inel} is the power density lost by electrons during inelastic collisions (i.e. excitation and ionization) and Q_a is the volumetric power density deposited by the electromagnetic fields, which is furnished by the W-module.

In the momentum and heat flux equations, the resistive terms are

$$\boldsymbol{F}_{res} = -m_e n_e\Big(\nu_e\boldsymbol{u}_e - \sum_{s\neq e}\nu_{es}\boldsymbol{u}_s\Big), \qquad \boldsymbol{Y}_{res} = -\frac{m_e\nu_e}{e}\boldsymbol{q}_e \tag{5.6}$$

where $\nu_{es}(T_e)$ is the collision frequency with heavy species s, and $\nu_e = \sum_{s\neq e}\nu_{es}$ is the total collision frequency of electrons. The terms representing anomalous transport are modeled here as [40]

$$\boldsymbol{F}_{ano} = \alpha_{ano}Bj_{\theta e}\mathbf{1}_\theta, \qquad \boldsymbol{Y}_{\text{ano}} = -\alpha_{\text{ano}}\,Bq_{\theta e}\mathbf{1}_\theta - \left(m_e\nu_q/e\right)q_{\parallel e}\mathbf{1}_\parallel, \tag{5.7}$$

where both α_{ano} and ν_q are phenomenological (constant) parameters that will be fitted later with the experimental results. The terms with α_{ano} represent the effect of high-frequency turbulence on quasi-steady electron transport, while the term with ν_q empirically reduces heat fluxes in the parallel direction, to capture the collisionless cooling observed in magnetically expanded plasma plumes [135]–[137]. Observe that the drift-diffusive equations (5.3) and (5.5) provide generalized Ohm and Fourier laws for $\boldsymbol{j_e}$ and $\boldsymbol{q_e}$. The numerical integration of the electron model in the MFAM is based on a semi-implicit scheme for time discretization and finite volume/gradient reconstruction methods for spatial discretization [40].

The S-module allows matching the boundaries of the quasi-neutral domain to either the thruster walls (using a sheath model) or the downstream plasma plume (using matching conditions with infinity) [138]. Provided the electron temperature T_e and the current densities of the ion species at the edge of the sheath, the S-module fixes the necessary electron current and heat fluxes and the local potential fall ϕ_{WQ} between a quasineutral boundary point Q and a wall point W (or infinity). The S-module accounts for material type, recombination, and secondary electron emission by providing different plasma-wall interaction models and fitting parameters. For the ceramic walls of the thruster, we implement locally $\boldsymbol{j_e} + \boldsymbol{j_i} = 0$. For downstream free loss (FL) surfaces, we determine a potential at infinity ϕ_∞ such that the plume is current-free globally, i.e. $\iint_{FL}\boldsymbol{j}\cdot\boldsymbol{n}\mathrm{d}S = 0$, with the integration domain extended to the whole free-loss (FL) surface [138].

In this work, Xe, Xe^+, and Xe^{++} are included in the I module. Xenon is introduced through the injector surface on the back wall of the thruster, shown in figure 5.5. The position and geometry of the injector is known to influence neutral depletion and overall performance [139]. For simplicity, the multi-hole injector is modeled as a uniform injection surface centered at the source axis. Based on the number and size of the holes, this is only a minor compromise for the model accuracy. The number of particles injected per time step is selected and population control strategies [37] are enforced to achieve a statistically sufficient number of particles per cell in the periphery of the plume. Not less than 100 particles are observed in each PIC cell in steady state. The number of total particles of all ion and neutral species in steady state approaches $4\cdot 10^6$.

Finally, the collisional mechanisms considered in this work are: single and double ionization; elastic electron-neutral and electron-ion collisions; and neutral excitation collisions. An effective excitation rate from ground state to the most important electronic excited states listed in [140] is implemented. Excited states are assumed to decay instantaneously to the ground state. This assumption is reasonable for radiative states, which spontaneously decay, the excitation energy being immediately lost. But not for metastable states, which could lead to additional ion production via stepwise ionization, or deposition of that energy back to the plasma via superelastic deexcitation processes [141]. Therefore, this simplification is conservative in terms of ionization and energy losses.

5.3.2. Electromagnetic wave model

The full-wave, frequency domain, cold-plasma model presented in [26] is used here for the W-module. Rather than a finite difference discretization as in that reference, we adopt a discretization of mixed Lagrange / vector finite elements similar to that in [41]. A major feature of the new implementation is that the present code can simulate arbitrary azimuthal modes m, while that of [41] only handles $m = 0$. This is central for HPT simulation, where the $m = 1$ mode is prevalent.

The wave equation for the fast electric field $\boldsymbol{\mathcal{E}}$,

$$\varepsilon_0\mu_0\frac{\partial^2\boldsymbol{\mathcal{E}}}{\partial t} + \nabla\times(\nabla\times\boldsymbol{\mathcal{E}}) = -\mu_0(\mathcal{J}_p + \mathcal{J}_a), \tag{5.8}$$

is solved for harmonic solutions of the form

$$\boldsymbol{\mathcal{E}}(z, r, \theta, t) = \Re\left[\boldsymbol{E}(z, r)\exp(-\mathrm{i}\omega t + im\theta)\right]. \tag{5.9}$$

Similar expansions are used in $\mathcal{J}_p$ and $\mathcal{J}_a$, the plasma and antenna current densities. Ignoring the slow ion response to the wave fields, the complex magnitude of the plasma current, $\boldsymbol{J}_p$, is expressed using the cold plasma dielectric tensor formalism [19] as:

$$\boldsymbol{J}_p = -i\omega\varepsilon_0(\overline{\overline{\kappa}} - \overline{\overline{1}})\cdot\boldsymbol{E}, \tag{5.10}$$

where $\overline{\overline{1}}$ is the identity tensor and the $\overline{\overline{\kappa}}$ the dielectric tensor, which takes the following form in the $\{\mathbf{1}_\parallel, \mathbf{1}_\perp, \mathbf{1}_\theta\}$ vector basis:

$$\overline{\overline{\kappa}}(z, r) = \begin{pmatrix} P & 0 & 0 \\ 0 & (R+L)/2 & -i(R-L)/2 \\ 0 & i(R-L)/2 & (R+L)/2 \end{pmatrix}, \tag{5.11}$$

with

$$R = 1 - \frac{\omega_{pe}^2}{\omega(\omega + \mathrm{i}\nu_e - \omega_{ce})}, \qquad L = 1 - \frac{\omega_{pe}^2}{\omega(\omega + \mathrm{i}\nu_e + \omega_{ce})}, \qquad P = 1 - \frac{\omega_{pe}^2}{\omega(\omega + \mathrm{i}\nu_e)}.$$

The electron cyclotron and plasma frequencies, $\omega_{ce} = eB_a/m_e$ and $\omega_{pe} = \sqrt{ne^2/(m_e\varepsilon_0)}$, are the main plasma parameters in the electromagnetic model, while the electron collisionality ν_e is an input from the slow plasma transport code.

The weak form of equation (5.8) after expanding in ω and m is:

$$\begin{aligned}\iint_{\Omega}\left\{\left[\left(\nabla_t+\mathbf{1}_{\boldsymbol{\theta}}\frac{im}{r}\right)\times\mathbf{T}^{(m)}\right]\cdot\left[\left(\nabla_t-\mathbf{1}_{\boldsymbol{\theta}}\frac{im}{r}\right)\times\mathbf{E}^{(m)}\right]-k_0^2\mathbf{T}^{(m)}\cdot\bar{\bar{\kappa}}\cdot\mathbf{E}^{(m)}\right\}dS+\\+ik_0\int_{\delta\Omega}\left[\hat{n}\times\mathbf{T}^{(m)}\right]\cdot\left[\hat{n}\times\mathbf{E}^{(m)}\right]dl=i\mu_0\omega\iint_{\Omega}\mathbf{T}^{(m)}\cdot\boldsymbol{J}_{\boldsymbol{a}}^{(m)}ds\end{aligned}\tag{5.12}$$

where Ω and $\delta\Omega$ are the simulation domain and its enclosing boundary, and $\boldsymbol{T}^{(m)}$ is a test function. As in [41], a mixed element discretization is used with a Nédélec basis for (E_z, E_r) and a Lagrange basis for E_θ. This conforming mixed element approach has proven to be successful in preventing artificial accumulation of spurious current [115], [142].

The time-averaged power density deposited into the plasma, which is the main input to the transport code from the W-module, is

$$Q_a^{(m)}=\frac{1}{2}\Re\left((\boldsymbol{J}_p^{(m)})^*\cdot\boldsymbol{E}^{(\boldsymbol{m})}\right).\tag{5.13}$$

for each azimuthal mode m. Due to orthogonality, each mode can be solved separately. Previous studies on HPTs using helical antennas have shown the prevalence of $m = 1$ in total plasma resistivity [112], [143]. This prevalence is also confirmed for the current cusped configuration later in this work, and therefore only the $m = 1$ mode will be considered in the results.

Finally, to close the problem, the antenna current density, $\boldsymbol{J}_a$, and the boundary conditions must be given as input to the W-module. A half-helical antenna, identical to the one reported in [108], is used. The W-module domain, shown in figure 5.5 is larger than the transport domain, adding a vacuum region around it, and terminated at perfect electric conductor (PEC) walls (which would mimic a small vacuum chamber). On the axis of symmetry, regularity/smoothness boundary conditions are used [26].

The selection of the call frequency of the W-module (i.e., the number of PIC steps per wave call) is a compromise between very frequent EM calls and numerical stability. The local mesh size for the W-module is selected so that there are at least 20 nodes per wavelength in average. This allows one to resolve the fine wave structures [26]. Additionally, to avoid noise at sharp transitions in plasma density [108], the effective electron collisionality has been smoothly reduced from its computed value to 0 in the last $0.05R$ by the lateral and back walls of the thruster. The deposited power profile has been checked to be insensitive to small variations in the thickness of the numerical transition region around this value.

5.4. Comparison of experimental and numerical results

In Section 5.4.1, the experimental measurements are used to determine the value of the empirical parameters α_{ano} and ν_q in the transport code, while a sensitivity analysis for these two parameters is presented in section 5.4.2.

5.4.1. Model fitting

The experimental data has been used to fit $\alpha_{ano} = 0.0165$ and $\nu_q = 3.5 \cdot 10^7$ s^{-1} in the simulations. The agreement on plasma electron density n_e can be discussed in view of figure 5.3(a). The expansion rate agrees well in the first part of the expansion $\dot{m} = 12.5$ sscm, while it is marginally slower than the experiments for $\dot{m} = 20$ sccm.

Once adjusted to a common reference, the electrostatic potential ϕ in Figure 5.3(b) shows fairly good agreement between the experiments and simulations.

In both n_e and ϕ, a slight slope change is observed downstream in the simulated results for $\dot{m} = 12.5$ sscm that is not recorded in the experimental measurements. This could be related to a minor decrease in the divergence rate of the ion streamlines observed in the last part of the domain (not shown).

The electron temperature T_e is shown in Figure 5.3(c). Overall trends are similar in both experiments and simulation results. The local maximum coincides well with the location of the ECR (see Figure 5.2), which is a secondary location for the absorption of RF power by electrons [126], [127]. The cooling rate after the maximum is well captured by the model. Nevertheless, simulation results exhibit a negative bias with respect to experiments, especially for $\dot{m} = 20$ sccm, and partially miss the behavior of the experimental data in the vicinity of the source exit. Note, however, that the difference falls within a factor of 2 from the measurements, which is within the expected uncertainty for the experimental determination of T_e with probes, as explained in Section 5.2.2.

Finally, the normalized ion current density, including singly and doubly charged contributions, in Figure5.3 (d) shows good agreement between experimental and numerical results at low angles from the centerline, up to ±25 deg. The lateral wings at high angles, which are present in the experiments, are not captured by the simulations. The ion current and plasma density in these regions is expected to depend on the background pressure of the vacuum chamber [144]. The ion current profile in the simulation is also known to be highly sensitive to anomalous cross-field diffusion, controlled here by α_{ano}, and to conditions upstream at the source [40].

5.4.2. Sensitivity analysis

To assess the sensitivity of the simulations to changes in phenomenological parameters α_{ano} and ν_q, a parametric study is performed for the case $\dot{m} = 12.5$ sscm. According to [40], the anomalous transport parameter α_{ano} affects the cross-field transport, especially in near-collisionless regions such as the plume. Increasing α_{ano} increases plume divergence and plasma losses to the walls inside the thruster. Increasing the anomalous collisionality ν_q in the heat flux equation reduces the parallel conductivity, making magnetic lines less isothermal. A higher ν_q increases the electron cooling rate in the plume and also enables a higher T_e inside the thruster.

Figure 5.6(a) shows the plasma density along the symmetry axis for different values of α_{ano}. The increase in anomalous transport results in a lower, faster-decreasing electron density in the plume. When comparing $\alpha_{ano} = 0.015$ to $\alpha_{ano} = 0.018$, a density difference is observed approaching a factor 2 in the plume. The effects of ν_q on the plasma density are less noticeable.

Figure 5.6(b) displays the effect of ν_q on T_e along the axis. As ν_q increases, the electron cooling rate in the parallel direction increases, and the peak of T_e near the ECR surface in the MN becomes more pronounced. Electron cooling in a MN without downstream power deposition is well known and has been studied using kinetic models [45], [102], [145]; in this case, power deposition near the ECR surface is noticeable and affects the results of the simulations, as indicated above. The qualitative effect of increasing α_{ano} on the electron temperature is a nearly uniform upward displacement of the curve driven by changes in the plasma density, and hence the EM power deposition per electron.

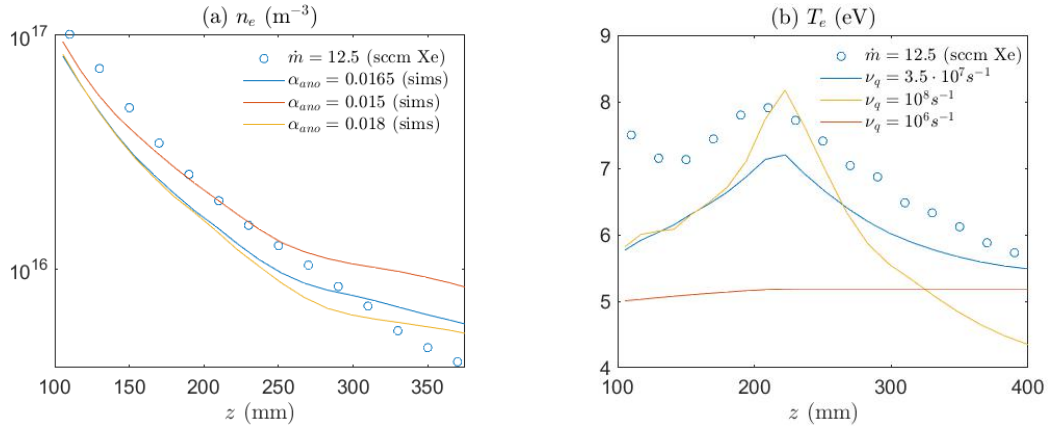

Figure 5.6: Sensitivity analysis on the plasma density and electron temperature with varying α_{ano} and ν_q.

In summary, it is found that the simple phenomenological models used here, which rely on uniform values of α_{ano} and ν_q in the full simulation domain, perform reasonably well in the quest to reproduce the trends of experimental results. However, the absolute values do not match the measurements exactly (although they generally fall within the measurement error). It is worth mentioning that more complex turbulent models (e.g. with nonuniform maps) could be used, but at the probable cost of overfitting and loss of generality across similar devices and different operating points.

5.5. Detailed analysis of the HPT discharge

Once the simulation parameters have been fitted to agree reasonably well with the limited experimental results, we analyze in detail the plasma discharge for the case $\dot{m} = 12.5$ Xe sscm $\equiv 1.23$ mg/s. The characteristic values / ranges of the plasma conditions found in the simulation domain are shown in Table 5.1.

5.5.1. Wave-Plasma Interaction and Electromagnetic Power Deposition

The magnitude and phase of the $m = 1$ azimuthal electric field of the W-module solution, which is the predominant component excited by helical antennas [16], are shown in Figure 5.7. The field is strongest inside the source, decaying in the plume and thruster surroundings. Despite the lower magnitude, propagation takes place in the MN up to the ECR surface. Beyond it, since the plasma

is overdense for the applied frequency, the fields become evanescent [19], [26].

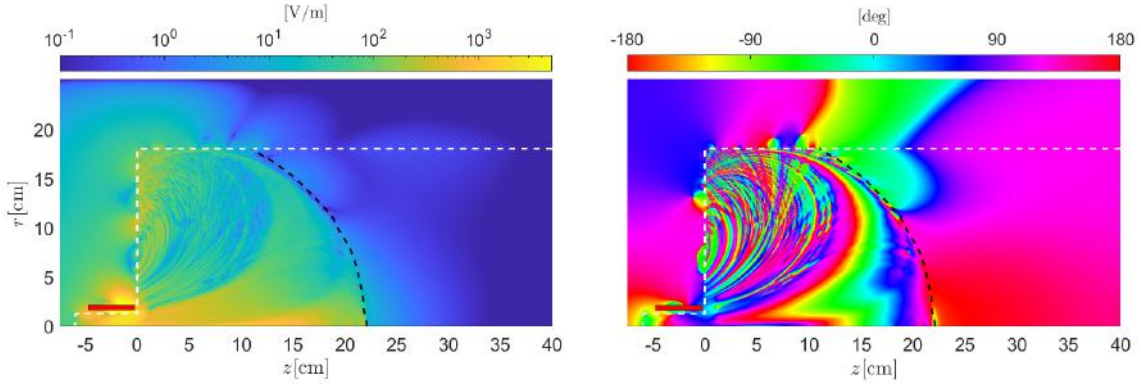

Figure 5.7: E_θ^1 field magnitude (left) and phase angle (right). The dashed black line corresponds to the ECR surface.

Along the axis, a low $k_\parallel$ helicon mode is seen to propagate in the source and near-plume. The plume periphery presents shorter wavelengths, consistent with the Trivelpiece-Gould waves expected at the plasma edge [110]. These structures exhibit a high perpendicular wave number $k_\perp$. Both kinds of wave (helicon and Trivelpiece-Gould) correspond to the right-hand polarized whistler wave at different propagation angles with respect to $\boldsymbol{B}$, and both vanish upon arriving at the ECR surface. At this location, electromagnetic power is mainly absorbed and cannot propagate beyond. On a side note, we mention that there is another ECR surface in this simulation setup in the neighborhood of the singular point inside the plasma vessel. However, its effects are minor due to the limited spatial extent of that transition.

The power absorption profile is shown in the top row of Figure 5.8. Due to the linearity of the wave problem, these maps can also be interpreted as the local plasma resistivity (save for a factor). Most of the power is absorbed within the source. This agrees well with plasma-wave theory, predicting an absorption approximately proportional to the plasma density for similar magnitude propagating fields and suggests a good coupling between the RF antenna and the plasma inside the source. In the zoomed-in view of the source, we see that the maximum deposition is located near the axis, peaking at the vicinity of the magnetic separatrix.

The bottom row of Figure 5.8 shows the power absorbed *per electron*. According to the electron energy equation, this quantity determines the local heating of electrons, and thus affects to a large extent the profile of T_e. Per-particle absorption peaks inside the source but spreads into the plume, with local maxima at the vicinity of the ECR surface near the symmetry axis, revealing the importance of the particle-specific power deposition in that region of the MN. There is no energy deposition downstream of the ECR surface. Although earlier work has relied on computing absorption only within the thruster plasma source[146], these results suggest that local heating may affect the structure of the plume and drive the electron temperature profile outside the source.

So far, we have exclusively focused on the fields carried by EM waves in azimuthal mode $m = 1$. This was done on the basis of extensive past evidence on the predominant power coupling of helical antennas in helicon sources [18]. However, wave behavior is known to be highly dependent on the applied magnetic field [19], and the question arises as to the extent to which the previous mechanisms of propagation and absorption would still be valid in our cusped-field

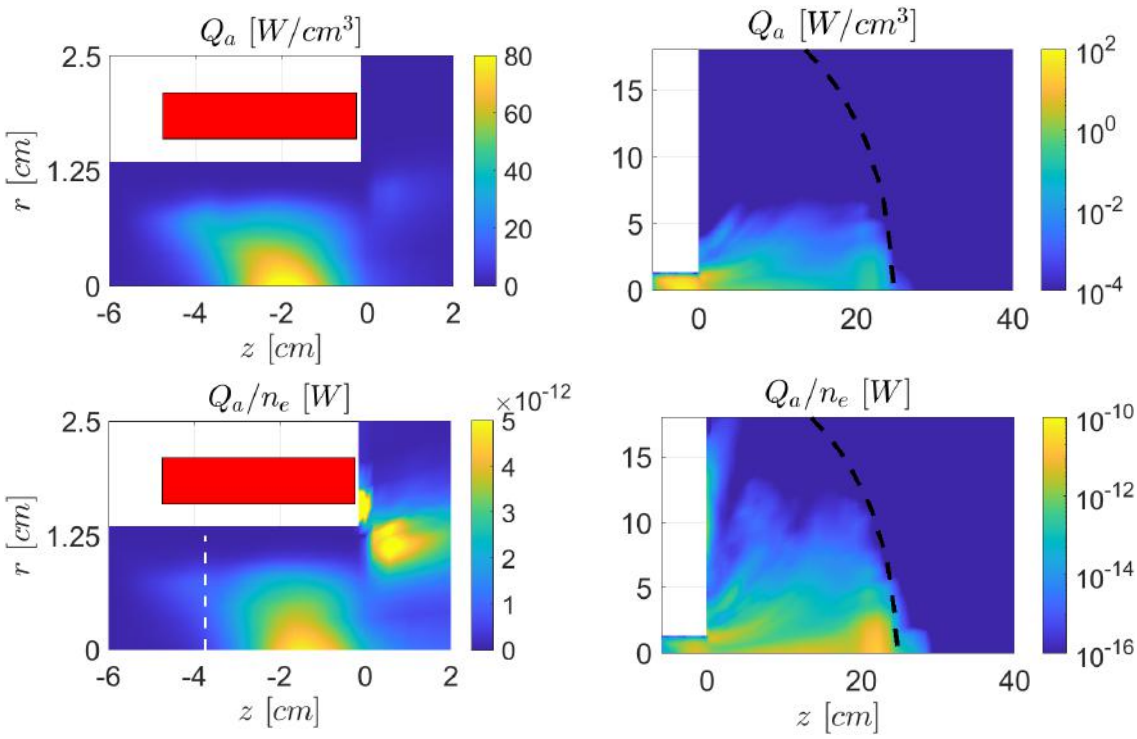

Figure 5.8: Electromagnetic Power Deposition (top row), power per electron (bottom). Zoom on the source region (left column) and full transport domain (right column). The magnetic field separatrix is shown as a white dashed line in the zoom view plots. The ECR resonance is shown as a black dashed line in the full view plots.

topology. Figure 5.9 shows the fraction of the total power deposition contributed by each of the four modes considered in the steady state discharge. Although the power deposited by $m = -1$ is higher than in a classical topology [26], it can be seen that $m = 1$ is still the main contributor. As suggested by the results for $m = \pm 3$, the power of the higher modes decreases rapidly with m. Additionally, the majority of the power is deposited in the dense plasma of the source regardless of the mode. Therefore, we conclude that our approximation, that is, considering only $m = 1$ in coupled simulations, is justified, with a loss of accuracy comparable to other problem uncertainties such as wave and transport coupling or antenna modeling.

5.5.2. 2D Plasma Discharge Profiles

Figure 5.10 shows 2D maps of the main magnitudes of the plasma response. Some of the principal features are qualitatively similar to those reported in [40] for an EPT with a quasi-axial magnetic field and localized power deposition inside the thruster. Here, the cusped magnetic topology and the more spread power deposition give rise to some peculiarities.

The electron temperature T_e inside the source in Figure 5.10 responds mainly to the power deposition map, which, as shown in Figure 5.8, is centered at the antenna location and mainly downstream of the magnetic cusp. The radial magnetic lines near the cusp separate hot and cool very efficiently, resulting in a stark difference in T_e left and right of the cusp: while T_e after the cusp is around 5 eV, it is below 2 eV left of it. Naturally, T_e is also affected by wall losses, inelastic collisions, and convection/heat fluxes. As parallel transport is very efficient, we observe

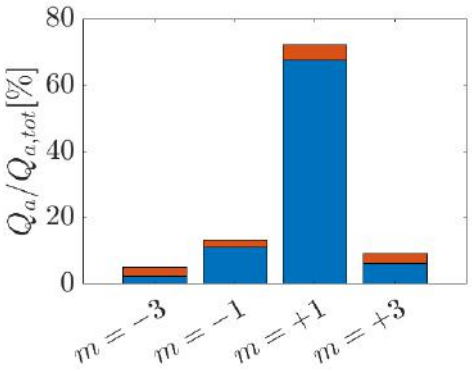

Figure 5.9: Fraction of the total electromagnetic power deposition in the source (blue) and plume (orange) regions for each azimuthal wave number.

a near-isothermal behavior along magnetic lines on this scale.

The low T_e inwards of the magnetic cusp means low plasma production and neutral depletion there, as the plot of n_n in Figure 5.10 suggests. Ionization of neutrals becomes efficient as T_e increases when crossing the cusp and neutrals are depleted. Additionally, the neutral density rises locally near the walls, driven by ion surface recombination. The plasma density peaks around the magnetic cusp section, but unfortunately, this plasma is not transported exclusively downstream, but upstream as well, which is found to be a major loss mechanism of this HPT field configuration.

In Figure 5.10, the map of the electrostatic potential ϕ inside the thruster roughly follows that of $\ln n_e$. However, the peak of ϕ occurs downstream from the peak of n_e. The large plasma production near the peak of ϕ flows both downstream and upstream, facilitated by the axial magnetic lines guiding electron motion and the unmagnetized character of the ions. Downstream the cusp, the decrease of n_e is due to plasma acceleration. Except in the proximity of the lateral wall, the electric field $-\nabla\phi$ becomes essentially axial where the magnetic lines are axial. The low radial electric field is a consequence of the existence of an azimuthal electron current that produces a radial magnetic force, shown in Figure 5.12 that compensates for pressure gradients [31], [40].

The map of T_e in the plume region, shown in the top left of Figure 5.10, also merits discussion. The electron temperature remains around its maximum value in the near-plume due to the mild cooling rate. Although the gradient of T_e is also mainly in the perpendicular direction in the plume, certain parallel variations can be observed at this scale. The local maximum near the ECR location on the axis, reported in Section 5.4.1, is consistent with the peak in power deposition per electron there, which helps raise the local T_e. Another local maximum of T_e occurs in the periphery of the plume, on magnetic lines that do not connect to the plasma source. This behavior, which has not yet been validated experimentally, is driven by low n_e, low energy losses, and low perpendicular transport in this region, combined with moderate RF power deposition per particle. Finally, the electrostatic potential map in the plume of Figure 5.10 also features a prominently axial gradient, as inside the source. This behavior suggests a low plume divergence, as discussed in the next section.

Figure 5.11 shows the in-plane ion flux (top, dominated by singly charged ions) and the total electron flux (middle), $\tilde{\boldsymbol{j}}_i = j_{zi}\mathbf{1}_z + j_{ri}\mathbf{1}_r$ and $\tilde{\boldsymbol{j}}_e = j_{ze}\mathbf{1}_z + j_{re}\mathbf{1}_r$. There is a significant flux of particles into the back and lateral walls of the source. Moreover, very few ions generated upstream of the

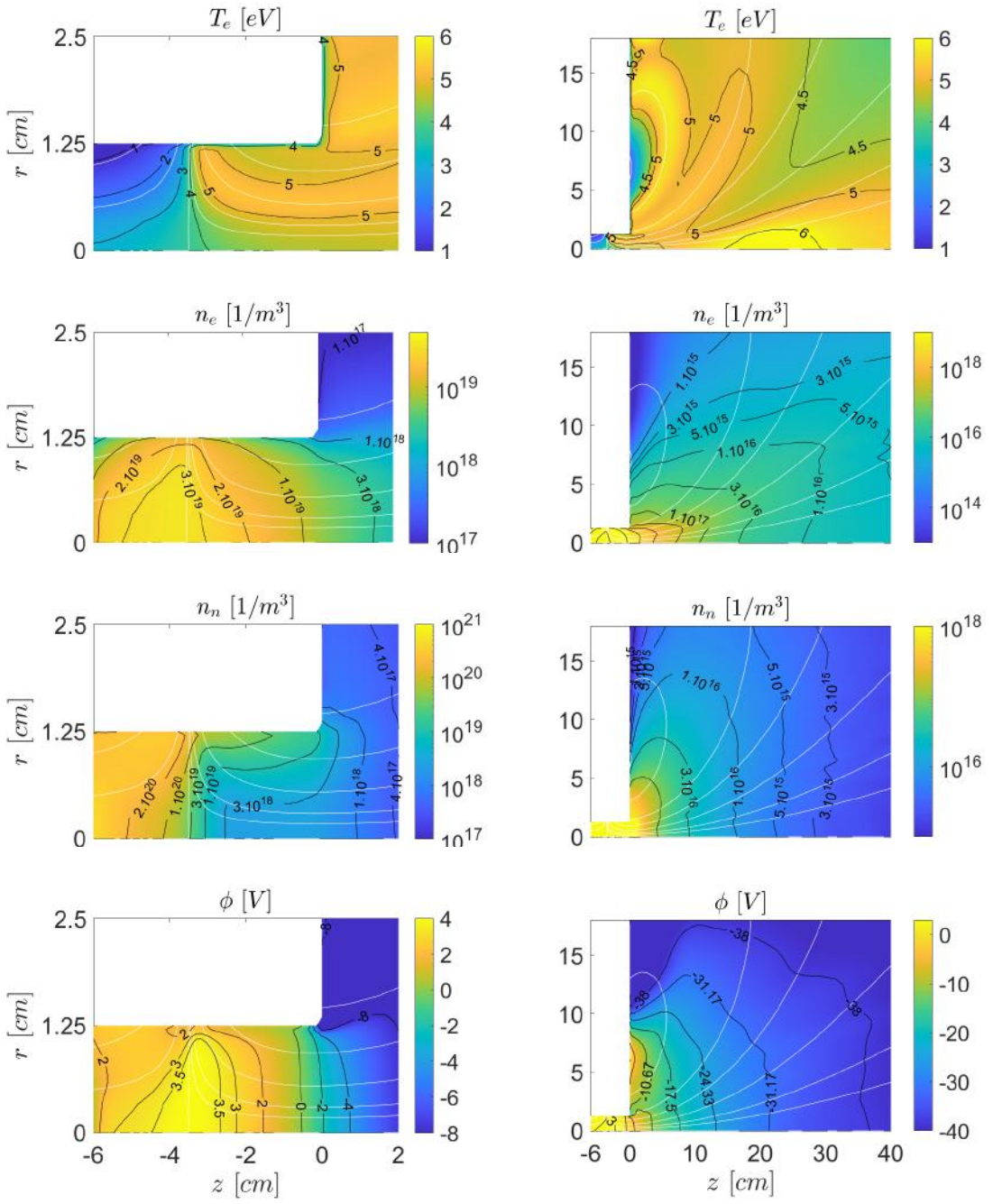

Figure 5.10: Electron temperature (1st row), plasma density (2nd row), neutral density (3rd row), and plasma potential (4th row). Zoom in on the source region (left column) and full transport domain view (right column). The solid white lines are magnetic field streamlines.

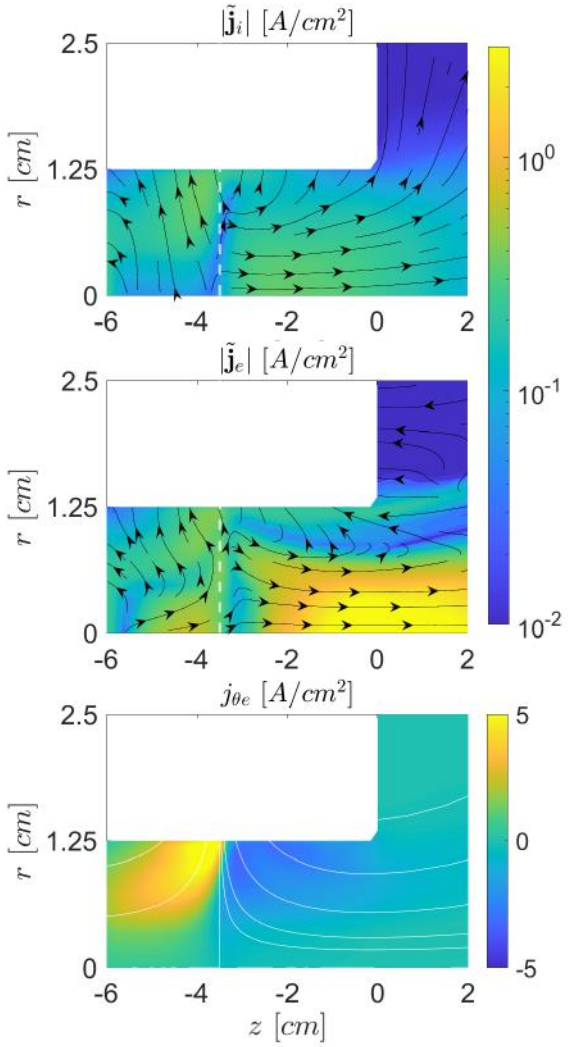

Figure 5.11: Total ion (top) and electron (middle) current density and particle flux vectors; and azimuthal electron current (bottom). The magnetic field separatrix is shown as a white dashed line.

magnetic cusp separatrix are capable of crossing it. As a consequence, ion production to the left of the cusp is almost completely lost to the dielectric walls. Considering that ions are only weakly magnetized, the ion dynamics is driven solely by the potential map. Downstream of the separatrix, ions accelerate and expand, with a non-negligible fraction of them impacting the lateral wall. Electrons, on the other hand, feature a large axial current near the axis and a compensating return current at larger radii to keep the plasma emission globally current-free.

The azimuthal current densities are such that $j_{\theta e} \gg j_{\theta i}$ by about a factor 200, and the electron contribution constitutes the bulk of the plasma azimuthal current, essential in magnetic confinement and thrust generation. The map of $j_{\theta e}$ at the source is shown in Fig. 5.11 (bottom). From the momentum equation (5.3), the perpendicular pressure gradient, the perpendicular electric field, and to a minor extent, classical resistivity contribute to determining this current. As can be observed, $j_{\theta e}$ peaks near the lateral wall around the location of the cusp, switching signs on each side.

The radial and axial magnetic force densities generated by the interaction of this azimuthal

current with the applied magnetic field, respectively $j_{\theta e}B_z$ and $-j_{\theta e}B_r$, are shown in Figure 5.12. The radial magnetic force is negative in the source and confines the electrons away from the lateral wall, whereas the axial magnetic force is positive and negative left and right of the cusp, respectively. Combined, the two forces push the electrons to the singular point of the field, where the highest plasma density n_e occurs.

From the point of view of magnetic thrust generation (that is, the volume integral of $-j_{\theta e}B_r$), it is evident that the electron currents to the left of the cusp contribute positively to thrust, while those to the right of the cusp exert a comparable negative (drag) contribution, driven by the geometry of the field and the direction of the electron pressure and electrostatic potential gradients. The axial magnetic force in each of these two regions amounts to approximately 4.7 and −2.9 mN, respectively. The positive thrust generation is resumed downstream in the MN, where 3.2 mN are generated up to the end of the simulation domain. This is roughly 45% of the total thrust of the device, a fraction comparable to that of other MNs [101]. In addition to the magnetic thrust, the pressure thrust (on the wall of the plasma source) yields about 2.2 mN extra.

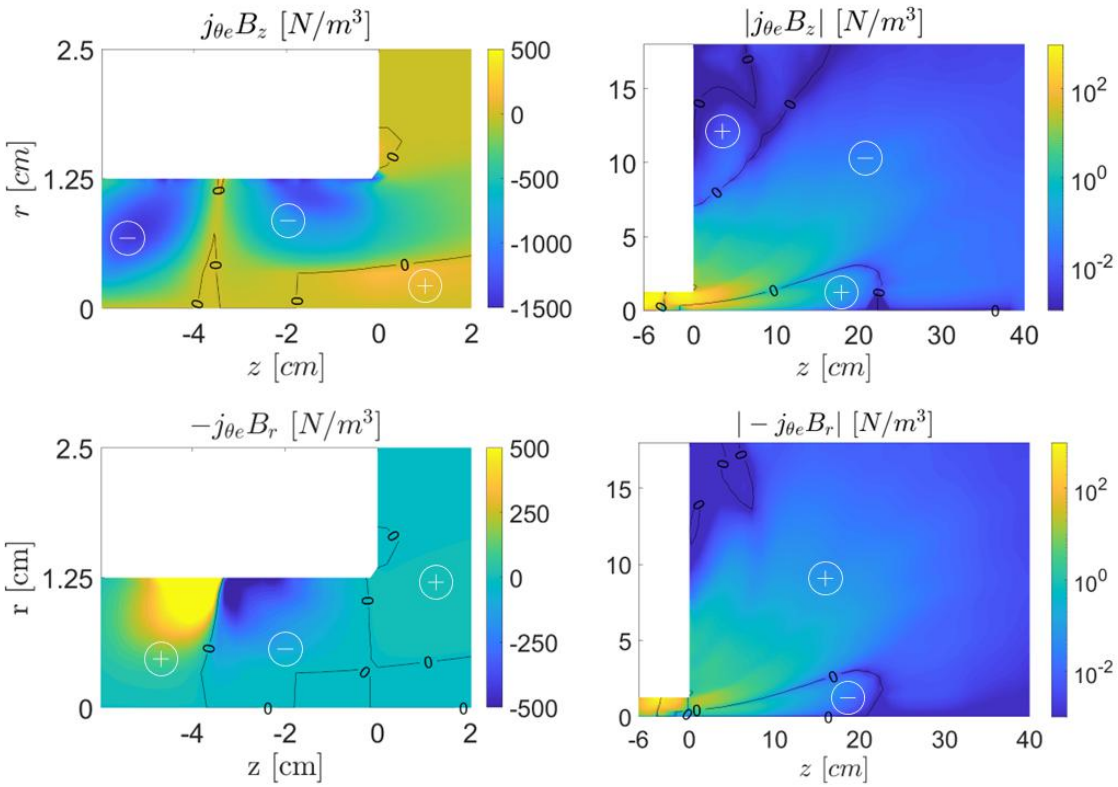

Figure 5.12: Radial (top) and axial (bottom) magnetic force in the plasma. The force direction is indicated by ± signs.

Figure 5.13 shows the electron and total ion fluxes to the boundaries of the domain. While these fluxes differ at the top and right plume boundaries, their integral satisfies the global current-free condition. Figure 5.13 (right) shows that the maximum current is reached just at $z = -3.5$ cm, demonstrating not only the poor confinement in the source, but also that the cusped magnetic field drives the particles directly onto the walls at that location.

The energy fluxes in the bottom row of Figure 5.13 follow similar trends. In most of the inner wall of the plasma source, the energy carried by the electrons (advective and heat flux terms)

is larger than the ion energy. Poor confinement in the neighborhood of the magnetic separatrix drives a strong convective energy flux to the lateral wall. This important energy sink and the need to reionize the particles that recombine at the walls lead to the low plasma temperature shown in Figure 5.10. Secondary electron emission is small, with a yield less than 20 % in all source walls, due to the moderate electron temperature and ion impact energies.

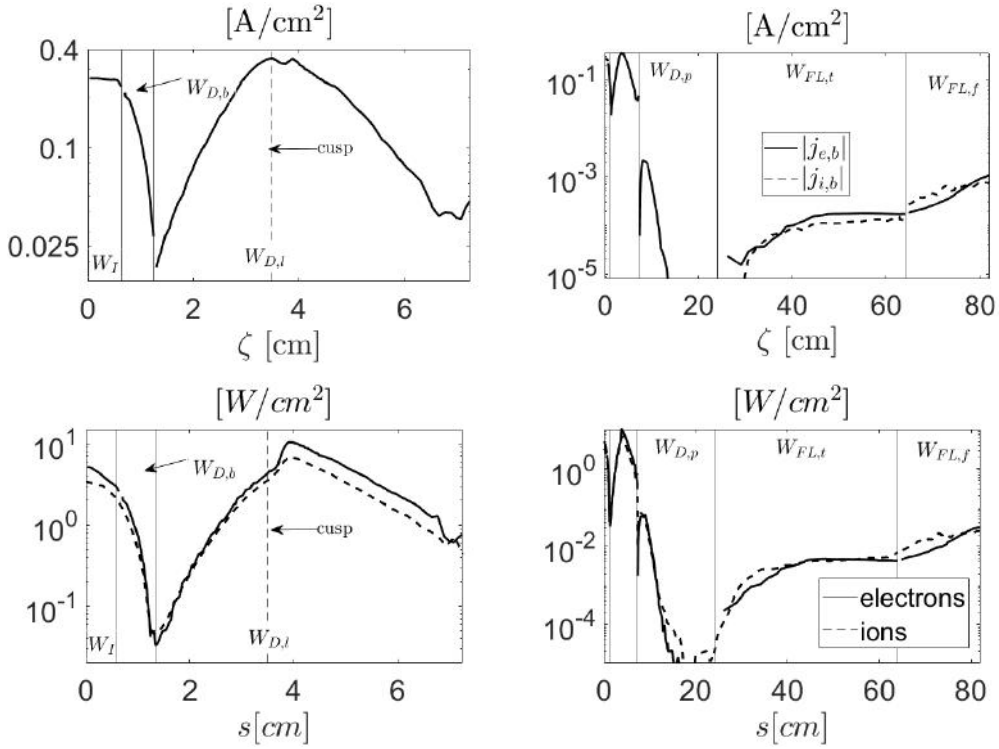

Figure 5.13: Electron and total ion current densities (top row) and energy fluxes (bottom row) to source dielectric walls (left column) and all domain boundaries (right column). The arc length coordinate s moves clockwise along the boundary from $(z, r) = (-6, 0)$. Refer to Figure 5.5 to identify each boundary wall W. The dashed line in the left plots indicates the location of cusp.

5.5.3. Balances of plasma production and energy

The efficiency of the thruster is analyzed here through different balances. The first variable of interest is the total ion mass production rate, $\dot{m}_{i,prod}/\dot{m}$. In steady state, this ion production is distributed as

$$\dot{m}_{i,prod} = \dot{m}_{i\infty} + \dot{m}_{i,lat} + \dot{m}_{i,back} \tag{5.14}$$

with $\dot{m}_{i\infty}$ the flow of ions through the free-flow boundaries and $\dot{m}_{i,lat}$ and $\dot{m}_{i,back}$ the ion flows that recombine at the lateral and back wall, respectively. For the case simulated here, the utilization of the propellant mass is $\eta_u = \dot{m}_{i\infty}/\dot{m} \simeq 89\%$ and the production efficiency is $\eta_{prod} = \dot{m}_{i\infty}/\dot{m}_{i,prod} \simeq 9\%$; both values are consistent with the high densities and the large chamber length. This means that plasma ionization is very efficient, but plasma confinement is very poor. Indeed, on average, every neutral is ionized 10 times after 9 recombinations in the walls. A balance equivalent to (5.14) can be done in terms of total ion electric currents, that is, $I_{i,prod} = I_{i\infty} + I_{i,lat} + I_{i,back}$, which results from integrals of the current in Fig. 5.13. Ratios for mass flows and currents are very similar since the amount of doubly-charged ions is small; for instance, the downstream ion mass flow consists

of 91.5% of singly-charged ions and 8.5% of doubly-charged ions.

The power balance can be expressed as

$$P_a = P_\infty + P_{lat} + P_{back} + P_{ion} + P_{exc} \tag{5.15}$$

with the terms on the right hand side being, respectively, the mechanical power in the beam leaving the plume domain, the mechanical power lost in the lateral walls and the back walls of the source, and the power spent in ionization and excitation collisions. The first three are integrals along sections of the curves of Figure 5.13. The ratios to the absorbed power P_a are the following:

$$\frac{P_\infty}{P_a} \simeq 12\%, \quad \frac{P_{lat}}{P_a} \simeq 33\%, \quad \frac{P_{back}}{P_a} \simeq 1.6\%, \quad \frac{P_{ion}}{P_a} \simeq 22\%, \quad \frac{P_{exc}}{P_a} \simeq 31\%, \tag{5.16}$$

i.e. a 35% of P_a is lost in the walls and a 53% is lost in ionization and excitation. These large losses are due to the combination of poor plasma confinement and a very long chamber. Comparable high wall losses have been observed in other numerical [147] and experimental studies [148], showing about a 40 % loss of the total power budget in both low- and high-power devices. Despite the relatively low T_e (approximately 5 eV), there is multiple ion recombination and neutral reionization, as illustrated by the production efficiency of only 9%. The low fraction of useful energy explains the low T_e, which leads to excitation energy losses being higher than the ionization losses.

It is of interest to compare these performances with those of Ref. [40] for an HPT of similar geometry and power, but with a quasi-axial magnetic topology. The ratio of the back to the lateral wall areas is about 10% in the two cases. The ratio of back to lateral wall energy losses is about 4.5% here and it was about 50% in Ref. [40]. Thus, the magnetic cusp has improved the confinement of the back wall by moving plasma production downstream of the ring cusp. However, the overall confinement is worse, as illustrated by η_{prod}, which is 16% (almost double) in [40]. In that case, 44% of P_a is lost in the walls and a 36% is lost in ionization and excitation. The higher percentage of wall losses in [40] is due to the higher T_e (about 11 eV) that also comes with a considerable reduction in excitation losses. This is again an indication of the complex energy balance in these thrusters and the delicate optimization of design and operation conditions.

The thrust calculated here is $F \simeq 7.5$ mN, which yields a thrust efficiency $\eta_F = F^2/(2\dot{m}P_a) \simeq 5.1\%$, (compared to 11.5% in [40]). To understand the different sources of thrust inefficiency, η_F is factorized as [40]:

$$\eta_F = \eta_{disp}\eta_{div}\eta_{ene}, \quad \eta_{disp} = \frac{F^2}{2\dot{m}P_\infty^{(z)}}, \quad \eta_{div} = \frac{P_\infty^{(z)}}{P_\infty}, \quad \eta_{ene} = \frac{P_\infty}{P_a}, \tag{5.17}$$

where: $P_\infty^{(z)}$ is the flow of axial energy in the beam, the only one that may be used to generate thrust; η_{disp} takes into account that the plasma beam is not monoenergetic, and constituted of particles of different electric charges; η_{div} assesses the plume divergence; and η_{ene} is the energy efficiency. For our simulation we have: $\eta_{ene} \simeq 12\%$, as mentioned above, which is the main cause of the poor efficiency of the device; $\eta_{div} \simeq 59\%$, which corresponds to a divergence half angle of $\arccos \sqrt{\eta_{div}} \simeq 40$ deg; and $\eta_{disp} \simeq 72\%$, value that comes out mainly from the non-monoenergetic downstream plasma flow, with an 11% constituted of slow neutrals and a 7% of doubly-charged ions, with double energy than the 82% of singly-charged ions.

Finally, to assess the effect of vacuum chamber background pressure on the thruster performance figures (and in the plasma profiles), and to validate our modeling approach, an additional simulation was carried out including the injection of cold neutrals (300 K) through the free-loss boundaries at the plume of figure 5.5, corresponding to a typical pressure of 10^{-5} mbar in our vacuum chamber. This preliminary study of background pressure effects indicates that (1) the discharge in the ionization chamber is essentially unaffected; (2) the plume region maintains its overall characteristics and the effect is mild, consisting of a slight decrease in electron temperature ($\simeq$ 0.5 eV), a decrease in potential fall ($\simeq$ 4 V), and a slight increase in plume divergence ($\simeq$ 3 deg); (3) the ionization and entrainment of background gas into the plume increases the resulting ion current by 5% (this artificially pumps the utilization efficiency to 93%); (4) the combined effects result in a decrease in thrust by 5%. This is consistent with the findings of Wachs et al. [149], where the loss in ion beam energy (due to the lower potential fall) appears to weigh more than the additional "free" neutral mass flow on the overall efficiency of the device. These observations could be relevant when extrapolating vacuum chamber measurements to estimate the propulsive performance of a device under free-space conditions.

5.6. Summary

An experimental and numerical analysis of the discharge of a cusped Helicon Plasma Thruster has been conducted. After the anomalous collisionality parameters of the model were adjusted, simulations successfully captured the trends of the experimental plasma profiles, providing a partial validation of the model. The numerical results reproduce the presence of a secondary maximum of electron temperature T_e near the downstream ECR surface, although differences of up to 50% in absolute value are observed in the high mass flow rate case. The azimuthal profile of the ion current density j_i is also well described by the code up to moderate angles, beyond which the experimental data present lateral wings.

The results suggest that anomalous transport exists in this device, augmenting cross-field transport and reducing parallel heat fluxes, and highlight the importance of accurately modeling these effects. While a rather simple two-parameter model has been used, additional experimental measurements could help define more advanced ones. The sensitivity analysis on these two parameters shows a strong dependence of the plasma response in the plume, and—without a predictive anomalous transport theory,—stresses the need of a tuning process in general.

The magnetic ring cusp greatly determines the plasma response inside the source. In this HPT configuration, the deposition of energy is located close to the center of the antenna, which is downstream of the cusp. This causes the region inward to the cusp to be of low temperature and displaces to the cusp the main ionization region. The cusp also divides the regions of back and forward ion currents, and of positive (inward) and negative (outward) magnetic thrust inside the source; the external magnetic thrust is positive again in the MN. The net magnetic thrust amounts to 70% of the total generated thrust.

The different causes of performance loss have been described. As in other helicon plasma thruster designs, plasma currents to walls are very large, implying high ion recombination, and multiple re-ionization, which in turn increase the losses due to ionization and excitation. This results in low energy efficiency and, consequently, low thrust efficiency. Compared to thrusters

with a quasi-axial magnetic field, the presence of a ring-cusp seems to reduce the losses to the lateral wall. This could be a major advantage of this configuration. Nevertheless, the overall lower electron temperature reached in the current design leads to enhanced excitation losses, and this offsets the improvement mentioned above. Further work should identify whether design or operating point modifications can exploit the lower wall losses of the cusped case while increasing the electron temperature to increase thrust efficiency, as suggested by some experimental studies [121], [122].

Finally, a numerical contribution has been the improvement of the W-module of HYPHEN-EPT with new Finite Element algorithms capable of reproducing any azimuthal wavenumber m. These are shown to be more accurate than the previous Finite Difference ones. For the half-helical antenna of the HPT, $m = +1$ is the dominant mode (with ~70% of the deposited power), and the modes $m = -1$ and $+3$ are subdominant. The computed wavefields indicate that most of the RF power is absorbed inside the source and downstream of the magnetic cusp. Furthermore, the power absorbed per electron is seen to have a local maximum on the axis near the downstream ECR surface, which correlates with the peak in T_e observed in experiments and simulations. Being relatively far from the plasma source, the role of ECR in plasma heating, despite being studied in some early work [127], has been ignored in some HPT numerical investigations (e.g. [40], [146]).

6. *An implicit, conservative electrostatic particle-in-cell algorithm for magnetic nozzles*

The contents of the following chapter have been published in [71] and are reproduced here without modifications.

An electrostatic, implicit particle-in-cell (PIC) model for collisionless, fully magnetized, paraxial plasma expansions in a magnetic nozzle is introduced with exact charge, energy, and magnetic moment conservation properties. The approach is adaptive in configuration space by the use of mapped meshes, and exploits the strict conservation of the magnetic moment to reduce the dimensionality of velocity space. A new particle integrator is implemented, which allows particle substepping without the need to stop particle motion at every cell face for charge conservation. Particle substeps are determined from accuracy considerations, and are allowed to span multiple cells. Novel particle injection and expansion-to-infinity boundary conditions are developed, including a control loop to prevent the formation of spurious sheaths at the edges of the domain. The algorithm is verified in a periodic magnetic mirror configuration, a uniform plasma test case (to test particle injection), and a propulsive magnetic nozzle. The algorithm's computational complexity is shown to scale favorably with timestep, and linearly with the number of particles and grid cells for resolutions well beyond typical simulation needs. Numerical experiments demonstrate that the proposed algorithm is more than an order of magnitude faster than a semi-Lagrangian Vlasov code running on a similar machine, and we estimate speedups of that order compared to explicit PIC algorithms.

6.1. Introduction

A guiding divergent magnetic field can be used to expand a plasma in a controlled and directed manner to generate thrust. This is the principle behind the magnetic nozzle (MN) [32], [150], a device used to convert plasma thermal energy into macroscopic kinetic energy contactlessly, which constitutes an essential component of several plasma propulsion technologies such as the helicon plasma thruster [10], [29], [92], the electron cyclotron resonance thruster [41], [151], [152], the applied-field magnetoplasmadynamic thruster [153], [154], and the variable specific impulse magnetoplasma rocket [6]. In contrast to a classical (material) de Laval nozzle, where the pressure force on the device walls is the mechanism limiting the radial expansion of the gas and leading to the generation of mechanical thrust, in a MN it is the Lorentz force on the charged particles that confines their radial expansion and generates magnetic thrust.

The expansion in the MN is quasi-collisionless, which limits the applicability of closed-fluid models. For this reason, kinetic models have been used to understand, in particular, the electron response, which is intimately linked to the development of the ambipolar electrostatic potential responsible for the acceleration of the ions. Martínez-Sánchez et al. [102] established a steady-state, semi-analytical paraxial model of the expansion of an initially Maxwellian plasma in a converging-diverging magnetic field. They showed the presence of different electron subpop-

ulations (free-streaming, reflected, and doubly-trapped electrons) depending on the connectivity of their trajectories with the upstream plasma source and infinity downstream, as determined by barriers of an effective potential that results from the electrostatic field and the magnetic mirror force. That study revealed the existence of electron cooling and electron anisotropization on the divergent side, different for each electron subpopulation. The overall electron species exhibits a behavior that corresponds to the weighted average of the three subpopulations. Although that model solves for the distribution function of ions and electrons whose trajectories connect with the boundary conditions of the problem, it is unable to resolve the distribution of doubly trapped electrons, which was hypothesized to coincide with the distribution upstream. The model was later used to explore approximate closure relations [136], and was extended to two-dimensional MNs [145].

Sánchez et al. [45] explored the problem of electron kinetics in a MN with a time-dependent Vlasov code, and the same team later added weak resistivity to the electron dynamics [46]. These two mechanisms enabled the self-consistent study of doubly trapped electrons, as these regions are populated during the transient plume formation and by collisional diffusion. However, in addition to the high computational cost of this kinetic code, numerical difficulties were identified in the definition of the upstream and downstream boundary conditions (BCs). The choice of BCs in those studies led to the formation of undesired Debye sheaths in simulations that do not correspond with the expansion of a MN plasma into free space. This forced the truncation of the analysis domain to about half of the simulation domain. In other studies, the open-boundary BCs used prevented simulation of steady-state plasma expansion, as the time evolution of the plume had to be stopped before the particles reached the end of the domain [155], [156].

Advances in the proper treatment of BCs in kinetic simulations were presented by Li et al. [157]. That study showed that, when Dirichlet conditions for the potential at the entrance and homogeneous Neumann conditions at the exit are used, if all electrons reaching the downstream boundary are removed from the simulation, a numerical instability develops in the whole domain. Rather, a more consistent approach is to acknowledge that most of these electrons do not have the mechanical energy to reach infinity downstream and must be reflected based on the value of the total potential fall $\phi_\infty - \phi_0$, a magnitude that must be determined self-consistently during the simulation to enforce global current ambipolarity in the plasma jet. However, the reference employed an explicit particle-in-cell (PIC) approach, which was limited to very small domains due to computational constraints. Andrews et al. proposed yet another strategy based on a multipole expansion that yields non-stationary Robin-type boundary conditions on Poisson's equation [158].

Recently, a class of implicit electrostatic PIC algorithms have been proposed [65] that are exactly charge- and energy-conserving and able to leverage adaptive meshing without loss of those conservation properties [159]. These algorithms have been extended to deal efficiently with low-frequency electromagnetic regimes [160], [161] and strongly magnetized regimes [162]. The ability of these schemes to use time steps much larger than plasma and cyclotron frequencies, along with the preservation of strict conservation properties, makes them particularly attractive for the simulation of MNs in multiple dimensions and arbitrary magnetization regimes.

In this study, we take the first step in this direction by exploring the use of implicit electrostatic PIC algorithms for paraxial magnetic nozzles in the strongly magnetized regime. We built on previous studies and adapt a novel particle mover (particularly suitable for strongly magne-

tized regimes [162]) to mapped adaptive meshes. Such grids are convenient to simulate plasma expansions with PIC codes, since having a local cell size scaling roughly with the inverse of the expected plasma density allows for a comparable number of macroparticles per cell and therefore a comparable resolution in velocity space. Also, the spatial gradient length increases downstream, so a lower spatial resolution is sufficient there. Moreover, a dynamic outflow field boundary condition in one spatial dimension is rigorously derived that captures the plasma expansion towards infinity without introducing numerical artifacts (such as artificial sheaths) or forcing arbitrary conditions on the electric field. We demonstrate the new implicit 1D PIC solver on several examples, including a magnetic mirror, a uniform plasma, and a paraxial magnetic nozzle. For the latter, we compare our results with published data [45], finding a good agreement. We show that our model avoids domain-termination sheaths and outperforms [45] in accuracy and computational time. Finally we study the performance of the new algorithm in the MN problem, including the scaling of CPU wall time with different numerical parameters and the speedup with respect to other methods.

The rest of the paper is structured as follows: Section 6.2 introduces the quasi 1D paraxial model, field equations and the particle discretization of phase space. Section 6.3 addresses the numerical discretization and solution of the model via an implicit particle in cell algorithm, including the generalization of the new segment-averaged mover [163] to mapped geometries. It also proves the global energy and local charge conservation properties of the method. Section 6.4 introduces the newly developed injection algorithm and dynamic downstream boundary condition for MNs. Section 6.5 discusses the verification of the code with three numerical examples. The first (6.5.1) demonstrates conservation properties and the effect of the magnetic mirror force in a simplified periodic geometry; the second (6.5.2) demonstrates the ability of the code to handle particle injection in an implicit PIC context with a uniform plasma verification example; and the third (6.5.3) compares the full MN model against literature results. Finally, Section 6.6 presents a summary of this work.

6.2. Model

The kinetic model describes the collisionless, quasineutral expansion of a plasma from an upstream source into vacuum along the axis of an axisymmetric, convergent-divergent magnetic field $\mathbf{B}$, known as magnetic nozzle (MN). The maximum B is located at $z = 0$ and is referred to as magnetic throat. The plasma is composed of strongly-magnetized electrons e and singly-charged ions i that satisfy

$$\frac{m_s v_{\perp s}}{q_s B} \ll L_\perp \ll L_\parallel, \qquad \frac{m_s}{q_s B} \ll \tau, \tag{6.1}$$

for $s = i, e$ with mass m_s, charge q_s and perpendicular (to $\mathbf{B}$) velocity $v_{\perp s}$; where $L_\parallel$, $L_\perp$ are the characteristic gradient lengths in the parallel and perpendicular directions and τ the characteristic time of change of the fields.

6.2.1. Paraxial drift-kinetic equation

Under the assumptions above, the magnetic moment of each charged particle $\mu_s = m_s v_\perp^2/(2B)$ is a conserved adiabatic invariant, and the gyroaveraged distributions $f_s(\mathbf{x}, v_\parallel, \tilde{\mu}, t)$ $(s = i, e)$ (with

$\tilde{\mu} = \mu_s/m_s$ the mass-scaled magnetic moment) along the axis respond to the drift-kinetic Vlasov equation (DKE) in conservative form [164]:

$$\frac{\partial f_s}{\partial t} + \frac{1}{B(\mathbf{x})}\left[\nabla\cdot(v_\parallel \mathbf{B} f_s) + \frac{\partial}{\partial v_\parallel}\left(\left(\frac{q_s}{m_s}E_\parallel - \tilde{\mu}\mathbf{b}\cdot\nabla B\right)B f_s\right)\right] = 0, \tag{6.2}$$

where $E_\parallel = -\mathbf{b}\cdot\nabla\phi$ is the parallel electrostatic field, with $\phi(\mathbf{x}, t)$ the electrostatic potential. Perpendicular drifts are negligible in the regime described by the orderings in Eq. (6.1), and are strictly zero on the axis of symmetry (see below). The factor $B(\mathbf{x})$ in this equation is the Jacobian determinant of the transformation from $(\mathbf{x}, v_\parallel, v_\perp^2/2)$ to $(\mathbf{x}, v_\parallel, \tilde{\mu})$ coordinates:

$$J_\mu = \left|\frac{\partial(\mathbf{x}, v_\parallel, v_\perp^2/2)}{\partial(\mathbf{x}, v_\parallel, \tilde{\mu})}\right| = B(\mathbf{x}). \tag{6.3}$$

Noting that the phase-space flow $\left(v_\parallel\mathbf{B}, B(\frac{q_s}{m_s}E_\parallel - \tilde{\mu}\mathbf{b}\cdot\nabla B)\right)$ is incompressible (as required for the conservation of phase-space volume),

$$\nabla\cdot(v_\parallel\mathbf{B}) + \frac{\partial}{\partial v_\parallel}\left(B\left(\frac{q_s}{m_s}E_\parallel - \tilde{\mu}\mathbf{b}\cdot\nabla B\right)\right) = 0, \tag{6.4}$$

the DKE can be rewritten in characteristic form as:

$$\partial_t f_s + v_\parallel\mathbf{b}\cdot\nabla f_s + \left(\frac{q_s}{m_s}E_\parallel - \tilde{\mu}\mathbf{b}\cdot\nabla B\right)\frac{\partial f_s}{\partial v_\parallel} = 0. \tag{6.5}$$

In general, in an axially symmetric configuration, $\mathbf{B} = \mathbf{B}(z, r)$. If the magnetic field variation in the r-direction is slow enough (which implies $\partial B/\partial r|_{R_b(z)} \ll B/R_b$, where $R_b(z)$ is the characteristic radius of a fully magnetized plasma beam), one can neglect the r-coodinate and only consider the coordinate along the symmetry axis z, and have:

$$v_\parallel \approx v_z \;;\; E_\parallel \approx E_z \;;\; \mathbf{B} \approx B(z)\mathbf{z}.$$

To recover the solenoidal property of the magnetic field (and phase-space incompressibility), we require the paraxial Jacobian factor $J^B = 1/B(z)$ in the definition of the divergence, such that:

$$\nabla\cdot\mathbf{B} = \frac{1}{J^B}\partial_z(J^B B) = 0.$$

This Jacobian is proportional to the flux-tube area by flux conservation, i.e., $A_{\mathrm{ft}}(z) \propto 1/B(z) = J^B$. The characteristic form of the paraxial DKE equation reads (from Eq. 6.5):

$$\partial_t f_s + v_z\partial_z f_s + \left(\frac{q_s}{m_s}E_z - \tilde{\mu}\partial_z B\right)\frac{\partial f_s}{\partial v_z} = 0, \tag{6.6}$$

with the corresponding conservative form (noting that $J_\mu J^B = 1$):

$$\partial_t f_s + \frac{\partial}{\partial z}(v_z f_s) + \frac{\partial}{\partial v_z}\left(\left(\frac{q_s}{m_s}E_z - \tilde{\mu}\partial_z B\right)f_s\right) = 0. \tag{6.7}$$

The corresponding particle representation of f_s is given by:

$$f_s(z, v_z, \tilde{\mu}, t) = \sum_{p \in s} w_p \delta(z - z_p(t)) \delta(v_z - v_{z,p}(t)) \delta(\tilde{\mu} - \tilde{\mu}_p(t)), \tag{6.8}$$

where $\delta(z)$ denotes the Dirac delta function, w_p is the weight of the p-th particle of species s. Introducing the particle ansatz (6.8) into the Vlasov equation (6.6) yields the axial particle motion governing equations:

$$\frac{\mathrm{d}w_p}{\mathrm{d}t} = 0, \tag{6.9}$$

$$\frac{\mathrm{d}\tilde{\mu}_p}{\mathrm{d}t} = 0, \tag{6.10}$$

$$\frac{\mathrm{d}z_p}{\mathrm{d}t} = v_{z,p}, \tag{6.11}$$

$$\frac{\mathrm{d}v_{z,p}}{\mathrm{d}t} = \frac{q_p}{m_p} E_z(z_p) - \tilde{\mu}_p \left.\frac{\mathrm{d}B}{\mathrm{d}z}\right|_{z_p}. \tag{6.12}$$

Zeroth and first moments of f_s give charge and current densities affected by the paraxial Jacobian (as required [66] since particles carry charges and currents, not densities), and are given by:

$$J^B \rho(z, t) = J^B \sum_s q_s \int dv_z d\tilde{\mu} J_\mu \, f_s(z, v_z, \mu, t) = \sum_p q_p w_p \delta(z - z_p(t)), \tag{6.13}$$

$$J^B j_z(z, t) = J^B \sum_s q_s \int dv_z d\tilde{\mu} J_\mu \, v_z f_s(z, v_z, \mu, t) = \sum_p q_p w_p v_{z,p}(t) \delta(z - z_p(t)). \tag{6.14}$$

6.2.2. Electrostatic field equation

The particle system is closed with an evolution equation for the electrostatic field. Instead of using Poisson's equation directly, as is customary in classical PIC algorithms, and with the goal of achieving strict numerical energy conservation in mind, we begin by considering Ampere's law [65],

$$\epsilon_0 \frac{\partial \mathbf{E}}{\partial t} + \mathbf{j} = \frac{1}{\mu_0} \nabla \times \mathbf{B}. \tag{6.15}$$

Taking the divergence of this equation gives:

$$\epsilon_0 \frac{\partial}{\partial t} \nabla \cdot \mathbf{E} + \nabla \cdot \mathbf{j} = 0. \tag{6.16}$$

Introducing the scalar electric potential $\mathbf{E} = -\nabla\phi$, one arrives at the final field equation used in this study:

$$\epsilon_0 \frac{\partial}{\partial t} \nabla^2 \phi = \nabla \cdot \mathbf{j}. \tag{6.17}$$

Note that this equation recovers the charge conservation equation if one replaces the Poisson equation or, equivalently, the same equation can also be derived by temporally differentiating Poisson's equation and using conservation of charge. Equations (6.6) and (6.17) for f_s and ϕ must be complemented with the necessary initial and boundary conditions. In particular, at the upstream plasma source, it is assumed that the one-sided part of f_s ($s = i, e$) with $v_z > 0$ is known. Boundary conditions for the field are presented in Section 6.4.

It is worth observing that the equation of axial momentum (6.12) can be expressed in terms of the effective potential $U_{\mathrm{eff},s}$, defined in [102] as

$$U_{\mathrm{eff},s}(z, t; \tilde{\mu}) = \frac{q_s}{m_s}\phi(z, t) + \tilde{\mu}B(z), \tag{6.18}$$

for $s = i, e$, so $\mathrm{d}v_{z,p}/\mathrm{d}t = -\mathrm{d}U_{\mathrm{eff},s}/\mathrm{d}z|_{z_p}$. At every instant of time, while ϕ is monotonically decreasing along the MN in the cases of interest, $U_{\mathrm{eff},s}$ is generally nonmonotonic, at least for some $\tilde{\mu}$. This creates potential barriers that cause the distributions of ions and electrons to subdivide into free-streaming, reflected, and trapped subpopulations, depending on the connectivity of their trajectories with the upstream plasma source and infinity downstream [102], [136], [145]. These subpopulations are cleanly delimited in steady state, where ϕ depends only on z. Naturally, in a time-dependent context, $U_{\mathrm{eff},s}$ varies in time, and the boundaries between these subpopulations become dynamic. Therefore, initially free particles may become trapped during the transient setup of the plasma beam [45], and vice versa, as ϕ evolves and their mechanical energy changes.

6.2.3. Transformation of the spatial coordinate

At this point, and for the purpose of spatial adaptivity, it is useful to consider analytically deformed grids using a mesh map $z(\xi)$. In 1D, the Jacobian of the transformation is simply $J_\xi = \mathrm{d}z/\mathrm{d}\xi$. To ensure strict numerical energy conservation, we employ a hybrid push [66], [165], [166] that evolves the position of the particle in the logical space ξ, while the particle velocity is evolved in the Cartesian coordinate v_z. Following equation (6.10) $\tilde{\mu}_p$ is exactly conserved and there is no need to evolve it. Additionally, this approach recovers the advantage of fast particle grid localization and grid-particle interpolations in a structured grid computational space, while avoiding troublesome inertial forces in the particle equation of motion due to the presence of the map [167]. The evolution of the particle position in logical space ξ_p is found by dividing equation 6.11 by J_ξ to find:

$$\frac{\mathrm{d}\xi_p}{\mathrm{d}t} = \frac{v_{z,p}}{J_\xi}. \tag{6.19}$$

Regarding the momentum equation (6.12), we similarly write the Cartesian electric field as $E_z = -\partial\phi/\partial z = E_\xi/J_\xi$, with $E_\xi = -\partial\phi/\partial\xi$ (which is directly computable on the logical grid), to find:

$$\frac{\mathrm{d}v_{pz}}{\mathrm{d}t} = -\frac{q_p}{m_p}\left(\frac{E_\xi}{J_\xi}\right)_{\xi_p} - \frac{\mu_p}{m_p}\left.\frac{\mathrm{d}B}{\mathrm{d}z}\right|_{\xi_p}. \tag{6.20}$$

The logical representation of the field equation Eq. (6.17) in 1D reads:

$$\epsilon_0\partial_t\partial_\xi\left(Jg^{\xi\xi}\partial_\xi\phi\right) = \partial_\xi\left(Jj^\xi\right), \tag{6.21}$$

where $\partial_\xi = \partial/\partial\xi$. The Jacobian $J = J_\xi J^B$ includes both the mesh map contribution J_ξ and the paraxial Jacobian $J^B = 1/B(z)$. In 1D, the contravariant metric tensor has just one component given by $g^{\xi\xi} = (J_\xi)^{-2}$, and the contravariant current density vector reduces to just one component, $j^\xi = \mathbf{j}\cdot\nabla\xi = j_z/J_\xi$. Equation (6.21), in 1D logical coordinates ξ and in the paraxial approximation, finally reads:

$$\epsilon_0\partial_t\partial_\xi\left(\frac{J^B}{J_\xi}\partial_\xi\phi\right) = \partial_\xi(Jj^\xi), \tag{6.22}$$

where the contravariant current component is found from the Cartesian particle velocity component $v_{z,p}$ as in [66]:

$$Jj^\xi = \sum_p q_p\frac{v_{z,p}}{J_\xi}\delta(\xi-\xi_p(t)) = \sum_p q_p\frac{\mathrm{d}\xi_p}{\mathrm{d}t}\delta(\xi-\xi_p(t)). \tag{6.23}$$

6.3. Numerical Implementation

6.3.1. Particle enslavement and subcycling

After a suitable discretization, one may use Eqs. (6.19) and (6.20) with the new particle coordinates $\mathbf{X_2} = \left\{\xi^{n+1}, v_z^{n+1}\right\}_p$ and Eq. (6.21) for the new potential at the cell centers $\mathbf{X_1} = \left\{\phi_i^{n+1}\right\}$ to obtain a nonlinear residual vector $\mathbf{F}(\mathbf{X_1}, \mathbf{X_2}) = 0$, which can be solved iteratively. However, such a formulation renders the number of unknowns too large for practical deployment in current massively parallel computers.

A practical implementation can be realized by noticing that the new particle coordinates are themselves functions of the potential, from which it follows that a new residual can be written $\mathbf{F}_1(\mathbf{X}_1, \mathbf{f}_2(\mathbf{X}_1)) = \mathbf{G}(\mathbf{X}_1) = 0$ [65]. Finding $\mathbf{f}_2(\mathbf{X}_1)$ requires an orbit integral, that is, for each particle, and given the electric potential on the cell faces $\mathbf{X_1} = \phi_i^{n+1}$, the equations of motion need to be integrated to accumulate the moments to form the residual vector $\mathbf{G}(\phi_i^{n+1})$. This procedure, known as *particle enslavement* [65], allows a global nonlinear solver, in our case a Jacobian Free Newton Krylov (JFNK) method, to handle a much reduced system of equations with no compromise on the accuracy of the solution.

Particle enslavement in an implicit PIC context provides great versatility for the integration of particle orbits. In particular, particle sub-stepping or subcycling will be employed [65]. Instead of using the overall time step Δt to integrate the particle orbits numerically, different $\Delta\tau_p^\nu$ per substep ν (suitably determined, as discussed below) are used such that $\sum\Delta\tau_p^\nu = \Delta t$. This approach can leverage the difference of scales between the slow field dynamics, characterized by Δt, and the fast particle dynamics, represented by $\Delta\tau_\nu^p$, to allow for accurate orbit integrals while avoiding expensive calls to memory because the particle coordinates are stored in local registers during the computation of subsequent substeps.

In earlier implicit PIC implementations [65], the simultaneous enforcement of local charge and energy conservation is achieved by adjusting intermediate $\Delta\tau_p^\nu$ to make particles stop at cell faces. Consequently, the number of cell crossings, and thus of substeps, grows proportionally to Δt and scales with the grid resolution (proportionally to the number of nodes in 1D [168]). In

practice, this hinders efficiency gains from the use of large Δt. Recently, a new particle mover has been proposed [162] that allows particles to cross several cells in a single substep while still conserving global energy and local charge exactly. The present work generalizes the new mover to nonuniform mapped meshes.

6.3.2. Particle orbit integration

We describe next the discretization of the particle equations of motion, the timestep estimator, and the orbit integration algorithm in mapped geometries. A key innovation of our approach is the ability of particles to traverse multiple cells in a single substep without spoiling conservation properties.

Crank-Nicolson discretization

A fully implicit, time centered, second-order and non-dissipative Crank-Nicolson discretization [65] is used,

$$\frac{\xi_p^{\nu+1} - \xi_p^{\nu}}{\Delta\tau_p^{\nu}} = \left(\frac{v_z}{J_\xi}\right)_p^{\nu+1/2}, \tag{6.24}$$

$$\frac{v_{z,p}^{\nu+1} - v_{z,p}^{\nu}}{\Delta\tau_p^{\nu}} = a^{\nu+1/2} = \frac{q_p}{m_p}\left(\frac{E_\xi}{J_\xi}\right)_p^{\nu+1/2} - \tilde{\mu}_p \frac{B_p^{\nu+1} - B_p^{\nu}}{v_{z,p}^{\nu+1/2}\Delta\tau_p^{\nu}}, \tag{6.25}$$

where $v_{z,p}^{\nu+1/2} = (v_{z,p}^{\nu+1} + v_{z,p}^{\nu})/2$, and $a^{\nu+1/2}$ is the particle acceleration computed at $(\Delta\tau/2, (\xi_p^{\nu+1} + \xi_p^{\nu})/2)$ from the electric and magnetic mirror forces. The definition of the Jacobian average over the substep, $J_\xi^{\nu+1/2}$, will account for multiple cell-crossings per particle substep, and is reported later in this section (Sec. 6.3.2). The discretization proposed for the mirror force term, $\tilde{\mu}_p(\mathrm{d}B/\mathrm{d}z)$ in the right hand side of Eq. (6.25), uses Eq. 6.24 to substitute $\Delta z^{\nu} = v_{z,p}^{n+1/2}\Delta\tau_p^{\nu}$ in the denominator and will be shown to conserve energy exactly.

The coupling between $\xi_p^{\nu+1}$ and $v_{z,p}^{\nu+1/2}$ via the mid-orbit electric field $E_{\xi,p}^{\nu+1/2}$ implies that an additional non-linear solve per particle is needed inside the mover. The system of equations is well posed for large time-steps, and simple Picard iterations achieve convergence to a very tight tolerance in a few steps [169].

Figure 6.1 shows an example of a particle's trajectory during and integration time step and the position of the most important field and particle variables in the computational space-time grid. The spatial 1D grid extends from $i = 1/2$ to $i = n_z + 1/2$. Integer indices denote cell centers, and half-integer indices denote cell faces or boundaries; n_z is the total number of cells in the domain. The particles are allowed to cross several cells in each substep ν instead of stopping at cell faces. This new strategy [162] has several advantages. The criteria for the selection of the substep τ_p^{ν} is only based on physical considerations. Free-streaming particles, not subject to strong-field gradients, can be advanced with fewer substeps while a time estimator for $\Delta\tau_p^{\nu}$ (discussed below) keeps numerical error of the Crank-Nicolson scheme under control.

The electric field (which determines the acceleration) must be scattered to the particles, accounting for all cell crossings during a substep $\Delta\tau^{\nu}$. In practice, this is done using a segment-

averaging approach [162]:

$$E_{\xi,p}^{\nu+1/2} = \sum_i E_{\xi,i+1/2}^{n+1/2} \left\langle S_1\left(\xi_{i+1/2} - \xi_p^{s+1/2}\right)\right\rangle_p^{\nu}, \tag{6.26}$$

where $E_{\xi,i+1/2}^{n+1/2} = (E_{\xi,i+1/2}^{n+1} + E_{\xi,i+1/2}^{n})/2$ and the orbit average of the first-order spline function S_1 is defined by weighting the distance traveled through each crossed segment ($\Delta\xi^s$) over the total length of the substep ($\Delta\xi^\nu$) [162]:

$$\left\langle S_1\left(\xi_{i+1/2} - \xi_p^{s+1/2}\right)\right\rangle_p^{\nu} = \frac{1}{\Delta\xi_p^\nu} \sum_{s\in\nu} S_1\left(\xi_{i+1/2} - \xi_p^{s+1/2}\right)\Delta\xi_p^s. \tag{6.27}$$

Here, the sum is over the collection of segments that make up the substep ν.

The segment averaging procedure, described above for the electric field in the particle push, results in significant efficiency gains compared to the previous particle subcycling approach [65] as shown and explained in Section 6.5.3.

Substep timestep estimator

A suitable substep timestep estimator is important to minimize the possibility of particle tunneling across a potential barrier [65] (which could happen, for instance, if the timestep is too large for the particle to resolve the scale of variation of the potential barrier). In our implementation, we estimate the timestep to ensure that the truncation error per Crank-Nicolson step is within a specified tolerance. The truncation error $\mathcal{E}_{\Delta\tau}$ of the Crank-Nicolson discretization in Eqs. (6.24),(6.25) for the position update is given by [162]:

$$\mathcal{E}_{\Delta\tau} = \frac{1}{12}\left(\frac{\mathrm{d}a}{\mathrm{d}\tau}\right)^{\nu}\Delta\tau^3 + O(\Delta\tau^4). \tag{6.28}$$

The substep time step can be determined from the desired maximum truncation error in a given substep as [162]:

$$\Delta\tau_p^\nu = \left(\frac{12\mathcal{E}_{\Delta\tau}}{|\mathrm{d}a/\mathrm{d}\tau|^\nu}\right)^{\frac{1}{3}}, \tag{6.29}$$

where $|\mathrm{d}a/\mathrm{d}\tau|^\nu$ is to be estimated along the substep as described below. In previous studies, the time derivative of the acceleration was computed by pushing the particle using Euler's scheme (constant field) and with a small time step $\delta t = 10^{-8}$, $\left(\frac{da}{d\tau}\right)^\nu \simeq \left(a^{\nu+\delta t} - a^\nu\right)/\delta t$. This estimate is then used as an initial guess for $\Delta\tau_p^\nu$. However, this approach provides a suitable error estimate only if the particle remains within a cell (where the numerical field is assumed to vary linearly). In this study, a given substep may cross several cells, and the estimate of $|\mathrm{d}a/\mathrm{d}\tau|^\nu$ should be adjusted accordingly. Here, we compute it by taking an L_1-norm (other norms are possible as well) of the change of acceleration across all cells crossed by the particle as:

$$\left|\frac{\mathrm{d}a}{\mathrm{d}\tau}\right|^\nu = \sum_{s\in\nu}\left|\frac{\mathrm{d}a}{\mathrm{d}\tau}\right|_s. \tag{6.30}$$

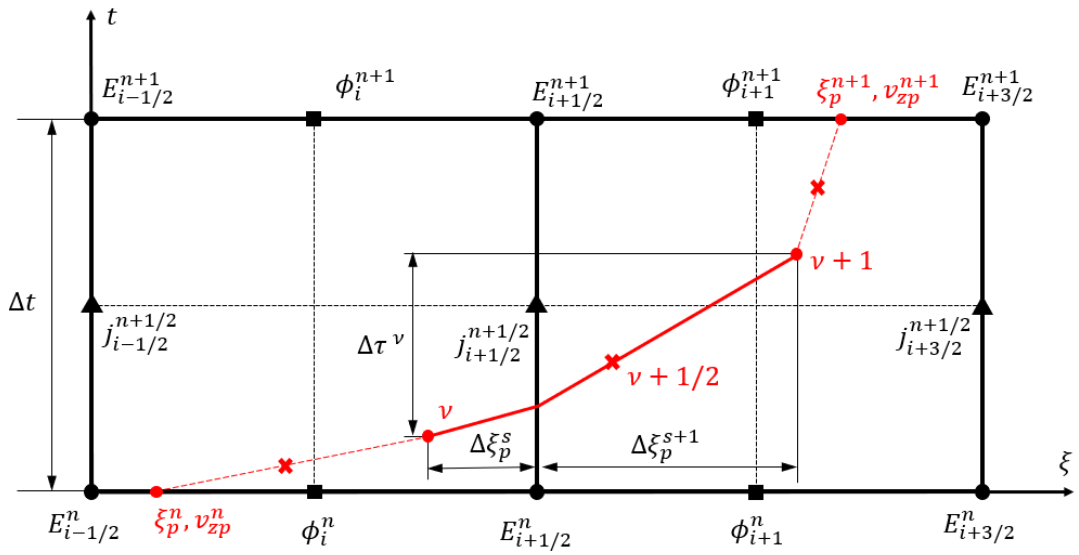

Figure 6.1: Space-time diagram showing the location of the computed grid quantities and an example particle trajectory (red line), which comprises three substeps, and the central suborbit (solid red line) that crosses two different cells, comprising two segments. While the velocity $v_p^{\nu+1/2}$ is unique for both segments within this suborbit, their slope in computational space may be different because the map Jacobian J_ξ in general varies from cell to cell.

The terms $|\mathrm{d}a/\mathrm{d}\tau|_s$ are computed internally in the particle mover taking the field difference between the initial and final points in the segment. If the prescribed tolerance $\mathcal{E}_{\Delta\tau}$ is not met, the substep in Eq. (6.29) is reduced by a factor $\eta < 1$, $\Delta\tau_p^\nu \to \eta\Delta\tau_p^\nu$. We find that $\eta = 0.5$ works well. This procedure is described in Algorithm 1.

Orbit integration algorithm

The numerical update of the computational coordinate and physical velocity follows from Eqs.6.24,(6.25):

$$\xi_p^{\nu+1} = \xi_p^\nu + \Delta\tau_p^\nu (v_z/J_\xi)_p^{\nu+1/2}, \tag{6.31}$$

$$v_{z,p}^{\nu+1/2} = v_{z,p}^\nu + 0.5\Delta\tau_p^\nu \left(\frac{q_p}{m_p} \left(\frac{E_\xi}{J_\xi} \right)_p^{\nu+1/2} - \tilde{\mu}_p \frac{B_p^{\nu+1} - B_p^\nu}{v_{z,p}^{\nu+1/2} \Delta\tau_p^\nu} \right). \tag{6.32}$$

After the iteration, the new-time velocity is found as:

$$v_{z,p}^{\nu+1} = 2v_{z,p}^{\nu+1/2} - v_{z,p}^\nu. \tag{6.33}$$

The equations are updated until convergence to a very tight relative tolerance, $O(10^{-13})$, in $v_{z,p}^{\nu+1/2}$ and $\xi_p^{\nu+1}$. To scatter the field to the position of the particle at mid orbit according to Eq. 6.26, cell crossings are detected and the distance along cell segments travelled by the particle, $\Delta\xi_p^s$, is computed. Although $B(z)$ is in principle known everywhere in the domain, it is generally faster to interpolate its value at the particle position from stored discrete values at cell faces with a

negligible compromise in accuracy as long as the field is smooth:

$$B_p^\nu = \sum_i B_{i+1/2} S_1\left(\xi_{i+1/2} - \xi_p^\nu\right). \tag{6.34}$$

In previous studies [66], the conversion of the physical velocity for the computation of the new logical position $\xi_p^{\nu+1}$ in Eq. 6.31 was performed with $(J_\xi)_p^{\nu+1/2}$ calculated at the midpoint of the cell in which the particle is located. The new mover takes into account the mesh map across all cells that the particle crosses during a substep. A straight line in the physical space $t - z$ translates into a curved trajectory in the computational space $\xi - t$. However, there still exists a linear relationship between the velocity and the total computational length traveled by the particle, i.e., $\Delta\xi_p^\nu \propto (1/(J_\xi)_p^{\nu+1/2}) v_{z,p}^{\nu+1/2}$ that can be used as the new definition of the mid-orbit Jacobian. In order to find $(J_\xi)_p^{\nu+1/2}$, we require that the total substep time is equal to the sum of the time the particle spends in each cell,

$$\Delta\tau_p^\nu = \sum_{s\in\nu} \Delta\tau_p^s. \tag{6.35}$$

Using Eq. (6.24), this relationship can be written as:

$$\Delta\xi_p^\nu / (v_{z,p}^{\nu+1/2} / (J_\xi)_p^{\nu+1/2}) = \sum_{s\in\nu} \Delta\xi_p^s / (v_{z,p}^{\nu+1/2} / (J_\xi)_p^{s+1/2}). \tag{6.36}$$

Canceling out the velocity on both sides (since it is constant per substep ν), we find a suitable interpolation formula for the Jacobian over a given particle substep:

$$(J_\xi)_p^{\nu+1/2} = \frac{1}{\Delta\xi_p^\nu} \sum_{s\in\nu} (J_\xi)_p^{s+1/2} \Delta\xi^s. \tag{6.37}$$

Note that the $\Delta\xi^s$ factors were already computed for the scattering of the electric field and are therefore readily available. The Jacobian at the particle position $(J_\xi)_p^{s+1/2}$ is linearly interpolated from the values at the cell faces $J_{\xi,i+1/2}$ as:

$$(J_\xi)_p^{s+1/2} = \sum_i S_1\left(\xi_{i+1/2} - \xi_p^{s+1/2}\right) J_{\xi,i+1/2}, \tag{6.38}$$

giving:

$$(J_\xi)_p^{\nu+1/2} = \frac{1}{\Delta\xi_p^\nu} \sum_{s\in\nu} \sum_i S_1\left(\xi_{i+1/2} - \xi_p^{s+1/2}\right) J_{\xi,i+1/2} \Delta\xi^s, \tag{6.39}$$

which is very similar to Eq. (6.27), and can therefore be computed along very efficiently. The segment-averaged Jacobian factor in Eq. (6.39) is then used in the particle equations of motion, Eqs. (6.24) and (6.25). A full description of the new particle mover algorithm is provided in Algorithm 1.

Algorithm 1 Particle mover. The mover takes in the particle states and electrostatic potential at $t = t^n$ and the electrostatic potential estimate at $t = t^{n+1}$, and returns the new particle states and the electric current density.

for each particle **do**
  Initialize remaining integration time $\mathrm{d}t$ to the desired orbit time step: $\mathrm{d}t = \Delta t$
  while $\mathrm{d}t > 0$ **do** ▷ **Full orbit loop**
    Estimate substep timestep $\Delta\tau_p^\nu$ ▷ Equations (6.29), (6.30)
    $\Delta\tau_p^\nu = \min(\mathrm{d}t, \Delta\tau_p^\nu)$
    while residual > tol **do** ▷ **Substep loop**
      Compute substep length $\Delta\xi_p^\nu = (v_z/J_\xi)_p^{\nu+1/2}\Delta\tau_p^\nu$
      Determine particle direction and number of crossed cells
      for each segment **do** ▷ **Segment loop**
        Compute segment length $\Delta\xi_p^s$
        Interpolate electric field at segment midpoint ▷ Equations (6.26),(6.27)
        Interpolate Jacobian $(J_\xi)_p^{s+1/2}$ and add to segment-averaged Jacobian ▷ Equations (6.38), (6.39)
        Accumulate acceleration rate-of-change per segment, $(\mathrm{d}a/\mathrm{d}\tau)^s$ ▷ Equation (6.30)
      end for
      Compute the effective electric field $E_{\xi,p}^{\nu+1/2}$ ▷ Equation (6.26)
      Update velocity $v_p^{\nu+1/2}$ ▷ Equation (6.32)
      Compute the new mid-orbit Jacobian $(J_\xi)_p^{\nu+1/2}$ ▷ Equation (6.39)
      Compute the residual in position and velocity ▷ Equations (6.24), (6.25)
      if $\sum_{s\in\nu} |\mathrm{d}a/\mathrm{d}\tau|^s > 12\mathcal{E}_{\Delta\tau}/(\Delta\tau_p^\nu)^3$ **then** ▷ Section 6.3.2
        $\Delta\tau_p^\nu \to \eta\Delta\tau_p^\nu$
        Go to 7
      end if
    end while
    Add particle contribution to current $(Jj^\xi)_{i+1/2}^{n+1/2}$ (per-segment operation) ▷ Equation (6.45)
    Compute remaining integration time: $\mathrm{d}t \to \mathrm{d}t - \Delta\tau_p^\nu$
  end while
end for

6.3.3. Field solver

We now consider the spatial discretization of Eq. 6.21. For convenience and without loss of generality, regular unit cell computational grids will be used (i.e. $\Delta\xi = 1$). With this choice, $J = \Delta\mathrm{V}_i$ is the effective physical cell volume and the standard second-order finite-difference derivative discretization simplifies to

$$\partial_\xi(Jj^\xi)_i \approx (Jj^\xi)_{i+1/2} - (Jj^\xi)_{i-1/2}. \tag{6.40}$$

The Laplacian of the scalar potential is discretized using a second-order conservative scheme,

$$(\nabla_\xi^2\phi)_i = \partial_\xi\left(\frac{J^B}{J_\xi}\partial_\xi\phi\right)_i \approx \left(\frac{J^B}{J_\xi}\right)_{i+1/2}(\phi_{i+1} - \phi_i) - \left(\frac{J^B}{J_\xi}\right)_{i-1/2}(\phi_i - \phi_{i-1}). \tag{6.41}$$

The discrete form of Eq. (6.21) reads,

$$(\nabla^2_\xi \phi)^{n+1}_i = (\nabla^2_\xi \phi)^n_i + \Delta t \left[(J j^\xi)_{i+1/2} - (J j^\xi)_{i-1/2} \right]^{n+1/2}. \tag{6.42}$$

The solution for the new potential ϕ^{n+1} requires the inversion of the Laplacian operator under suitable boundary conditions. This can be done either in the nonlinear residual itself, or as a pre-conditioner; in either case, a simple tridiagonal solve or an iterative solve using a Krylov method [170] can be used for this purpose, and both are optimal in one dimension improving the condition of the system for a faster non-linear solver convergence. The nonlinear residual vector for the JFNK solver is simply the difference between ϕ^{n+1} and the previous guess. From the potential, the covariant component of the electric field is found as:

$$E^n_{\xi,i+1/2} = -(\partial_\xi \phi)^n_{i+1/2} \approx \phi^n_i - \phi^n_{i+1}. \tag{6.43}$$

The modified current density at the mid timestep is computed as the orbit average along the particle substeps,

$$(J j^\xi)^{n+1/2}_{i+1/2} = \frac{1}{\Delta t} \sum_p \sum_{\nu \in n} (J j^\xi)^{\nu+1/2}_{i+1/2,p} \Delta \tau^\nu_p, \tag{6.44}$$

where the sum in ν is over all substeps that make up the full timestep n, and:

$$(J j^\xi)^{\nu+1/2}_{i+1/2,p} = q_p \left(\frac{v_z}{J_\xi} \right)^{\nu+1/2}_p \left\langle S_1 \left(\xi_{i+1/2} - \xi^{s+1/2}_p \right) \right\rangle^\nu_p. \tag{6.45}$$

Here, the same segment-averaged shape function is used as in the scattering of the electric field to the particle positions, Eq. (6.26). This finally gives:

$$(J j^\xi)^{n+1/2}_{i+1/2} = \frac{1}{\Delta t} \sum_p \sum_{\nu \in n} q_p \Delta \xi^\nu_p \left\langle S_1 \left(\xi_{i+1/2} - \xi^{s+1/2}_p \right) \right\rangle^\nu_p. \tag{6.46}$$

6.3.4. Conservation properties

We demonstrate next exact global energy and local charge conservation theorems for the proposed discrete particle representation of the paraxial model.

Global energy conservation

From the Crank-Nicolson discretization in Eq. (6.25),

$$\frac{v^{\nu+1}_{z,p} - v^\nu_{z,p}}{\Delta \tau^\nu_p} + \tilde{\mu}_p \frac{B^{\nu+1} - B^\nu}{v^{\nu+1/2}_{z,p} \Delta \tau^\nu_p} = \frac{q_p}{m_p} \left(\frac{E_\xi}{J_\xi} \right)^{\nu+1/2}_p, \tag{6.47}$$

and multiplying by $m_p v^{\nu+1/2}_{z,p}$ and recalling that $\mu_p B = m_p v^2_{\perp,p}/2$, we find:

$$\frac{m_p}{2} \left[(v^{\nu+1}_{z,p})^2 - (v^\nu_{z,p})^2 + (v^{\nu+1}_{\perp,p})^2 - (v^\nu_{\perp,p})^2 \right] = q_p \left(\frac{E_\xi}{J_\xi} \right)^{\nu+1/2}_p v^{\nu+1/2}_{z,p} \Delta \tau^\nu_p. \tag{6.48}$$

The left-hand side can easily be identified as the variation of the total kinetic energy per particle in a substep ΔK_p^ν. Summing over all particles and substeps per particle results in:

$$\begin{aligned}
K^{n+1} - K^n &= \sum_p q_p \sum_{\nu\in n} \Delta\tau_p^\nu v_{z,p}^{\nu+1/2} (E_\xi/J_\xi)_p^{\nu+1/2} \\
&= \sum_p q_p \sum_{\nu\in n} \Delta\tau_p^\nu (v_z/J_\xi)_p^{\nu+1/2} \sum_i E_{\xi,i+1/2}^{n+1/2} \left\langle S_1\left(\xi_{i+1/2} - \xi_p^{s+1/2}\right)\right\rangle_p^\nu \\
&= \sum_i E_{\xi,i+1/2}^{n+1/2} (Jj^\xi)_{i+1/2}^{n+1/2} \Delta t \\
&= -\sum_i (\partial_\xi \phi^{n+1/2})_{i+1/2} (Jj^\xi)_{i+1/2}^{n+1/2} \Delta t \\
&= \sum_i \phi_i^{n+1/2} (\partial_\xi J j^\xi)_i^{n+1/2} \Delta t \\
&= \sum_i \phi_i^{n+1/2} \epsilon_0 \frac{(\nabla_\xi^2 \phi^{n+1})_i - (\nabla_\xi^2 \phi^n)_i}{\Delta t} \Delta t \\
&= -\frac{\epsilon_0}{2} \sum_i \left[\phi_i^{n+1} (\nabla_\xi^2 \phi^{n+1})_i - \phi_i^n (\nabla_\xi^2 \phi^n)_i\right] \\
&= -\frac{\epsilon_0}{2} \sum_i \left[\left(\frac{J^B}{J_\xi}\right)_{i+1/2} \left(J_\xi {E_z}^{n+1}\right)_{i+1/2}^2 - \left(\frac{J^B}{J_\xi}\right)_{i+1/2} \left(J_\xi {E_z}^n\right)_{i+1/2}^2\right] \\
&= -\frac{\epsilon_0}{2} \sum_i \left[\left(E_{z,i+1/2}^{n+1}\right)^2 - \left(E_{z,i+1/2}^n\right)^2\right] J_{i+1/2} \\
&= -\left(W_E^{n+1} - W_E^n\right),
\end{aligned} \tag{6.49}$$

from which total conservation of energy follows. Above, the second line substitutes the scattering formula for the covariant field, Eq. (6.26), the third line commutes the sums and introduces the weighted sum for the current density per each particle and substep ν, Eq. (6.44). The fifth equality holds after integration by parts with periodic boundaries (which is the simplest case as it trivially eliminates boundary terms, although the proof can also be extended to reflective boundaries [162] and collisional plasmas with more advanced boundaries [68]), and the discrete field equation, Eq. (6.42), is introduced in the sixth equality. The seventh equality follows from the self-adjointness of the discrete Laplacian operator. The eighth equation follows from discrete integration by parts, allowed by the conservative discretization of the Laplacian operator Eq. (6.41) and the periodic boundary conditions [66]:

$$\begin{aligned}
\sum_i \phi_i (\nabla_\xi^2 \phi)_i &= \sum_i \phi_i \left[\left(\frac{J^B}{J_\xi}\right)_{i+1/2} (\phi_{i+1} - \phi_i) - \left(\frac{J^B}{J_\xi}\right)_{i-1/2} (\phi_i - \phi_{i-1})\right] \\
&= -\sum_i \left(\frac{J^B}{J_\xi}\right)_{i+1/2} (\phi_{i+1} - \phi_i)(\phi_{i+1} - \phi_i) \\
&= -\sum_i \left(\frac{J^B}{J_\xi}\right)_{i+1/2} E_{\xi,i+1/2}^2 = -\sum_i \left(\frac{J^B}{J_\xi}\right)_{i+1/2} (J_\xi E_z)_{i+1/2}^2 \\
&= -\sum_i (J^B J_\xi)_{i+1/2} (E_z)_{i+1/2}^2.
\end{aligned} \tag{6.50}$$

The ninth equality follows when noting that $J = J^B J_\xi$ is the cell volume (since $\Delta\xi = 1$), resulting in the final equality for the change in the total electrostatic energy. Therefore, the total energy is conserved:

$$H^n = K^n + W_E^n = K^{n+1} + W_E^{n+1} = H^{n+1}. \tag{6.51}$$

Local charge conservation

Next, we show charge conservation per particle per substep ν, from which local charge conservation follows. In the continuum, we have the following continuity condition,

$$\frac{\partial \rho}{\partial t} + \nabla \cdot \mathbf{j} = 0, \tag{6.52}$$

which in discrete form and in mapped geometry reads:

$$\frac{\left(J\rho^{n+1}\right)_i - (J\rho^n)_i}{\Delta t} + \frac{\left(Jj^\xi\right)_{i+1/2}^{n+1/2} - \left(Jj^\xi\right)_{i-1/2}^{n+1/2}}{\Delta\xi} = 0. \tag{6.53}$$

Pulling the orbit-average sum out, we can write the continuity condition as:

$$\sum_{\nu\in n}\left(\frac{\left(J\rho^{\nu+1}\right)_{i,p} - (J\rho^\nu)_{i,p}}{\Delta\tau_p^\nu} + \frac{\left(Jj^\xi\right)_{i+1/2,p}^{\nu+1/2} - \left(Jj^\xi\right)_{i-1/2,p}^{\nu+1/2}}{\Delta\xi}\right) = 0. \tag{6.54}$$

At this point, it is sufficient to require charge conservation per substep ν. The charge density term can be decomposed into segment contributions s, yielding:

$$\sum_{s\in\nu}\left[\left(J\rho^{s+1}\right)_{i,p} - (J\rho^s)_{i,p}\right] + \Delta\tau_p^\nu \frac{\left(Jj^\xi\right)_{i+1/2,p}^{\nu+1/2} - \left(Jj^\xi\right)_{i-1/2,p}^{\nu+1/2}}{\Delta\xi} = 0, \tag{6.55}$$

where s and $s+1$ are the start and end points of the segment, respectively. Substituting Eq. (6.45) for the current density and Eq. (6.27) for the segment-averaged spline, we arrive at:

$$\sum_{s\in\nu}\left[\left(J\rho^{s+1}\right)_{i,p} - (J\rho^s)_{i,p} + q_p\Delta\xi_p^s \frac{S_1\left(\xi_{i+1/2} - \xi_p^{s+1/2}\right) - S_1\left(\xi_{i-1/2} - \xi_p^{s+1/2}\right)}{\Delta\xi}\right] = 0, \tag{6.56}$$

where we have used that $\Delta\tau_p^\nu (v_z/J_\xi)_p^{\nu+1/2} = \Delta\xi_p^\nu$ per Eq. (6.24), which we require to be satisfied per segment. We now introduce the accumulation of the charge density using a second-order B-spline S_2 (instead of the first-order spline S_1 used for the current) [65],

$$(J\rho^s)_{i,p} = q_p S_2\left(\xi_i - \xi_p^s\right), \tag{6.57}$$

and the final charge-conservation condition reads:

$$\frac{S_2\left(\xi_i - \xi_p^{s+1}\right) - S_2\left(\xi_i - \xi_p^s\right)}{\Delta\xi_p^s} + \frac{S_1\left(\xi_{i+1/2} - \xi_p^{s+1/2}\right) - S_1\left(\xi_{i-1/2} - \xi_p^{s+1/2}\right)}{\Delta\xi} = 0, \tag{6.58}$$

which is exactly satisfied by the properties of the B-splines involved [65], proving local charge conservation to machine accuracy.

6.4. Magnetic nozzle boundary conditions

At the upstream boundary of a magnetic nozzle, we must prescribe the distributions of forward particles (i.e., with $v_z > 0$), and only these. Particles are subsequently allowed to leave the domain through the upstream boundary (reflected particles) or reach infinity downstream (free-streaming particles). In the smooth paraxial expansion, no strong non-neutralities are expected to form.

Numerical simulations with finite domains must also correctly model the expansion to infinity beyond the end of the domain, in particular for the electrons. Since the electrostatic potential ϕ continues to decrease beyond the domain boundary to a value at infinity ϕ_∞, a fraction of the electrons reaching the boundary of the finite domain will not reach infinity, and are actually reflected electrons. The solution must satisfy a global condition on the electric current leaving the plasma source (e.g., zero current for space plasma thruster applications). Likewise, BCs must compensate for the different amounts of reflected ions and electrons present at the upstream boundary and resize their input distributions to avoid introducing any spurious non-neutral sheaths into the solution. Finally, injection must be performed smoothly to avoid introducing artificial oscillations in the simulation.

6.4.1. Upstream boundary condition and particle injection

Particles are injected through the left boundary with known forward ion and electron distribution functions:

$$f_s^+ = n_s^* \hat{f}_s^+, \tag{6.59}$$

for $s = i, e$, where $\hat{f}_s^+$ is a normalized distribution function and n_s^* is twice the density of injected particles. For the verification cases of Section 6.5, the following two-temperature (parallel semi-Maxwellian and perpendicular Maxwellian) distribution is employed:

$$f_s^+ (z = z_0, v_z > 0, \tilde{\mu}, t) = n_s^* \left(\frac{m_s}{2\pi}\right)^{3/2} (T_{\parallel s}^*)^{-1/2} (T_\perp^*)^{-1} \exp\left(-\frac{m_s v_z^2}{2T_{\parallel s}^*}\right) \exp\left(-\frac{m_s \tilde{\mu} B_0}{T_{\perp s}^*}\right), \quad s = i, e \tag{6.60}$$

where $T_{\parallel s}^*$, $T_{\perp s}^*$ are the parallel and perpendicular temperatures of species s and $B_0 = B(z_0)$.

As in other PIC codes [171], to model the injection particle flux as accurately as possible, we sample the component of the velocity normal to the boundary from the flux distribution $g_s^+ \propto v_z \hat{f}_s^+$ instead of f_s^+. The cumulative distribution function for the Maxwellian flux can be readily inverted in closed form resulting in a simple sampling procedure. Injected particles must be distributed not only in velocity space, but also in time, to avoid particle lumping and flux discontinuities caused by a finite integration Δt. An implicit PIC implementation offers a natural procedure for particle injection, even if Δt can be up to two orders of magnitude larger than in classic explicit PIC methods. A uniformly distributed random integration time step $\Delta t_e \in [0, \Delta t]$ is assigned to each injected particle. The injected particles are then pushed as described in Sec. 6.3 in that time step, including the subcycling procedure and their contribution to the moments weighted as for any other particle. This injection procedure is remarkably simple and inexpensive compared to other techniques proposed for second order-accurate injection in explicit algorithms [171].

In a MN, some of the injected particles are reflected back in the domain toward the upstream boundary. As the amount of reflected ions and electrons differs in general, fixing both n_i^* and n_e^* a priori can lead to the formation of artificial non-neutral layers at injection, because the integrated density of ions and electrons (traveling forward and backward) may not match. Instead, n_e^* and/or n_i^* need to be computed as part of the solution to ensure quasineutrality there. In the present implementation, the injection density of forward ions n_i^* is fixed to produce a prescribed ion current I_i, but the injection density of forward electrons n_e^*, which adapt faster to changes in the electrostatic potential due to their larger mobility, is dynamically varied in time according to a simple heuristic proportional control law with gain G_1, i.e. $\Delta n_e^* = G_1 \rho_{i=0}$, where the charge density $\rho_{i=0}$ is weighted at the center of the first cell and accounts for both newly injected and reflected particles. Other control strategies have been used successfully in previous MN studies [45], [145], [157].

To determine the electric field at the first cell face, $E_{\xi,1/2}$, the potential ϕ_0 on a ghost cell $i = 0$ to the left of the domain is needed. A homogeneous Dirichlet condition is imposed for the potential for ϕ_0. Additionally, to update the electrostatic potential at ϕ_1, we need to calculate the electric current density $(J j^\xi)_{1/2}$. This can be found by weighing as in any other cell face and then multiplying by two to estimate the contribution of particles outside of the domain. Alternatively, we may set $(J j^\xi)_{1/2} = 0$, to match the value of a current-free plasma expansion in steady state. Both approaches work and yield the same result, but the latter was seen to provide superior numerical performance and is used in this work.

6.4.2. Dynamic downstream open boundary

For practical finite domain sizes, part of the potential drop to infinity occurs beyond the downstream boundary of the domain. This means that a fraction of electrons traversing this boundary are reflected back outside of the domain and eventually return to it. Observe that this does not occur for ions because the decreasing potential further accelerates them to infinity.

Following a similar approach to that in [157], we sort the electrons that reach the end of the domain ($i = n_z$) according to their kinetic energies. Those with a kinetic energy over charge lower than the remaining potential fall to infinity, $\Delta\phi_\infty = \phi_{i=n_z} - \phi_\infty$, are reflected back, while the rest are removed from the simulation. However, rather than determining ϕ_∞ from the current-free condition $j_z = 0$ as in [157], we introduce a second control law aimed at offsetting the lack of neutrality in the last cell of the domain $\Delta\phi_\infty = G_2 \rho_{i=n_z}$, where $\rho_{i=n_z}$ is the charge density in the last cell of the domain. The condition $j_z = 0$ (or any other given value of the current density in the MN) is instead implemented through the BC for the electric field. We begin by integrating (6.22) in ξ to find:

$$J^B(z)\left(\epsilon_0 \frac{\partial E_z}{\partial t} + j_z\right) = C(t), \tag{6.61}$$

where we recall that $E_z = E_\xi / J_\xi$ and $j_z = J_\xi j^\xi$. The constant $C(t)$ might depend on time but does not depend on position. However, assuming downstream ambipolarity, i.e. $j_z = 0$ gives $C(t) = 0$ for all t. Taking time-centered finite differences,

$$E^{n+1}_{z,n_z+1/2} = E^n_{z,n_z+1/2} - (\Delta t/\epsilon_0) j^{n+1/2}_{z,n_z+1/2}. \tag{6.62}$$

The new electric field provides an inhomogeneous Neumann boundary condition for the electrostatic potential solver, consistent with the global-current free condition in steady state. The proposed approach eliminates the need to prescribe a downstream potential and the subsequent formation of a non-neutral layer as in [45], and allows computing the electric field at the last node self-consistently rather than imposing $E_{z,n_z+1/2} = 0$ as in [157].

Care is needed for the evaluation of the current density in the last cell face $(Jj^{\xi})_{n_z+1/2}$. Like on the upstream boundary, regular weighing followed by multiplication times two can be used to estimate the contribution of particles beyond the domain. Alternatively, the charge-conservation equation, Eq. (6.53), can be used to determine $(Jj^{\xi})_{n_z+1/2}$ from the already-available internal current density $(Jj^{\xi})_{n_z-1/2}$, and the charge densities $(J\rho^{n})_{n_z}$ and $(J\rho^{n+1})_{n_z}$ accumulated with a zeroth-order spline (i.e., adding the charge of all particles in the cell and dividing by its volume). Both approaches were tested and found to be equivalent; however, the latter offered slightly better numerical performance and is used in this work.

6.5. Algorithm verification

In this section, we present three different verification cases. First, the conservation properties of the implicit PIC algorithm (6.3.4) after the addition of the new segment mover, the paraxial geometry and the magnetic mirror force are demonstrated in an academic periodic magnetic mirror study case. Afterward, we test the fractional injection scheme (6.4.1) with a finite (non-periodic) uniform plasma configuration in which the injection plays the role of replenishing the natural outflow of particles through the boundaries. Finally, we put together all pieces and add the new dynamic downstream boundary condition (Sec. 6.4) to study a magnetic nozzle and compare it with the results in the literature.

6.5.1. Periodic magnetic mirror

To demonstrate strict conservation properties, we consider a periodic magnetic mirror, where the background magnetic field has a throat (maximum B) located at the boundaries of the domain,

$$B = B_0\left(1 + \frac{R-1}{R+1}\cos\left(\frac{2\pi z}{L}\right)\right), \tag{6.63}$$

where $R = B_{max}/B_{min} = 3$ is the mirror ratio, $L = 2\pi$ and $z \in [0, L]$.

We consider singly charged ions and electrons with $m_i/m_e = 1$ and equal temperatures, and a non-uniform mesh map with $n_z = 64$ and cell size proportional to $B(z)$ (i.e., $J_\xi = B(z)$), and $N_p = 1000$ particles per cell per species. For the validation case, the plasma is homogeneous, with uniform density (equal to unity in normalized units) and isotropic Maxwellian distributions, i.e., Eq. (6.60) with $T^*_{s,\parallel} = T^*_{s,\perp} = T^*_s$, and a flat electrostatic potential ϕ. The initial condition is an exact analytical stable equilibrium.

Since this initial condition is a stable equilibrium, any difference with respect to the analytical solution can be attributed to ordinary statistical PIC noise. After running the simulation for 200 $(\omega^*_{pe})^{-1}$, we do not observe any secular trend in the simulation, nor instability. The average density in the nominal simulation matches the expected analytical value of unity, and its standard deviation

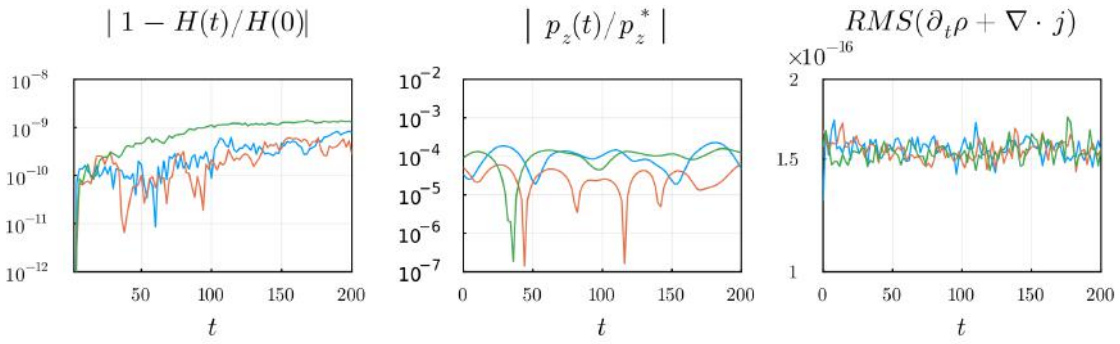

Figure 6.2: Self-consistent periodic magnetic mirror solution for different parallel-to-perpendicular temperature ratios: $T_\perp^* = T_\parallel^*$ (green), $T_\perp^* = 2T_\parallel^*$ (orange), and $T_\perp^* = T_\parallel^*/2$ (blue). From left to right: conservation of global energy, total momentum, and root mean square of the local charge residual.

$\sigma[n_e]$ scales as $1/\sqrt{N_p}$, as expected from the standard Monte Carlo error scaling: for instance, we find $\sigma = 2.7\%$ for $N_p = 1000$, and $\sigma = 1.9\%$ for $N_p = 2000$, i.e., a decrease of $1/\sqrt{2}$. For this example, we do not observe any noticeable dependence of the noise level with Δt when varied from 1 to 10 $(\omega_{pe}^*)^{-1}$.

Figure 6.2 shows the evolution of the relative error in the conservation of global energy, total axial momentum, and spatial root mean square of the residual in the charge conservation equation. The instantaneous total energy of the system is the sum of the kinetic energy of each particle and the electric field energy as defined in Eq. (6.49), while the total axial momentum of the plasma is given by:

$$p_z = \sum_s m_s \sum_p w_p v_{z,p,s}. \tag{6.64}$$

The relative error in energy conservation remains below 10^{-9}, which is considerably lower than the upper bound imposed by the relative tolerance of the non-linear solver (10^{-6}). In the presence of an externally applied magnetic field, the momentum of individual particles is not generally conserved (indeed, this is the contactless thrust generation mechanism in a MN). Nevertheless, the symmetry of this periodic configuration results in cancelation of the particle contributions to axial momentum, so that $p_z(t) = 0\ \forall t$. The error in total axial momentum conservation, normalized with $p_z^* = \sum_s \sqrt{T_s^* m_s} \sum w_p$, is kept acceptably low and does not present secular trends. To that end, we must mention the role of the substep time step estimator (Sec. 6.3.2) in keeping the truncation error of the Crank Nicolson mover within the defined tolerance ($\mathcal{E}_{\Delta\tau} = 10^{-3}$). Finally, the root mean square (RMS) of the residual of the local charge conservation equation (computed as indicated in Sec. 6.3.4) computed over all cells shows errors at machine accuracy ($\sim 10^{-16}$).

Adding temperature anisotropy to f_s modifies the steady-state density profiles in the mirror. Figure 6.3 depicts sample results, with $T_\perp^*/T_\parallel^* > 1$ resulting in a density profile that peaks at the minimum of the magnetic field B (as more particles are trapped by the magnetic mirror), and $T_\perp^*/T_\parallel^* < 1$ leading to the the opposite behavior. In all cases, conservation properties behave similarly to the isotropic temperature case, as evidenced by Figure 6.2.

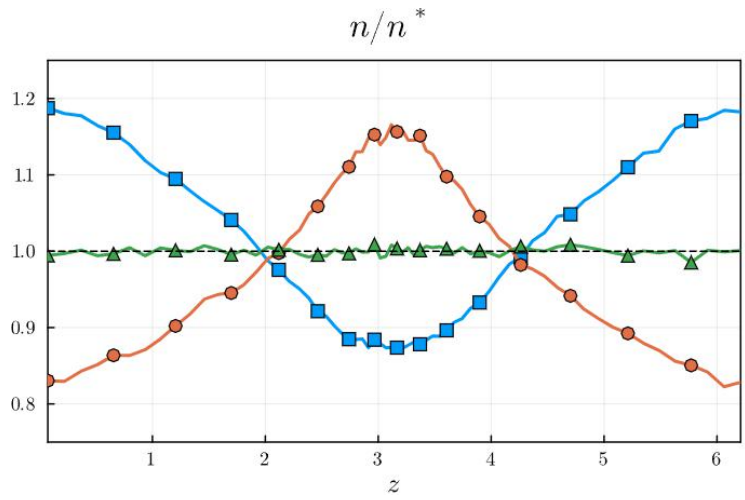

Figure 6.3: Steady-state plasma density over initial plasma density for different parallel-to-perpendicular temperature ratios: $T_\perp^* = T_\parallel^*$ (▲), $T_\perp^* = 2T_\parallel^*$ (●), and $T_\perp^* = T_\parallel^*/2$ (■). The analytical solution for $T_\perp^* = T_\parallel^*$ is indicated by a black dashed line.

6.5.2. Particle injection in a uniform plasma

We next verify the particle injection BC without the generation of artificial electrostatic oscillations or particle lumping. We consider a uniform Maxwellian plasma at rest in a uniform B field. To compensate for particles leaving the domain, the injection BC is applied at the two ends of the domain, where a semi-Maxwellian distribution with the same parameters as the initial distribution is prescribed for both ions i and electrons e. The quasineutrality controls at both ends are not active in this test case ($G_1 = G_2 = 0$). As before, we set isotropic and equal temperatures for both species and select a mass ratio $m_i = m_e = 1$. The same non-uniform grid as in the mirror case is used ($n_z = 64$), with the same number of particles per cell and species, $N_p = 1000$. Periodic BCs are applied to the electrostatic potential. The initial condition is again a stable exact equilibrium. Our simulations demonstrate that plasma uniformity is maintained in time within expected particle noise levels. No boundary layers are observed, demonstrating the effectiveness of the boundary injection treatment.

This setup is in fact ideally suited to study the impact of timestep on particle noise. The standard deviation $\sigma(n_e)$ of the plasma density with respect to the uniform value n_e^* across all time steps and cells as a function of timestep is shown in Figure 6.4. The noise level is again consistent with Monte Carlo estimates ($1/\sqrt{N_p} \sim 3\%$), and shown to decrease slightly with increasing Δt in the range 1 - 5 $(\omega_e^*)^{-1}$. We hypothesize that this behavior is due to the sampling multiplication effect of the orbit averaging of the current density moment weighting in the implicit time-marching scheme, but at any rate its impact is small.

6.5.3. Magnetic nozzle modeling

We simulate next the plasma expansion in a propulsive magnetic nozzle. We aim to verify the interoperation of all elements of the algorithm, and in particular, the dynamic downstream boundary condition. We compare our simulation results with the nominal MN simulation of [45]. That study presents a solution of the fully magnetized plasma flow in a paraxial convergent-divergent mag-

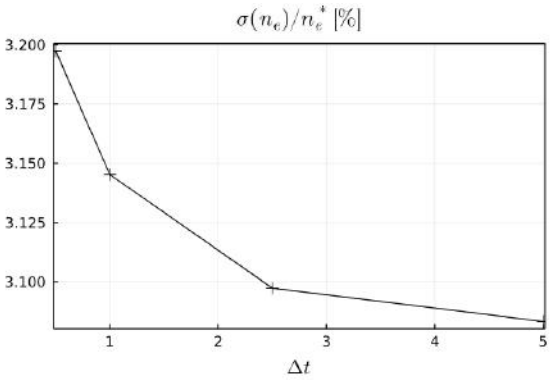

Figure 6.4: Standard deviation of the electron density across all cells and timesteps with respect to the analytical solution ($n_i(z) = n_e(z) = n_e^* \; \forall \; z$) as a function of the implicit timestep size Δt.

netic field, using a time-explicit semi-Lagrangian scheme. Consequently, it provides a suitable benchmark for the comparison and verification of our algorithm.

Simulation setup

Physical and numerical parameters are chosen to mimic the study in Ref. [45], and are as follows. The magnetic topology is generated by a current loop of radius r_L placed at $z = 0$,

$$\boldsymbol{B}(z) = B_0 \frac{r_L^3}{\left(r_L^2 + z^2\right)^{3/2}} \mathbf{1}_z. \tag{6.65}$$

The domain extends from $z = -0.5 r_L$ to $z = 16 r_L$, where it is terminated by a dielectric wall. Distribution functions for forward electrons and ions are prescribed at the domain entrance as in equation (6.60), with $T^*_{\parallel e} = T^*_{\perp e} = T^*_{\parallel i} = T^*_{\perp i} \equiv T^*$. To force charge neutrality at injection, the study in the reference adjusted n_i^* depending on the number of reflected electrons, while keeping n_e^* fixed. In our study, we instead vary n_e^* and fix the ion injection current, which we consider to be more physical; see Section 6.4.1. A reduced mass ratio $m_i/m_e = 100$ is used in the reference, which we also employ for the purposes of comparison. The normalized Debye length based on n_e^* and T^* is $\lambda_D^*/r_L = 0.02$, which is quite large in relation to devices of practical interest. In [45] a non-uniform phase-space grid with 1501 nodes in z, 77 in $v_\parallel$ and 101 in μ; and a time step of 0.03 $(\omega_{pe})^{-1}$, is used. In our simulations, we use coarser non-uniform spatial grids. The nominal grid is shown in Figure 6.5.

In [45], both boundaries are free-loss surfaces for outgoing particles. Dirichlet BCs are applied on the electrostatic potential at the upstream and downstream boundaries, with the downstream potential value adjusted iteratively after convergence to steady state to achieve a current-free expansion, in particular they find $I_i = -I_e \approx 0.074 e n_e^* \sqrt{T_e^*/m_e}$. Instead, our BCs are those described in section 6.4. To favor the comparison of the reference, we consider to two nominal simulation cases:

A **Dielectric downstream wall**: This simulation reproduces the physical setup of the simulation in [45], described above. To model the absorbing dielectric wall, the dynamic downstream electron reflection control is turned off, and all electrons reaching the end of the

domain are removed, while the current-free condition on the electric field of section 6.4.2 is maintained. As a consequence, a non-neutral layer forms downstream as in [45]. The comparison with [45] and [145] allows us to verify all elements of the implicit algorithm, except for the electron reflection control.

B **Expansion to infinity**: By activating the dynamic downstream electron reflection control, we simulate the expansion of the plasma to infinity while avoiding the formation of any non-neutral layers.

Cases A and B use the nominal grid of figure 6.5. We will also consider refined versions of cases A and B (i.e., with smaller time step, finer grid, larger number of particles, and tighter tolerances), which are identified as cases AF, BF, to provide an appropriate baseline for error estimation and test the convergence of our results. The specific numerical parameters used in all simulations are reported in Table 6.1. The only setup difference between A and B is the activation of the downstream electron reflection control ($G_{2,B} \neq 0$), allowing the simulation of an expansion to infinity. Lastly, we will also present two variants of simulation case B, identical in all aspects to it except that they use a hydrogen plasma (case BH) and a xenon plasma (case BXe), to illustrate the use of realistic ion-to-electron mass ratios m_i/m_e.

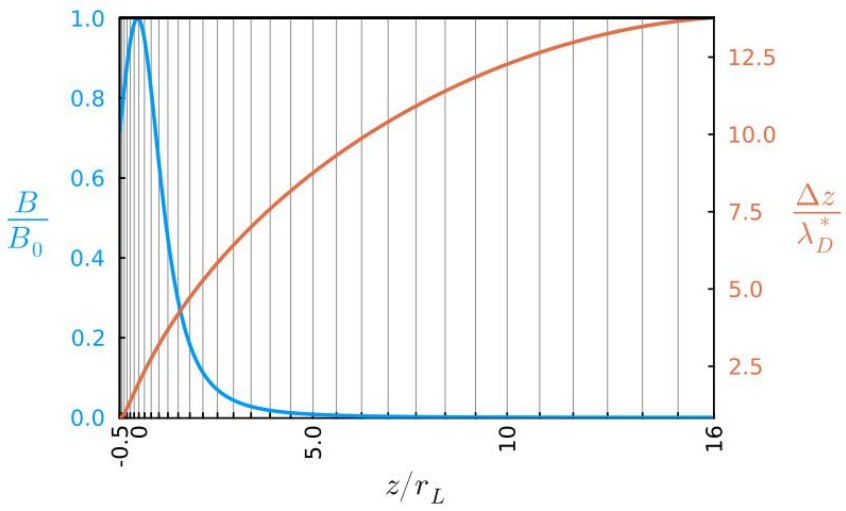

Figure 6.5: Simulation domain for the MN verification case: Magnetic field strength, grid and cell spacing for the nominal case.

Transient plume expansion

Figure 6.6 shows four snapshots of the evolution of the electrostatic potential $e\phi/T_e^*$ and the charge imbalance $(n_i - n_e)/(n_i + n_e)$ in the domain for simulations A and B. In the initial stages [$t = 500\ (\omega_{pe}^*)^{-1}$], the lighter electrons rush downstream ahead of the heavier ions, creating a expansion front with negative charge followed by positive charge. During the transient plume expansion, electrons bouncing off the moving expansion front, with its sharp potential drop, lose mechanical energy to the time-varying field. This promotes the formation of a trapped population of electrons [45], [102], [145], discussed later in this study.

Both simulations follow a similar response until the electron/ion expansion front reaches the end of the domain. Around $t = 2000\ (\omega_{pe}^*)^{-1}$, the electron front has left the domain, while

Table 6.1: Nominal Simulation Parameters. The minimum of N_p occurs at the entrance (we observe about a four-fold increase in N_p at the exit for our non-uniform grid, Figure 6.5).

Numerical Parameter	Nominal (A and B)	Fine (AF and BF)
Number of cells n_z	128	256
Cell length at entrance	1.5 λ_D^*	0.75 λ_D^*
Cell length at exit	12.5 λ_D^*	6.25 λ_D^*
Integration time-step Δt	5.0 $(\omega_{pe}^*)^{-1}$	2.5 $(\omega_{pe}^*)^{-1}$
Simulation time	12500 $(\omega_{pe}^*)^{-1}$	12500 $(\omega_{pe}^*)^{-1}$
Minimum particles/cell steady state $N_{pe} \approx N_{pi}$	~ 1000	~ 2000
Total particles at steady state	$\sim 6 \cdot 10^5$	$\sim 2.4 \cdot 10^6$
JFNK solver tolerance	10^{-4}	10^{-6}
Maximum substep estimator truncation error $\mathcal{E}_{\Delta\tau}$	10^{-3}	10^{-5}
Injection quasineutrality control gain G_1	0.5	0.125
Downstream electron reflection control gain G_2	0.0 (A) 0.025 (B)	0.0 (AF) 0.0125 (BF)

the ion front is still traveling downstream, resulting in significant charge separation downstream. Thereafter, the two simulations diverge. Around $t = 3500\ (\omega_{pe}^*)^{-1}$, a non-neutral thick sheath has begun to form in simulation A, whereas non-neutrality has started to vanish in simulation B owing to the downstream dynamic electron control, which gradually adjusts the value of the electrostatic potential downstream to promote quasineutrality in the last cell. Finally, a steady-state sheath forms in simulation A, and a smooth, quasineutral steady-state solution develops in simulation B, as illustrated for $t = 10000\ (\omega_{pe}^*)^{-1}$.

For simulation B, the duration of the transition to quasineutrality is governed by the reflection control parameters (downstream control gain G_2). Figure 6.7 shows the evolution of the potential at the last node of the grid, $\phi_{i=n_z}$, and at infinity, ϕ_∞, for different control gains G_2. As can be observed, once particles start to reach the downstream boundary, ϕ_∞ quickly stabilizes around its asymptotic value, which is independent of the gain G_2 chosen. This independence is expected, as ϕ_∞ controls the net electron current in the MN, and therefore the global current-free condition determines ϕ_∞ as a function of ion current and the thermal electron speed at injection [145]. The potential at the last node, $\phi_{i=n_z}$, also tends to an asymptotic value that is independent of G_2, but its time evolution is sensitive to this parameter, with lower values of G_2 corresponding to longer transients. For this simulation case, gains around $G_2 \simeq 0.1$ enable reaching the steady-state value of $\phi_{i=n_z}$ roughly at the same time as the steady-state value ϕ_∞, and therefore allow for fast convergence to the final solution. The maximum value of G_2 is limited by the appearance of instabilities in the solution, which occur when the characteristic control frequency becomes comparable to the other frequencies of the problem.

Varying the normalized Debye length λ_D^*/r_L while keeping all other parameters unchanged (not shown) proves that λ_D^*/r_L influences the size of the non-neutral layer downstream in simulation A, but plays a negligible role in simulation B, because the full expansion is quasineutral in the latter.

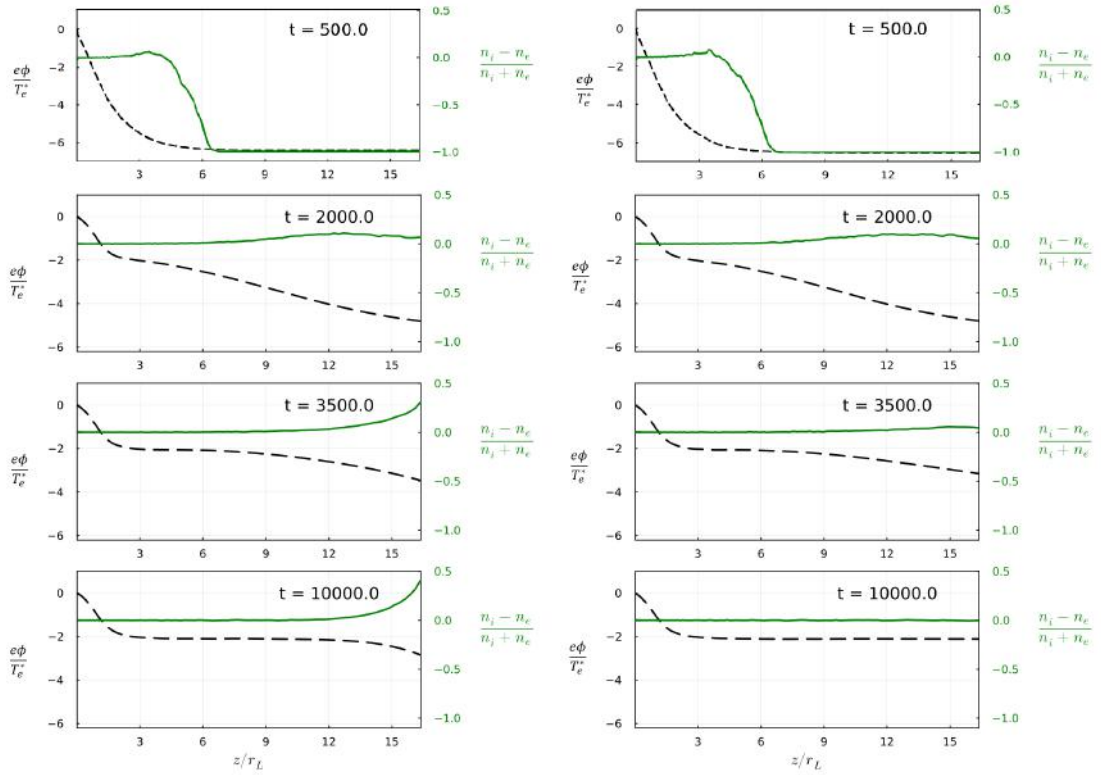

Figure 6.6: Evolution of the potential for simulation cases A (left column) and B (right column). Dashed line (left axis) is the potential ϕ, solid line (right axis) is a measure of quasineutrality.

Steady-state solution

Figure 6.8 (a) shows the steady state results of simulations A and B. Results are averaged over time using a moving mean with a window $\sim 500\ (\omega_{pe}^*)^{-1}$ for smoother results. The decreasing electrostatic potential ϕ reflects electrons upstream and accelerates ions downstream, helping to convert the thermal energy of electrons into the directed kinetic energy of ions. The first part of the expansion is essentially identical for simulations A and B: most of the potential drop occurs here, and between the throat $z = 0$ (where $e(\phi_0 - \phi_t)/T_e^* \approx 0.4$) and $z = 2r_L$ we find the region of maximum acceleration, with an almost constant electric field. After this point, the potential transitions to an essentially flat profile around $z = 3r_L$, with $e(\phi_0 - \phi)/T_e^* \approx 2.1$. Differences between simulations A and B arise in the last part of the expansion, where simulation A displays the wide sheath before the dielectric wall, whereas simulation B continues its slow decrease to infinity. It should be noted that the wall potential in simulation A and the potential at infinity for simulation B are virtually identical ($\approx 2.9\ T_e^*/e$).

The ion density n_i is shown in Fig. 6.8(b) from the throat to the end of the domain. After a region of rapid acceleration, driven by the strong electric field near the throat, the ion velocity approaches an asymptotic value and the ion density becomes nearly proportional to B, in agreement with the one-dimensional steady-state continuity equation $n_i u_i / B = const$. The ion density exhibits the same trend in the two simulations A and B, with negligible differences. The electron density n_e, not shown here, closely follows the ion density everywhere except in the downstream sheath in simulation A.

Figures 6.8(c) and (d) show $T_{e\parallel}$ and $T_{i\parallel}$, while panels (e) and (f) present the ratios $T_{e\perp}/B$ and

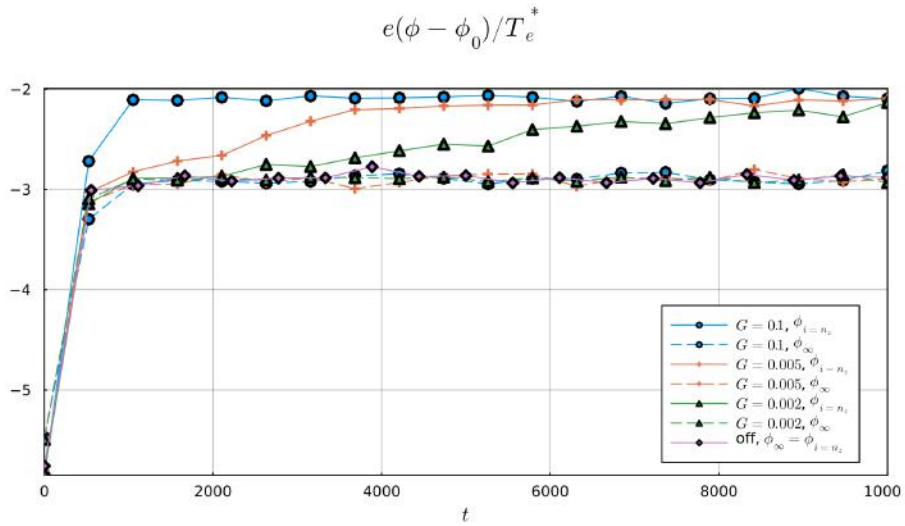

Figure 6.7: Potential drop at infinity $e(\phi_\infty - \phi_0)/T_e^*$ (dashed) and at the last cell of the domain $e(\phi_{i=n_z} - \phi_0)/T_e^*$ (solid) for different electron reflection control gains.

$T_{i\perp}/B$. This presentation choice makes manifest that in an expansion to infinity, the parallel temperatures become asymptotically constant, while the perpendicular temperatures vanish as $O(B)$ [172]. Indeed, as can be observed, the plotted quantities are quite uniform in most of the domain, except in the initial part of the expansion, where rapid changes occur. Once again, simulations A and B display a near-identical behavior except in the last part of the domain, where simulation A is affected by the formation of the thick sheath downstream.

Figure 6.9 shows the steady-state densities of free, reflected, and trapped electrons as defined in [102] and in Section 6.2, for simulations A and B. As the population of trapped electrons is disconnected from the plasma source, its distribution depends on the transient plume expansion, wherein some electrons bouncing off the expansion front lose enough mechanical energy to become trapped. Our investigations shows that the fraction of trapped electrons is essentially independent of the control gain G_2 in simulation B, which determines the rate at which the quasineutral steady-state solution is reached. In the initial part of the expansion, reflected electrons account for roughly 90% of the total, while the number of trapped electrons is zero. The fractions then stabilize around 60% and 25%, respectively. Free electrons constitute roughly 10–15% of the total throughout the expansion. Simulations A and B show a nearly identical response in terms of electron population fractions, except —once again— downstream, where the thick sheath in simulation A reduces the fraction of reflected and trapped electrons to zero at the end of the domain, and all electrons become free. Arguably, this same transition to free electrons must also occur in simulation B in the expansion to infinity, albeit the scale at which this takes place is too large for practical interest.

Finally, figure 6.10 displays the steady state plasma expansion to infinity for H^+ and Xe^+ plasmas (simulation cases BH, BXe). It is seen that increasing m_i/m_e results in a larger potential fall to infinity and a slightly higher electron temperature, consistent with the findings of Ref. [44].

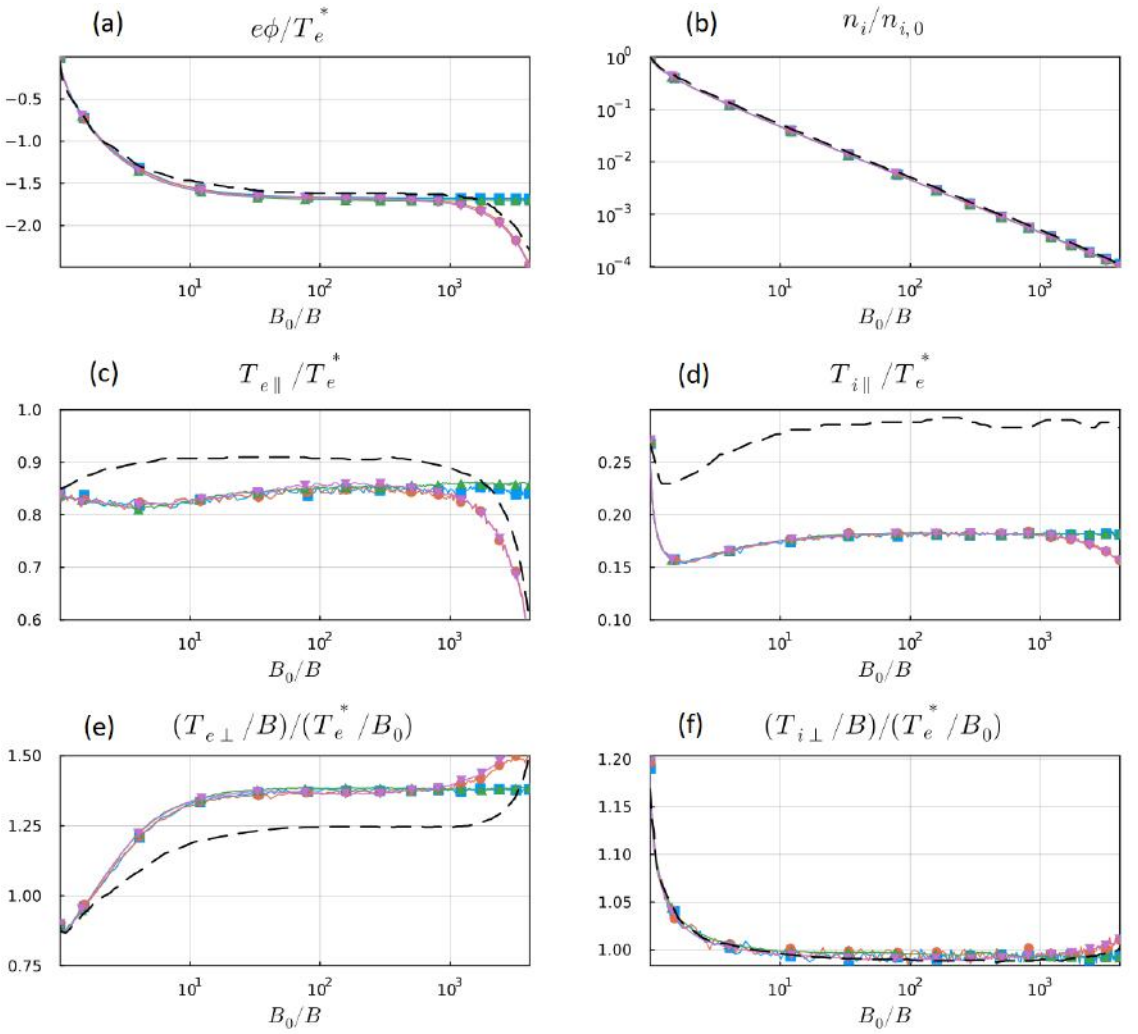

Figure 6.8: Steady-state potential (a) ion density (b), electron (c) and ion (d) parallel temperatures, and electron (e) and ion (f) perpendicular temperatures for nominal simulations A (●), B (■) and refined simulations *AF* (▼) and *BF* (▲). The black dashed lines correspond to the results of Sanchez et al. [45].

Verification

We verify our MN solution in two ways. Firstly, we compare the steady state A and B simulation results against the refined simulations AF and BF (Table 6.1) in figure 6.8. It is visually apparent that the differences are small, with $T_{\|e}$ showing the largest differences, below 3% in the central part of the expansion for A and the downstream boundary for B, where electrons are reflected. We therefore conclude that the A and B simulation results are converged.

Secondly, we compare our simulation A results against the recent results documented in Ref. [45]. This comparison is also shown in figure 6.8. The normalized electrostatic potential $e\phi/T_e^*$ in figure 6.8(a) demonstrates excellent agreement upstream. However, a difference of $\approx 0.25\ T_e^*/e$ soon develops that continues all the way to the wall. This difference is noteworthy, because the final value of the potential governs the current of free electrons, which must coincide with the ion current as dictated by the current-free condition in the MN, as discussed above. This condition is well satisfied in our conservative simulations.

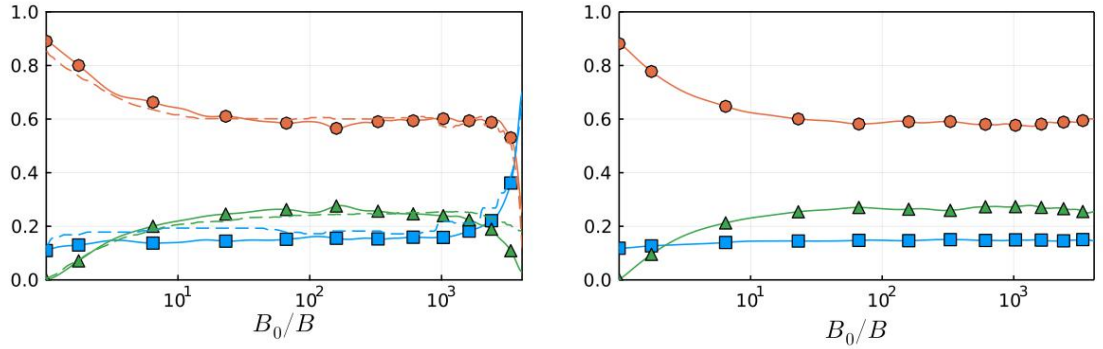

(a) Simulation A

(b) Simulation B

Figure 6.9: Fraction of free n_{ef}/n_e (■), reflected n_{er}/n_e (●) and trapped n_{et}/n_e (▲) in simulations A (left) and B (right). The dashed lines correspond to the results of Sanchez et al. [45].

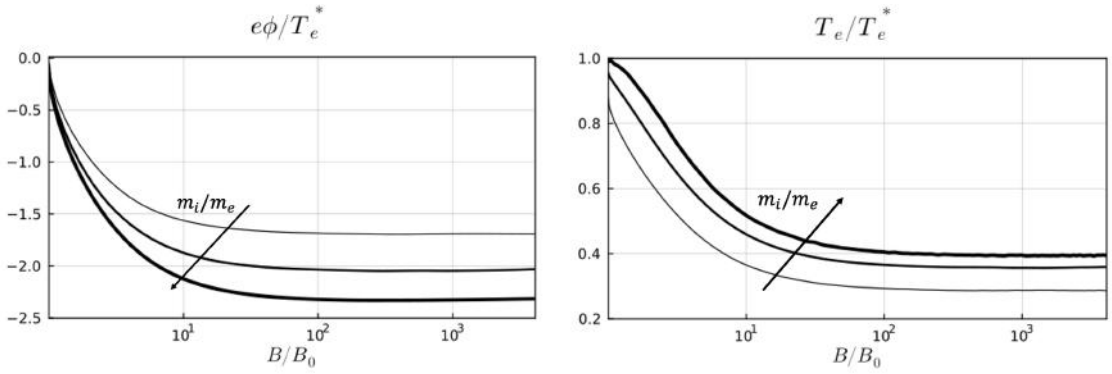

Figure 6.10: Steady-state potential (left) and total temperature $T_e = (2T_{\perp e} + T_{\parallel e})/3$ (right) for case B ($m_i/m_e = 100$), H^+ ($m_i/m_e = 1836$), and Xe^+ ($m_i/m_e \sim 240000$).

Relatedly, as shown in figure 6.9, the fractions of free, reflected, and trapped electrons, while showing overall good agreement with those in Ref. [45], display small but significant differences in the fraction of free electrons, which is consistently larger in the data from [45]. This larger fraction is consistent with a smaller total potential drop in that study.

These discrepancies in ϕ and the mismatch in the fraction of free electrons explain the the rest of plasma variables shown in figure 6.8: While the ion density coincides well with the verification data upstream, the latter is consistently about 5% higher downstream. The comparison of electron and ion temperatures shows that, although the qualitative trends and behaviors remain similar, there are apparent differences in the electron perpendicular and parallel temperatures and in the ion parallel temperature. Plasma density, but especially electron and ion temperatures, are particularly sensitive to the composition of the electron population [145].

Further comparison against the work of Merino et al. [44], [145] shows that the total potential drop in our simulations is within 0.05 T_e^*/e of those steady-state results, even if they do not simulate the region before the magnetic throat. The smaller discrepancy in this key quantity, together with the conservation properties of the algorithm and the good convergence of our simulations upon numerical parameter variation, supports the verification of our simulations.

Algorithm performance

Several numerical parameters (timestep size, number of particle per cell, and number of cells) have been varied in the nozzle simulation to study their impact on the total CPU wall-clock time. The results are shown in Figure 6.11. Wall-clock times were obtained with our Julia code, using 20 threads on an Intel Xeon (R) 4316 computer. No MPI parallelization was used in this 1D version of the implicit algorithm.

In terms of the implicit timestep size (figure 6.11-left), performance is affected by competing effects. On the one hand, there is an inverse proportional relationship between Δt and the total number of steps. On the other hand, an increase in Δt may result in an increase in the number of substeps per particle; it may also result in an increase of the number of function evaluations N_{FE} (each requiring a full particle push) as the number of JFNK iterations increases for convergence. As the electrons are the more mobile species, it is mainly the cost associated to the electrons that increases with Δt. The balance between these effects determines the wall-clock time speedup as a function of Δt. As in earlier implicit PIC studies [168], we observe computational advantage for moderate implicit timesteps, but eventual saturation when Δt is increased beyond $\Delta t > 10(\omega_{pe})^{-1}$ This is expected, as for sufficiently large Δt, the cost is completely dominated by the particle orbit integration, which scales linearly with the timestep owing to the need to resolve the orbit's physical features. Therefore, in an electrostatic context, employing much larger timesteps is not advantageous from a performance standpoint (see performance discussion below).

Incidentally, this implies that, for sufficiently large mass ratios (such as in the simulations BH and BXe of figure 6.10), the wall time to steady state of the proposed algorithm scales similarly as other PIC algorithms with the square root of the ion-to-electron mass ratio, $\sqrt{m_i/m_e}$, since the Δt must be selected according to the characteristic time of electrons, rather than the residence time of ions. Consistently, the BH and BXe simulation cases, using the same $\Delta t = 5(\omega_{pe})^{-1}$ as in simulation B, take 4 and 48 times more wall time, respectively, to reach steady state. To accelerate the more expensive BXe simulation, we pushed $\Delta t = 10(\omega_{pe})^{-1}$ and halved the number of particles, still achieving results with acceptable noise levels in just 24 times the wall time of simulation B.

In terms of the total number of particles (or the number of particles per cell N_p when the number of cells is kept constant; figure 6.11-center), the CPU wall-clock time scales sublinearly with the number of particles for moderate number of particles, but eventually recovers linear scaling, as expected. The transient sublinear scaling is attributed to the cost contribution of grid-related operations, which are independent of the number of particles.

The most remarkable result is the scaling of the wall-clock time with the number of cells, n_z (figure 6.11-right). In earlier implicit PIC studies employing particle push subcycling [168], it was predicted and observed that the computational complexity scaled as n_z^2. At the root of this behavior is the particle subcycling, and in particular the need for particles to stop at cell faces for charge conservation. The particle mover proposed in this study removes this requirement, decoupling the cost of particle motion from the choice of underlying grid.

The efficiency gain in our approach stems from the fact that a single Picard solve for the CN system (this is the nonlinear iteration on $v_{z,p}^{\nu+1/2}$ and $\xi_p^{\nu+1}$) per full substep (potentially comprising multiple segments and cell crossings) is performed, instead of a Picard solve per segment. To

quantify these gains, we conducted code profiling to determine the cost of all operations within the per-segment loop (lines 10–13 in Algorithm 1), denoted as C_{seg}, and the total cost of a substep for a particle that executes only one segment C_{sub} (lines 3–25, including current accumulation). Profiling revealed that segment operations, accounting for 18% of the C_{sub} (including field scattering), are comparable to other costly parts such as the computation of the residual of the CN system (lines 15–17) and the initial substep timestep estimator (line 3), both located outside the per-segment loop and taking 17% and 14% of C_{sub}, respectively (the current accumulation step, line 23, lies outside the Picard loop, and has negligible cost, $< 5\%$). In previous movers [65], segment crossings directly led to new substeps, making the orbit cost proportional to the number of segments s, $C_{old} = s\, C_{sub}$. However, in our new implementation, there is a fixed cost for operations outside the per-segment loop, and only those within the loop scale with the number of cell crossings:

$$C_{new} = C_{sub} + (s-1)C_{seg} = C_{sub}\left(1 + (s-1)\frac{C_{seg}}{C_{sub}}\right) \approx C_{sub}\left(1 + \frac{(s-1)}{5.5}\right).$$

There results an acceleration potential of:

$$\frac{C_{new}}{C_{old}} = \frac{1}{s} + \frac{(s-1)}{5.5s} \xrightarrow{s\gg 1} \frac{1}{5.5},$$

which is appreciable. Additionally, for $s < C_{sub}/C_{seg} \sim 5.5$, the cost of the mover is only weakly dependent on the number of crossings.

As a result, figure 6.11-right demonstrates an almost perfect linear scaling of the wall-clock time with n_z while keeping the number of particles per cell and Δt constant. This scaling seems quite robust to the natural increase of cell crossings per particle and timestep as n_z increases: for $n_z = 128$, less than 20% of the electrons undergo 1 cell crossing or more in one Δt, whereas for $n_z = 512$, this fraction goes up to 73%. Eventually, for sufficiently large n_z such that the number of substeps $s \propto n_z$, we expect to recover the quadratic scaling $t_{tot} \sim n_z^2$ observed in earlier studies [168]. Meanwhile, the number of substeps per Δt, in average 1.72, remains essentially independent of n_z and the number of cell crossings. Also important for this scaling is the fact that JFNK performance is largely independent of n_z, a consequence of the efficient inversion of the Laplacian operator in 1D.

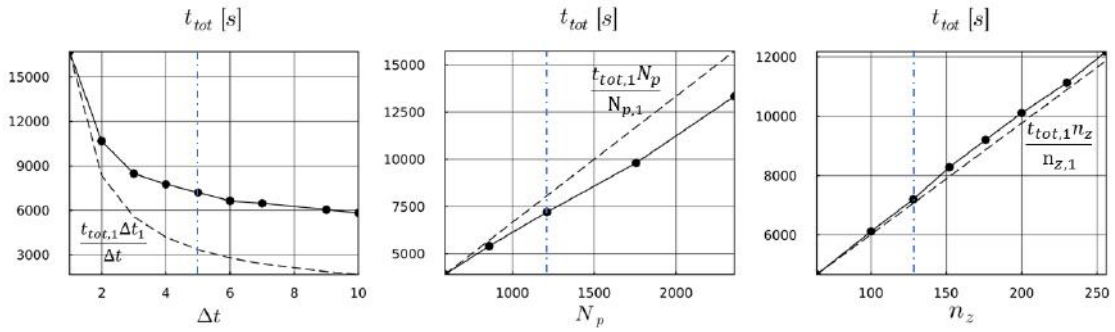

Figure 6.11: Total CPU wall time as a function of Δt (left), the number of particles per cell at steady state N_p (center) and number of cells in the domain with a constant number of particles per cell n_z(right). Reference scaling laws are shown with dashed lines in each plot.

We estimate next the wall-clock speedup of the implicit PIC algorithm vs. explicit PIC using

the back-of-the envelope estimate derived and verified in Ref. [65]:

$$\frac{CPU_e}{CPU_i} \sim \frac{1}{(5\lambda_D/l)^{d+1}} \frac{1}{N_{FE}} \tag{6.66}$$

where l is a characteristic length for the macroscopic fields variation, λ_D is the Debye length, d is the spatial dimension and N_{FE} is the number of non-linear function evaluations, i.e., the sum of the number of Krylov iterations for each of the Newton iterations in a given time step. Typical values of the implicit substep and cell sizes vs. the explicit ones have been taken into account in the speedup estimate above [65]. It is also assumed that a substep in the implicit algorithm has a computational complexity similar to that of an explicit push. As a result, the speedup estimate is independent of the timestep. If we estimate the characteristic length as the distance between the nozzle entrance and its throat, $l \sim 50\lambda_D$, and taking $N_{FE} \sim 14$ from the nominal simulation case B, there results a speedup estimate of ~ 7, which is significant. Larger speedups are expected in higher dimensions and in the electromagnetic case [173]. Note that no correction to this estimate has been made to account for the improved efficiency of the segment-based mover. Consequently, this can be understood as a lower bound for the potential gains of the algorithm. The use of more advanced preconditioners [168] may unlock further performance improvements by decreasing the number of nonlinear iterations, N_{FE}, but this exploration is beyond the scope of this study.

Another useful performance datapoint is the wall-clock-time comparison with the semi- Lagrangian Vlasov code in Ref. [45]. That study employed 1501 cells in z and took approximately 2.5 days on a comparable machine with multithreading [174]. This gives a speedup of $O(30)$ per simulation for comparable or superior accuracy. Roughly, this allows us to perform simulations with the realistic Xenon mass ratio $m_i/m_e = 240000$ at the same cost as that for the former method with $m_i/m_e = 100$.

6.6. Summary

A novel implicit particle-in-cell paraxial model has been proposed, targeting the simulation of magnetic nozzles in electric propulsion systems. The new model has demonstrated exact conservation properties in closed systems, and the ability to employ, stably, much longer timesteps than inverse plasma frequencies and cell sizes much larger than the Debye length. As a result, the model can employ fewer grid cells than an explicit code, which in turn leads to a significant reduction in the total number of macroparticles required for the simulation. The conservation of global energy and local charge is important for the long-term accuracy of the simulation and the taming of temporal [65] and finite-grid [175] instabilities prevalent in explicit PIC models when such resolutions are employed.

Compared to previous implicit PIC studies, our model builds on developments presented in [65] and the generalization to mapped meshes presented in [66], essential to simulate plasma expansions efficiently. The novel and efficient segment-based mover [162], which allows particles to travel several cells in a single substep, was also generalized for the first time to mapped meshes. Other new features that are particularly advantageous for the study of magnetic nozzles are the introduction of the 1D paraxial geometry, the magnetic mirror force term, a new particle injection algorithm, and the dynamic downstream electric field boundary condition that overcomes the

issues in capturing infinite plasma expansions in finite domains found in earlier studies.

The complete model has been verified, first in a periodic magnetic mirror that showcases the action of the mirror force and the conservation properties of the algorithm, and later in a relevant magnetic nozzle study. The MN example was analyzed thoroughly, observing only minor differences with previous literature results and demonstrating convergence and low sensitivity to *ad hoc* control parameters to preserve quasineutrality asymptotically. The algorithm is shown to scale favorably with the implicit timestep (i.e., larger timesteps lead to faster simulation times), and linearly (i.e., optimally) with both the number of particles and the number of grid cells in a broad range of resolution parameters.

7. *Conclusions*

7.1. Main takeaways and significance

On the basis of the linearized, cold-plasma, frequency-domain theory, a two-dimensional axisymmetric full-wave model has been developed for the electromagnetic wave propagation and power absorption in electrodeless plasma thruster (EPT) discharges. The new simulation tool, named PWHISTLER, eases the modeling process of electromagnetic phenomena in magnetized plasmas by increasing the simulation speed —from setup to solution and postprocessing— and accuracy. The solver is implemented leveraging the FEniCSx library [85]. It uses the finite element (FE) method to solve the inhomogeneous wave equation in magnetized plasmas in the frequency domain. This method is also advantageous because of its use of unstructured meshes, which allows complex geometries and local refinement strategies. This refinement is crucial for mitigating high-frequency spurious noise near critical resonant and cutoff surfaces. Verification of the code was conducted, performing tests based on the method of manufactured solutions (MMS) and analyzing the effect of mesh refinement on numerical error. Compared to previous solvers, the new tool introduces several noteworthy advances, such as Fourier azimuthal modes for the spectral decomposition and solution of 3D problems in a 2D spatial discretization and waveport boundary conditions.

A previously developed finite difference (FD) code was used to study the propagation and absorption of EM waves in a realistic Helicon Plasma Thruster (HPT) prototype. Although most of the power absorption takes place inside the cylindrical source, the fraction of power taken in by the plasma plume is not negligible. The magnetic nozzle allows the fields to propagate towards the electron-cyclotron resonance (ECR) surface, which is always present downstream. The wavelength and direction of propagation correspond to a helicon wave around the axis of the device. In the outer regions of the plume, the waves have a shorter wavelength and a larger perpendicular component, resembling the Trivelpiece-Gould mode. The ECR surface was demonstrated to concentrate some of the power absorption and is critical in confining the radiation away from the device, as the fields become evanescent beyond it.

The thesis has presented experimental and numerical studies of a cusped HPT. These are enabled by the new capabilities of the PWHISTLER code, which is coupled to the hybrid plasma transport solver HYPHEN. The numerical results successfully align with experimental plasma trends, particularly after adjusting the anomalous collisionality parameters. The model effectively captures a secondary maximum in electron temperature near the downstream Electron Cyclotron Resonance (ECR) surface. Additionally, the code accurately predicts the azimuthal profile of the ion current density up to moderate angles. The study underscores the influence of the magnetic ring cusp within the HPT. This feature shapes the plasma response and divides regions of plasma currents and magnetic thrust inside the source. It is observed that the net magnetic thrust constitutes a substantial portion of the total generated thrust. The study also highlights performance losses, as in other HPTs, primarily as a result of high plasma currents to the walls, leading to significant ion recombination. The ring-cusp design, while reducing losses to the lateral wall, is

countered by a lower electron temperature, which increases excitation losses. This results in lower energy and thrust efficiency. These findings point to potential future modifications in design or operation to optimize the balance between reduced wall losses and increased electron temperature, thereby enhancing thrust efficiency.

Finally, the thesis presented a novel implicit particle-in-cell (PIC) paraxial model designed for magnetic nozzles. The implicit PIC method allows for longer time steps and larger mesh spacing than traditional methods, significantly reducing computational time and resource requirements. Major efficiency gains come from the need for fewer mesh cells and the reduced number of macroparticles. The model ensures long-term accuracy by conserving global energy and local charge, addressing instabilities common in explicit PIC models. The new model builds on previous implicit PIC studies by incorporating features specifically tailored for magnetic nozzle studies. These include the introduction of 1D paraxial geometry, a magnetic mirror force term, an innovative particle injection algorithm, and a dynamic downstream electric field boundary condition. Additionally, it generalizes an efficient segment-based mover [162] to mapped meshes, allowing particles to traverse several cells in a single suborbit. Verification of the model was performed against published data, demonstrating its accuracy and effectiveness in a periodic magnetic mirror and a magnetic nozzle study, showing minor differences from the previous literature and low sensitivity to control parameters. Its favorable scaling with the implicit timestep and with the number of particles and mesh points mark a notable improvement over earlier implementations. This development of this novel code could pave the way for the optimization of new devices and the improvement of understanding of complex physical phenomena in EPT devices, which are currently prohibitively expensive to study with high-dimensional kinetic models.

In summary, this thesis significantly advances the physical understanding and numerical modeling of low-temperature plasma physics for electric propulsion, and in particular for electrodeless plasma thrusters. Together, the aforementioned developments present a comprehensive toolkit for the modeling of EPTs. PWHISTLER's speed and practicality make it ideal for design applications, while the accuracy of the PIC algorithm is valuable for fundamental research. This dual approach enriches the field and addresses diverse modeling needs.

7.2. Future work

With regard to cold-plasma full-wave simulations, there are ongoing efforts to demonstrate the application of PWHISTLER, coupled with the HYPHEN transport solver, to Electron Cyclotron Resonance Thrusters (ECRTs), using the new waveport boundary condition. The numerical capabilities will also be enhanced with the introduction of Perfectly Matched Layer (PML) domain truncation [81] and a possible extension to 3D simulations enabled by the use of iterative solvers and/or advanced computer architectures, e.g. distributed computing. HPT studies shall continue with parametric investigations and optimization of the novel cusped-field magnetic topology.

The main challenge in plasma modeling for electric propulsion, and in particular EPT modeling, is arguably to bridge the gap between the two approaches discussed earlier: mid-fidelity, high-dimensional models that can be executed within a few hours or days on moderately sized computers, and high-fidelity kinetic solvers that, while requiring significantly more computational resources, are needed for capturing various physical phenomena critical to the overall behavior of

the device, in a predicted and validated way. The essence of implicit PIC algorithms is to combine these attributes. They aim to provide affordable, self-consistent, and highly accurate simulations, a capability not offered by current methodologies.

To study essential electromagnetic phenomena coupled to non-linear and kinetic effects in EPTs, the electrostatic algorithm presented in this thesis shall be extended with an electromagnetic solver. To this end, the Darwin approximation [63] for electromagnetic fields will be used. Electromagnetic implicit methods effectively circumvent the limitations set by the CFL (Courant-Friedrichs-Lewy) condition and the local Debye length and provide multiorder-of-magnitude savings compared to explicit EM PIC algorithms [160]. Nevertheless, such methods have not yet been implemented in electric propulsion studies, and there are multiple open research challenges including the development of appropriate boundary conditions and particle collisions.

Realistic thruster simulations also require an increase in the dimensionality of simulation domains. In fact, implicit PIC savings (compared to traditional methods) have been shown to grow significantly with spatial dimensions [173]. This makes them exceptionally suitable for long-term, two- or three-dimensional realistic thruster simulations. The compute speed provided by implicit methods can be further enhanced by employing modern high-performance computing (HPC) techniques, including graphics processing unit (GPU) parallelization and distributed computing. In summary, the generalization of implicit methods, combined with the advent of faster computing technologies, is expected to enable routine kinetic electromagnetic thruster simulations in the midterm.

Even more advanced methods are the implicit asymptotic preserving (AP) PIC algorithms that are currently being developed by several research groups [162], [176]. This scheme is a key breakthrough, allowing for timesteps that substantially exceed the particle gyroperiods. In scenarios where large timesteps are utilized, the algorithm ensures that averaged particle drifts are accurately preserved while also maintaining the capacity to recover detailed particle orbits in cases of shorter timesteps (or longer gyroperiods). A particularly notable aspect of this scheme is its ability to efficiently and seamlessly handle particles transitioning between magnetized and unmagnetized regimes. This dual capability is advantageous for the comprehensive simulation of diverse plasma environments encountered in EPTs.

Model validation is crucial for the electric propulsion community, and further validation campaigns will be conducted incorporating additional experimental data. These efforts aim to demonstrate the effectiveness of the diverse approaches for the study of different types of thrusters and new prototypes.

Bibliography

[1] E. Choueiri, "A critical history of electric propulsion: The first 50 years (1906-1956)," *Journal of Propulsion and Power*, vol. 20, no. 2, pp. 193–203, 2004.

[2] K. Tsiolkovsky, *Reactive Flying Machines*. Moscow: Izdatel'stvo Akademii Nauk SSSR. Foreign Languages Publishing House, 1935.

[3] D. M. Goebel, I. Katz, and I. G. Mikellides, *Fundamentals of electric propulsion*. John Wiley & Sons, 2023.

[4] D. R. Lev, G. D. Emsellem, and A. K. Hallock, "The rise of the electric age for satellite propulsion," *New Space*, vol. 5, no. 1, pp. 4–14, 2017.

[5] E. Ahedo, "Plasmas for space propulsion," *Plasma Physics and Controlled Fusion*, vol. 53, no. 12, p. 124 037, 2011. [Online]. Available: http://stacks.iop.org/0741-3335/53/i=12/a=124037.

[6] F. Diaz and R. Chang, "The VASIMR rocket," *Scientific American*, vol. 283, no. 5, pp. 90–97, 2000.

[7] K. Takahashi, C. Charles, R. Boswell, and A. Ando, "Performance improvement of a permanent magnet helicon plasma thruster," *Journal of Physics D: Applied Physics*, vol. 46, no. 35, p. 352 001, 2013.

[8] S. Shinohara, H. Nishida, T. Tanikawa, T. Hada, I. Funaki, and K. P. Shamrai, "Development of electrodeless plasma thrusters with high-density helicon plasma sources," *IEEE Transactions on Plasma Science*, vol. 42, no. 5, pp. 1245–1254, 2014.

[9] F. Trezzolani, A. Lucca Fabris, D. Pavarin, *et al.*, "Low power radio-frequency plasma thruster developement and testing," in *33th International Electric Propulsion Conference*, ser. IEPC 2013-153, 2013.

[10] J. Navarro-Cavallé, M. Wijnen, P. Fajardo, and E. Ahedo, "Experimental characterization of a 1 kw helicon plasma thruster," *Vacuum*, vol. 149, pp. 69–73, 2018. DOI: 10.1016/j.vacuum.2017.11.036.

[11] T. Lafleur, C. Charles, and R. Boswell, "Characterization of a helicon plasma source in low diverging magnetic fields," *Journal of Physics D: Applied Physics*, vol. 44, p. 055 202, 2011.

[12] D. B. Miller and E. F. Gibbons, "Experiments with an electron cyclotron resonance plasma accelerator," *AIAA Journal*, vol. 2, no. 1, pp. 35–41, Jan. 1964. DOI: 10.2514/3.2210. [Online]. Available: https://doi.org/10.2514/3.2210.

[13] G. Crimi, A. Eckert, and D. Miller, "Microwave driven magnetic plasma accelerator studies (cyclops)," General Electric Company, Space Sciences Laboratory, Missile and Space Division, Tech. Rep., 1967.

[14] J. Sercel, "An experimental and theoretical study of the ECR plasma engine," Ph.D. dissertation, California Institute of Technology, 1993.

[15] J. Jarrige, P. Elias, F. Cannat, and D. Packan, "Characterization of a coaxial ecr plasma thruster," in *44th AIAA Plasmadynamics and Lasers Conference, San Diego*, 2013.

[16] F. Chen and D. Arnush, "Generalized theory of helicon waves. i. normal modes," *Physics of Plasmas*, vol. 4, p. 3411, 1997.

[17] M. R. Inchingolo, M. Merino, and J. Navarro-Cavallé, "Plume characterization of a waveguide ecr thruster," *Journal of Applied Physics*, vol. 133, no. 11, p. 113 304, 2023. DOI: 10.1063/5.0138780.

[18] D. Arnush and F. Chen, "Generalized theory of helicon waves. II. excitation and absorption," *Physics of Plasmas*, vol. 5, pp. 1239–1254, 1998.

[19] T. H. Stix, *Waves in plasmas*. Springer Science & Business Media, 1992.

[20] G. Chen, A. Arefiev, R. Bengtson, B. Breizman, C. Lee, and L. Raja, "Resonant power absorption in helicon plasma sources," *Physics of Plasmas*, vol. 13, p. 123 507, 2006.

[21] F. Chen, "Permanent magnet helicon source for ion propulsion," *Plasma Science, IEEE Transactions on*, vol. 36, no. 5, pp. 2095–2110, 2008.

[22] D. Melazzi and V. Lancellotti, "ADAMANT: A surface and volume integral-equation solver for the analysis and design of helicon plasma sources," *Computer Physics Communications*, vol. 185, no. 7, pp. 1914–1925, 2014.

[23] B. Tian, E. Ahedo, and J. Navarro, "Investigation of plasma-wave interaction in helicon antenna thrusters," in *50th AIAA/ASME/SAE/ASEE Joint Propulsion Conference*, 2014.

[24] Y. Mouzouris and J. E. Scharer, "Wave propagation and absorption simulations for helicon sources," *Physics of Plasmas*, vol. 5, no. 12, pp. 4253–4261, 1998.

[25] B. Tian, M. Merino, and E. Ahedo, "Two-dimensional plasma-wave interaction in an helicon plasma thruster with magnetic nozzle," *Plasma Sources Science and Technology*, vol. 27, no. 11, p. 114 003, 2018. DOI: 10.1088/1361-6595/aaec32.

[26] P. Jiménez, M. Merino, and E. Ahedo, "Wave propagation and absorption in a helicon plasma thruster source and its plume," *Plasma Sources Science and Technology*, vol. 31, no. 4, p. 045 009, 2022. DOI: 10.1088/1361-6595/ac5ecd.

[27] Á. Sánchez Villar, "Modeling the plasma discharge in an electron-cyclotron-resonance thruster," eng, Ph.D. dissertation, Universidad Carlos III de Madrid, Leganés, Spain, 2022.

[28] E. Ahedo, "Plasma dynamics in a helicon thruster," in *Progress in Propulsion Physics*, ser. EUCASS Advances in Aerospace Sciences, L. T. DeLuca, C. Bonnal, O. J. Haidn, and S. M. Frolov, Eds., vol. IV, Torus Press, 2013, ch. 3, pp. 337–354.

[29] C. Charles and R. Boswell, "Current-free double-layer formation in a high-density helicon discharge," *Applied Physics Letters*, vol. 82, no. 9, pp. 1356–1358, 2003.

[30] A. Fruchtman, G. Makrinich, and J. Ashkenazy, "Two-dimensional equilibrium of a low temperature magnetized plasma," *Plasma Sources Science and Technology*, vol. 14, pp. 152–167, 2005. DOI: 10.1088/0963-0252/14/1/017.

[31] E. Ahedo and J. Navarro-Cavallé, "Helicon thruster plasma modeling: Two-dimensional fluid-dynamics and propulsive performances," *Physics of Plasmas*, vol. 20, no. 4, p. 043 512, 2013. DOI: 10.1063/1.4798409.

[32] E. Ahedo and M. Merino, "Two-dimensional supersonic plasma acceleration in a magnetic nozzle," *Physics of Plasmas*, vol. 17, no. 7, p. 073 501, 2010. DOI: 10.1063/1.3442736.

[33] I. Mikellides and I. Katz, "Numerical simulations of Hall-effect plasma accelerators on a magnetic-field-aligned mesh," *Physical Review E*, vol. 86, no. 4, p. 046 703, 2012.

[34] A. L. Ortega, I. G. Mikellides, and V. H. Chaplin, "Numerical simulations for the assessment of erosion in the 12.5-kw hall effect rocket with magnetic shielding (hermes)," in *35th International Electric Propulsion Conference, Atlanta, GA, IEPC-2017-154*, 2017.

[35] M. Merino, D. García-Lahuerta, and E. Ahedo, "Plasma acceleration in a magnetic arch," *Plasma Sources Science and Technology*, vol. 32, no. 6, p. 065 005, Jun. 2023. DOI: 10.1088/1361-6595/acd476. [Online]. Available: https://dx.doi.org/10.1088/1361-6595/acd476.

[36] L. Brieda and M. Keidar, "Development of the starfish plasma simulation code and update on multiscale modeling of hall thrusters," in *48th AIAA/ASME/SAE/ASEE Joint Propulsion Conference & Exhibit*, 2012, p. 4015.

[37] A. Domínguez-Vázquez, F. Cichocki, M. Merino, P. Fajardo, and E. Ahedo, "Axisymmetric plasma plume characterization with 2D and 3D particle codes," *Plasma Sources Science and Technology*, vol. 27, no. 10, p. 104 009, 2018. DOI: 10.1088/1361-6595/aae702.

[38] J. M. Fife, "Hybrid-pic modeling and electrostatic probe survey of hall thrusters," Ph.D. dissertation, Massachusetts Institute of Technology, 1998.

[39] F. I. Parra, E. Ahedo, J. M. Fife, and M. Martínez-Sánchez, "A two-dimensional hybrid model of the Hall thruster discharge," *Journal of Applied Physics*, vol. 100, no. 2, p. 023 304, 2006.

[40] J. Zhou, A. Domínguez-Vázquez, P. Fajardo, and E. Ahedo, "Magnetized fluid electron model within a two-dimensional hybrid simulation code for electrodeless plasma thrusters," *Plasma Sources Science and Technology*, vol. 31, no. 4, p. 045 021, 2022.

[41] A. Sánchez-Villar, J. Zhou, M. Merino, and E. Ahedo, "Coupled plasma transport and electromagnetic wave simulation of an ECR thruster," *Plasma Sources Science and Technology*, vol. 30, no. 4, p. 045 005, 2021. DOI: 10.1088/1361-6595/abde20.

[42] M. Magarotto, S. Di Fede, N. Souhair, S. Andrews, and F. Ponti, "Numerical suite for cathodeless plasma thrusters," *Acta Astronautica*, vol. 197, pp. 126–138, 2022.

[43] A. Sánchez-Villar, M. Merino, and E. Ahedo, "A numerical parametric investigation on the optimal design and operation of coaxial ECR thrusters," in *Space Propulsion Conference 2021*, March 17-19: Association Aéronautique et Astronautique de France, 2021.

[44] M. Merino, J. Mauriño, and E. Ahedo, "Kinetic electron model for plasma thruster plumes," *Plasma Sources Science and Technology*, vol. 27, no. 3, p. 035 013, 2018. DOI: 10.1088/1361-6595/aab3a1.

[45] G. Sánchez-Arriaga, J. Zhou, E. Ahedo, M. Martínez-Sánchez, and J. J. Ramos, "Kinetic features and non-stationary electron trapping in paraxial magnetic nozzles," *Plasma Sources Science and Technology*, vol. 27, no. 3, p. 035 002, 2018.

[46] J. Zhou, G. Sánchez-Arriaga, and E. Ahedo, "Time-dependent expansion of a weakly-collisional plasma beam in a paraxial magnetic nozzle," *Plasma Sources Science and Technology*, vol. 30, no. 4, p. 045 009, 2021. DOI: 10.1088/1361-6595/abeff3.

[47] A. Marín-Cebrián, A. Domínguez-Vázquez, P. Fajardo, and E. Ahedo, "Kinetic plasma dynamics in a radial model of a Hall thruster with a curved magnetic field," *Plasma Sources Science and Technology*, vol. 31, no. 11, p. 115 003, Nov. 2022. DOI: 10.1088/1361-6595/ac9a6b. [Online]. Available: https://doi.org/10.1088/1361-6595/ac9a6b.

[48] E. Bello-Benítez and E. Ahedo, "Axial-azimuthal, high-frequency modes from global linear-stability model of a Hall thruster," *Plasma Sources Science and Technology*, vol. 30, no. 3, p. 035 003, Mar. 2021. DOI: 10.1088/1361-6595/abde21.

[49] P. Jiménez, J. Zhou, J. Navarro-Cavallé, P. Fajardo, M. Merino, and E. Ahedo, "Analysis of a cusped helicon plasma thruster discharge," *Plasma Sources Science and Technology*, vol. 32, no. 10, p. 105 013, 2023. DOI: 10.1088/1361-6595/ad01da.

[50] C. Birdsall and A. Langdon, *Plasma Physics via Computer Simulation*. Bristol: Institute of Physics Publishing, 1991.

[51] F. Taccogna, R. Schneider, S. Longo, and M. Capitelli, "Kinetic simulations of a plasma thruster," *Plasma Sources Science and Technology*, vol. 17, no. 2, p. 024 003, 2008.

[52] A. Marín-Cebrián, A. Domínguez-Vázquez, P. Fajardo, and E. Ahedo, "Radial particle-in-cell simulations of a Hall Thruster discharge with different anomalous transport models," in *Space Propulsion Conference 2021*, March 17-19: Association Aéronautique et Astronautique de France, 2021.

[53] T. Lafleur, S. Baalrud, and P. Chabert, "Theory for the anomalous electron transport in hall effect thrusters. i. insights from particle-in-cell simulations," *Physics of Plasmas*, vol. 23, p. 053 502, 2016.

[54] J. Adam, A. Herón, and G. Laval, "Study of stationary plasma thrusters using two-dimensional fully kinetic simulations," *Physics of Plasmas*, vol. 11, pp. 295–305, 2004.

[55] P. Coche and L. Garrigues, "A two-dimensional (azimuthal-axial) particle-in-cell model of a hall thruster," *Physics of Plasmas*, vol. 21, p. 023 503, 2014.

[56] T. Lafleur and P. Chabert, "The role of instability-enhanced friction on 'anomalous' electron and ion transport in Hall-effect thrusters," *Plasma Sources Science and Technology*, vol. 27, p. 015 003, 2017.

[57] F. Taccogna, F. Cichocki, D. Eremin, G. Fubiani, and L. Garrigues, "Plasma propulsion modeling with particle-based algorithms," *Journal of Applied Physics*, vol. 134, no. 15, p. 150 901, Oct. 2023. DOI: 10.1063/5.0153862. [Online]. Available: https://doi.org/10.1063/5.0153862.

[58] W. Villafana, B. Cuenot, and O. Vermorel, "3d particle-in-cell study of the electron drift instability in a Hall thruster using unstructured grids," *Physics of Plasmas*, vol. 30, no. 3, 2023. DOI: 10.1063/5.0133963. [Online]. Available: https://doi.org/10.1063/5.0133963.

[59] C. Cui and J. Wang, "Grid-based Vlasov simulation of collisionless plasma expansion," *Physics of Plasmas*, vol. 9, no. 28, p. 093 510, 2021. DOI: 10.1063/5.0058635.

[60] J. Porto, P.-Q. Elias, and A. Ciardi, "Anisotropic electron heating in an electron cyclotron resonance thruster with magnetic nozzle," *Physics of Plasmas*, vol. 30, no. 2, 2023.

[61] J. C. P. Hernandez and P.-Q. Elias, "Two-dimensional kinetic modeling of the power deposition in a coaxial ECR thruster," in *International Electric Propulsion Conference 2022 (IEPC 2022)*, 2022.

[62] A. B. Langdon, "Effects of the spatial grid in simulation plasmas," *Journal of Computational Physics*, vol. 6, no. 2, pp. 247–267, 1970.

[63] D. W. Hewett, "Elimination of electromagnetic radiation in plasma simulation: The Darwin or magneto inductive approximation," in *Space Plasma Simulations: Proceedings of the Second International School for Space Simulations, Kapaa, Hawaii, February 4–15, 1985*, Springer, 1985, pp. 29–40.

[64] G. Chen and L. Chacón, "An energy-and charge-conserving, nonlinearly implicit, electromagnetic 1d-3v Vlasov–Darwin particle-in-cell algorithm," *Computer Physics Communications*, vol. 185, no. 10, pp. 2391–2402, 2014.

[65] G. Chen, L. Chacón, and D. C. Barnes, "An energy-and charge-conserving, implicit, electrostatic particle-in-cell algorithm," *Journal of Computational Physics*, vol. 230, no. 18, pp. 7018–7036, 2011.

[66] L. Chacón, G. Chen, and D. Barnes, "A charge-and energy-conserving implicit, electrostatic particle-in-cell algorithm on mapped computational meshes," *Journal of Computational Physics*, vol. 233, pp. 1–9, 2013.

[67] X. Chen and J. Sanmartin, "Low work-function thermionic emission and orbital-motion-limited ion collection at bare-tether cathodic contact," *Physics of Plasmas*, vol. 22, no. 5, p. 053 504, 2015. DOI: 10.1063/1.4919945.

[68] D. Eremin, "An energy-and charge-conserving electrostatic implicit particle-in-cell algorithm for simulations of collisional bounded plasmas," *Journal of Computational Physics*, vol. 452, p. 110 934, 2022.

[69] S. Mattei, K. Nishida, M. Onai, J. Lettry, M. Tran, and A. Hatayama, "A fully-implicit particle-in-cell Monte Carlo collision code for the simulation of inductively coupled plasmas," *Journal of Computational Physics*, vol. 350, pp. 891–906, 2017.

[70] D. Eremin *et al.*, "Electron dynamics in planar radio frequency magnetron plasmas: Ii. heating and energization mechanisms studied via a 2d3v particle-in-cell/Monte Carlo code," *Plasma Sources Science and Technology*, vol. 32, no. 4, p. 045 008, 2023.

[71] P. Jiménez, L. Chacón, and M. Merino, "An implicit, conservative electrostatic particle-in-cell algorithm for paraxial magnetic nozzles," *Journal of Computational Physics*, p. 112 826, 2024.

[72] J. D. Jackson, *Classical electrodynamics*. American Association of Physics Teachers, College Park, MD, 1999.

[73] M. Merino *et al.*, "Wave propagation and absorption in ECR plasma thrusters," in 35^{th} *International Electric Propulsion Conference*, Atlanta, GA: Electric Rocket Propulsion Society, 2017.

[74] S. Shinohara, *High-Density Helicon Plasma Science: From Basics to Applications*. Springer Nature, 2023.

[75] F. Filleul *et al.*, "Helicon waves in a converging-diverging magnetoplasma," *Plasma Sources Science and Technology*, vol. 32, no. 11, p. 115 015, 2023.

[76] D. Arnush, "The role of trivelpiece–gould waves in antenna coupling to helicon waves," *Physics of Plasmas*, vol. 7, p. 3042, 2000.

[77] J.-M. Jin and D. J. Riley, *Finite element analysis of antennas and arrays*. John Wiley & Sons, 2009.

[78] D. M. Pozar, *Microwave engineering*. John wiley & sons, 2011.

[79] J.-C. Nédélec, "A new family of mixed finite elements in $\mathbb{R}^3$," *Numerische Mathematik*, vol. 50, no. 1, pp. 57–81, 1986.

[80] L. García-Castillo and M. Salazar-Palma, "Second-order nédélec tetrahedral element for computational electromagnetics," *International Journal of Numerical Modelling: Electronic Networks, Devices and Fields*, vol. 13, no. 2-3, pp. 261–287, 2000.

[81] A. Greenwood and J. Jin, "A novel efficient algorithm for scattering from a complex BOR using mixed finite elements and cylindrical PML," *IEEE transactions on antennas and propagation*, vol. 47, no. 4, pp. 620–629, 1999.

[82] T. Lafleur, C. Charles, and R. Boswell, "Plasma control by modification of helicon wave propagation in low magnetic fields," *Physics of Plasmas*, vol. 17, no. 7, 2010.

[83] R. Kinder and M. Kushner, "Noncollisional heating and electron energy distributions in magnetically enhanced inductively coupled and helicon plasma sources," *Journal of Applied Physics*, vol. 90, p. 3699, 2001.

[84] I. Kamenski and G. Borg, "An evaluation of different antenna designs for helicon wave excitation in a cylindrical plasma source," *Physics of Plasmas*, vol. 3, p. 4396, 1996.

[85] A. Logg, K.-A. Mardal, and G. Wells, *Automated solution of differential equations by the finite element method: The FEniCS book*. Springer Science & Business Media, 2012, vol. 84.

[86] C. Geuzaine and J.-F. Remacle, "Gmsh: A 3-D finite element mesh generator with built-in pre-and post-processing facilities," *International journal for numerical methods in engineering*, vol. 79, no. 11, pp. 1309–1331, 2009.

[87] V. Hernandez, J. E. Roman, and V. Vidal, "Slepc: A scalable and flexible toolkit for the solution of eigenvalue problems," *ACM Transactions on Mathematical Software (TOMS)*, vol. 31, no. 3, pp. 351–362, 2005.

[88] J. Zhou, "Modeling and simulation of the plasma discharge in a radiofrequency thruster," Ph.D. dissertation, Universidad Carlos III de Madrid, Leganés, Spain, 2021.

[89] G. W. Stewart, "A krylov–schur algorithm for large eigenproblems," *SIAM Journal on Matrix Analysis and Applications*, vol. 23, no. 3, pp. 601–614, 2002.

[90] G. Chen, L. Chacón, and D. C. Barnes, "An efficient mixed-precision, hybrid cpu–gpu implementation of a nonlinearly implicit one-dimensional particle-in-cell algorithm," *Journal of Computational Physics*, vol. 231, no. 16, pp. 5374–5388, 2012.

[91] K. Yee, "Numerical solution of initial boundary value problems involving maxwell's equations in isotropic media," *IEEE Transactions on antennas and propagation*, vol. 14, no. 3, pp. 302–307, 1966.

[92] T. Ziemba, J. Carscadden, J. Slough, J. Prager, and R. Winglee, "High power helicon thruster," in *41th AIAA/ASME/SAE/ASEE Joint Propulsion Conference & Exhibit*, ser. AIAA 2005-4119, 2005.

[93] M. West, C. Charles, and R. Boswell, "Testing a helicon double layer thruster immersed in a space-simulation chamber," *Journal of Propulsion and Power*, vol. 24, no. 1, pp. 134–141, 2008.

[94] D. Pavarin *et al.*, "Design of 50W helicon plasma thruster," in *31th International Electric Propulsion Conference*, ser. IEPC 2009-205, 2009.

[95] J. Navarro-Cavallé, M. Wijnen, P. Fajardo, M. Merino, and E. Ahedo, "Experimental performances of a 1 kw hpt by means of plasma diagnostics," in 35^{th} *International Electric Propulsion Conference*, Atlanta, GA: Electric Rocket Propulsion Society, 2017.

[96] O. Batishchev, "Minihelicon plasma thruster," *IEEE Transactions on Plasma Science*, vol. 37, no. 8, pp. 1563–1571, 2009.

[97] J. Navarro-Cavallé *et al.*, "Development and characterization of the helicon plasma thruster prototype hpt05m," in 36^{th} *International Electric Propulsion Conference*, Vienna, Austria: Electric Rocket Propulsion Society, 2019.

[98] K. Takahashi, "Helicon–type radiofrequency plasma thrusters and magnetic plasma nozzles," *Reviews of Modern Plasma Physics*, vol. 3, p. 3, 2019. DOI: 10.1007/s41614-019-0024-2.

[99] F. Chen, "Plasma ionization by helicon waves," *Plasma Physics and Controlled Fusion*, vol. 33, no. 4, p. 339, 1991.

[100] F. Chen, "Physics of helicon discharges," *Physics of Plasmas*, vol. 3, no. 5, pp. 1783–1793, 1996.

[101] M. Merino and E. Ahedo, "Magnetic nozzles for space plasma thrusters," in *Encyclopedia of Plasma Technology*, J. L. Shohet, Ed., vol. 2, Taylor and Francis, 2016, pp. 1329–1351.

[102] M. Martínez-Sánchez, J. Navarro-Cavallé, and E. Ahedo, "Electron cooling and finite potential drop in a magnetized plasma expansion," *Physics of Plasmas*, vol. 22, no. 5, p. 053 501, 2015. DOI: 10.1063/1.4919627.

[103] K. Takahashi, "Magnetic nozzle radiofrequency plasma thruster approaching twenty percent thruster efficiency," *Scientific Reports*, vol. 11, no. 1, pp. 1–12, 2021. DOI: 10.1038/s41598-021-82471-2.

[104] G. Chen and L. L. Raja, "Fluid modeling of electron heating in low-pressure, high-frequency capacitively coupled plasma discharges," *Journal of applied physics*, vol. 96, no. 11, pp. 6073–6081, 2004.

[105] D. Bose, T. Govindan, and M. Meyyappan, "Modeling of a helicon plasma source," *IEEE Transactions on Plasma Science*, vol. 31, pp. 464–470, 2003.

[106] M. Magarotto, D. Melazzi, and D. Pavarin, "3d-virtus: Equilibrium condition solver of radio-frequency magnetized plasma discharges for space applications," *Computer Physics Communications*, vol. 247, p. 106 953, 2020.

[107] J. Zhou, D. Pérez-Grande, P. Fajardo, and E. Ahedo, "Numerical treatment of a magnetized electron fluid within an electromagnetic plasma thruster code," *Plasma Sources Science and Technology*, vol. 28, no. 11, p. 115 004, 2019.

[108] P. Jiménez, M. Merino, and E. Ahedo, "Preliminary investigation of the electromagnetic fields in the far plume of a helicon plasma thruster," in *Space Propulsion Conference 2021*, Association Aéronautique et Astronautique de France, 2021.

[109] B. Breizman and A. Arefiev, "Radially localized helicon modes in nonuniform plasma," *Physical Review Letters*, vol. 84, pp. 3863–3866, 2000.

[110] D. Blackwell, T. Madziwa, D. Arnush, and F. Chen, "Evidence for trivelpiece-gould modes in a helicon discharge," *Physical review letters*, vol. 88, no. 14, p. 145 002, 2002.

[111] A. Domínguez-Vázquez, "Axisymmetric simulation codes for hall effect thrusters and plasma plumes," Ph.D. dissertation, Universidad Carlos III de Madrid, Leganés, Spain, 2019.

[112] B. Tian, "Modeling of physical processes in radio-frequency plasma thrusters," Ph.D. dissertation, 2017.

[113] J. Zhou, P. Jiménez, M. Merino, P. Fajardo, and E. Ahedo, "Numerical Simulations of the Plasma discharge in a Helicon Plasma Thruster," in 36^{th} *International Electric Propulsion Conference*, Vienna, Austria: Electric Rocket Propulsion Society, 2019.

[114] C.-D. Munz, P. Omnes, R. Schneider, E. Sonnendrücker, and U. Voss, "Divergence correction techniques for maxwell solvers based on a hyperbolic model," *Journal of Computational Physics*, vol. 161, no. 2, pp. 484–511, 2000.

[115] J.-C. Nédélec, "Mixed finite elements in $\mathbb{R}^3$," *Numerische Mathematik*, vol. 35, no. 3, pp. 315–341, 1980.

[116] M. U. Siddiqui, C. Cretel, J. Synowiec, A. G. Hsu, J. A. Young, and R. Spektor, "First performance measurements of the phase four rf thruster," Paper IEPC-2017-431. 2017.

[117] F. Trezzolani *et al.*, "Development and testing of a miniature helicon plasma thruster," in *35th International Electric Propulsion Conference, Atlanta, GA, IEPC-2017-519*, 2017.

[118] K. Takahashi and A. Ando, "Enhancement of axial momentum lost to the radial wall by the upstream magnetic field in a helicon source," *Plasma Physics and Controlled Fusion*, vol. 59, p. 054 007, 2017.

[119] F. Taccogna and L. Garrigues, "Latest progress in Hall thrusters plasma modelling," *Reviews of Modern Plasma Physics*, vol. 3, no. 1, p. 12, 2019.

[120] V. Virko, Y. Virko, V. Slobodyan, and K. Shamrai, "The effect of magnetic configuration on ion acceleration from a compact helicon source with permanent magnets," *Plasma Sources Science and Technology*, vol. 19, p. 015 004, 2010.

[121] S. Ito, T. Nakamura, H. Nishida, and S. Shinohara, "Performance of rf plasma thruster for various magnetic field configurations by permanent magnets," in *Proceedings of the 34th International Electric Propulsion Conference*, ser. IEPC-2015-412, 2015.

[122] K. Takahashi, "Comparison of vacuum-immersed helicon thrusters terminated by upstream magnetic and physical walls," *Journal of Physics D: Applied Physics*, 2023.

[123] M. Ruiz *et al.*, "Results of the first helicon plasma thruster (hpt) coupling test campaign within the hipatia project," in *37th International Electric Propulsion Conference*, 2022.

[124] J. Perales-Díaz *et al.*, "Hybrid plasma simulations of a magnetically shielded Hall thruster," *Journal of Applied Physics*, vol. 131, no. 10, p. 103 302, 2022. DOI: 10.1063/5.0065220.

[125] A. E. Vinci and S. Mazouffre, "Enhanced electron heating in the magnetic nozzle of a radio-frequency plasma via electron cyclotron resonance," *Europhysics Letters*, vol. 141, no. 4, p. 44 002, 2023.

[126] C. Chung, S. Kim, and H.-Y. Chang, "Electron cyclotron resonance in a weakly magnetized radio-frequency inductive discharge," *Physical review letters*, vol. 88, no. 9, p. 095 002, 2002.

[127] T. Lafleur, C. Charles, and R. Boswell, "Electron–cyclotron damping of helicon waves in low diverging magnetic fields," *Physics of Plasmas*, vol. 18, no. 4, 2011.

[128] Á. Sánchez-Villar *et al.*, "Comparison of a hybrid model and experimental measurements for a dielectric-coated coaxial ECR thruster," *Plasma Sources Science and Technology*, vol. 32, no. 1, p. 014 002, 2023. DOI: 10.1088/1361-6595/acb00c.

[129] A. E. Vinci, S. Mazouffre, V. Gómez, P. Fajardo, and J. Navarro-Cavallé, "Laser-induced fluorescence spectroscopy on xenon atoms and ions in the magnetic nozzle of a helicon plasma thruster," *Plasma Sources Science and Technology*, vol. 31, no. 9, p. 095 007, 2022.

[130] I. D. Sudit and F. F. Chen, "Rf compensated probes for high-density discharges," *Plasma Sources Science and Technology*, vol. 3, no. 2, p. 162, 1994.

[131] R. B. Lobbia and B. E. Beal, "Recommended practice for use of langmuir probes in electric propulsion testing," *Journal of Propulsion and Power*, vol. 33, no. 3, pp. 566–581, 2017. DOI: 10.2514/1.B35531.

[132] M. Merino and E. Ahedo, "Fully magnetized plasma flow in a magnetic nozzle," *Physics of Plasmas*, vol. 23, no. 2, p. 023 506, 2016. DOI: 10.1063/1.4941975.

[133] J. M. Little and E. Y. Choueiri, "Electron demagnetization in a magnetically expanding plasma," *Physical review letters*, vol. 123, no. 14, p. 145 001, 2019.

[134] A. Eduardo, "Using electron fluid models to analyze plasma thruster discharges," *Journal of Electric Propulsion*, vol. 2, no. 1, p. 2, 2023.

[135] J. Little and E. Choueiri, "Electron cooling in a magnetically expanding plasma," *Physical Review Letters*, vol. 117, no. 22, p. 225 003, 2016.

[136] E. Ahedo, S. Correyero, J. Navarro, and M. Merino, "Macroscopic and parametric study of a kinetic plasma expansion in a paraxial magnetic nozzle," *Plasma Sources Science and Technology*, vol. 29, no. 4, p. 045 017, 2020. DOI: 10.1088/1361-6595/ab7855.

[137] J. Y. Kim, K.-J. Chung, K. Takahashi, M. Merino, and E. Ahedo, "Kinetic electron cooling in magnetic nozzles: Experiments and modeling," *arXiv preprint arXiv:2212.07161*, 2022.

[138] A. Domínguez-Vázquez, J. Zhou, A. Sevillano-González, P. Fajardo, and E. Ahedo, "Analysis of the electron downstream boundary conditions in a 2D hybrid code for Hall thrusters," in 37^{th} *International Electric Propulsion Conference*, Boston, MA, June 19-23: Electric Rocket Propulsion Society, 2022.

[139] K. Takahashi, Y. Takao, and A. Ando, "Modifications of plasma density profile and thrust by neutral injection in a helicon plasma thruster," *Applied Physics Letters*, vol. 109, no. 19, 2016.

[140] M. Hayashi, "Bibliography of electron and photon cross sections with atoms and molecules published in the 20th century. Xenon," National Institute for Fusion Science, Tech. Rep., 2003.

[141] M. Lieberman and A. Lichtenberg, *Principles of plasma discharges and materials processing*. John Wiley and Sons, Hoboken, NJ, 2005.

[142] P. Monk, *Finite element methods for Maxwell's equations*. Oxford University Press, 2003.

[143] F. Chen, "The low-field density peak in helicon discharges," *Physics of Plasmas*, vol. 10, p. 2586, 2003.

[144] B. Wachs and B. Jorns, "Background pressure effects on ion dynamics in a low-power magnetic nozzle thruster," *Plasma Sources Science and Technology*, vol. 29, no. 4, p. 045 002, 2020.

[145] M. Merino, J. Nuez, and E. Ahedo, "Fluid-kinetic model of a propulsive magnetic nozzle," *Plasma Sources Science and Technology*, vol. 30, no. 11, p. 115 006, 2021. DOI: 10.1088/1361-6595/ac2a0b.

[146] N. Souhair, M. Magarotto, E. Majorana, F. Ponti, and D. Pavarin, "Development of a lumping methodology for the analysis of the excited states in plasma discharges operated with argon, neon, krypton, and xenon," *Physics of Plasmas*, vol. 28, no. 9, p. 093 504, 2021.

[147] T. Lafleur, "Helicon plasma thruster discharge model," *Physics of Plasmas*, vol. 21, no. 4, p. 043 507, 2014.

[148] J. M. Mulcahy *et al.*, "Heat flux estimation of a plasma rocket helicon source by solution of the inverse heat conduction problem," *International Journal of Heat and Mass Transfer*, vol. 52, no. 9-10, pp. 2343–2357, 2009.

[149] B. Wachs and B. Jorns, "Background pressure effects on ion dynamics in a low-power magnetic nozzle thruster," *Plasma Sources Science and Technology*, vol. 29, no. 4, p. 045 002, 2020.

[150] S. Andersen, V. Jensen, P. Nielsen, and N. D'Angelo, "Continuous supersonic plasma wind tunnel," *Phys. Fluids*, vol. 12, no. 3, pp. 557–560, 1969.

[151] H. Kuninaka and S. Satori, "Development and demonstration of a cathodeless electron cyclotron resonance ion thruster," *Journal of Propulsion and Power*, vol. 14, no. 6, pp. 1022–1026, 1998.

[152] T. Vialis, "Développement d'un propulseur plasma à résonance cyclotron électronique pour les satellites," Ph.D. dissertation, SORBONNE UNIVERSITE, 2018.

[153] A. Sasoh and Y. Arakawa, "Electromagnetic effects in an applied-field magnetoplasmadynamic thruster," *Journal of Propulsion and Power*, vol. 8, no. 1, pp. 98–102, 1992.

[154] G. Krülle, M. Auweter-Kurtz, and A. Sasoh, "Technology and application aspects of applied field magnetoplasmadynamic propulsion," *J. Propulsion and Power*, vol. 14, no. 5, pp. 754–763, 1998.

[155] Y. Hu and J. Wang, "Fully kinetic simulations of collisionless, mesothermal plasma emission: Macroscopic plume structure and microscopic electron characteristics," *Physics of Plasmas*, vol. 24, no. 3, p. 033 510, 2017.

[156] L. Brieda, "Model for steady-state fully kinetic ion beam neutralization studies," *IEEE Transactions on Plasma Science*, vol. 46, no. 3, pp. 556–562, 2018.

[157] M. Li, M. Merino, E. Ahedo, and H. Tang, "On electron boundary conditions in PIC plasma thruster plume simulations," *Plasma Sources Science and Technology*, vol. 28, no. 03, p. 034 004, 2019. DOI: 10.1088/1361-6595/ab0949.

[158] S. Andrews, S. Di Fede, and M. Magarotto, "Fully kinetic model of plasma expansion in a magnetic nozzle," *Plasma Sources Science and Technology*, 2022.

[159] L. Chacón, G. Chen, and D. Barnes, "A charge-and energy-conserving implicit, electrostatic particle-in-cell algorithm on mapped computational meshes," *Journal of Computational Physics*, vol. 233, pp. 1–9, 2013.

[160] G. Chen and L. Chacón, "An energy-and charge-conserving, nonlinearly implicit, electromagnetic 1d-3v vlasov–darwin particle-in-cell algorithm," *Computer Physics Communications*, vol. 185, no. 10, pp. 2391–2402, 2014.

[161] G. Chen and L. Chacon, "A multi-dimensional, energy-and charge-conserving, nonlinearly implicit, electromagnetic vlasov–darwin particle-in-cell algorithm," *Computer Physics Communications*, vol. 197, pp. 73–87, 2015.

[162] G. Chen and L. Chacón, "An implicit, conservative and asymptotic-preserving electrostatic particle-in-cell algorithm for arbitrarily magnetized plasmas in uniform magnetic fields," *arXiv preprint arXiv:2205.09187*, 2022.

[163] Z. Chen *et al.*, "Electric potential barriers in the magnetic nozzle," *Phys. Rev. E*, vol. 101, p. 053 208, 5 May 2020. DOI: 10.1103/PhysRevE.101.053208. [Online]. Available: https://link.aps.org/doi/10.1103/PhysRevE.101.053208.

[164] R. D. Hazeltine and J. D. Meiss, *Plasma confinement*. Courier Corporation, 2003.

[165] D. W. Swift, "Use of a hybrid code for global-scale plasma simulation," *Journal of Computational Physics*, vol. 126, no. 1, pp. 109–121, 1996.

[166] J. Wang, D. Kondrashov, P. Liewer, and S. Karmesin, "Three-dimensional deformable-grid electromagnetic particle-in-cell for parallel computers," *Journal of plasma physics*, vol. 61, no. 3, pp. 367–389, 1999.

[167] C. Fichtl, J. Finn, and K. Cartwright, "An arbitrary curvilinear-coordinate method for particle-in-cell modeling," *Computational Science & Discovery*, vol. 5, no. 1, p. 014 011, 2012.

[168] G. Chen, L. Chacón, C. A. Leibs, D. A. Knoll, and W. Taitano, "Fluid preconditioning for newton–krylov-based, fully implicit, electrostatic particle-in-cell simulations," *Journal of computational physics*, vol. 258, pp. 555–567, 2014.

[169] O. Koshkarov, L. Chacón, G. Chen, and L. F. Ricketson, "Fast nonlinear iterative solver for an implicit, energy-conserving, asymptotic-preserving charged-particle orbit integrator," *Journal of Computational Physics*, vol. 459, no. LA-UR-21-30956, 2022.

[170] Y. Saad and M. H. Schultz, "Gmres: A generalized minimal residual algorithm for solving nonsymmetric linear systems," *SIAM Journal on scientific and statistical computing*, vol. 7, no. 3, pp. 856–869, 1986.

[171] K. Cartwright, J. Verboncoeur, and C. Birdsall, "Loading and injection of maxwellian distributions in particle simulations," *Journal of Computational Physics*, vol. 162, no. 2, pp. 483–513, 2000.

[172] J. Ramos, M. Merino, and E. Ahedo, "Three dimensional fluid-kinetic model of a magnetically guided plasma jet," *Physics of Plasmas*, vol. 25, no. 6, p. 061 206, 2018. DOI: 10.1063/1.5026972.

[173] G. Chen and L. Chacon, "A multi-dimensional, energy-and charge-conserving, nonlinearly implicit, electromagnetic Vlasov–Darwin particle-in-cell algorithm," *Computer Physics Communications*, vol. 197, pp. 73–87, 2015.

[174] G. Sánchez-Arriaga, Private Communication, 2023.

[175] D. Barnes and L. Chacón, "Finite spatial-grid effects in energy-conserving particle-in-cell algorithms," *Computer Physics Communications*, vol. 258, p. 107 560, 2021.

[176] L. F. Ricketson and L. Chacón, "An energy-conserving and asymptotic-preserving charged-particle orbit implicit time integrator for arbitrary electromagnetic fields," *Journal of Computational Physics*, vol. 418, p. 109 639, 2020.